INAUGURAL-DISSERTATION

zur Erlangung der Doktorwürde

der

Naturwissenschaftlich-Mathematischen Gesamtfakultät

der

Ruprecht-Karls-Universität Heidelberg

vorgelegt von

M.Sc. Katharina Rück, geb. Rübenacker

aus Würzburg

INAUGURAL-DISSERTATION

zur Erlangung der Doktorwürde

der

Naturwissenschaftlich-Mathematischen Gesamtfakultät

der

Ruprecht-Karls-Universität Heidelberg

vorgelegt von

M.Sc. Katharina Rück, geb. Rübenacker

aus Würzburg

Tag der mündlichen Prüfung: 14.07.2017

Synthesis and evaluation of novel picolinic acid-based bispidine ligands and their metal complexes for the application in nuclear medicine

Gutachter:

Prof. Dr. Peter Comba

Prof. Dr. Roland Krämer

This thesis has been accomplished at the Institute of Inorganic Chemistry at Heidelberg University from May 2014 until May 2017 and was supervised by Prof. Dr. Peter COMBA. Experimental work was also performed under the supervision of Dr. Holger STEPHAN at the Institute of Radiopharmaceutical Cancer Research of the Helmholtz Zentrum Dresden-Rossendorf (HZDR) in October 2015 as well as under the supervision of Prof. Dr. Chris ORVIG at the University of British Columbia (UBC) in Vancouver between June and August 2016. Experimental work with the bispa ligand Hbispa[1b] (**B1b**) was carried out by Laura GRIMM during her bachelor thesis. Radiochemical studies with the hexadentate bispa ligands were performed by coworkers of Dr. Holger STEPHAN and Prof. Dr. Jens PIETZSCH at HZDR. The radiochemistry of the octadentate bispa ligand was investigated at Tri University Meson Facility (TRIUMF), Canada's national laboratory for particle and nuclear physics and accelerator-based science in Vancouver, by Dr. Caterina RAMOGIDA with assistance of Una JERMILOVA.

Parts of the presented thesis have been or will be published in scientific journals:

- P. Comba, L. Grimm, C. Orvig, K. Rück, H. Wadepohl, Synthesis and coordination chemistry of hexadentate picolinic acid-based bispidine ligands, *Inorg. Chem.* **2016**, *55*, 12531-12543.
- P. Comba, U. Jermilova, C. Orvig, B. O. Patrick, C. F. Ramogida, K. Rück, C. Schneider, M. Starke, An octadentate picolinic acid-based bispidine ligand for the application in nuclear medicine, *Chem. Eur. J.*, *submitted manuscript*.
- P. Comba, M. Jakob, K. Rück, H. Wadepohl, Tuning of the properties of a picolinic acid-based bispidine ligand for stable copper(II) complexation, *manuscript in preparation*.
- P. Comba, M. Kerscher, K. Rück, M. Starke, Bispidines for tumor imaging, *manuscript in preparation*.

Oral presentations:

- Bispidine ligands for the application in targeted tumor imaging, *NanoTracking Meeting*, Lipari, Italy, **2015**.
- Bispidine ligands for the potential application in nuclear medicine, *German Coordination Chemistry Meeting*, Kiel, Germany, **2016**.

Research symposium poster publications:

- P. Comba, J. Pietzsch, K. Rübenacker, H. Stephan, H. Wadepohl, A new hexadentate picolinic acid-based bispidine ligand for the potential application in nuclear medicine, *German Coordination Chemistry Meeting*, Paderborn, Germany, **2015**.
- P. Comba, J. Pietzsch, K. Rück, M. Starke, H. Stephan, H. Wadepohl, Bispidine ligands for the potential application in nuclear medicine, *International Symposium on Radiopharmaceutical Sciences*, Dresden, Germany, **2017**.

Für meine wunderbare Familie.

Und ganz besonders für meinen Opa Karl,

der immer fest an mich geglaubt hat.

Table of molecules

Listed are all molecules that are mentioned in this thesis, serially numbered according to appearance as structural formula. While all compounds are given numerical designations, many have been labeled additionally with their particular acronyms. In some cases these abbreviations were used in the discussion instead of the respective numbers.

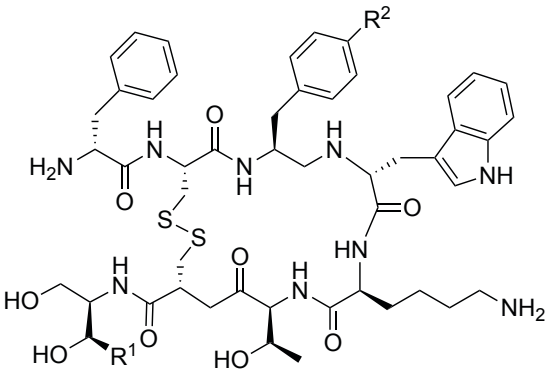

1, Octreotide (OC) R^1=H; R^2=H
2, Tyr3-Octreotide (TOC) R^1=H; R^2=OH
3, Octreotate (TATE) R^1=O; R^2=OH

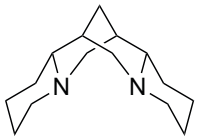

4, sparteine

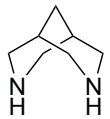

5, bispidine

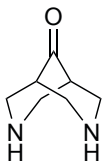

6, bispidone

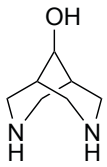

7, bispidol

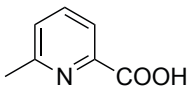

8

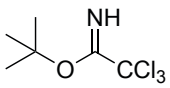

9

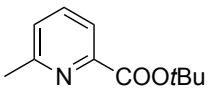

10

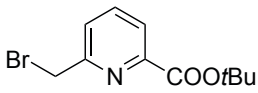

11

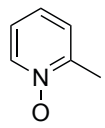

12

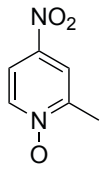

13

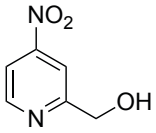

14

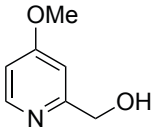

15

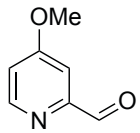

16

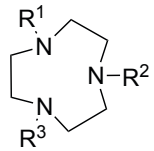

L1, tacn R^1=R^2=R^3=H
L4, NOTA R^1=R^2=R^3=CH_2-COOH
L12, NO1PA2PY R^1=CH_2pa; R^2=R^3=CH_2py

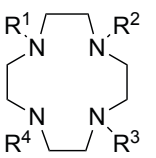

L2, cyclen R^1=R^2=R^3=R^4=H
L5, DOTA R^1=R^2=R^3=R^4=CH_2COOH
L13, DOTP R^1=R^2 =R^3=R^4=$CH_2PO(OH)_2$
L14, DO1PA R^1=CH_2pa; R^2=R^3=R^4=H

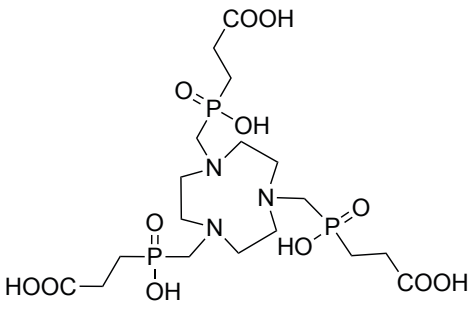

L27, TRAP

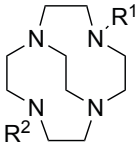

L15, CB-cyclen $R^1=R^2=H$
L16, CB-DO2A $R^1=R^2=CH_2COOH$

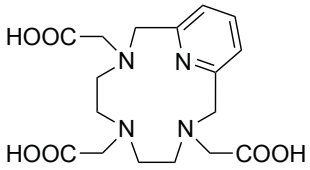

L28, PCTA

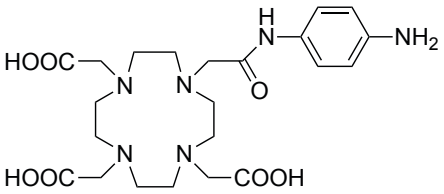

L33, DOTA-AA

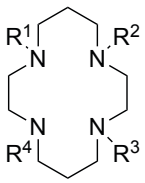

L3, cyclam $R^1=R^2=R^3=R^4=H$
L6, TETA $R^1=R^2=R^3=R^4=CH_2COOH$
L17, TETP $R^1=R^2=R^3=R^4=CH_2PO(OH)_2$
L18, TE1PA $R^1=CH_2pa$; $R^2=R^3=R^4=H$

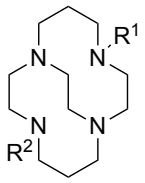

L19, CB-cyclam $R^1=R^2=H$
L20, CB-TE2A $R^1=R^2=CH_2COOH$
L21, CB-TE1A1P $R^1=CH_2COOH$; $R^2=CH_2PO(OH)_2$
L22, CB-TE2P $R^1=R^2=CH_2PO(OH)_2$
L23, CB-TE1PA $R^1=CH_2pa$; $R^2=H$

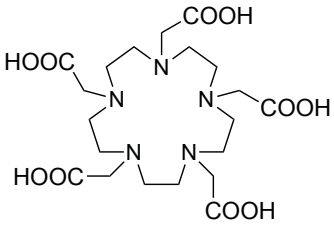

L7, PEPA

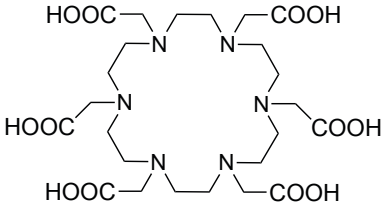

L8, HEHA

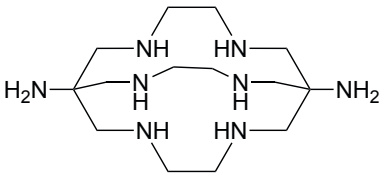

L24, DIAMSAR

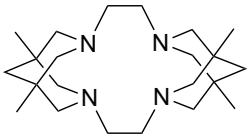

L37

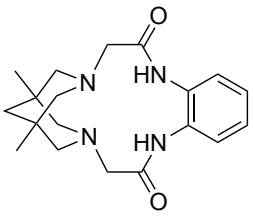

L25, BBDT

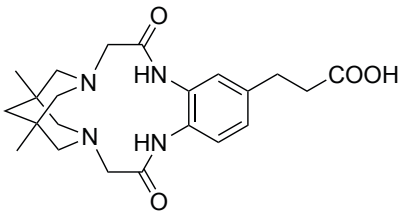

L38

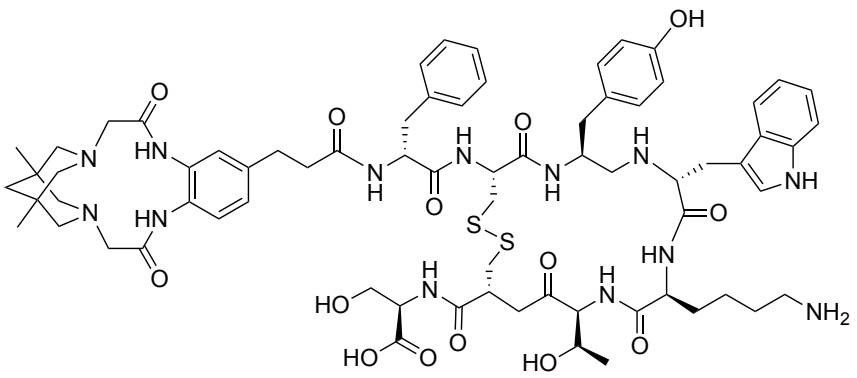

L38-TATE

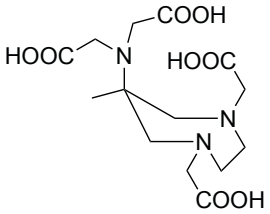

L29, AAZTA

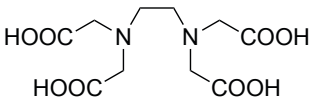

L9, EDTA

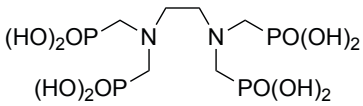

L36, EDTMP

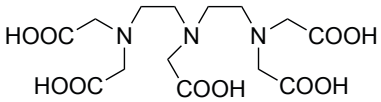

L10, DTPA

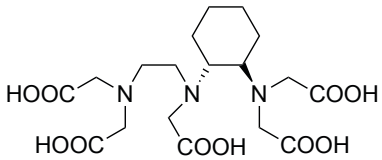

L34, CHX-*A*^{II}-DTPA

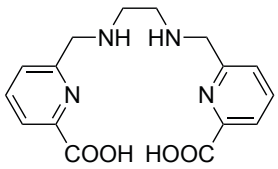

L30, H_2dedpa

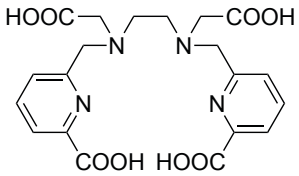

L35, H_4octapa

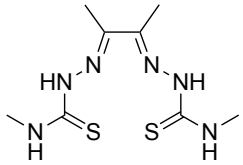

L11, ATSM

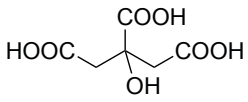

L26, citric acid

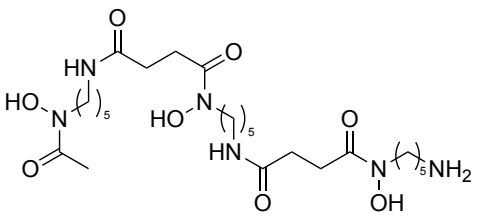

L31, DFO

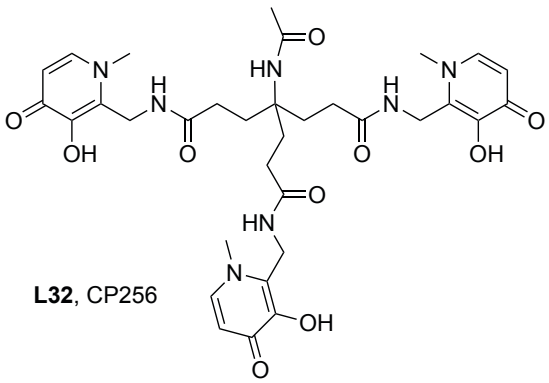

L32, CP256

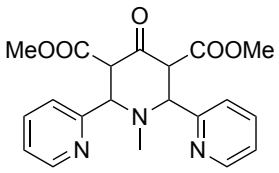

P1

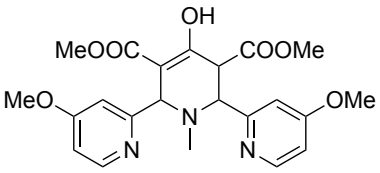

P2

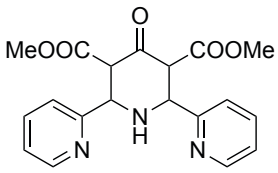

P3

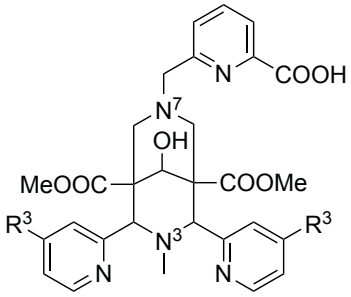

B1a, Hbispa[1a] R^3=H
(*p*-MeO)B1a, (R^3=OMe
(*p*-MeO)Hbispa[1a]

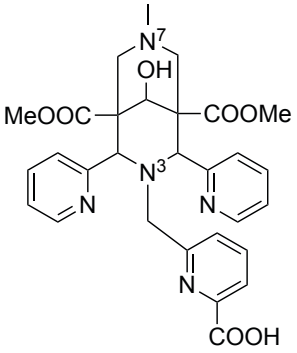

B1b, Hbispa[1b]

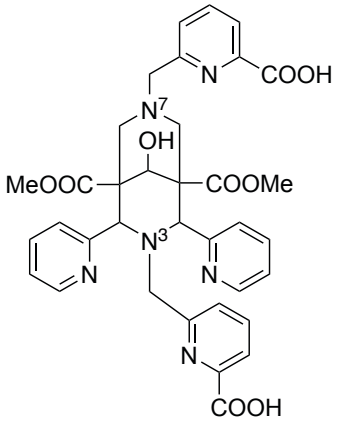

B2, H_2bispa[2]

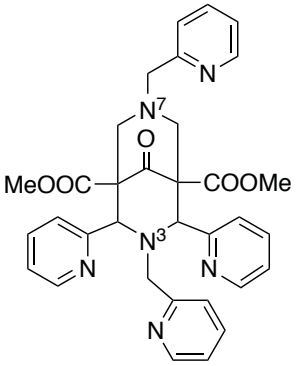

B3, N_2py_4

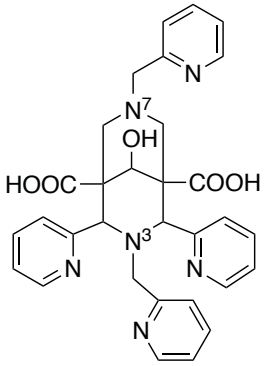

B6

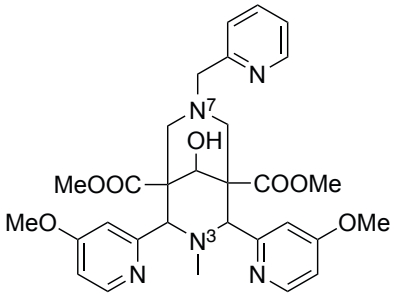

(*p*-MeO)B4

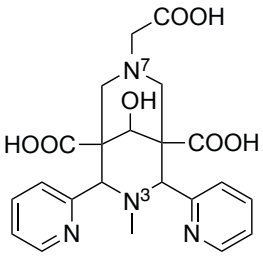

B5

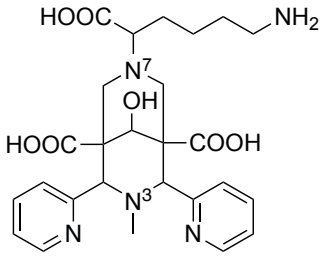

B7

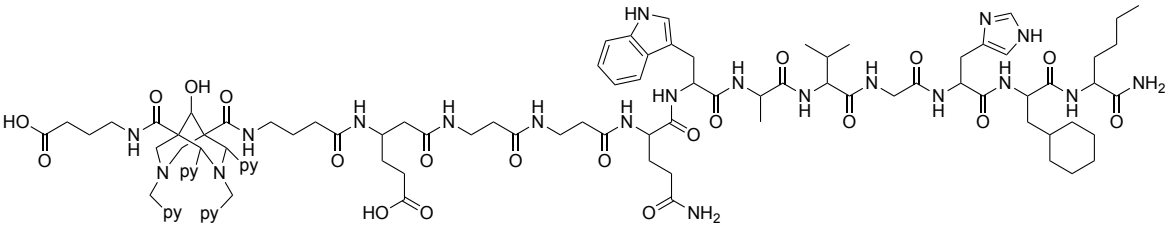

B6-BBN

The ligands are generally depicted in their uncharged form. In the corresponding metal complexes, these compounds can be completely or partially deprotonated. For optimized comprehensibility the numerical designations or acronyms of the molecules are used regardless of ligand protonation state. However, the protonation states can be derived from the oxidation states of the metal ions and the overall charge of the complexes. Instead of the complete notation $[M(ligand)](X)_n$ for metal-ligand complexes with counterions X, the abbreviation M-ligand is often used for clarity. In addition, the brackets commonly used to indicate radioactive nuclides are omitted, *i.e.* ^{64}Cu instead of $[^{64}Cu]$ *etc*.

List of abbreviations

A	AAZTA	1,4-bis-(hydroxycarbonyl methyl)-6-[bis(hydroxylcarbonyl methyl)]-amino-6-methyl-perhydro-1,4-diazepine
	AIBN	azobis(isobutyronitrile)
	AOM	angular overlap model
	ATSM	diacetyl-bis(*N*4-methylthiosemicarbazone)
B	BAT	brown adipose tissue
	BBDT	(1^1s,1^3s,1^5s,1^7s)-1^1,1^5-dimethyl-1^3,1^7,4,6-tetraaza-1(3,7)-bicyclo[3.3.1]nonana-5(1,2)-benzenacyclooctaphane-3,7-dione
	BBN	bombesin
	BFC	bifunctional chelator
	BODIPY	boron-dipyrromethene
	BSS	bismuth subsalicylate
C	CB	cross-bridged
	CB-cyclam	1,4,8,11-tetraazabicyclo[6.6.2]hexadecane
	CB-cyclen	1,4,7,10-tetraazabicyclo[5.5.2]tetradecane
	CB-DO2A	2,2'-(1,4,7,10-tetraazabicyclo[5.5.2]tetradecane-4,10-diyl)-diacetic acid
	CB-TE1A1P	2-(11-(phosphonomethyl)-1,4,8,11-tetraazabicyclo[6.6.2]hexadecan-4-yl)acetic acid
	CB-TE1PA	6-((1,4,8,11-tetraazabicyclo[6.6.2]hexadecan-4-yl)methyl)-picolinic acid
	CB-TE2A	2,2'-(1,4,8,11-tetraazabicyclo[6.6.2]hexadecane-4,11-diyl)diacetic acid
	CB-TE2P	((1,4,8,11-tetraazabicyclo[6.6.2]hexadecane-4,11-diyl)bis-(methylene))bis(phosphonic acid)
	CCDC	Cambridge Crystallographic Data Centre
	CHX-A''-DTPA	2,2'-((2-(((1*R*,2*S*)-2-(bis(carboxymethyl)amino)cyclo-hexyl)-(carboxymethyl)amino)ethyl)azanediyl)diacetic acid
	CN	coordination number
	COSY	correlation spectroscopy
	CP256	4-acetylamino-4-[2-[(3-hydroxy-1,6-dimethyl-4-oxo-1,4-dihydro-pyridin-2-ylmethyl)-carbamoyl]-ethyl]-heptane-dioic acid bis-[(3-hydroxy-1,6-dimethyl-4-oxo-1,4-dihydro-pyridin-2-ylmethyl)-amide]

	CT	computed tomography
	cyclam	1,4,8,11-tetraazacyclotetradecane
	cyclen	1,4,7,10-tetrazacyclododecane
D	d	day(s)
	DFO	desferrioxamine B
	DGA	*N,N,N',N'*-tetrakis-2-ethylhexylglycolamide
	DIAMSAR	3,6,10,13,16,19-hexaazabicyclo[6.6.6]icosane-1,8-diamine
	DMB	dimethoxybenzyl group
	DMF	dimethylformamide
	DMSO	dimethyl sulfoxide
	DO1PA	6-((1,4,7,10-tetraazacyclododecan-1-yl)methyl)picolinic acid
	DOTA	1,4,7,10-tetraazacyclododecane-1,4,7,10-tetraacetic acid
	DOTA-AA	2,2',2''-(10-(2-((4-aminophenyl)amino)-2-oxoethyl)-1,4,7,10-tetraazacyclododecane-1,4,7-triyl)triacetic acid
	DOTP	((1,4,7,10-tetraazacyclododecane-1,4,7,10-tetrayl)tetrakis-(methylene))tetrakis(phosphonic acid)
	DTPA	diethylenetriaminepentaacetic acid
E	EA	elemental analysis
	EC	electron capture
	EDC	3-(ethyliminomethyleneamino)-*N,N*-dimethylpropan-1-amine
	EDTA	ethylenediaminetetraacetic acid
	EDTMP	ethylenediaminetetramethylene phosphonic acid
	e.g.	*exempli gratia* (for example)
	EGF	epidermal growth factor
	EGFR	epidermal growth factor receptor
	EOB	end of bombardment
	EPR	enhanced permeability and retention
	ESI	electrospray ionization
	ESR	electron spin resonance
	Eq.	equation
	Et_2O	diethyl ether

	etc.	*et cetera* (and so forth)
	EtOAc	ethyl acetate
F	FDG	fluorodeoxyglucose
G	GRP	gastrin-releasing peptide
	GRPR	gastrin-releasing peptide receptor
H	h	hour(s)
	H_2bispa[2]	6,6'-((9-hydroxy-1,5-bis(methoxycarbonyl)-2,4-di(pyridin-2-yl)-3,7-diazabicyclo[3.3.1]nonane-3,7-diyl)bis(methylene))-dipicolinic acid
	H_2dedpa	1,2-[[6-(carboxy)-pyridin-2-yl]-methylamino]ethane
	H_4octapa	*N,N'*-bis(6-carboxy-2-pyridylmethyl)-ethylenediamine-*N,N'*-diacetic acid
	Hbispa[1a]	6-((9-hydroxy-1,5-bis(methoxycarbonyl)-7-methyl-6,8-di(pyridin-2-yl)-3,7-diazabicyclo[3.3.1]nonan-3-yl)methyl)picolinic acid
	(*p*-MeO)Hbispa[1a]	6-((9-hydroxy-1,5-bis(methoxycarbonyl)-6,8-bis(4-methoxy-pyridin-2-yl)-7-methyl-3,7-diazabicyclo[3.3.1]nonan-3-yl)methyl)picolinic acid
	Hbispa[1b]	6-((9-hydroxy-1,5-bis(methoxycarbonyl)-7-methyl-2,4-di(pyridin-2-yl)-3,7-diazabicyclo[3.3.1]nonan-3-yl)methyl)picolinic acid
	HATU	1-[bis(dimethylamino)methylene]-1*H*-1,2,3-triazolo[4,5-b]pyridinium 3-oxide hexafluorophosphate
	HEHA	1,4,7,10,13,16-hexaazacyclohexadecane-*N,N',N'',N''',N'''',N'''''*-hexaacetic acid
	HEPES	4-(2-hydroxyethyl)-1-piperazine ethanesulfonic acid
	HMBC	heteronuclear multiple-bond correlation spectroscopy
	HPLC	high performance liquid chromatography
	HR	high resolution
	HSQC	heteronuclear single-quantum correlation spectroscopy
	H(TFA)	trifluoroacetic acid
	HZDR	Helmholtz-Zentrum Dresden-Rossendorf
I	IC	internal conversion
	ID	injected dose
	i.e.	*id est* (that is)
	IR	infrared

	IT	isomeric transition
	iTLC	instant thin layer chromatography
L	LET	linear energy transfer
M	mAb	monoclonal antibody
	MeCN	acetonitrile
	MeOH	methanol
	MES	2-(*N*-morpholino)ethanesulfonic acid
	min	minute(s)
	MP	mobile phase
	MRI	magnetic resonance imaging
	MS	mass spectrometry
N	N_2py_4	dimethyl 9-oxo-2,4-di(pyridin-2-yl)-3,7-bis(pyridin-2-ylmethyl)-3,7-diazabicyclo[3.3.1]nonane-1,5-dicarboxylate
	NBS	*N*-bromosuccinimide
	NHE	normal hydrogen electrode
	NIR	near-infrared
	NMR	nuclear magnetic resonance
	NOTA	1,4,7-triazacyclononane-1,4,7-triacetic acid
	NO1PA2PY	6-((4,7-bis(pyridin-2-ylmethyl)-1,4,7-triazonan-1-yl)methyl)-picolinic acid
O	OC	octreotide
P	PAGE	polyacrylamide gel electrophoresis
	PBS	phosphate-buffered saline
	PCTA	3,6,9,15-tetraazabicyclo[9.3.1]-pentadeca-1(15),11,13-triene-3,6,9,-triacetic acid
	PEG	polyethylene glycol
	PEPA	1,4,7,10,13-pentaazacyclopentadecane-*N,N',N'',N''',N''''*-pentaacetic acid
	PET	positron emission tomography
	p.i.	post injection
Q	QSPR	quantitative structure-property relationship
R	RCY	radiochemical yield

	ref.	reference
	RGD	amino acids Arg-Gly-Asp
	RIT	radioimmunotherapy
	RP	reverse phase
	rpm	revolutions per minute
S	SD	standard deviation
	SDS	sodium dodecyl sulfate
	SEC	size exclusion chromatography
	SHE	standard hydrogen electrode
	SPECT	single photon emission computed tomography
	SST	somatostatin
	SSTR	somatostatin receptor
T	tacn	1,4,7-triazacyclononane
	TATE	octreotate
	TE1PA	6-((1,4,8,11-tetraazacyclotetradecan-1-yl)methyl)picolinic acid
	TETA	1,4,8,11-tetraazacyclotetradecane-1,4,8,11-tetraacetic acid
	TETP	((1,4,8,11-tetraazacyclotetradecane-1,4,8,11-tetrayl)tetrakis-(methylene))tetrakis(phosphonic acid)
	TFA	trifluoroacetate
	TLC	thin layer chromatography
	TOC	Tyr3-octreotide
	TRAP	1,4,7-triazacyclononane-1,4,7-tris[methyl(2-carboxyethyl)-phosphinic acid
	TRIUMF	Tri University Meson Facility
U	UBC	University of British Columbia
	UV	ultraviolet
V	VEGFR	vascular endothelial growth factor receptor
	vs.	*versus*
	vis	visible
W	WAT	white adipose tissue
Z	z.B.	zum Beispiel (for example)

Abstract

Defeating cancer is one of the major challenges that humankind is facing today. To this end, nuclear medicine offers promising approaches, especially in cases where conventional methods like chemotherapy or irradiation are not effective. Due to the versatility of metallic radionuclides and their facile insertion into suitable targeting compounds, the usage of radiometal-based pharmaceuticals has become increasingly popular. Such radiopharmaceuticals consist of two main parts: a radioactive metal ion and a vector moiety (*e.g.* a peptide, an antibody, or a nanoparticle). The radiometal ion determines the mode of action *via* its decay, whereas the vector moiety governs the delivery of the radiolabeled agent to the diseased target structure (see **Figure I**). Depending on the nuclear properties of the metal ion, radiopharmaceuticals can be used for either diagnostic or therapeutic purposes. The incorporation of the radionuclide into the targeting vector is commonly performed using a bifunctional chelator (BFC) that possesses a coordination site for stable complexation of the metal ion as well as a suitable linker for conjugation to the vector moiety.

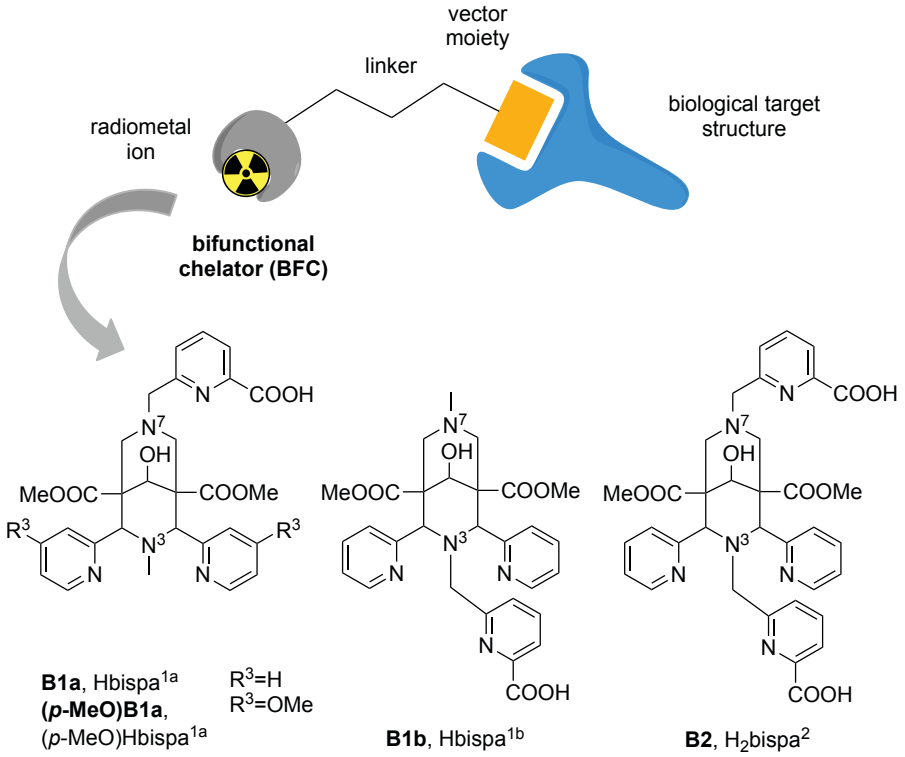

Figure I. Schematic representation of a metal-based radiopharmaceutical and the bispa ligands synthesized and evaluated in this thesis.

The work presented in this thesis focused on the development of new ligand systems for application as metal-chelating units in radiopharmaceuticals. The main requirements for BFCs are fast complex formation and stable metal ion coordination under physiological conditions. Previously, the rigid and highly preorganized bispidine scaffold has been shown to provide a suitable platform for the design of BFCs for nuclear imaging using copper(II)-64, a promising radionuclide for positron emission tomography (PET). In the present study, picolinic acid groups, known to be excellent metal-binding moieties, are incorporated into the bispidine backbone to further improve the thermodynamic stability of the copper(II) bispidine complexes. This new class of chelators is refered to as the "bispa" ligands. Moreover, through the modification it was intended to expand the spectrum of the bispdine ligands to the complexation of other metal ions relevant to radiopharmacy. By the introduction of one or two picolinic acid groups into the bispidine scaffold, hexa- and octadentate bispa ligands were prepared as shown in **Figure I**. These novel ligands were evaluated in various non-radioactive and radioactive metal complexation studies concerning their potential application in nuclear medicine.

The coordination chemistry of the isomeric hexadentate bispa ligands Hbispa[1a] (**B1a**) and Hbispa[1b] (**B1b**), as well as of the *para*-methoxy substituted **B1a** derivative (*p*-MeO)Hbispa[1a] (**(*p*-MeO)B1a**) was investigated. To this end, complexation reactions of the N_5O-type bispa ligands with the metal ions cobalt(II), nickel(II), copper(II), zinc(II), and gallium(III) were performed. The resulting metal complexes were characterized by means of standard structural and spectroscopic methods. In the next step, the bispa ligands were evaluated in radiochemical investigations with the PET nuclides copper(II)-64 and gallium(III)-68. The human serum challenge experiments and biodistribution studies with radiolabeled $^{68}Ga^{III}$-**B1a** revealed an inadequate complex stability, indicating that the hexadentate bispa ligands are not suited for applications involving the hard gallium(III) ion. The $^{64}Cu^{II}$-bispa systems, in contrast, showed auspicious properties including fast complex formation under mild conditions with molar activities as high as 200 GBq/µmol. In addition, excellent *in vivo* stability and favorable clearance behavior of the complexes were observed. These results are consistent with the high preorganization of the bispa ligands for copper(II) complexation and the high formation constants of the complexes determined by potentiometric titrations.

Using the bispa ligand H_2bispa[2] (**B2**), the very first octadentate bispidine system was synthesized and examined for nuclear medicine. In the present thesis, the coordination chemistry of the N_6O_2-type ligand was investigated with the metal ions indium(III), lutetium(III), and lanthanum(III). Furthermore, the ligand **B2** was evaluated in combination

with the radioactive metal ions $^{111}In^{III}$ (imaging), $^{177}Lu^{III}$ (therapy), and $^{225}Ac^{III}$ (therapy). The metal-**B2** complexes showed stabilities *vs.* human serum comparable to or higher than those of the respective complexes based on the macrocyclic "gold standard" chelator DOTA. Moreover, radiolabeling of **B2** with $^{111}In^{III}$ and $^{225}Ac^{III}$ could be performed quantitatively at room temperature, which is a major advantage in comparison to DOTA.

In conclusion, the new hexa- and octadentate bispa ligands were shown to display promising properties regarding the stable complexation of diagnostic as well as therapeutic radiometal ions. In future investigations, these results will promote the development of functionalized derivatives of the respective ligands towards the putative application as BFCs in nuclear medicine.

Kurzfassung

Der Kampf gegen Krebs stellt eine der großen Herausforderungen unserer heutigen Zeit dar. Diesbezüglich bietet die Nuklearmedizin vielversprechende Ansätze, vor allem dort, wo konventionelle Methoden wie Chemotherapie und Bestrahlung nicht hinreichend wirksam sind. Aufgrund der vielseitigen Einsetzbarkeit metallischer Radionuklide und ihrer leichten Insertion in zielsuchende Verbindungen haben Radiometall-basierte Wirkstoffe in den letzten Jahren zunehmend an Bedeutung gewonnen. Prinzipiell bestehen solche Radiopharmaka aus zwei grundlegenden Komponenten, einem Radiometallion und einer Vektoreinheit (z.B. Peptid, Antikörper, oder Nanopartikel). Das radioaktive Metallion bestimmt durch seinen Zerfall die Wirkungsweise des Medikaments, während der Vektor zur spezifischen Erkennung der krankhaften Zielstruktur dient (siehe **Abbildung I**). Abhängig von den nuklearen Eigenschaften des jeweiligen Metallions können diese Radiopharmaka entweder für diagnostische oder für therapeutische Zwecke genutzt werden. Die Einführung des Radionuklids in die Vektoreinheit erfolgt im Allgemeinen mithilfe bifunktioneller Chelatoren (BFCs), die sowohl in der Lage sind, das Metallion zu komplexieren, als auch über einen Linker zur Kopplung an den Vektor verfügen.

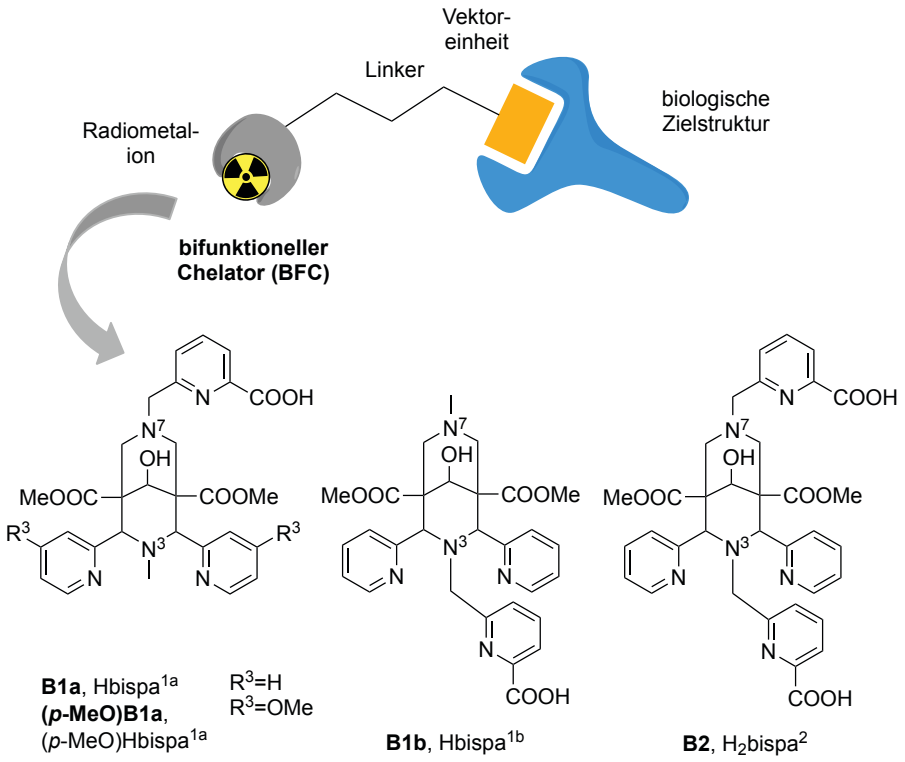

Abbildung I. Schematische Darstellung eines Metall-basierten Radiopharmakons, sowie die in dieser Arbeit dargestellten und untersuchten bispa-Liganden.

Die hier vorgestellte Arbeit beschäftigt sich mit der Entwicklung neuer Ligandensysteme für die Anwendung in Radiopharmaka. Die Hauptanforderungen an BFCs sind dabei schnelle Komplexbildung und eine stabile Bindung des Metallions unter physiologischen Bedingungen. Es wurde bereits gezeigt, dass das starre und hoch präorganisierte Bispidingerüst eine geeignete Plattform für das Design von BFCs für die nukleare Diagnostik mittels Kupfer(II)-64 im Rahmen der Positronen-Emissions-Tomographie (PET) darstellt. Um die thermodynamische Stabilität der entsprechenden Kupfer(II)-Bispidinkomplexe zu erhöhen, wurden hier nun Picolinsäure-Gruppen (*picolinic acid*, pa), bekannt als exzellente Metall-bindende Einheiten, in das Bispidinrückgrat eingeführt. Die auf diesem Wege erhaltenen Chelatoren werden als "bispa"-Liganden bezeichnet. Darüber hinaus sollte durch diese Modifizierung das Spektrum der Bispidine auf weitere radiomedizinisch relevante Metallionen ausgedehnt werden. Durch die Einführung von ein oder zwei Picolinsäuren am Bispidingerüst wurden hexa- und oktadentate bispa-Liganden dargestellt (siehe **Abbildung I**). Diese neuen Ligandensysteme wurden anschließend in verschiedenen Studien mit nicht-radioaktiven und radioaktiven Metallionen hinsichtlich ihrer potentiellen Anwendung in der Nuklearmedizin evaluiert.

Die Koordinationschemie der isomeren hexadentaten bispa-Liganden Hbispa[1a] (**B1a**) und Hbispa[1b] (**B1b**), sowie des *para*-Methoxy substituierten Derivats (*p*-MeO)Hbispa[1a] (**(*p*-MeO)B1a**) wurde untersucht. Dazu wurden Komplexierungsreaktionen der N_5O-Liganden mit den Metallionen Cobalt(II), Nickel(II), Kupfer(II), Zink(II), und Gallium(III) durchgeführt. Die strukturellen und spektroskopischen Eigenschaften der so erhaltenen Metall-Komplexe wurden anschließend mittels Standardmethoden analysiert. Im nächsten Schritt wurden die bispa-Liganden in radiochemischen Untersuchungen mit den PET-Nukliden Kupfer(II)-64 und Gallium(III)-68 evaluiert. Konkurrenzexperimente mit humanem Serum und Bioverteilungsstudien zeigten, dass der radiomarkierte $^{68}Ga^{III}$-**B1a** Komplex unter den beschriebenen Bedingungen nicht stabil ist. Demnach erwiesen sich die neuen bispa-Liganden als ungeeignet für Anwendungen mit dem harten Metallion Gallium(III). Im Gegensatz dazu zeigten die $^{64}Cu^{II}$-bispa Systeme vielversprechende Eigenschaften wie schnelle Komplexbildung unter milden Bedingungen mit hohen molaren Aktivitäten von bis zu 200 GBq/µmol. Zudem wurden eine hohe *in vivo*-Stabilität sowie eine schnelle Ausschleusung der Komplexe aus dem Körper beobachtet. Diese Ergebnisse sind in Übereinstimmung mit der hohen Präorganisation der bispa-Liganden für die Komplexierung von Kupfer(II) und den hohen Komplexbildungskonstanten, die mittels potentiometrischer Titration bestimmt wurden.

Mit dem bispa-Liganden H_2bispa^2 (**B2**) wurde das erste oktadentate Bispidin synthetisiert und im Hinblick auf nuklearmedizinische Anwendungen studiert. In der vorliegenden Arbeit wurde die Koordinationschemie des N_6O_2-Liganden mit den Metallionen Indium(III), Lutetium(III), und Lanthan(III) untersucht. Darüber hinaus wurde **B2** mit den radioaktiven Metallionen $^{111}In^{III}$ (Bildgebung), $^{177}Lu^{III}$ (Therapie), und $^{225}Ac^{III}$ (Therapie) evaluiert. Die Metall-**B2** Komplexe zeigten in Gegenwart von humanem Serum vergleichbare oder bessere Stabilitäten als die entsprechenden Komplexe basierend auf dem makrozyklischen "Goldstandard" DOTA. Zudem konnte **B2** bei Raumtemperatur quantitativ mit $^{111}In^{III}$ und $^{225}Ac^{III}$ radiomarkiert werden, was einen deutlichen Vorteil im Vergleich zu DOTA darstellt.

Es wurde somit gezeigt, dass die neuen hexa- und oktadentaten bispa-Liganden stabile Komplexe mit diagnostisch sowie therapeutisch interessanten Radiometallionen bilden. Diese Ergebnisse werden die Entwicklung und Untersuchung von Derivaten der hier vorgestellten Liganden in Richtung deren Verwendung als BFCs in der Nuklearmedizin vorantreiben.

Table of contents

1 State of the art

1.1 Metal-based radiopharmaceuticals

1.1.1 Introduction

The fascination for metal complexes, especially for their diverse range of impressive colors, goes far back to ancient times, long before Alfred Werner (1866-1919) first defined the concept of coordination compounds in 1893.[1-4] Nowadays, metal complexes are used and investigated in a variety of different areas, *e.g.* as highly specific molecular catalysts (homogeneous catalysis),[5] as biomimetic enzyme models[6-8] and as diagnostic or therapeutic metal-based drugs.[9,10] Prominent examples for metallodrugs are platinum(II) anticancer therapeutics like cisplatin and derivatives thereof,[11] gold(I) complexes against arthritis (*e.g.* auranofin),[12,13] and bismuth(III) compounds for the treatment of gastrointestinal disorders (*e.g.* bismuth subsalicylate, BSS).[14,15] In addition, gadolinium(III)-based contrast agents for magnetic resonance imaging (MRI)[16] as well as diagnostic radiopharmaceuticals like $^{99m}Tc^{I}$-sestamibi (Cardiolite) are known.[17,18]

The focus of this work lies on the application of metal complexes in nuclear medicine. Over the past decades, radiometal-based pharmaceuticals have become increasingly popular.[17,19,20] Such radiopharmaceutical agents consist of four components: the radiometal ion itself, which is tightly bound by a bifunctional chelator (BFC), a vector or targeting moiety (*e.g.* peptides or antibodies), and a molecular linker connecting the BFC with the vector (see **Figure 1**).[21]

Figure 1. Schematic representation of a metal-based radiopharmaceutical and its components.

It is essential for the intended use that the vector moiety is able to recognize a biological target *in vivo*, allowing site-specific delivery and accumulation of the radiopharmaceutical. Once attached to the target structure, the decay of the radiometal can be used to localize

(diagnosis) or destroy (treatment) diseased tissues (see Chapter 1.1.2).[21] The periodic table (see **Figure 2**) provides a wide variety of elements with radioisotopes suitable for nuclear imaging and radiotherapy.[22]

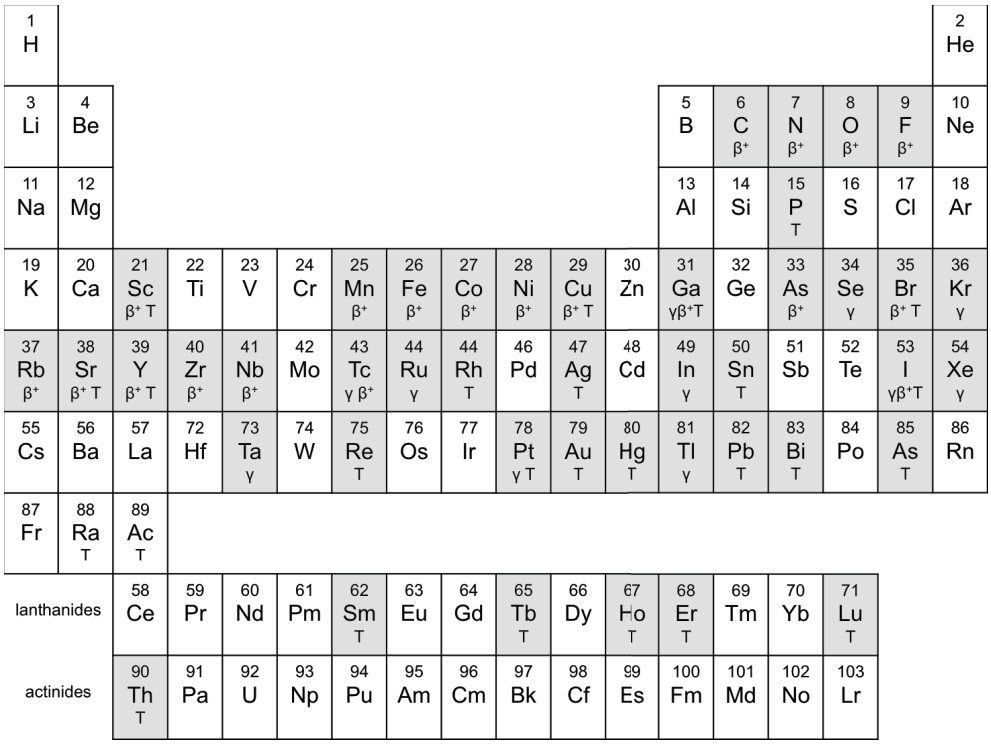

Figure 2. Periodic table highlighting elements suitable for nuclear imaging (γ or β^+) or radiotherapy (T). Adapted from reference [22].

Radiometals offer advantages over non-metallic nuclides like radiohalogens in terms of flexibility, modularity, and simplicity. Depending on the intended application, one can choose from numerous radiometals with different decay schemes, energies, physical half-lives, and production methods. Furthermore, radiometallation reactions are generally fast and can take place under ambient conditions. In contrast, the incorporation of radiohalogens into organic systems *via* covalent bond linkage often requires multiple synthetic steps including harsh conditions and difficult purification procedures.[19]

In the following, nuclear medicine techniques will be presented (Chapter 1.1.2) complemented by a discussion of the factors relevant for the design of metalloradio-pharmaceuticals (Chapters 1.1.3 to 1.1.7).

1.1.2 Nuclear medicine

Nuclear decay processes used for medical applications

Radioactivity is a property of unstable atomic nuclei leading to spontaneous emission of ionizing radiation. A substance containing such a labile nucleus is thus considered radioactive. The nucleus changes its state by emitting particles or photons and this transformation process is commonly termed nuclear disintegration or decay.[23] The objective of this subchapter is not to provide a thorough introduction to the basic physics of radioactivity, but to highlight nuclear decay processes resulting in radiation suitable for medical applications (see **Figure 3**). There are three major forms of nuclear disintegration, *i.e.* alpha (α) decay, beta (β) decay, and gamma (γ) decay. During α decay a doubly ionized helium-4 atom (α particle) is ejected from the parent radionuclide and this radiation can be used for targeted alpha therapy (TAT).[24,25] The term β decay is used to describe different processes involving nuclei with unbalanced proton to neutron ratios. Radionuclides with an excess of neutrons for example, decay *via* conversion of a neutron into a proton accompanied by the emission of an electron, the so-called beta minus (β^-) particle (therapeutic applications). Proton rich nuclei, on the other hand, may attempt to reach stability by converting a proton into a neutron with the emission of a beta plus (β^+) particle (positron), the antiparticle of the electron. After ejection, the positron recombines with a suitable electron resulting in the emission of two γ rays, and these can be detected for diagnostic purposes (see subsection 'Imaging' for more details). Another process related to β decay is electron capture (EC). Here an unstable nucleus captures an inner orbiting electron (often from the K- or L-shell of the atom) followed by conversion of this electron and a proton into a neutron and subsequent ejection of a neutrino.[24] Thus, EC itself does not produce ionizing radiation but it creates a vacancy in the electron cloud of the decaying atom. Such vacancies are quickly filled by electrons from higher energy levels. These electron transitions then result in the emission of characteristic X rays or low energy electrons, collectively called AUGER electrons (radiotherapy).[24,26] The effect on the nucleus of EC is the same as positron emission and both decays compete with each other. However, the latter process requires a certain energy for the ejected positron and is thus not possible for every radionuclide. Following these types of decays (α and β), the nucleus often remains in an excited state and the excess energy can be emitted as γ photons (imaging). Furthermore, all described disintegration processes lead to nuclear transmutation, *i.e.* the conversion of a chemical element or an isotope into another. In contrast, γ decay involves transitions between different states of the same atom.[24]

Excited or metastable radionuclides can release their excess energy in the form of electromagnetic radiation (isomeric transition, IT). A prominent example for this is technetium-99m.[18,24,27] Alternatively, the energy can be transferred to an electron, resulting in its emission from the atom (internal conversion, IC).[24] These conversion electrons can be used in radiotherapy and additionally IC (just as EC) also leaves a vacant site in the electron shell (see above).[24,28] Often, not only one but several decay modes are accessible for a specific radionuclide and occur with a certain probability. In addition, if the daughter nuclide of a nuclear disintegration is radioactive itself, a number of consecutive decays will take place until a stable end product is formed.[24]

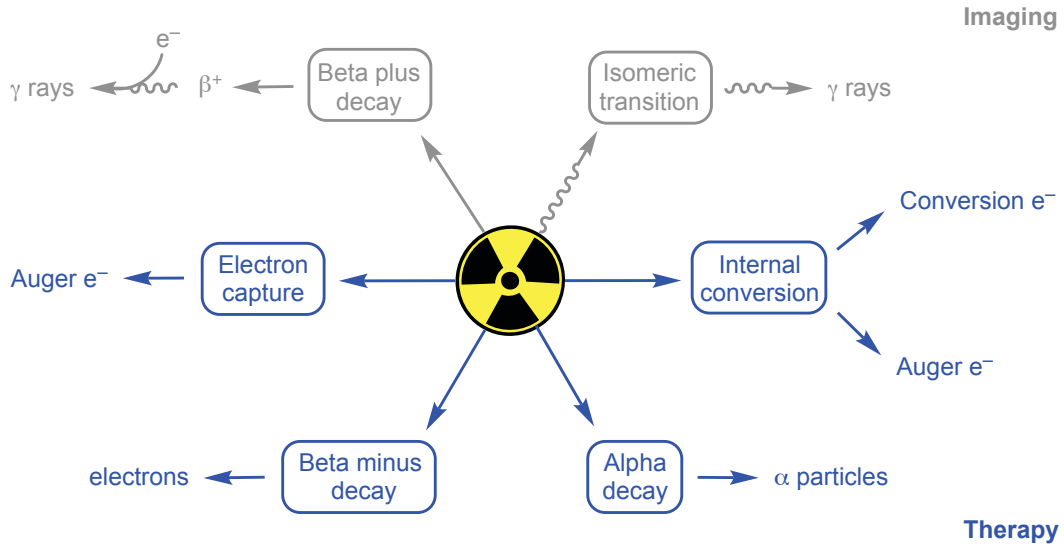

Figure 3. Nuclear decay processes leading to ionizing radiation used in nuclear medicine for either diagnostic or therapeutic purposes.

Imaging

Diagnostic imaging techniques like single photon emission computed tomography (SPECT) or positron emission tomography (PET) use either gamma (γ) or positron (β^+) emitting radionuclides, respectively (see **Figure 4**). These non-invasive methods are well-established imaging modalities and have already been extensively reviewed in the literature.[24,29-34] They are used for the early detection of tumors in oncology, as well as for brain and cardiac (heart) imaging.[29] By monitoring the spatial and temporal distribution of the administered radiotracer, nuclear imaging provides functional information regarding the physiological condition of the patient.[24] For example, thallium(I) is known to accumulate in healthy heart muscle (myocardium), but not in infarcted or poorly perfused tissues. Hence, the chloride salt of the cation $^{201}Tl^+$ can be used as a myocardial perfusion

imaging agent.[22,24,35] Both, SPECT and PET, are based on the detection of γ rays and subsequent data conversion into three-dimensional images by appropriate computer programs.[30] The following main aspects have to be considered when choosing a suitable diagnostic radioisotope: the half-life of the nuclide should allow for the preparation of the radiopharmaceutical, its administration to the patient, and its detection before it is eliminated from the body. Furthermore, the energy of the γ ray has to be high enough to be detectable by the gamma cameras, but at the same time, the radiation exposure to the patient should be kept as low as possible. In case of SPECT, the ideal γ ray energy range given by the detector is between 100-200 keV and the radionuclide should be chosen accordingly.[36] For PET, on the other hand, a β^+-emitting nuclide is required. When a positron is ejected, it travels through matter for a short distance (in the range of a few millimeters[37]) losing energy by interaction with surrounding material. After the positron loses most of its kinetic energy, it combines with a suitable electron, resulting in two 511 keV γ rays at an angle of 180 ° (annihilation process). Those photons are recorded by coincidence detectors that are arranged in a circular array (see **Figure 4**).[21,34] The range of charged particles like positrons in matter depends on the energy of the particle and the density of the medium. Low energy β^+ emission, *i.e.* a small range in matter, is consequently better suited for PET in order to obtain good resolution.[34] PET shows in comparison with SPECT higher resolution in the range of ~5 mm (as opposed to ~10 mm for SPECT) and higher sensitivity with tracer concentrations of ~10^{-8} to 10^{-10} M (compared to ~10^{-6} M for SPECT).[38,39] In terms of multimodal imaging, the functional information gained by either SPECT or PET are often combined with methods delivering detailed anatomical data like computed tomography (CT) and MRI.[24,32,36]

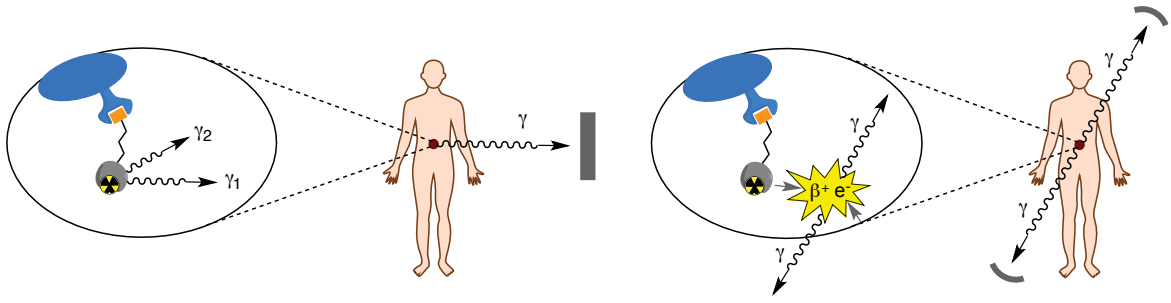

Figure 4. Schematic representation of SPECT (left) and PET (right) imaging. Adapted from reference [21].

Therapy

The application of radiopharmaceuticals for the treatment of diseases is termed radiotherapy. In case of radioimmunotherapy (RIT) antibodies are used as vector moieties and a detailed presentation of vectors and biological targets is given in Chapter 1.1.3. In contrast to nuclear imaging, radiotherapy aims to deliver a sufficiently large radioactive dose to the diseased target to destroy it without harming surrounding healthy tissue. Essential for an effective treatment is the use of radionuclides that can cause irreparable DNA damage in the respective cells. To this end, emitters of alpha (α) and beta minus (β^-) particles, as well as conversion and AUGER electrons are used.[21,26,40] An important factor related to the interaction of radiation with matter is the so-called linear energy transfer (LET). This value is used to quantify the amount of energy deposited by ionizing radiation per unit length of the path in soft tissue and is typically given in kiloelectron volts per micrometer (keV/µm).[34] Each particle displays different nuclear properties in terms of decay energy, penetration depth and LET (see **Table 1**). Beta particles have a long path length of 0.5-10 mm[21] corresponding to a low LET in the range of 0.2 keV/µm[26] in biological tissue and are thus well-suited for the treatment of large, solid tumors. Alpha particles, on the other hand, with their short range of 40-100 µm[21] and high LET of 80 keV/µm[26] show ideal properties for treating micrometastases and lymphomas.[41] In comparison to those particles, AUGER electrons have the lowest energy (ca. 1-10 keV) and the smallest range (1-20 µm).[21] When working with AUGER electrons, it is therefore important that the radiolabeled drug is localized in the cell nucleus close to the DNA, *i.e.* the radiosensitive target.[26,42] Besides showing therapeutically useful emissions, the radionuclide should ideally also release a small amount of γ radiation (about 10 % of the decay, ~150 keV), as this allows to monitor the distribution of the radiopharmaceutical.[43]

Table 1. Nuclear properties of particles used for radiotherapy.[21,26]

Particles	Typical energy of decay	Typical range in biological tissue[(a)]	LET [keV/µm]
AUGER electrons	~1-10 keV	1-20 µm (< 1 cell diameter)	4-26
β^- particles	0.1-2.2 MeV	0.5-10 mm (50-1000 cell diameters)	0.2
α particles	5-8 MeV	40-100 µm (< 10 cell diameter)	80

[(a)] Based on an average cell diameter of 10 µm.

Theranostics

The term “Theranostics“ in nuclear medicine refers to the use of a radiopharmaceutical for combined therapy and diagnosis.[44-46] This implies that a targeting vector is first labeled with a diagnostic radionuclide to perform low dose imaging and to deliver therapeutically relevant information, *i.e.* about the heterogeneity of the diseased tissue, the receptor expression on the cell surface, as well as the biodistribution and clearance of the radiopharmaceutical. Based on this information, personalized treatment using the same vector labeled with a suitable therapeutic nuclide can then be performed.[44,47] Ideally, radioisotopes of the same element are used for theranostic purposes. This way, one can benefit from the fact that isotopes of a given element display identical chemical properties. A vector moiety can thus be radiolabeled with different isotopes while the biological properties of the compound are not altered.[48] Examples for this application are the copper isotopes ^{64}Cu (β^+ emitter, PET) and ^{67}Cu (β^- emitter, therapy).[49-51] Some other so-called „matched pairs“ are *e.g.* $^{44/47}$Sc,[52] $^{67/68}$Ga,[53,54] and $^{86/90}$Y[55,56]. Alternatively, radionuclides from different chemical elements can be used. In this case, it is important to perform *in vivo* studies to confirm the pharmacological similarity of the differently radiolabeled agents.[45] There are some versatile chelators available which can effectively radiolabel various metal ions.[48] Prominent examples are DOTA (1,4,7,10-tetraazacyclododecane-1,4,7,10-tetraacetic acid), DTPA (diethylenetriaminepentaacetic acid), and H_4octapa (*N,N'*-bis(6-carboxy-2-pyridylmethyl)-ethylenediamine-*N,N'*-diacetic acid), as well as derivatives thereof. All of them bind firmly to radiometal ions like indium(III)-111 (γ emitter, SPECT) and lutetium(III)-177 (β^- emitter, therapy), which can thus be used with the same ligand systems.[48,57,58] Either way, this clearly demonstrates the aforementioned modularity of metallic radionuclides.[19]

Whether radioisotopes are used for diagnostic, therapeutic or combined purposes, the crucial part for all those applications is the *in vivo* delivery strategy, which will be discussed in the next chapter.

1.1.3 Biological targets and vector moieties

A radiopharmaceutical consists of two main parts: a radionuclide that determines the mode of action *via* its decay, and a targeting vector, often a biomolecule, responsible for the localization of the radiolabeled drug. A central topic in nuclear medicine is the diagnosis and treatment of cancer in its various forms. During cancer pathogenesis the corresponding cells undergo certain molecular changes and thus provide suitable targets

for radiopharmaceuticals. Some typical traits of cancerous tissues are fast cell proliferation accompanied by enhanced formation of cardiovascular structures (neoangiogenesis), and upregulation of receptor gene expression.[59-61] The fast construction of new blood vessels leads to structural defects and thus eventually to increased porosity, known as enhanced permeability and retention (EPR) effect.[62] This phenomenon allows for the passive transport of functional nanoparticles into tumor cells. In general, nanoparticles are well-suited for the development of drugs as they allow the use of various materials like iron oxide, silica, or gold and offer a large surface for the adsorption of active compounds.[63-66] Small molecule tracers, like the ubiquitous fluorinated glucose derivative ^{18}F-fluorodeoxyglucose (^{18}F-FDG)[67,68] or the radiolabeled amino acid ^{11}C-methionine,[69] on the other hand, mimic metabolic substrates and are hence accumulated in fast-growing tumor cells.[70] However, the focus here will be on receptor targeting with radiolabeled biomolecules like peptides[57,71,72] or antibodies[73-75]. This approach relies on the over-expression of cell surface receptors in various human tumors compared to healthy tissues as depicted in **Figure 5**. Selected examples of such molecular targets together with their associated vector moieties are given in **Table 2**.

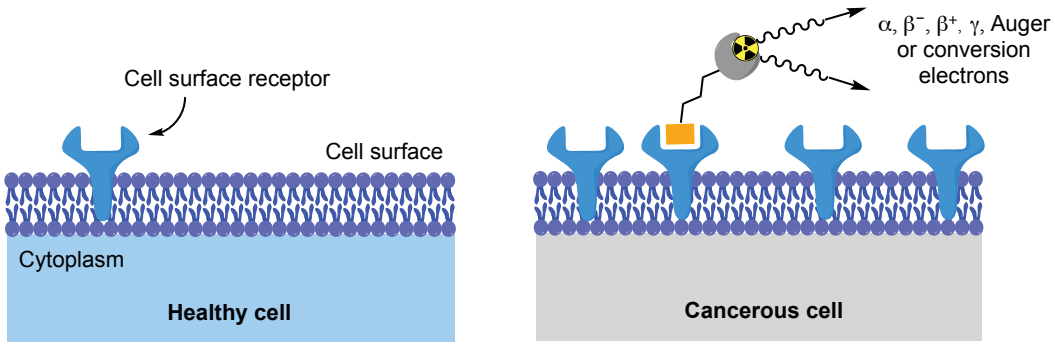

Figure 5. Over-expression of cell surface receptors in cancerous tissue in comparison to healthy tissue. Adapted from reference [21].

Some receptors do not only bind, but also internalize the targeting molecules, capturing them in the cell.[72] For AUGER electron emitters this is especially favorable as they have to be close to the nucleus in order to cause a cytotoxic effect.[42] The specific recognition between receptor and respective biomolecule can be described according to the so-called „lock and key theory“,[76] which is a fundamental principle in biochemistry (see reference [77] for modifications of this concept). Most commonly, peptides or antibodies, particularly monoclonal antibodies (mAbs), are used as vector moieties for surface receptors. The biological half-life of these compounds usually depends on their molecular size, *i.e.* the larger the molecule, the longer it circulates in the blood.[21] A large antibody

such as Immunoglobulin G with a molecular weight of 150 kDa has a blood clearance time of 3-4 weeks, whereas a monovalent 25 kDa antibody fragment is excreted in less than 10 hours.[75] For diagnostic purposes the properties of the biomolecule have to be matched to those of the respective radionuclide, especially with its physical half-life. This means that antibodies, with their relatively long blood circulation, need to be labeled with a radionuclide having a comparably long half-life like for example actinium-225 ($t_{1/2}$ = 10.0 d[27]).[21,75] In contrast, peptides usually display high uptake in target tissue and fast clearance from the body.[72] For RIT the prolonged circulation of antibodies is a major drawback, as it causes an undesired radiation burden in healthy tissues. An interesting approach to solving this problem is the so-called pretargeting strategy, which is based on non-covalent or covalent interactions between pretargeted mAbs and small radiolabeled effector molecules.[78] Often the receptor's native vector molecule cannot be used as part of a radiopharmaceutical because of rapid degradation *in vivo* (peptides) or slow blood circulation (antibodies).[21] Therefore, much effort has been put into developing suitable analogs to overcome these shortcomings while preserving the binding ability to the target receptor.[71,75,79]

Table 2. Selected peptide and antibody receptors over-expressed in human tumor cells.[21,57,71,75]

Target receptor	Biomolecule (peptide or antibody)	Tumor type
$\alpha_v\beta_3$ Integrin	Arg-Gly-Asp (RGD)	Brain, lung, prostate, ovary, breast, skin cancer (neoangiogenic vessels)
Somatostatin receptor (SSTR)	Somatostatin (SST) Octreotide (OC) Octreotate (TATE)	Neuroendocrine and gastro-enteropancreatic tumors, non-HODGKIN's lymphoma, carcinoids, paragangliomas, melanoma, breast, brain, renal, small cell lung cancer, medullary thyroid cancer
Gastrin-releasing peptide receptor (GRPR)	Gastrin-releasing peptide (GRP) Bombesin (BBN)	Prostate, breast, pancreas, gastric, colorectal, small cell lung cancer
HER-2/*neu* receptor	Trastuzumab (Herceptin)	Breast cancer
Epidermal growth factor receptor (EGFR)	Epidermal growth factor (EGF)	Breast, colorectal, head and neck cancer
Vascular endothelial growth factor receptor (VEGFR)	Bevacizumab (Avastin)	Metastatic colorectal cancer

Numerous receptor / vector pairs as shown in **Table 2** are available and the underlying principle shall now be illustrated using the somatostatin receptors (SSTRs) as an example. Somatostatin (SST) is a cyclopeptide hormone modulating multiple cellular signal transduction pathways *via* its corresponding transmembrane receptors.[80] Several human SST receptors were characterized[80,81] and found to be over-expressed in various tumor types (see **Table 2**) in comparison to healthy tissues.[82-84] Thus, SST receptor-positive tumors can be targeted using the peptide hormone somatostatin. However, naturally occurring SST is problematic for this purpose because of its short plasma half-life (< 3 minutes).[81,85] Intensive structure-activity studies have led to the synthesis of a variety of SST derivatives.[79,86-88] In this context, it is important to preserve the structural feature (pharmacophore) of the original compound that is necessary for its molecular recognition by the receptor. A prominent example of an SST analog is the short-chain cyclopeptide octreotide (OC) **1** (see **Figure 6**).[87] The replacement of the amino acid L-tryptophan (L-Trp) by its corresponding D-enantiomer significantly increased the potency of octreotide (and other analogs) compared to native SST. Furthermore, octreotide is protected against enzymatic degradation by the D-phenylalanine (D-Phe) at its N-terminus and the amino alcohol at its C-terminus.[79] Other derivatives based on the cyclic octapeptide are Tyr3-octreotide (TOC) **2** and octreotate (TATE) **3**.[57,79,81,88]

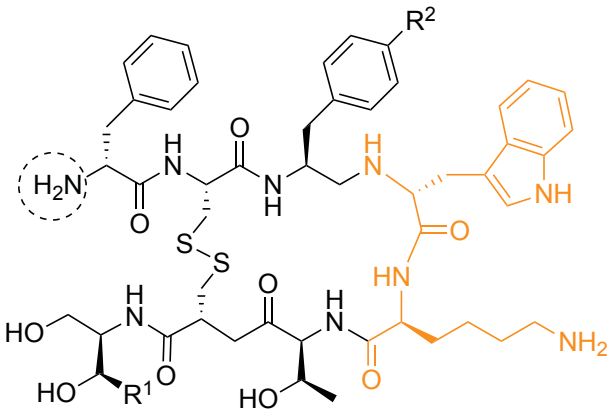

1, Octreotide (OC) R^1=H; R^2=H
2, Tyr3-Octreotide (TOC) R^1=H; R^2=OH
3, Octreotate (TATE) R^1=O; R^2=OH

Figure 6. Chemical structure of somatostatin analogs with the pharmacophore (orange) and the functional group used in conjugation reactions (dashed circle) highlighted.[21,81,87,88]

After the successful identification of suitable biological targets and vector moieties, the next crucial step is to incorporate the radionuclide into the biomolecule. In the case of

radiometal-based applications, one possibility is direct labeling of the compound with the respective nuclide. Examples of peptides and antibodies directly labeled with ^{99m}Tc and ^{188}Re have been reported,[89-94] even though the binding is generally non-specific.[95] However, the commonly used strategy for metalloradiopharmaceuticals involves the introduction of a bifunctional chelator (BFC) into the targeting vector *via* a molecular linker (Chapter 1.1.4) and subsequent radiolabeling of the attached ligand (Chapter 1.1.5).[95,96] Numerous vector-ligand conjugates have been developed based on this so-called BFC method and selected examples will be presented in subsections of Chapter 1.2.

1.1.4 Linker – bioconjugation strategies

Usually, a linker moiety bearing a functional group suitable for bioconjugation is attached to a ligand. The resulting bifunctional chelator (BFC) is subsequently coupled to the respective targeting biomolecule. Important in this context is the placement of the BFC with respect to the biological vector, as neither the binding ability of the chelate to metal ion nor the target affinity of the biomolecule should be affected by the conjugation mode. Other aspects to be considered are the reaction conditions of the conjugation procedure, as targeting vectors are often sensitive biomolecules and, therefore, susceptible to decomposition when heated. The bioconjugation should consequently occur fast and at ambient temperatures.[21]

Commonly used conjugation strategies connecting a BFC and a vector moiety proceed *via* peptide (**A**), thiourea (**B**), thioether (**C**) or triazole (**D**) bond formation (see **Figure 7**).[21,97,98] Typical reactive groups on the side of the biomolecule are amines (*e.g.* lysines) or thiols (cysteines) and the BFC must hence contain compatible functionalities. Primary amines for example can be coupled with carboxylic acids forming amide bonds (**A**), as well as with isothiocyanates resulting in thiourea derivatives (**B**).[97] In case of peptide bond formation, the carboxylic acid has to be activated using coupling agents like EDC (3-(ethyliminomethyleneamino)-*N,N*-dimethylpropan-1-amine) or HATU (1-[bis(dimethyl-amino)methylene]-1*H*-1,2,3-triazolo[4,5-b]pyridinium 3-oxide hexafluorophosphate).[99] Thiols, on the other hand, can be reacted with maleimides (**C**) with the added advantage that sulfhydryl groups are reactive at neutral pH in contrast to most amine functions.[97] Another approach involves the introduction of terminal alkynes and azides into the chelate and the biomolecule, respectively. Both functional groups can then be combined to 1,2,3-triazoles in a so-called “click reaction“ using copper(I) catalysts (**D**).[100] These bioorthogonal cycloadditions are characterized by high selectivity in the presence of

various functionalities and are widely used in the labeling of biomolecules like peptides.[98,101,102] The application of copper(I) catalysts in a reaction involving chelates, can lead to metal ion complexation. However, there are several procedures for the removal of copper ions described in the literature, including extraction with aqueous EDTA (ethylenediaminetetraacetic acid) solutions[103] and precipitation using sodium sulfide.[104] In addition, there has been tremendous progress in the development of click reactions that proceed in the absence of a metal catalyst.[105,106]

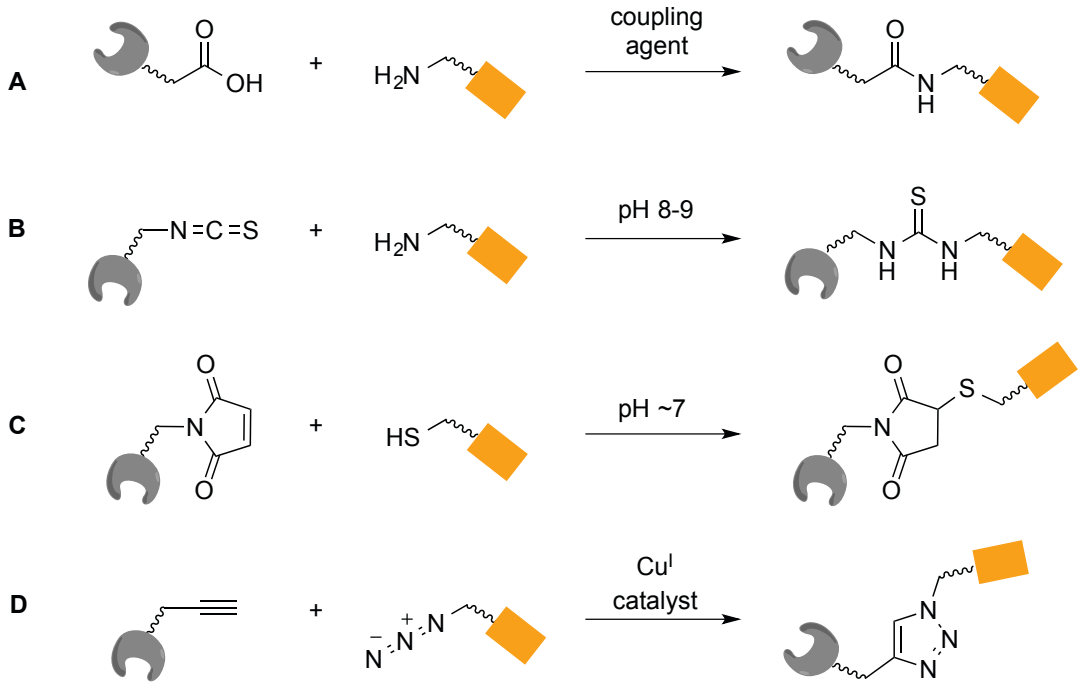

Figure 7. Examples for bioconjugation of a bifunctional chelator to a vector moiety. Adapted from reference [21].

Depending on the length of the linker, it can be useful to insert an additional spacer between the BFC and the biomolecule in order to avoid interference between these two moieties. In addition, a spacer can influence the pharmacokinetics and biodistribution of the conjugate by modifying its hydrophilicity. Such spacers often consist of amino acids, aliphatic and aromatic hydrocarbons, or low molecular polyethylene glycol (PEG) chains.[71,107-109]

1.1.5 Bifunctional chelators[i]

A bifunctional chelator (BFC), as implied by the name, provides two functionalities, *i.e.* a linker for covalent attachment to the biomolecule and a chelating moiety for stable complexation of the radiometal ion. The linker can either be connected to an existing functional group of the ligand or an additional reactive site needs to be introduced. The latter option is preferable, as the first approach potentially uses a coordinating function and can thus influence the donor properties or even reduce the number of possible donor atoms.[40] By far the most important requirement for BFCs is the formation of metal complexes with high thermodynamic stability (equilibrium on the side of the complex) and inertness (slow dissociation rate) under physiological conditions. For the intended use as part of a radiopharmaceutical, it is essential that the complex remains stable in the presence of competing metal ions and native chelators like enzymes or transport proteins.[48,110,111] Potential complex dissociation *in vivo* could lead to negative side effects including the accumulation of highly toxic radiometal ions in non-target tissues (see Chapter 1.1.7).[112,113] In the case of applications involving short-lived radioisotopes or heat sensitive biomolecules like antibodies as targeting vectors, fast radiolabeling of the BFC under ambient conditions is desirable. However, one has to consider that the rate constants of metal ion complexation and release (forward and reverse reaction) are connected *via* the complex stability constant K and hence a reasonable balance of the discussed properties is needed in order to obtain a suitable metal-BFC system.[48] The overall pharmacokinetics of radiolabeled drugs depend on the physicochemical properties of all components, and the hydrophilicity and charge of the metal complex thus influence biodistribution and clearance of the respective radiopharmaceutical.[110,114]

BFCs are often built up on the basis of polyaza-systems with high denticity allowing full saturation of the coordination sphere of the respective metal ion. In general, there are two categories of BFCs, those with macrocyclic and those with acyclic ligand scaffolds. Based on the tri- and tetraazamacrocycles tacn (**L1**, 1,4,7-triazacyclononane), cyclen (**L2**, 1,4,7,10-tetrazacyclododecane), and cyclam (**L3**, 1,4,8,11-tetraazacyclotetradecane), a broad variety of systems has been developed with the carboxylic acid-substituted frameworks NOTA (**L4**, 1,4,7-triazacyclononane-1,4,7-triacetic acid, N_3O_3-type ligand), DOTA (**L5**, 1,4,7,10-tetraazacyclododecane-1,4,7,10-tetraacetic acid, N_4O_4). and TETA

[i] Reproduced in part with permission from P. Comba, L. Grimm, C. Orvig, K. Rück, H. Wadepohl, *Inorg. Chem.* **2016,** *55*, 12531-12543, Copyright 2016 American Chemical Society.; Parts of this chapter will be published in P. Comba, U. Jermilova, C. Orvig, B. O. Patrick, C. F. Ramogida, K. Rück, C. Schneider, M. Starke, *Chem. Eur. J.*, *submitted manuscript.*

(**L6**, 1,4,8,11-tetraazacyclotetradecane-1,4,8,11-tetraacetic acid, N_4O_4) being the most popular ones.[115,116] With regard to bigger metal ions larger macrocycles like PEPA (**L7**, 1,4,7,10,13-pentaazacyclopentadecane-*N,N',N'',N''',N''''*-pentaacetic acid, N_5O_5)[117] and HEHA (**L8**, 1,4,7,10,13,16-hexaazacyclohexadecane-*N,N',N'',N''',N'''',N'''''*-hexaacetic acid, N_6O_6)[118] were investigated.[119-121]

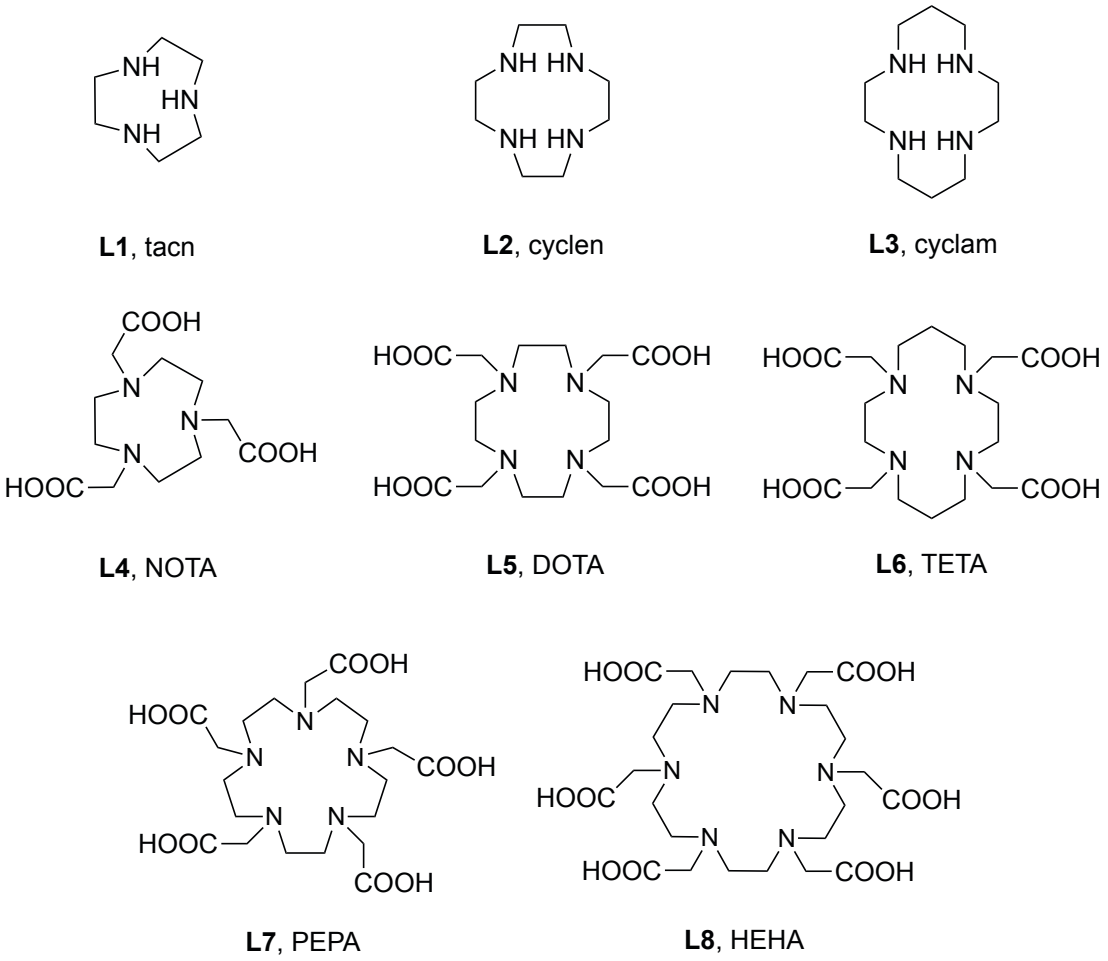

L1, tacn **L2**, cyclen **L3**, cyclam

L4, NOTA **L5**, DOTA **L6**, TETA

L7, PEPA **L8**, HEHA

Figure 8. Selected polyaza macrocycles.

The substitution pattern of the macrocycles is not limited to carboxylic acids but also includes other pendent donor groups like phosphonic or picolinic acids.[115,122-125] Furthermore, there are cross-bridged[122,123,126] and various functionalized derivatives available.[48] Metal ion complexes of macrocyclic systems usually show high thermodynamic stabilities, but often require high temperatures and extended reaction times for formation, which is a major drawback when working with heat sensitive antibodies as the targeting moiety.[40] DOTA (**L5**), for example, needs elevated temperatures for radiolabeling with basically all radiometal ions, *e.g.* $^{44/47}Sc^{III}$, $^{86/90}Y^{III}$,

$^{111}In^{III}$, $^{177}Lu^{III}$, and $^{225}Ac^{III}$, but it is nevertheless probably the most widely used chelator to date owing to the high *in vivo* stability of its metal complexes and to the commercial availability of many bifunctional derivatives.[48]

Acyclic systems, on the other hand, are able to quantitatively label radiometal ions within minutes at mild temperatures.[48,110] DTPA (**L10**, diethylenetriaminepentaacetic acid, N_3O_5), a prominent acyclic chelator, is known for its fast radiolabeling kinetics with many metal ions (*e.g.* $^{44/47}Sc^{III}$, $^{86/90}Y^{III}$, $^{111}In^{III}$, and $^{177}Lu^{III}$), but suffers from stability issues *in vivo*, especially in comparison with macrocycles like DOTA.[48] Despite its poor stability, DTPA is used in the first clinically approved peptide-based imaging agent $^{111}In^{III}$-DTPA-octreotide (OctreoScan®) for the diagnosis of somatostatin receptor positive neuroendrocrine tumors.[40,127-129] In order to improve the *in vivo* stability, several DTPA analogs with preorganizing groups at the carbon backbone have been synthesized,[40,48] including the C-functionalized derivative CHX-A$''$-DTPA.[130,131] For both, macrocyclic and acyclic chelates, the introduction of an additional linker into the ligand scaffold often requires extended synthetic routes and the use of protecting groups.[40]

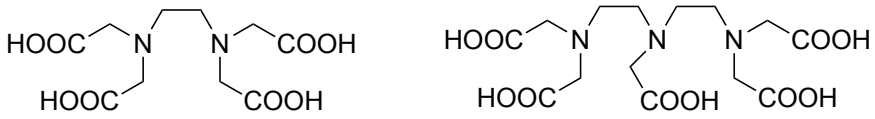

L9, EDTA **L10,** DTPA

Figure 9. Selected acyclic polyaza systems functionalized with carboxylic acid groups.

Overall, there is a large number of different bifunctional chelators that will be displayed in more detail in Chapter 1.2. Which of these ligand systems is finally chosen, depends on the electronic and steric preferences of the respective metal ion.[132]

1.1.6 Radiometal ions

The choice of the radiometal ion is dependent on the medical objective (diagnosis, therapy; target structure), and hence on the respective decay mode and physical half-life $t_{1/2}$ (see **Table 3**). Ideally, the radionuclide should be readily available at reasonable cost containing essentially no stable isotopes (carrier).[24] Such "carrier-free"[ii] nuclides possess high specific activities[iii] and are thus preferred in radiopharmaceutical preparations as they minimize the required amount of the respective drug and consequently the toxicity for the patient.[24] The production methods for clinically used radiometals commonly involve particle accelerators (*e.g.* cyclotrons: ^{64}Cu, ^{67}Ga, ^{111}In), nuclear reactors (^{89}Sr, ^{99}Mo, ^{153}Sm), or radionuclide generators (*e.g.* ^{68}Ge / ^{68}Ga, ^{90}Sr / ^{90}Y, ^{99}Mo / ^{99m}Tc).[24] When a metal ion is then considered for medical applications, its coordination chemistry has to be taken into account which is where inorganic chemistry plays a major role.[19,96,136] This comprises aqueous hydrolysis chemistry, redox behavior, and affinity to native biological chelators.[21,48,137] Crucial for matching chelators and metal ions is a high degree of compatibility between these two components. Important factors are the size of the respective metal ion, as it has to fit into the binding site of the ligand, and its preferences regarding type and number of donor atoms, as well as coordination geometry.[132,137] In this context, the hard-soft acid-base (HSAB) principle can be a useful tool, as it divides metal ions (acids) and donor atoms (bases) into one of three classes, *i.e.* hard, borderline or soft. According to this concept a good fit between ligands and metal ions can be achieved when combining representatives of the same type.[138,139] The bifunctional chelator (BFC) should be selected depending on the unique properties of the metal ion. Preferable are, thereby, polydentate ligands which can occupy all coordination sites of the metal ion, resulting in its efficient encapsulation and shielding from the environment.[40] The energetics of metal ion complexation involves desolvation / solvation, metal-ligand bond formation, entropy changes, and steric effects. The steric energy is minimal when the structures of the metal-free and the coordinated ligand are identical, *i.e.* when the ligand is fully preorganized for the respective metal ion.[140-143]

[ii] The terms "carrier-free" (c.f.), "no-carrier-added" (n.c.a) and "carrier-added" (c.a.) are used in order to indicate the level of specific activity. "Carrier-free" means that the radionuclide is not contaminated with any isotope of the same element, whereas the description "no-carrier-added" only implies that no carrier was added intentionally. The expression "carrier-free" is difficult to quantitate and should hence be used with caution.[133-135]

[iii] Specific (radio)activity is defined as the measured radioactivity per gram of compound (unit [Bq/g]). In radiochemistry, the activity is often referred to using the amount of substance in mole and thus expressed as molar (radio)activity (measured radioactivity per mole of compound, unit [Bq/mol]).[135]

Table 3. Properties of some selected radiometal ions.

Metal ion	Ionic radius [pm] [(a)]	Radioactive nuclides	Half-life $t_{1/2}$[27]	Decay mode[27,144]	Possible medical application[52,145-147]
Sc^{III}	75	^{44}Sc	3.9 h	β^+ (94 %) EC (6 %)	PET
		^{47}Sc	3.4 d	β^- (100 %)	therapy
Cu^{II}	73	^{64}Cu	12.7 h	β^+ (17 %) EC (44 %) β^- (39 %)	PET, (therapy)
		^{67}Cu	2.6 d	β^- (100 %)	therapy
Ga^{III}	62	^{67}Ga	3.3 d	EC (100 %)	SPECT
		^{68}Ga	1.1 h	β^+ (89 %) EC (11 %)	PET
Y^{III}	90	^{86}Y	14.7 h	β^+ (32 %) EC (68 %)	PET
		^{90}Y	64.0 h	β^- (100 %)	therapy
Zr^{IV}	72	^{89}Zr	78.4 h	β^+ (23 %) EC (77 %)	PET
In^{III}	80	^{111}In	2.8 d	EC (100 %)	SPECT
Lu^{III}	98	^{177}Lu	6.7 d	β^- (100 %)	therapy
Bi^{III}	103	^{212}Bi	1.0 h	α (36 %) β^- (64 %)	
		^{213}Bi	45.6 min	α (2 %) β^- (98 %)	therapy
Ac^{III}	112	^{225}Ac	10.0 d	α (100 %)	therapy

[(a)] For coordination number (CN) 6.[148]

In contrast to the metal ions listed above, the group 7 elements technetium and rhenium can attain a wide range of oxidation states and coordination geometries.[17,44] The chemistry of technetium (^{99m}Tc)- and rhenium ($^{186/188}Re$)-based radiopharmaceuticals[18,149-155] is hence quite different to that of the radiometals listed in **Table 3** and is not considered in the present thesis.

1.1.7 Evaluation of metal-ligand complexes

As mentioned before, the radiometal ion complex as core component of a metalloradiopharmaceutical must be inert and stable. To evaluate the integrity of the metal-ligand moiety, different experiments with non-radioactive (“cold“) as well as radioactive (“hot“) isotopes are conducted. Initial studies of the coordination chemistry can for example

provide structural information on the “cold” metal complex in both solid state (X-ray analysis) and solution (*e.g.* NMR, nuclear magnetic resonance, and ESR, electron spin resonance, spectroscopy). Furthermore, the natural metal complex can be used as a standard for product identification in the studies with radioactive isotopes. In the following, various experiments evaluating the potential of the respective metal-ligand complex are described.

Thermodynamic stability

Complex formation constants as a measure of thermodynamic stability can be accessed by potentiometric titrations.[156-159] As a first step, the acid-base properties of the ligand need to be investigated in order to determine its protonation behavior. Therefore, a defined volume of an acidified ligand solution with known concentration is titrated with base while measuring the associated changes of the potential using a combination electrode. Based on the Nernst equation (Eq. 1) the measured potentials can be converted into pH values, provided that certain conditions are fulfilled.

$$E = E^0 + \frac{RT}{zF} \ln \frac{a(ox)}{a(red)} \qquad \text{Eq. 1}$$

R: universal gas constant, T: temperature, z: number of transferred electrons, F: Faraday constant, a(ox/red): activity of oxidized/reduced species, E: measured potential, E^0: standard potential of the electrode

Important requirements are constant ionic strength and temperature throughout the titration, allowing for the replacement of activities by concentrations in Equation 1. In order to keep the ionic strength constant, an inert electrolyte is used in excess. By inserting the respective values and, additionally, converting natural to common logarithm, the Nernst equation is simplified to:

$$E = E^0 - 0.059\ V \cdot pH \qquad \text{Eq. 2}$$

For the conversion of potential to pH by Equation 2, the standard potential E^0 of the electrode has to be determined prior to each measurement. In case of a simple ligand titration, there are two components necessary to describe the system, the ligand L and protons H. These again form the adducts LH, LH_2 *etc.*, where charges are usually omitted

for clarity. The corresponding equilibria can be expressed as either cumulative protonation (β) or stepwise deprotonation (K) constants.

Table 4. Comparison of cumulative protonation and stepwise deprotonation reactions.

	Cumulative protonation		Stepwise deprotonation	
1.	$L + H \rightleftharpoons LH$	$\beta_1 = \frac{[LH]}{[L][H]}$	$LH_2 \rightleftharpoons LH + H$	$K_1 = \frac{[LH][H]}{[LH_2]}$
2.	$L + 2\,H \rightleftharpoons LH_2$	$\beta_2 = \frac{[LH_2]}{[L][H]^2}$	$LH \rightleftharpoons L + H$	$K_2 = \frac{[LH]}{[L][H]}$

Usually, the described constants are given as their common logarithm, *i.e.* as $\log \beta_x$ or $-\log K_x$ (pKa_x). From this set of equations the following correlations can be derived:

$$\log \beta_1 = -\log K_2 = pKa_2 \qquad \text{Eq. 3}$$

$$\log \beta_2 = (-\log K_1) + (-\log K_2) = pKa_1 + pKa_2 \qquad \text{Eq. 4}$$

These relations can be easily extended to systems with any number of protonation steps. Based on the cumulative protonation constants an equation system including all relevant protonated species can be set up. Together with the measured potentials, the concentrations of all compounds involved, the autoprotolysis equilibrium of water and suitable start values for $\log \beta$, the system can be solved iteratively using a computer program like Hyperquad.[156,160,161]

As soon as the pKa values of the ligand are determined, metal-ligand titrations can be performed to evaluate the thermodynamic stability of the corresponding metal complex. In case of basic ligand systems the competition between the Lewis acids M (metal cation) and H is used to assess the stability constant K_{ML} of the complex ML. The pH decrease in comparison to the titration of the metal-free ligand is a quantitative measure for the complex stability, *i.e.* the lower the pH, the more stable the metal complex. Depending on the system and the pH range covered during titration, various species like protonated metal complexes (MLH), hydroxy compounds (MLH_{-1}), or oligonuclear species might need to be included to describe the system.[156] Many metal ions tend to hydrolyze and hence, the corresponding hydrolysis reactions have to be considered when working with these cations.[162]

The stability constant of highly stable metal complexes, that are required for nuclear medicine applications, can often not be determined by direct titration as described above. A key requirement for these measurements is a noticeable complex dissociation of at least 20 % within the range for accurate pH detection (2-12). If this is not the case, ligand-ligand competition titrations can be performed. Therefore, a competing ligand L' with a comparable affinity for the respective metal ion is needed. Moreover, the sums of the protonation constants of the ligands L and L' must be appreciably different. For the determination of the ML complex stability by this method, it is necessary that the pKa values of L and L', as well as the complex formation constant of L' with the metal ion are known.[156,163]

$$ML + H_nL' \rightleftharpoons ML' + H_mL + (n-m)\,H$$

In addition, the pM value is determined as an alternative criterion for metal ion affinity:

$$pM = -\log [M^{n+}] \qquad \text{Eq. 5}$$

The pM value is defined as the negative common logarithm of the free metal ion concentration under specified conditions (usually 1 µM total metal, 10 µM total ligand, pH 7.4, 25 °C). Comparisons of different ligand systems are straightforward, *i.e.* the larger the pM value, the higher the affinity of the chelate for the respective metal ion. The pM value is calculated from the stability constant log K_{ML}, taking into account ligand basicity (pKa values), metal ion hydrolysis, and (physiological) pH. This condition-dependent value is consequently considered more relevant for predicting *in vivo* stabilities than log K_{ML} values.[48,158,164-166]

In the case of copper(I/II) systems, RORABACHER *et al.* could show a correlation between redox potentials and $Cu^{II}L$ stabilities.[167] They found that $Cu^{I}L/Cu^{II}L$ potentials are inversely related to the common logarithm of copper(II) complex formation constants by investigating a wide range of ligand types. A negative potential consequently indicates a stable Cu^{II} complex. The identified correlation implies that the stability constants of copper(I) complexes with different ligands are relatively uniform. From this it can be concluded that Cu^{I}, as a d^{10} electronic system, exhibits little preference for specific coordination geometries or donor atoms. Provided that the amount of uncomplexed copper ion in both oxidation states is negligible, Equation 6 can be formulated for a temperature of 25 °C. The underlying relations are illustrated in the square scheme shown in **Figure 10**. Considering that log $K(Cu^{I}L)$ is nearly constant (see above) and that the

potential $E(Cu^{I}/Cu^{II})$ is a known value, one can calculate the $Cu^{II}L$ stability constant from the corresponding $Cu^{I}L/Cu^{II}L$ potential.[167,168]

$$E(Cu^{I}L/Cu^{II}L) = E(Cu^{I}/Cu^{II}) - 0.059\ V \cdot \log \frac{K(Cu^{II}L)}{K(Cu^{I}L)} \qquad \text{Eq. 6}$$

As redox potentials are easily accessible, this correlation is a useful tool for approximate estimations of copper(II) complex stabilities. However, a change of solvent can lead to significant changes as solvent molecules compete for the coordination sites on both Cu^{I} and Cu^{II} ions. Furthermore, only ligands that are uncharged in their unprotonated form were considered by RORABACHER *et al.* to exclude the influence of electrostatic effects.[167,168]

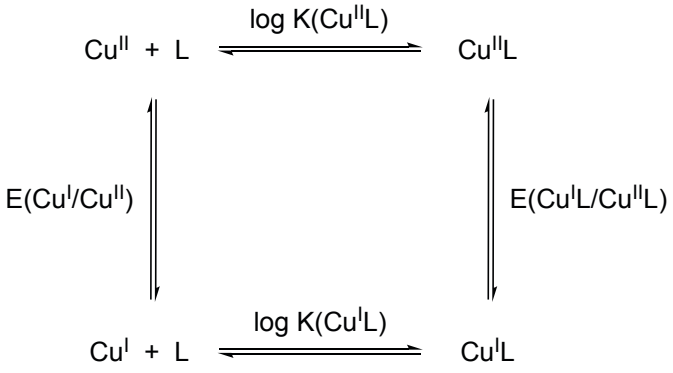

Figure 10. Correlation between redox potentials and stability constants for $Cu^{I}L/Cu^{II}L$ couples. Adapted from references [168,169].

Radiolabeling experiments

In further studies, usually the radiolabeling performance of the chelator with the respective metal ion is investigated as a function of concentration, temperature, and time. Ideally, one can radiolabel a small quantity of the ligand with a high amount of radioactive nuclide as this leads to a high specific activity of the resulting radiometal complex. Furthermore, fast radiolabeling at mild temperature (10-15 minutes, 25-37 °C) is best, especially with short-lived nuclides like, for example, gallium-68 ($t_{1/2}$ = 1.1 h[27]). However, even with longer half-life radionuclides, rapid labeling kinetics are desirable with respect to safety considerations and convenience of radiopharmaceutical preparation ("kit-type" formulations[150,170]).[48] The radiolabeling process is usually monitored by thin layer chromatography (TLC) and / or high performance liquid chromatography (HPLC). Chelator

and radiometal ion are combined and after a defined time, an aliquot of the sample is taken and analyzed by radio-TLC or radio-HPLC. For radio-TLC, an impregnated paper strip in combination with a suitable mobile phase is used to separate the formed radiolabeled ligand from the uncomplexed, "free" radiometal ions. The TLC plate is then measured in a well counter (*e.g.* a gamma well counter) in order to determine the intensity distribution. From that, the radiochemical yield (RCY), expressed as the percentage of radioactivity bound to the chelate, can be derived. In case of radio-HPLC, a column is used for separation (*e.g.* a C18 column) as well as a radiation detector for subsequent analysis, usually attached after the UV detector in the liquid line. The number and intensity of the peaks in the HPLC trace provide information on the radiochemical purity, *i.e.* the presence or absence of other radioactive compounds, whereas peak integration reveals the RCY.[144]

Competition assays

Challenges to the integrity of a metal complex can be either tested using other chelators with high affinity for the respective metallic center or metal ions that compete for the metal binding site of the ligand system under investigation. The usual procedure is to first radiolabel the chelator under the optimized conditions determined in previous labeling experiments. When quantitative radiolabeling (RCY > 99 %) is confirmed by TLC or HPLC, different competition assays can be carried out. One approach is the incubation of the preformed radiometal-ligand complex with strong metal chelators like cyclam (**L3**) or EDTA (**L9**).[171-173] Here again, TLC or HPLC is used to determine the ratio of radiometal-ligand to radiometal-(competing ligand) complex and thus the amount of transchelation. Therefore, a suitable system consisting of mobile phase and TLC plate or HPLC column, respectively, has to be found in order to clearly separate those two compounds. Experiments more relevant to *in vivo* conditions involve the use of blood serum or individual native biochelators (*e.g* superoxide dismutase and transferrin).[58,158,172-177] From a functional point of view, blood can be designated as "liquid tissue" as it consists of cells (erythrocytes, leukocytes, and lymphocytes) and plasma, a protein and electrolyte containing fluid. The liquid remaining after blood clotting is called serum, which is plasma without the coagulation factor fibrinogen.[178] Normally, human blood plasma has a total protein concentration between 65 to 80 g/L and consists of roughly 100 proteins including transport proteins such as ceruloplasmin, albumin, metallothionein, and transferrin, storage proteins like ferritin, as well as metal containing enzymes like extracellular superoxide dismutase (only small amounts).[178-180] By incubation of a radiolabeled ligand

with a biologically relevant mixture like blood serum, the stability of the complex to transchelation, and thus radiometal loss, can be evaluated over time using size exclusion chromatography (SEC)[58,158,174,181] or gel electrophoresis.[182]

Aside from proteins, the human body contains various metal ions such as Na^+, K^+, Ca^{2+}, Mg^{2+}, Zn^{2+}, Cu^{2+}, and Fe^{3+} in high (major elements) to low (trace elements) concentrations.[179,183] Hence, the radiometal-ligand complex needs to be stable in the presence of competing cations. Furthermore, selectivity of the chelator for the respective radiometal ion is crucial, as these often comprise metallic impurities depending on the production and purification method.[48,184,185] An important aspect to consider in general is the concentration ratio: usually radiopharmaceuticals are applied in very small quantities (nano- to picomolar levels) and under highly dilute conditions, so that competing chelators or metal ions (even if also only present in low concentrations) could be in excess of the radiolabeled drug, and thus exchange reactions may be favored.[39,48,184]

Lipophilicity and biodistribution studies

Although it might be possible to simulate extracellular conditions to a certain extent during *in vitro* experiments, actual uptake, distribution, and clearance of a radiopharmaceutical in living systems is complicated. These pharmacokinetic properties can be correlated with the lipophilicity of the drug and therefore 1-octanol-water partition coefficients are determined as an index of a compound's lipophilic character.[186,187] The partition coefficient $P_{o/w}$ is defined as the concentration of an unionized substance in the lipid phase (1-octanol) divided by its concentration in the aqueous phase (water) and is usually given in form of the common logarithm ($\log P_{o/w}$). In the case of ionized compounds, *e.g.* transition metal ion complexes, the degree of ionization (dependent on the pKa value of the substance and the pH of the system) must be considered. The distribution coefficient $D_{o/w}$ is thus the concentration ratio of the sum of both ionized and unionized forms of the respective compound between the two immiscible phases. It is important to note that $\log D_{o/w}$, in contrast to $\log P_{o/w}$ values, are pH-dependent properties and for *in vivo* applications, the most significant distribution coefficients are those at a pH of 7.4, the pH of blood serum.[186,188] A widely used method to determine the lipophilicity of a substance is the so-called shake-flask procedure, often in combination with radionuclides for analysis. Therefore, the compound to be examined is dissolved in either organic or aqueous phase and radiolabeled. Equilibrium partition is then achieved by agitation, before separating both phases and analyzing the amount of radiotracers present.[172,189,190]

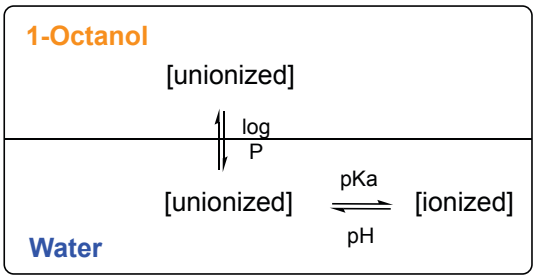

Figure 11. Illustration of 1-octanol-water partition. Adapted from reference [186].

Even though general predictions of biological behavior are difficult, one can state that rather low lipophilicity (log D < 0) often leads to renal clearance, whereas non-renal excretion is predominant at higher lipophilicity (log D > 0).[186,191] Based on such observations QSPR (quantitative structure-property relationships) models are developed in order to predict the biological properties of new conjugates. These approaches are useful tools, as they help to reduce the number of animal experiments and conserve resources.[186,188,192]

However, the ultimate test for radiopharmaceutical stability is carried out *in vivo*. Biodistribution studies in healthy animals (often mice or rats) are performed on radiometal-ligand complexes without conjugated vectors in order to gain information on uptake and clearance behavior, organ distribution, and complex stability under physiological conditions. Stable complexes are typically cleared rapidly from the animal *via* the renal (kidneys-bladder-urine) or the hepatobiliary (digestive system-liver-feces) tracts, depending on lipophilicity and metabolism. In case of unstable complexes, substantial uptake is observed in organs and tissues where the released radiometal ion is known to accumulate (*e.g.* Cu^{II} in the liver, Ga^{III} and the lanthanides in the bone).[48,113]

What is the further procedure from this stage onwards? After the introduction of a vector moiety, the stability of the conjugate needs to be examined as a basis for the potential application in nuclear medicine. In this case, tumor-bearing animals are used for the investigation of targeting and accumulation behavior of the radiolabeled drug. If the results are promising, clinical studies on patients (phase I-III) can be initiated with the ultimate goal to obtain market approval of the radiopharmaceutical. The typical time frame for this process is in the range of 5 to 10 years.[24,48]

In this introductory chapter the structure and use of receptor targeting radiometal labeled pharmaceuticals was presented. The individual components of such metal-based agents were thereby shown together with corresponding examples. To this day, there is no single

radionuclide or bifunctional chelator (BFC) that is optimal for all nuclear medicine applications in either imaging or therapy.[95] For this reason, new versatile ligand systems need to be developed and investigated with metal ions relevant for radiopharmaceutical purposes. The focus in the present thesis is hence on the metal-ligand unit of radiolabeled drugs. Therefore, new ligands are synthesized and evaluated with different metal ions. In the following chapters these radiometals (Chapter 1.2) as well as the ligand class of bispidines (Chapter 1.3) are considered in detail.

1.2 Selected radiometal ions – nuclear properties and coordination chemistry with emphasis on medical applications

A selection of metallic radionculides with interesting properties for nuclear medicine will be presented including copper-64, gallium-68, indium-111, lutetium-177, and actinium-225. The main focus of this discussion will be on radiometal production and decay characteristics as well as on non-radioactive coordination chemistry and radiopharmaceutical applications.

1.2.1 Copper-64

There are a number of radioactive copper isotopes suitable for nuclear imaging and therapy, *i.e.* ^{60}Cu, ^{61}Cu, ^{62}Cu, ^{64}Cu, ^{66}Cu, and ^{67}Cu.[146] Copper-64 is the most versatile of these radionuclides because of its unique decay properties involving β^- decay to ^{64}Zn (39 %), as well as electron capture (44 %) and positron emission (17 %) to ^{64}Ni with a maximum β^+ energy of 653 keV.[27,146,193] The copper isotope ^{64}Cu can hence be used for either therapeutic or diagnostic purposes, whereby the main application is PET imaging.[38,194,195] In contrast to PET radionuclides like ^{11}C ($t_{1/2}$ = 20.4 min[27]) and ^{18}F ($t_{1/2}$ = 109.8 min[27]), copper-64 displays a comparably long half-life of 12.7 hours and is thus compatible with small as well as large molecular carriers.[38,146,194] Together with the pure β^- emitter ^{67}Cu ($t_{1/2}$ = 2.6 d[27]) copper-64 builds a “matched pair“ for combined imaging and therapy.[49-51] ^{64}Cu is commercially available and can be produced by biomedical cyclotrona *via* the ^{64}Ni(p,n)^{64}Cu nuclear reaction.[21,196,197] Therefore, 12 MeV proton irradiation of enriched ^{64}Ni is performed, followed by separation of ^{64}Cu and other contaminants like cobalt isotopes from the ^{64}Ni target using anion exchange chromatography.[196-199]

The coordination chemistry of copper in the oxidation state +II has been extensively investigated and offers an excellent starting point for the development of copper-based radiopharmaceuticals.[137,153,200] However, certain special features have to be considered when working with this transition metal cation: according to the HSAB principle, copper(II) is classified as a “borderline” element and as such prefers nitrogen-containing donors like amines and pyridines.[138,139,200] Copper(II) has a d^9 electron configuration and builds paramagnetic metal complexes with coordination numbers (CN) of four to six corresponding to ionic metal radii between 57 and 73 pm.[148,200] Typical coordination modes of copper(II) approximate *pseudo* square planar, trigonal pyramidal, square

pyramidal and octahedral geometries.[200] Copper(II) is a JAHN-TELLER active system and in the case of 6-coordinate Cu^{II} ions this effect is often observed as an axial elongation.[2,200,201]

Copper(II) and its complexes are prone to reduction under physiological conditions, whereby the estimated threshold for typical bioreductants is –0.40 V *vs.* the normal hydrogen electrode (NHE).[137] The Cu^{II}/Cu^{I} reduction is suggested to be a cause for radiocopper loss *in vivo* since d^{10} copper(I) is significantly more labile towards ligand exchange.[21,200] It is hence important that a ligand selected for use with ^{64}Cu can either coordinate both Cu^{I} and Cu^{II} or stabilizes copper(II) in a way that prevents reduction.[194] Thereby it must be considered that Cu^{I}, in contrast to Cu^{II}, prefers soft polarizable ligands with sulfur and phosphorus donor atoms.[200] The redox behavior of copper can be exploited for imaging of oxygen deficiency (hypoxia) using bis(thiosemicarbazone) chelates like ATSM (**L11**, N_2S_2-type ligand).[202-204] The proposed mechanism involves formation of Cu^{I} species from copper(II) complexes like Cu^{II}-ATSM in hypoxic cells, followed by retention of the reduced compounds.[205]

A variety of different ligand systems has been investigated for the combination with the PET nuclide copper(II)-64 (see **Figure 12**).[48,137,146,194,200] To evaluate the potential of the chelates for nuclear medicine applications, radiolabeling and stability studies were performed. Macrocycles of varying size and substitution pattern were shown to form highly stable copper(II) complexes.[137,194] Tri- and tetraazamacrocycles were functionalized with carboxylic acid (**L4**, NOTA; **L5**, DOTA, and **L6**, TETA), phosphonic acid (**L13**, DOTP and **L17**, TETP) and picolinic acid pendent arms (**L12**, NO1PA2PY; **L14**, DO1PA, and **L18**, TE1PA).[115,116,124,125] The incorporation of an ethylene linker into the marcocyclic ring led to the corresponding cross-bridged derivatives like CB-TE2A (**L20**) or CB-TE2P (**L22**). Furthermore, substitution with different functional groups was also tested (*e.g.* **L21**, CB-TE1A1P).[122,123,126,206] In addition, various bifunctional systems with suitable linker moieties were developed.[48] The octadentate N_4O_4 macrocyclic chelate TETA (**L6**) has predominantly been examined for radiopharmaceutical purposes with copper(II)-64.[48] However, Anderson *et al.* showed in experiments on rats that $^{64}Cu^{II}$-TETA-D-Phe^{1}-octreotide ($^{64}Cu^{II}$-TETA-OC) is relatively unstable and undergoes significant transchelation towards native proteins like superoxide dismutase (SOD).[207] The abovementioned cross-bridged versions CB-TE2A (**L20**), CB-TE1A1P (**L21**), and CB-TE2P (**L22**) are therefore especially interesting as they show improved *in vivo* stability and radiolabeling kinetics in comparison to TETA.[208]

Sarcophagine hexaazamacrobicyclic cryptands are well-known for their fast and extremely strong copper(II) binding. The Sar-cage DIAMSAR (**L24**, N_6) and its derivatives have hence been investigated as chelates for $^{64}Cu^{II}$-based radiopharmaceuticals.[209-214] The lipophilicity of such nitrogen-rich ligands can have a negative impact on the biodistribution including accumulation in the liver and the digestive tract.[48] For this reason, Sar-derivatives with additional carboxylic acid functionalities have been developed.[215-217]

Another type of cyclic chelator are dioxotetraaza macrocycles, bearing amine and amide functions. Recently, COMBA and coworkers incorporated a bispidine moiety into this ligand scaffold. By subsequent variation of the ring size and flexibility, they found BBDT (**L25**) to form copper(II) complexes, which are stable in the presence of SOD and human serum. As with most macrocyclic systems, the radiolabeling properties of **L25** are not ideal since heating to 50 °C for more than 30 minutes is required.[177] In contrast to that, the bispidine system itself provides a suitable platform for the development of $^{64}Cu^{II}$ chelators showing fast labeling kinetics. Examples for such bispidine ligands are N_2py_4 (**B3**), **(*p*-MeO)B4**, and **B5**, depicted in **Figure 12**.[172,173,218] The application of bispidine ligands in nuclear medicine, especially for PET imaging, will be discussed in Chapter 1.3.

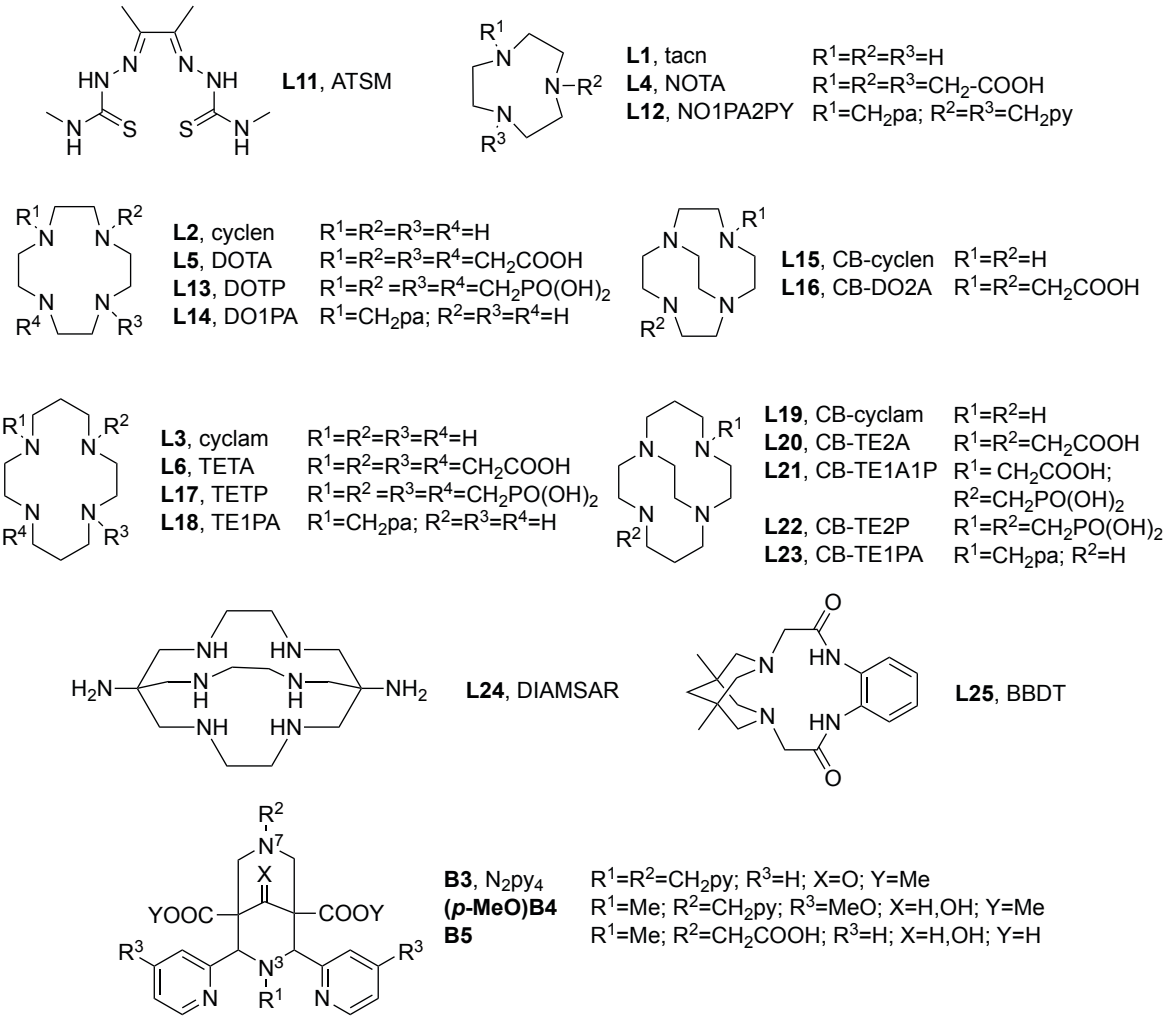

Figure 12. Selected copper(II) chelators.

As mentioned before, high complex stability is crucial to prevent radiometal loss *in vivo*. After iron and zinc, copper is the third most abundant trace metal in the human body.[146] As such, its metabolism is tightly regulated and there are a number of copper-binding biomolecules that can potentially compete with a chelator for $^{64}Cu^{II}$ coordination, including serum albumin, transcuprin, ceruloplasmin, metallothionein, and superoxide dismutase.[146,180] When excess Cu^{II} ions are injected into the blood stream, they immediately become bound to serum copper transport proteins like albumin or transcuprin. These proteins deposit the metal in the liver resulting in its rapid clearance from the blood. In the liver the copper is predominantly taken up by ceruloplasmin and in this form returns to the blood stream to be transferred to other organs.[146,219] Knowledge of the natural biodistribution of ionic Cu^{II} is essential for comparison with the pharmacokinetics of radiocopper(II)-labeled drugs.[146]

1.2.2 Gallium-68

For the application in nuclear medicine the gallium isotopes ^{67}Ga and ^{68}Ga are promising.[220] Accelerator-produced gallium-67 ($t_{1/2}$ = 3.3 d[27]) disintegrates by electron capture with emission of γ rays suitable for scintigraphy and additionally emits low energy AUGER and conversion electrons.[53,221] When coordinated to deprotonated citric acid (**L26**), gallium-67 can be used for the detection of tumors and inflammations.[17,221] However, the current research is predominantly focused on the short-lived isotope gallium-68 ($t_{1/2}$ = 1.1 h[27]), as it can be produced in a commercially available ^{68}Ge / ^{68}Ga generator system.[222,223] These generators produce ^{68}Ga through electron capture decay of its "parent" radionuclide ^{68}Ge. Efficient separation of both metals is achieved by ion exchange chromatography with the parent ^{68}Ge remaining on the column and the daughter ^{68}Ga being eluted using concentrated hydrochloric acid.[223] The long half-life of germanium-68 of 271 days allows the generator to be used for up to 1 year.[21,27,223] Gallium-68 decays by 89 % positron emission with a maximum β^+ energy of 1.9 MeV to ^{68}Zn.[27,222] The generator-based production of ^{68}Ga provides thus a feasible route to a PET nuclide without the need for an on-site cyclotron. In analogy to the successful application of the generator-produced radionuclide ^{99m}Tc for nuclear imaging, ^{68}Ga is expected to pose great potential for future developments.[194,223]

In aqueous solution, the only stable and relevant oxidation state of gallium is Ga^{III}, which exists in its hydrated form as $[Ga(H_2O)_6]^{3+}$ under acidic conditions.[21,194] This small and highly charged cation is a classic hard Lewis acid and consequently, has a strong affinity for hydroxides.[137-139] In the pH range of 3-7 insoluble $Ga(OH)_3$ is formed in the absence of suitable ligands and is hydrolyzed to the gallate anion $[Ga(OH)_4]^-$ above pH 7.[21,194] Gallium(III) typically builds metal complexes with coordination numbers (CN) of four to six in which the radius of the cation is in the range of 47-62 pm.[137,148] The development of ligand systems for Ga^{III} is focused on hexadentate chelators in order to ensure full encapsulation of the metal ion in a (distorted) octahedral geometry.[137] As a hard acidic cation, gallium(III) forms thermodynamically stable complexes with ligands containing anionic oxygen, and nitrogen donors, but was also found to exhibit a good affinity for thiolates.[137,194]

Due to the close similarity of the trivalent metal ions Ga^{III} and Fe^{III}, transchelation of gallium(III) by native iron binding proteins is a major issue for *in vivo* applications.[194] The strong affinity of Ga^{III} for the biological iron transporter transferrin is well known.[165] It is hence important that radiogallium(III) complexes are sufficiently stable in presence of this

blood serum protein to prevent ligand exchange, resulting in the accumulation of $^{67/68}Ga^{III}$ in the liver, lungs, and bone.[223,224]

Because of its short half-life, $^{68}Ga^{III}$ is predominantly used with small vector molecules like peptides.[54,71] Suitable gallium(III) chelators are needed for the incorporation of the radiometal ion into biomolecules and a selection thereof is presented in **Figure 13**. The macrocyclic frameworks NOTA (**L4**) and DOTA (**L5**) have been extensively investigated with $^{68}Ga^{III}$ and can be designated as "gold standards" for this radiometal.[48,54] The smaller-sized cycle NOTA is better suited for gallium(III) and the thermodynamic stability of Ga^{III}-DOTA is significantly lower than that of Ga^{III}-NOTA.[225] Nevertheless, conjugates such as $^{68}Ga^{III}$-DOTA-TOC and $^{68}Ga^{III}$-DOTA-TATE showed high *in vivo* stability.[226,227] In order to improve their gallium(III) binding properties for radiopharmaceutical application, derivatives of these macrocycles have been synthesized. In the case of the triazacyclononane-based chelator TRAP (**L27**, N_3O_3-type ligand), phosphinic acid arms with additional distal carboxylic acid groups have been introduced into the macrocyclic scaffold.[228,229] Of particular interest is the improved selectivity of **L27** for Ga^{III} in the presence of competing metal ions when compared to NOTA.[230] Another important feature is the potential of **L27** to be radiolabeled with $^{68}Ga^{III}$ under the highly acidic conditions of the ^{68}Ge / ^{68}Ga generator eluent, which is possible due to the low pKa of < 1 of the phosphinic acids.[229] A general problem when using macrocycles to complex short-lived radionuclides like $^{68}Ga^{III}$ is the often unfavorable chelation kinetics including either long reaction times or harsh conditions.[48,194] The heptadentate macrocyclic chelate PCTA (**L28**, N_4O_3) incorporates pyridine into the DOTA framework instead of a secondary amine.[231] Originally evaluated as a potential MRI contrast agent,[232] **L28** has been recently investigated with $^{68}Ga^{III}$. **L28** was thereby found to perform radiolabeling in less than 30 minutes at ambient temperature whilst maintaining the high stability associated with macrocycles.[233,234]

With regard to their fast complex formation, non-macrocyclic chelators are of special interest for application with $^{68}Ga^{III}$. Derivatives of the preorganized ligand system AAZTA (**L29**, N_2O_4 or N_3O_3) are promising new gallium(III) chelates with rapid radiolabeling kinetics and good preliminary stability results.[235,236] Another prominent ligand class is the so-called "pa-family" which uses picolinic acids (pa) as central binding units.[237-240] The first "pa" ligand to have been investigated for radiochemical purposes was the hexadentate scaffold H_2dedpa (**L30**, N_4O_2) showing ideal properties for $^{67/68}Ga^{III}$.[241-243] Due to the hardness of gallium(III), oxygen-rich chelators are quite suitable for this metal cation. The bacterial siderophore desferrioxamine B (DFO, **L31**, O_6) natively binds Fe^{III}

and also forms stable Ga^{III} complexes of high thermodynamic stability.[244,245] The tripodal tris(hydroxypyridinone) chelator CP256 (**L32**, O_6) is another pure oxygen donor ligand and can be radiolabeled with ^{68}Ga in 5 minutes at room temperature.[246] In addition, $^{68}Ga^{III}$-**L32** displayed high inertness to transferrin in competition studies.[246] It is expected that the further development of these promising acyclic ligand systems will have significant impact on $^{68}Ga^{III}$ PET imaging in the future.[194]

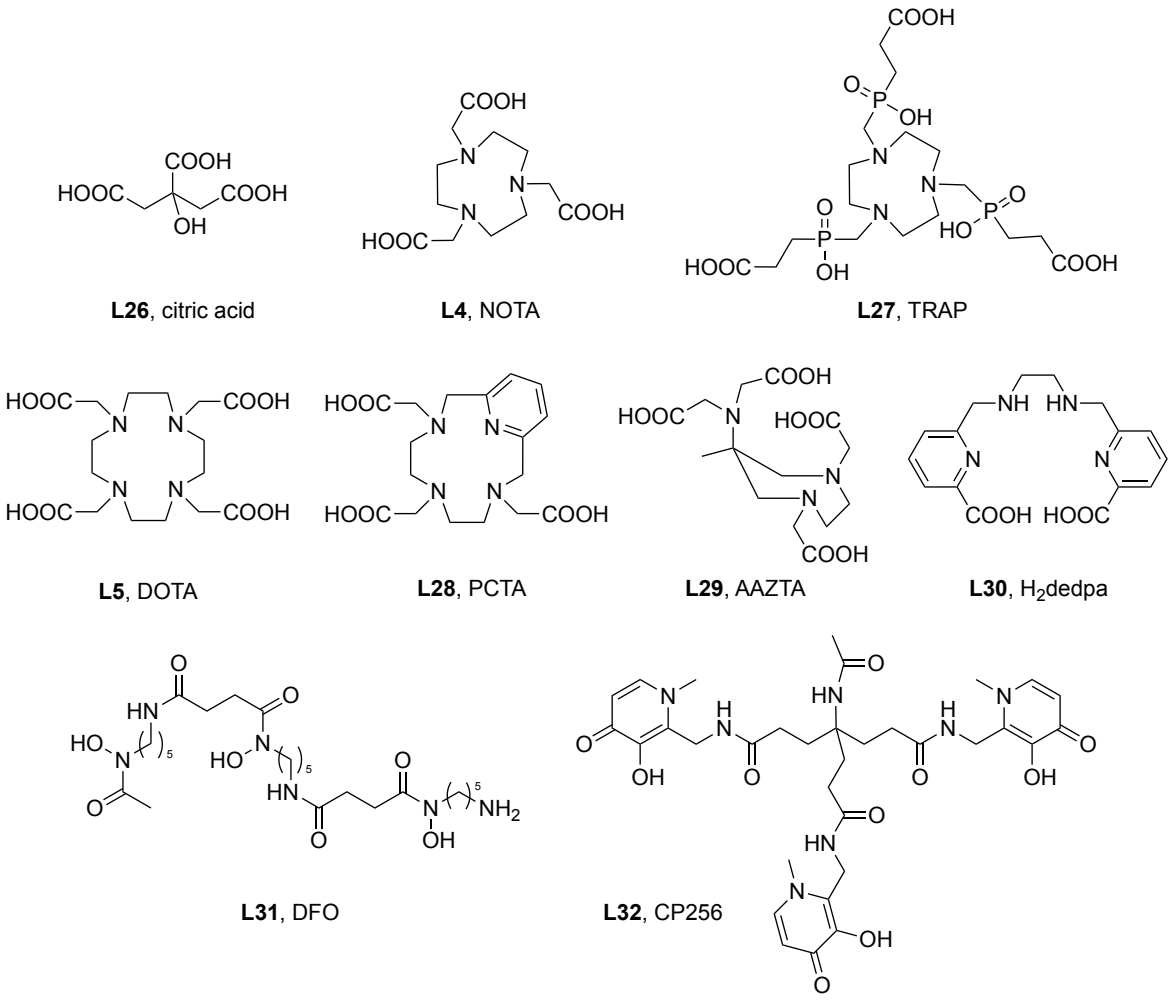

Figure 13. Selected gallium(III) chelators.

1.2.3 Indium-111

After ^{99m}Tc, ^{111}In is the most widely used metallic radionuclide for single photon emission computed tomography (SPECT). With a half-life of 2.8 days, ^{111}In decays *via* electron capture (EC) to ^{111}Cd emitting γ rays of 171 and 245 keV, and is hence ideally suited for nuclear imaging.[21,27] In addition, ^{111}In emits AUGER electrons and an $^{111}In^{III}$ radiolabeled peptide conjugate has been successfully evaluated for the treatment of neuroendocrine tumors.[44,247,248] ^{111}In is commercially produced by irradiation of a natural cadmium target with a proton beam *via* the ^{111}Cd(p,n)^{111}In or the ^{112}Cd(p,2n)^{111}In reaction. The subsequent separation of ^{111}In from the cadmium target is performed by either ion exchange or solvent extraction.[137]

As in the case of gallium, the only stable indium oxidation state under aerobic aqueous conditions is +III.[137] In comparison to Ga^{III}, In^{III} has a relatively large size with 62-92 pm for coordination numbers (CN) of 4-8.[148] Within the element group the "hardness" of a metal cation decreases with increasing ionic radius[138,139] and indium(III) hence displays a slightly enhanced affinity for softer donor atoms.[137] Furthermore, In^{III} attains CN of 7 or 8 in its complexes compared to predominantly 6-coordinate Ga^{III} complexes.[137] Such differences in the coordination chemistry of metal ions can have a significant impact on their *in vivo* behavior.[249] A selection of prominent indium(III) chelators is presented in **Figure 14**.

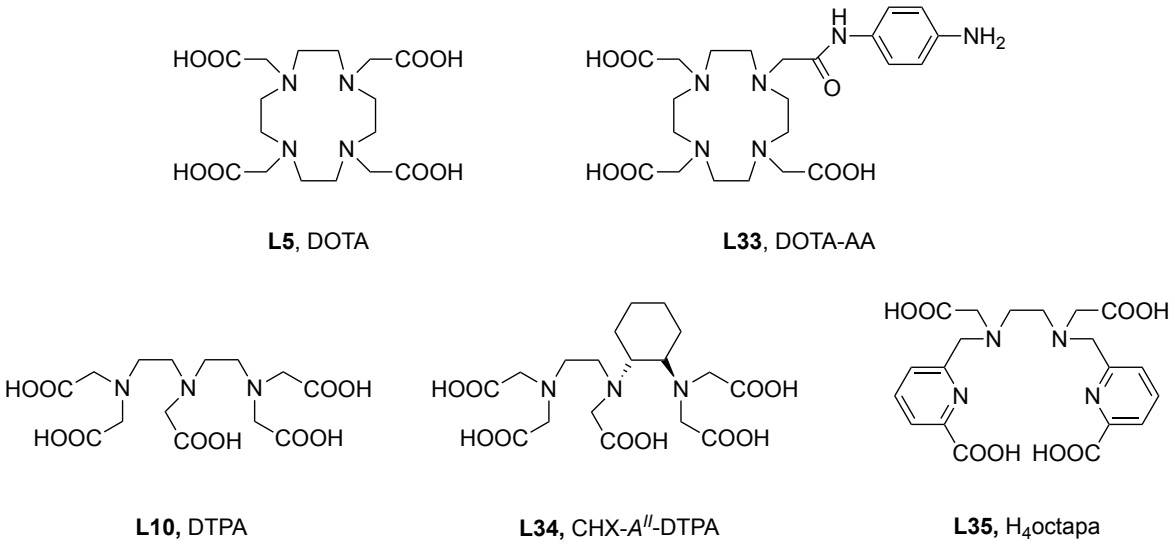

Figure 14. Selected indium(III) chelators.

The macrocycle DOTA (**L5**) and the acyclic ligand DTPA (**L34**) are the “gold standards” for $^{111}In^{III}$ radiolabeling.[48,137] The indium(III) DOTA complex is highly stable,[158,250] but requires elevated labeling temperatures to obtain high molar activities, which is problematic in combination with heat-sensitive biomolecules as vector moieties.[48,251] Despite the accumulating studies of the In^{III}-DOTA complex regarding its application as a radiopharmaceutical no X-ray structural data are available.[137,250-254] However, the solid state structure of the indium(III) complex based on the amide-substituted DOTA derivative DOTA-AA (**L33**) has been reported and is shown in **Figure 15** .[255] The central indium(III) ion is coordinated by the N_4O_4-ligand DOTA-AA by four amine-nitrogen, one carbonyl-oxygen, and three carboxylate-oxygen atoms. The N_4 coordination plane and the O_4 plane are twisted by an angle of ~28 ° with respect to each other resulting in a geometry between prismatic (theoretical twist angle of 0 °) and antiprismatic (45 °).[255] Such structures are referred to as twisted square-antiprismatic.[137]

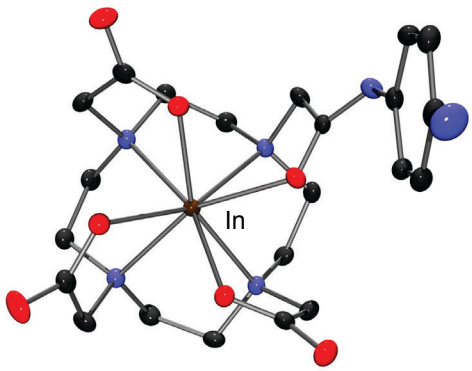

Figure 15. ORTEP plot of the complex In^{III}(DOTA-AA) (CCDC 228929).[255] Ellipsoids are shown at the 50 % probability level; co-crystallized solvent molecules, and hydrogen atoms are omitted for clarity.[256]

In contrast to the macrocyclic ligand DOTA, DTPA (**L10**) shows fast radiolabeling with $^{111}In^{III}$ within 5-10 minutes at room temperature.[48] Solid state X-ray analyses revealed that DTPA forms 7- or 8-coordinate indium(III) complexes with distorted pentagonal-bipyramidal or square-antiprismatic geometries, respectively (see **Figure 16**).[137,257-259] In the case of sevenfold coordination, one acetate arm is protonated and, in this form, is not involved in metal ion complexation.[257,259] Despite the non-optimal *in vivo* stability, derivatives of DTPA are incorporated in two approved $^{111}In^{III}$-labeled radiopharmaceuticals, known under the trade names OctreoScan® and ProstaScint®.[21,48,127-129,260,261] Whereas OctreoScan® ($^{111}In^{III}$-DTPA-octreotide) is based on a tumor-targeting peptide,

ProstaScint® ($^{111}In^{III}$-pendetide-capromab) uses a monoclonal antibody for the detection of prostate cancer.[127-129,260,261] Inspired by the successful application of DTPA in $^{111}In^{III}$ SPECT imaging, the preorganized cyclohexyl derivative CHX-*A''*-DTPA (**L34**, N_3O_5-type ligand) was developed, showing improved stability over DTPA with different metal ions.[48,130,131,262] However, as a consequence of the preorganization of the ligand scaffold the radiolabeling kinetics of CHX-*A''*-DTPA with $^{111}In^{III}$ are less favorable than those of DTPA. While DTPA can be labeled within 5-10 minutes at room temperature, CHX-*A''*-DTPA requires mild heating (25-60 °C) and extended reaction times of 30-60 minutes.[48]

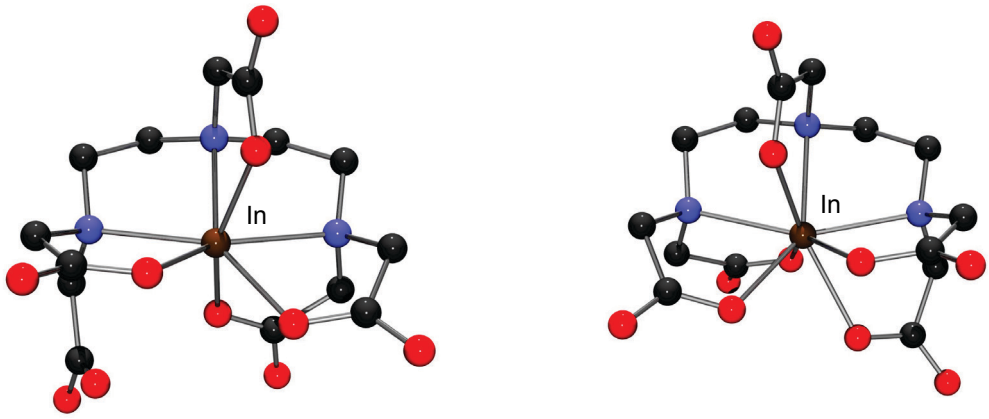

7-coordinate 8-coordinate

Figure 16. ORTEP plot of the complex anions of $C(NH_2)_3[In^{III}(DTPA)]$ (left, CCDC 1312572)[257] and $Na_2[In^{III}(DTPA)]$ (right, CCDC 1213339).[258] Ellipsoids are shown at the 50 % probability level; co-crystallized solvent molecules, counterions, and hydrogen atoms are omitted for clarity.[256]

Another promising indium(III) chelator is the picolinic acid-based ligand H_4octapa (**L35**, N_4O_4), which displays high *in vivo* stability as well as fast radiolabeling behavior.[58,158,240] So far, the solid state structure of the indium(III) octapa complex could not be determined. NMR studies in deuterated water and density functional theory (DFT) calculations, modeled in water, were performed for In^{III}-octapa and point to a 7- or 8-coordinate solution structure, respectively.[158]

1.2.4 Lutetium-177

Since the beginning of the past decade rapidly growing interest in lutetium-177 as a therapeutic radionuclide has been observed.[263,264] The increased use of ^{177}Lu is mainly attributed to its favorable radiochemical properties and its ease of production with high specific activity.[264] Lutetium-177 decays with a half-life of 6.7 days to stable hafnium-177 *via* the emission of β^- particles with low energies of 177, 385, and 498 keV used for radiotherapy.[27,264] Depending on the size, location, and characteristics of a specific tumor, the choice of the β^- emitting radionuclide for targeted therapy might be different.[111] For example, high energy β^- emitters such as ^{90}Y ($t_{1/2}$ = 2.7 d[27]) are preferable for the treatment of large solid tumors, whereas the low energy β^- emissions of ^{177}Lu are better suited for smaller tumors and metastases.[111,263] In addition, lutetium-177 also emits γ rays with maximum energies of 113 and 208 keV suitable for SPECT imaging and dosimetry calculations.[21,27] Another advantage of ^{177}Lu is that its long half-life allows for the distribution to users in remote regions with minimal activity loss from radioactive decay.[44,263] The most popular therapeutic radionuclide is iodine-131 ($t_{1/2}$ =8.0 d[27]), which has been routinely used as sodium iodide-131 (Na^{131}I) for the treatment of thyroid cancer for more than 60 years.[43] Radioiodine therapy is based on the highly selective uptake of free iodide from the blood to the thyroid gland *via* the sodium iodide symporter.[43,265] As a consequence of this unique biological mechanism, ^{131}I will continue to be the radionuclide of choice for the therapy of thyroid diseases. However, due to the similar nuclear characteristics of ^{131}I and ^{177}Lu, the radiolanthanide can be considered as the metallic analog of ^{131}I and might replace it in some non-thyroid applications.[264]

Lutetium-177 can be produced by charged particle acceleration in a cyclotron, but neutron irradiation using a nuclear reactor is the preferred route in terms of practicability and cost-effectiveness. Production of ^{177}Lu in a nuclear reactor can be performed in two ways, *i.e.* by the direct activation of enriched ^{176}Lu or through the indirect route by irradiation of ^{176}Yb followed by β^- decay to ^{177}Lu.[264]

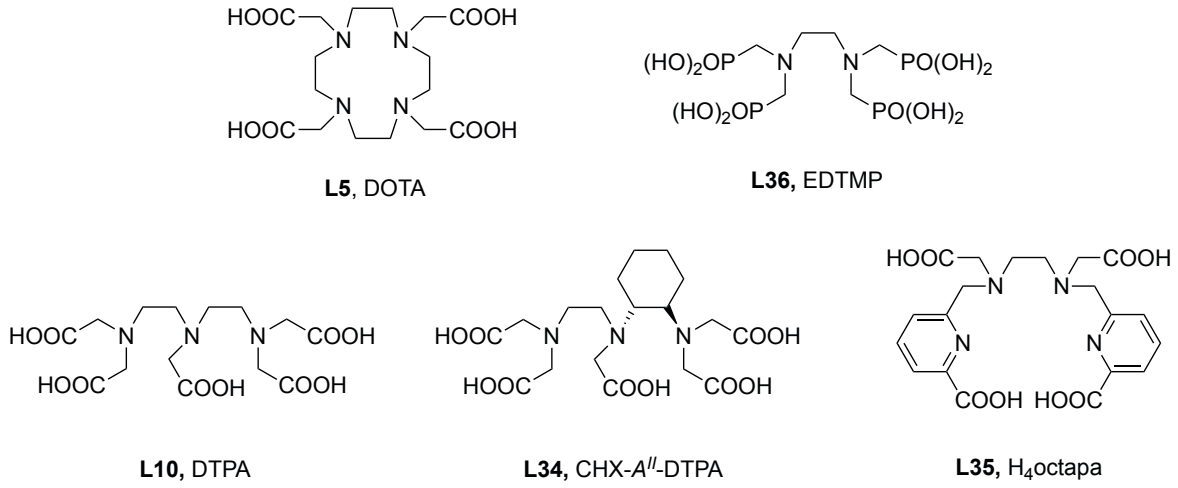

L5, DOTA

L36, EDTMP

L10, DTPA

L34, CHX-*A*^{II}-DTPA

L35, H_4octapa

Figure 17. Selected lutetium(III) chelators.

Lutetium is the heaviest member of the lanthanide group and as such possesses the smallest radius due to the lanthanide contraction.[44,264] The ionic radii reported for lutetium(III) complexes with coordination numbers of 6, 8, and 9 are 86, 98, and 103 pm, respectively.[148] As a typical lanthanide the only common oxidation state of lutetium is +III.[44,264] The coordination chemistry of the hard Lewis acid lutetium(III) is characterized by its tendency to form complexes with hard donors like oxygen, nitrogen, and fluoride. Furthermore, Lu^{III} prefers polydentate ligand systems usually resulting in 8- or 9-coordinate metal complexes.[264] In **Figure 17** a few examples of commonly used lutetium(III) chelators are depicted. The ubiquitous DOTA (**L5**) for instance acts as an octadentate ligand for lutetium(III) through the four nitrogen atoms of the macrocycle and the four oxygen atoms of the carboxylic acids.[266] A water molecule occupies a ninth coordination site resulting in a capped square antiprism complex geometry (see **Figure 18**).[264,266]

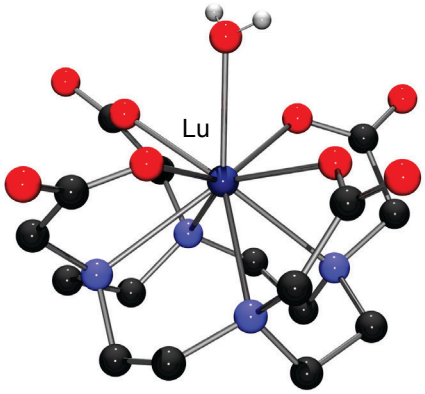

Figure 18. ORTEP plot of the complex anion of Na[Lu^{III}(DOTA)(H_2O)] (CCDC 1221968).[266] Ellipsoids are shown at the 50 % probability level; co-crystallized solvent molecules, counterions, and hydrogen atoms on carbon atoms are omitted for clarity.[256]

Despite the preference of lutetium(III) for high coordination numbers, the hexadentate chelate EDTMP (**L36**, N_2O_4-type ligand) was successfully evaluated with $^{177}Lu^{III}$ for the treatment of metastatic bone cancer.[267-270] In some countries $^{177}Lu^{III}$-EDTMP is already used as an agent for metastatic bone pain palliation.[263] However, to this day, the macrocycle DOTA is the most widely used chelator for $^{177}Lu^{III}$. Despite the relatively long half-life of $^{177}Lu^{III}$, DOTA-peptide conjugates have been evaluated for radiotherapy.[264] Very promising results were found for $^{177}Lu^{III}$-DOTA-TATE (Lutathera®), which efficiently targets neuroendocrine tumors.[271,272] Due to the relatively slow radiolabeling kinetics of DOTA with $^{177}Lu^{III}$ and the need for elevated reaction temperatures,[251,264] there is an increasing interest in acyclic chelators like DTPA (**L10**),[273,274] CHX-*A''*-DTPA (**L34**),[274-277] and H_4octapa (**L35**)[58] for the potential application with the radiolanthanide. Although the nuclear properties of $^{177}Lu^{III}$ are highly suitable for application involving monoclonal antibodies (mAbs) as targeting vectors, the clinical use of $^{177}Lu^{III}$-radiolabeled antibodies is not as widespread as that of the respective peptide-based agents. This might be explained by the more challenging preparation and characterization of antibodies in comparison to small peptides.[263] However, there are a number of mAbs, often functionalized with DOTA, which are currently in clinical trials for application with $^{177}Lu^{III}$.[264] A promising example is the development of $^{177}Lu^{III}$-DOTA-rituximab for radioimmunotherapy of Non-HODGKIN's lymphoma.[278,279]

1.2.5 Actinium-225

The ultimate goal of nuclear therapy is to create a “magic bullet” that specifically targets and destroys malignant cells without harming surrounding healthy tissue.[40,41] To this end, the properties of α particle-emitting nuclides, with their high linear energy transfer (LET) and short path length resulting in highly selective cytotoxicity, are ideal.[41,147] A promising radionuclide for molecular targeted α therapy (TAT) is actinium-225, which disintegrates with a half-life of 10.0 days producing six radionuclidic daughters in the decay cascade to virtually stable bismuth-209 ($t_{1/2}$ = 1.9•10^{19} y[280]).[27,281] As shown in **Figure 19**, four of these daughters are short-lived α emitters and ^{225}Ac can hence be designated as an α particle nanogenerator.[281] In addition to the net four α emissions, the decay of ^{225}Ac yields three β^- disintegrations, and two useful γ emissions of which the ^{213}Bi 440 keV γ emission is suitable for imaging and dosimetry studies.[281,282] ^{225}Ac can be obtained either from the natural decay of ^{233}U or from neutron irradiation of ^{226}Ra followed by successive capture decay reactions *via* ^{227}Ac, ^{228}Th to ^{229}Th.[281]

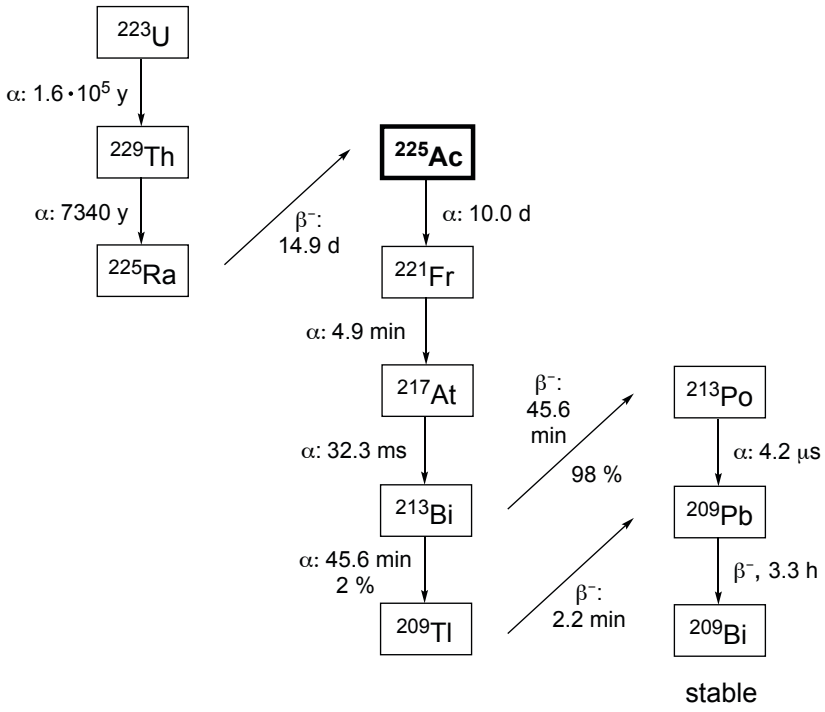

Figure 19. Decay scheme of uranium-233.[27,283]

There are no stable isotopes of actinium and the knowledge about the coordination chemistry of this element is hence limited. The properties of actinium(III) were usually inferred from the lanthanides, in particular from lanthanum(III). Due to the similar size of

La^{III} and Ac^{III}, La^{III} has been used as surrogate for Ac^{III} in the development of synthetic or analytical procedures.[284] However, it has been shown that there are significant electronical differences between lanthanides and actinides.[285-287] As a consequence of the limited understanding of actinium chemistry, the development of suitable Ac^{III} chelators is challenging. The ionic radius of actinium(III) was reported as 112 pm in six-fold coordination and the large size of the cation is likely suited to ligands with high denticity.[119-121,148,284,288] An important prerequisite for any ^{225}Ac^{III} chelator is the ability to stably bind the radionuclide as well as its daughters.[281] A selection of chelates studied for ^{225}Ac^{III} coordination is depicted in **Figure 20**.

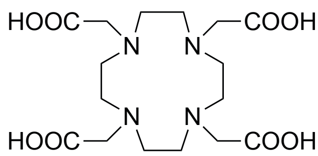

L5, DOTA

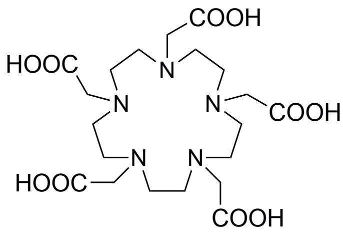

L7, PEPA

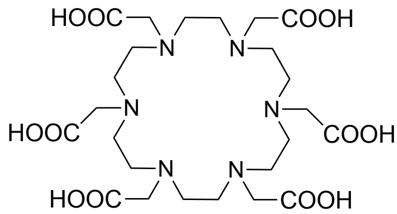

L8, HEHA

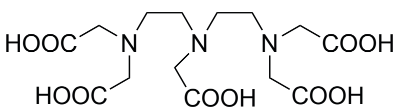

L10, DTPA

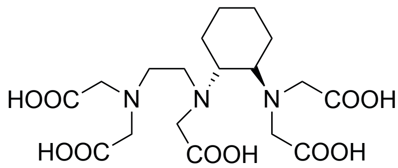

L34, CHX-*A''*-DTPA

Figure 20. Selected actinium(III) chelators.

Due to the large ionic radius of actinium(III) the 15- and 18-membered macrocycles PEPA (**L7**, N_5O_5-type ligand)[117] and HEHA (**L8**, N_6O_6),[118] were evaluated for the application with ^{225}Ac^{III}.[119-121,281] In biodistribution studies in healthy mice ^{225}Ac^{III}-radiolabeled PEPA showed an inadequate stability resulting in the substantial accumulation of activity in the liver, while ^{225}Ac^{III}-HEHA proved to be exceptionally stable.[119] Inspired by these results, the antibody conjugate HEHA-mAb201B was prepared and labeled with ^{225}Ac^{III} for targeted radioimmunotherapy (RIT) of lung tumors in mice. Although the radioconjugate effectively delivered large doses of ^{225}Ac^{III} to the tumors, the treatment also led to death of the laboratory animals within days.[289] More recently, the smaller macrocycle DOTA (**L5**, N_4O_4) has been shown to be the most suitable ^{225}Ac^{III} chelator so far based on different *in vitro* and *in vivo* studies.[281,288,290,291] DOTA was conjugated to the monoclonal antibody

HuM195 that targets the CD30 antigens on acute myeloid leukemia cells and the resulting radioconjugate $^{225}Ac^{III}$-DOTA-HuM195 has shown promise in clinical trials.[281,291] Due to the long half-life of actinium-225 of 10 days, the radionuclide is best suited for the application with antibodies as vectors. However, the conditions required for the labeling of the described macrocycles with $^{225}Ac^{III}$ are incompatible with antibody stability and retention of function. Therefore, a two-step procedure was developed for the preparation of a radiolabeled DOTA-antibody conjugate involving complexation of $^{225}Ac^{III}$ by a bifunctional DOTA derivative (50-60 °C, 30-60 min) followed by coupling of $^{225}Ac^{III}$-DOTA-NCS to the respective antibody.[288] Although the radioconjugate is accessible by this route, the presented method is not convenient for standard clinical use. For this reason, acyclic ligand systems, known for their fast radiolabeling kinetics with many metal ions at ambient temperature,[48] were also investigated with $^{225}Ac^{III}$.[119,121,288] However, the linear polyaminocarboxylic acids DTPA (**L10**, N_3O_5) and CHX-*A''*-DTPA (**L34**, N_3O_5) do not appear to be suitable $^{225}Ac^{III}$ chelators as evidenced by inadequate stability in Y^{III} challenge assays and animal studies.[119,121,288]

1.3 Bispidine ligands for nuclear medicine

The general term “bispidine” for the 3,7-diazabicyclo[3.3.1]nonane framework was derived from its chemical structure consisting of two condensed piperidine rings (bis-piperidine).[292] Bispidine derivatives with a keto or alcohol function at C9 are designated as bispidones or bispidols, respectively (see **Figure 21**). However, the term bispidine is often used as the general designation for compounds with the characteristic bicyclic backbone regardless of their substitution pattern. The bispidine scaffold occurs in nature in the form of the cyclic alkaloid sparteine (**4**), for example, which can be isolated from lupines and displays antiarrhythmic and antimicrobial activity.[293,294]

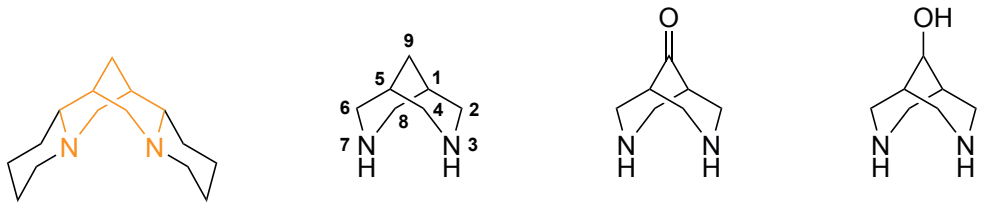

4, sparteine **5**, bispidine **6**, bispidone **7**, bispidol

Figure 21. From left to right: Chemical structures of sparteine, bispidine, bispidone and bispidol.

The standard procedure for the bispidone synthesis goes back to Mannich and Mohs, who described it in 1930 and is still used to date.[159,292] The bispidine system is built up in two consecutive double Mannich reactions starting from a primary amine, two aldehydes and dimethyl-1,3-acetonedicarboxylate as CH-acidic compound.[292,295,296] The resulting piperidone is usually obtained in the form of keto-enol tautomers, as shown in **Figure 22**.[295,297] Subsequently, it is reacted in a second condensation with formaldehyde and another amine to the respective bispidone.[292,295,296] By varying the residues R^1 and R^2 at the amine groups, a large number of differently substituted bispidones with variable denticity and donor atoms is accessible.[298] Due to the keto group at C9, bispidones are prone to ring opening *via retro* Michael reaction. This unfavorable side reaction can be avoided by reduction of the carbonyl function to the corresponding alcohol.[298,299] Furthermore, hydration of the C9 ketone upon coordination of the bispidone to a metal ion is observed frequently.[298] In addition to the C9 reduction to a monool, the ester groups can be either hydrolyzed[173] or reduced resulting in a triol.[300] The reductions, particularly that of the C9 carbonyl function, change the nucleophilicity of the amine donors of the

bispidine scaffold and consequently influence the stability of corresponding metal bispidine complexes.[301-303]

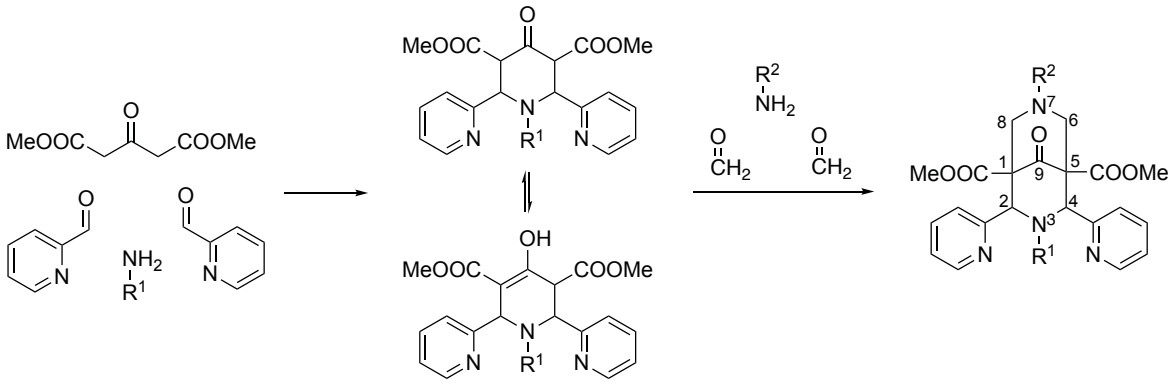

Figure 22. Standard bispidone synthesis *via* two double Mannich reactions.[298]

As diaza-derivatives of adamantane, bispidines possess a very rigid structure, which is highly preorganized for the coordination of metal ions. The first transition metal bispidine complexes were published by Stetter and Haller in 1957 and 1969.[304,305] Since then numerous bispidine compounds with different metal ions, such as vanadium(IV/V),[306] chromium(III),[307] manganese(II),[308,309] iron(II/III),[310,311] cobalt(II/III),[312-314] nickel(II),[315] copper(I/II),[218,316,317] zinc(II),[303] ruthenium(II),[318] and platinum(II)[319-321] have been reported. There are three isomers of the unsubstituted bispidine scaffold differing in the conformation of the two condensed piperidine rings (see **Figure 23**).[298] However, the only conformation suitable for metal ion coordination is the chair-chair form, which, in general, is energetically favored compared to the chair-boat or the boat-boat conformation.[132,298] With sterically demanding residues at N3 and N7, chair-boat isomers can be stabilized[298] and even a boat-boat form has been recently observed.[322] In the case of substituents in C2 and C4 position, there are additionally different possible configurations. Depending on the orientation of the residues one can distinguish between the exo-exo isomer (all axial), the endo-exo isomer (axial and equatorial) and the endo-endo isomer (all equatorial). The achiral endo-endo configuration is needed for the formation of metal complexes, as it allows the two donors at C2 and C4 to coordinate to the central metal ion.[298]

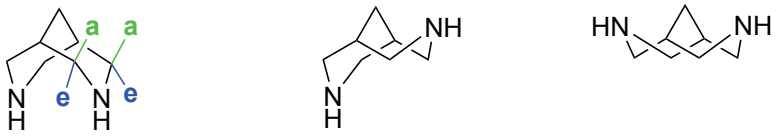

chair-chair chair-boat boat-boat

Figure 23. Conformational isomers of the bispidine scaffold with different axial (**a**) and equatorial (**e**) substituents at C2 and C4 of the chair-chair isomer.

By using different amines in the bispidone synthesis (**Figure 22**), numerous tetra-, penta- and hexadentate ligand systems have been synthesized, which adopt distorted square pyramidal or octahedral geometries upon metal ion coordination.[298] An important feature of the bispidine framework is the structural difference between N3 and N7. In metal bispidine complexes, the M-N7 bond is part of two six-membered chelate rings and hence more flexible than the M-N3 bond as part of two rigid five-membered chelates.[298,323] This usually leads to a longer bond from the metal center to N7 than to N3, but isomers with a short M-N7 and a longer M-N3 bond have also been reported.[307,324] Bispidine ligands are consequently preorganized for metal ions that favor tetragonal coordination geometries, *i.e.* for JAHN-TELLER-active systems such as copper(II).[303,325] For Cu^{II} bispidine complexes a *pseudo* JAHN-TELLER elongation has been observed along all three coordination axes,[326-329] which suggests that the corresponding minima are close to degenerate.[323] Hole size calculations[330] on bispidine ligands indicate that they have a relatively large metal binding site with averaged metal-donor distances of more than 2.1 Å and hence preferably stabilize lower as compared to higher oxidation states.[302]

An immense variety of bispidine derivatives together with their metal coordination chemistry and diverse applications have been described.[298,323,331,332] Transition metal bispidine complexes are used in copper(II)-catalyzed aziridination reactions,[333,334] in nickel-catalyzed C-C bond formation reactions using a nickel(II) precatalyst[335] and in the enantionselective copper(II)-catalyzed Henry reaction.[336] Further applications include oxygen activation by copper(I)[316,325,337-341] and cobalt(II),[312,314] as well as oxidation reactions by high-valent iron[342] and manganese[343] bispidine complexes. An interesting approach in medical chemistry is the investigation of bispidine analogs of cisplatin as potential cytostatic agents in cancer therapy.[319-321] In addition, bispidines provide a suitable platform for the development of new *in vivo* radiotracers.[323,331] For the application as bifunctional chelator (BFC) in nuclear medicine, the bispidine system must be conjugated to a targeting vector moiety. Bispidones are typically functionalized at three

possible positions, *i.e.* at the ester groups,[173] at the C9 keto function,[344] or at the tertiary amines of the ligand backbone.[172,345]

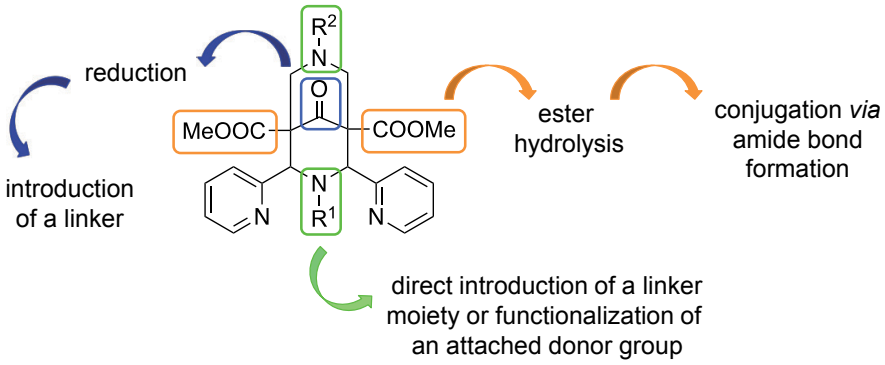

Figure 24. Possible functionalization sites at the bispidone scaffold.

Due to the high complementarity of bispidines and copper(II), these ligands are well-suited for the use as BFCs in $^{64}Cu^{II}$ PET imaging. The first bispidine to be investigated in this regard was the hexadentate ligand N_2py_4 (**B3**).[173,302] Preliminary investigations of **B3** with $^{64}Cu^{II}$ have shown fast radiolabeling under mild conditions and high stability in the presence of competing ligands as well as in rat plasma. After C9 reduction and ester hydrolysis of **B3**, the resulting bispidol **B6** was attached to a stabilized bombesin (BBN) analog, yielding the respective **B6-BBN** conjugate (see **Figure 26**). The radiopharmacological investigation of the $^{64}Cu^{II}$-labeled bispidine-bombesin conjugate was then performed by biodistribution and small animal PET studies.[173]

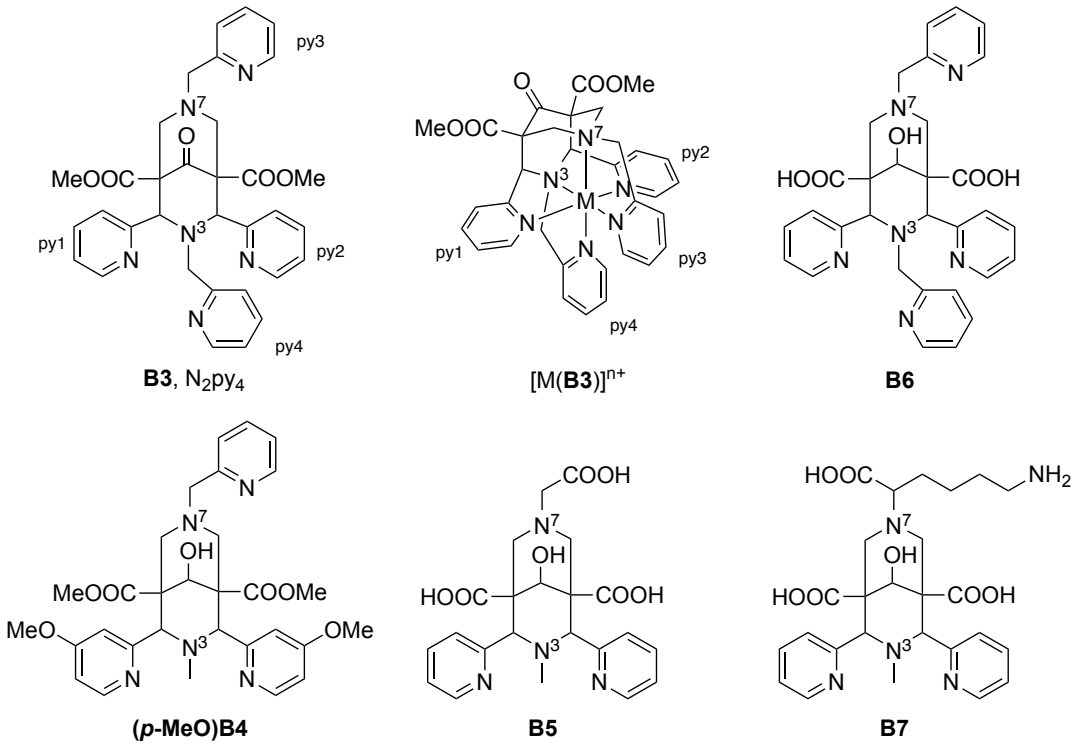

Figure 25. Classical bispidines investigated for nuclear medicine applications.

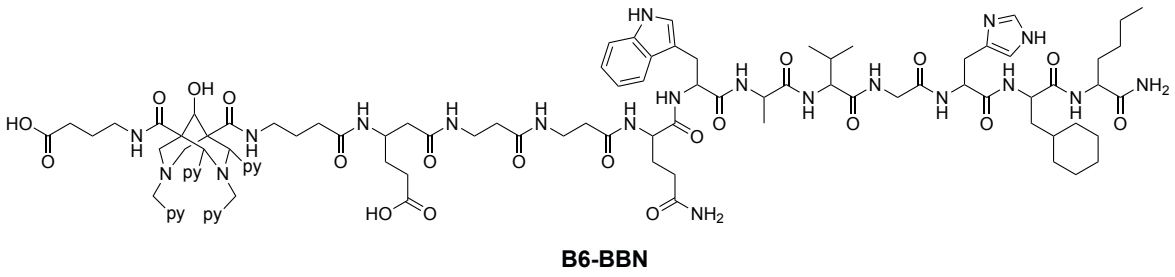

Figure 26. Bispidine-bombesin conjugate for tumor imaging studies.[173]

While studying tetra- and pentadentate bispidines COMBA *et al.* observed a correlation between the basicity of the aromatic donor groups at C2 and C4, and the stability of the corresponding copper(II) complexes.[172,317] In a systematic survey, tetradentate bispidines with different substituents in either the *ortho*-, *meta*-, or *para*-position of the pyridine donors were synthesized and their Cu^{II} complexes investigated by cyclic voltammetry.[317] It was shown that the increase of electron density upon introduction of a methoxy group in *para*-position of the pyridines resulted in a more stable copper(II) bispidine complex. A *para*-substituted nitro group, on the other hand, decreased the basicity of the pyridines and hence the complex stability.[317] These findings led to the synthesis of the *para*-

methoxy substituted pentadentate bispidol ligand **(*p*-MeO)B4**, which showed promising results in initial radiochemical investigations.[172]

Charbonnière *et al.* also work on pentadentate bispidol systems for $^{64/67}Cu^{II}$-based radiopharmaceuticals, but use a methylene carboxylic acid substituent instead of a picolyl group at N7 of the ligand backbone.[218] The high selectivity of **B5** for copper(II) and the kinetic inertness of the complex inspired the development of the recently published bifunctional version **B7**.[218,346] As a proof of principle, coupling of **B7** to biotin and to a model peptide was performed, but further studies are needed to evaluate the *in vivo* stability of these conjugates.[346]

In terms of dual imaging, bispidine systems were attached to fluorescent probes like the BODIPY (boron-dipyrromethene) chromophore,[344] the green rhodamine dye ATTO532, and the red cyanine dye Cy5.5.[345] The bispidine-dye conjugates were investigated with regard to combined PET and optical imaging.[344,345] The nuclear component can thereby be used to localize the diseased tissue followed by fluorescence-guided biopsy or surgery.[347,348]

Apart from the bispidines, discussed so far, there are also macrocyclic systems incorporating bispidine units like the cyclam-based tetraazamacrocycle **L37**.[349] Cyclic dioxotetraaza frameworks with a bispidine core and two amides have been investigated for medical applications. Three derivatives thereof have been reported with the benzene-appended macrocycle BBDT (**L25**) being the most promising copper(II) chelator for $^{64}Cu^{II}$ PET imaging.[177] Due to deprotonation of the amides upon metal ion coordination, Cu^{II}-**L25** is a neutral complex and redox chemistry indicates that +II as well as +III copper oxidation states are accessible. As expected for macrocyclic systems, radiolabeling is relatively slow, requiring heating to 50 °C for 30 minutes. Both challenge experiments and biodistribution studies performed on the copper(II)-64 **L25** complex confirm its high stability.[177] To further evaluate the potential of **L25**, the ligand was then modified by introduction of a carboxylic acid linker at the aromatic bridge yielding **L38**.[169] For a proof of concept study, this linker was coupled to the somatostatin analog TATE and the conjugate $^{64}Cu^{II}$-**L38**-TATE was investigated in preliminary animal studies with tumor-bearing mice.[350] In the next step this conjugate was combined with a fluorescent dye[351] and the corresponding investigations are currently in progress.

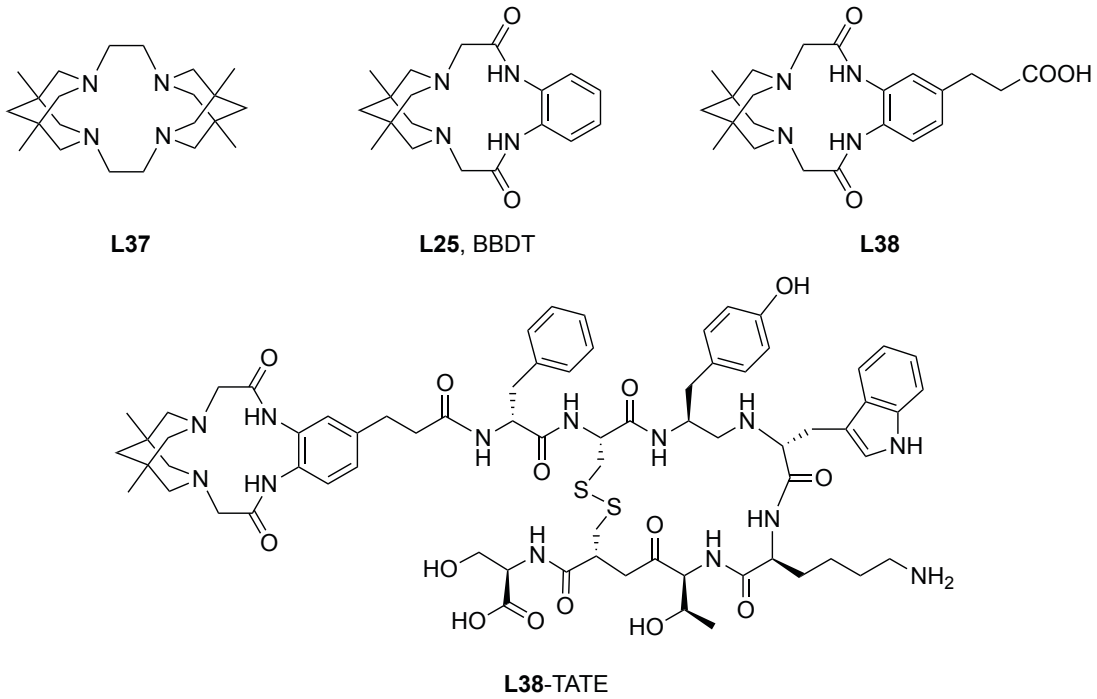

Figure 27. Macrocyclic bispidine chelators and the ligand-peptide conjugate **L38**-TATE.

2 Aim

It has previously been demonstrated that the highly preorganized and rigid bispidine ligands represent excellent copper(II) chelators for $^{64}Cu^{II}$ PET imaging.[172,173,218,346] In this study, picolinic acid groups, known to be excellent metal-binding moieties,[124,125,157,241,352-358] were incorporated into the bispidine backbone to further improve these ligands. The combination of the very versatile bispidine scaffold and picolinic acids (pa) leads to a new class of chelators, the so-called “bispa” ligands. Depending on the substitution pattern, different bispa derivatives are accessible as shown in **Figure 28**. The synthesis of the hexadentate bispa ligand Hbispa[1a] (**B1a**) was developed within the frame of a master thesis and first investigations with respect to metal complex stability were promising.[359] Building on these findings, the objective of the present thesis was to synthesize further bispa ligands with different structural features and denticities. The synthetic routes to these picolinic acid-based ligands and their characterization are described in Chapter 3.

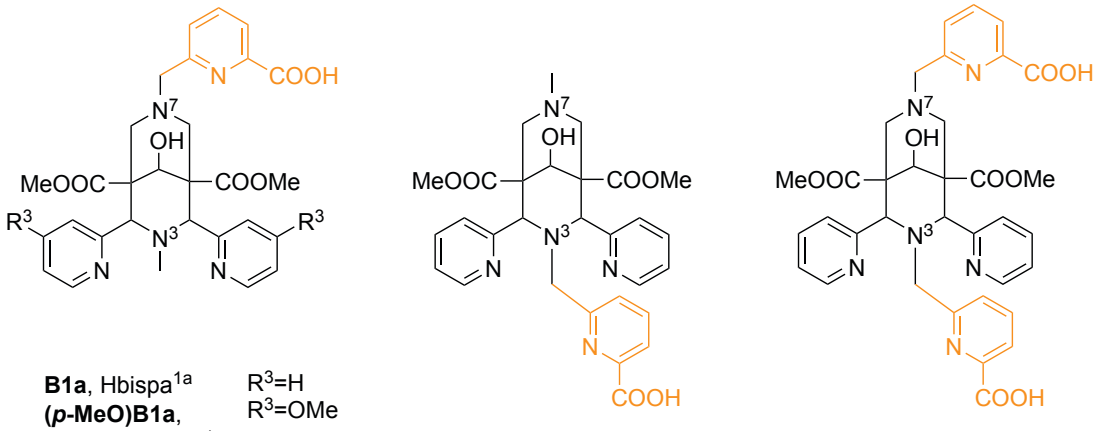

B1a, Hbispa[1a] R^3=H
(*p*-MeO)B1a, (*p*-MeO)Hbispa[1a] R^3=OMe

B1b, Hbispa[1b]

B2, H_2bispa[2]

Figure 28. Bispa ligands consisting of a bispidine scaffold (black) and picolinic acid moieties (orange).

In a second step, the coordination chemistry of the newly synthesized bispa ligands was investigated regarding potential nuclear medicine applications. At the beginning of the bispa project, the bispidine ligands studied for $^{64}Cu^{II}$ PET imaging mainly contained nitrogen donors.[172,173] The attachment of a picolinic acid moiety to the bispidine backbone involves the introduction of a carboxylate function, which might facilitate the coordination of hard metal ions such as gallium(III). One central aim of the present thesis was therefore to extend the scope of the bispidine ligands to other promising radiometal ions relevant for nuclear medicine. Similar to previously reported bispidine systems, the hexadentate bispa

ligands were expected to be well-suited for $^{64}Cu^{II}$, but were also investigated with $^{68}Ga^{III}$ as presented in Chapter 4. The octadentate chelator H_2bispa^2 (**B2**), on the other hand, was expected to be interesting for use with larger metal ions such as $^{111}In^{III}$, $^{177}Lu^{III}$, or $^{225}Ac^{III}$ (see Chapter 5). Furthermore, amine-substituted picolinates are rigid tridentate ligands and reduce the overall charge of metal complexes. As charge and hydrophilicity of a compound have an impact on the biodistribution, it is convenient for *in vivo* applications to have compounds with various charges at hand. For example, bispidines that only possess neutral nitrogen donors form copper(II) complexes with an overall charge of +2, whereas the charge of the new copper(II) bispa complexes is +1.

The final goal of the described project is to use bispa ligands as chelating unit in radiometal-based pharmaceuticals. To this end, the potential of the unfunctionalized bispa ligands was tested in various radiochemical studies, including radiolabeling experiments and competition assays, as well as lipophilicity and biodistribution studies. These investigations were performed in order to obtain information about radiolabeling kinetics, complex stability and *in vivo* behavior of the compounds.

3 Synthesis of picolinic acid-based bispidine ligands[iv]

The synthetic route to the new picolinic acid-based bispidine ligands proceeds *via* the build-up of the respective bispidine scaffold, which is then coupled to a suitable picolinic acid derivative. For the coupling to the bispidine fragment, the picolinic acid must be modified by protection of the carboxylic acid and by introduction of a substitutable unit, *e.g.* a halide. Due to the standard preparation of bispidones *via* Mannich reactions, the bispidine backbone contains two methyl ester groups.[292] To avoid their hydrolysis, a *tert*-butyl protecting group is used for the picolinic acid, as this group can be removed selectively in the presence of methyl esters. The *tert*-butyl ester protected picolinic acid derivative **11** was synthesized in two steps according to a slightly modified literature-known procedure, as shown in **Figure 29**.[360] The commercially available starting material 6-methylpicolinic acid **8** was first esterified to **10** using *tert*-butyl-2,2,2-trichloroacetimidate **9** and then transformed to the alkyl bromide derivative **11** with *N*-bromosuccinimide (NBS) and the radical initiator azobis(isobutyronitrile) (AIBN). This protected fragment was then coupled to a secondary amine of the bispidine scaffold, as described in the following chapters.

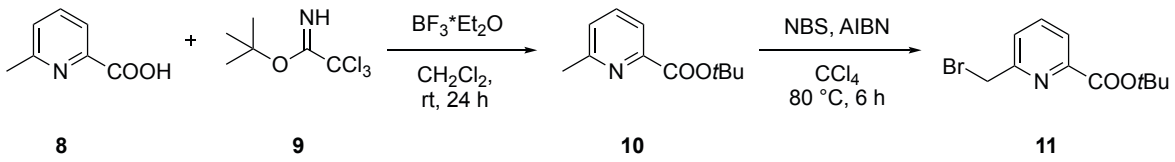

Figure 29. Synthesis of the protected picolinic acid fragment *tert*-butyl 6-(bromomethyl)picolinate **11** starting from 6-methylpicolinic acid **8**.

[iv] Reproduced in part with permission from P. Comba, L. Grimm, C. Orvig, K. Rück, H. Wadepohl, *Inorg. Chem.* **2016**, *55*, 12531-12543, Copyright 2016 American Chemical Society.; Parts of this chapter will be published in P. Comba, U. Jermilova, C. Orvig, B. O. Patrick, C. F. Ramogida, K. Rück, C. Schneider, M. Starke, *Chem. Eur. J.*, *submitted manuscript.*

3.1 Synthesis and characterization of hexadentate bispa ligands

Hexadentate bispa ligands are accessible by introduction of picolinic acid at either N7 or N3 of the bispidine backbone. Further derivatives can be synthesized by functionalization of the pyridines attached to the C2 and C4 positions. The synthesis and characterization of the hexadentate bispa ligands, shown in **Figure 30**, are presented in the following.

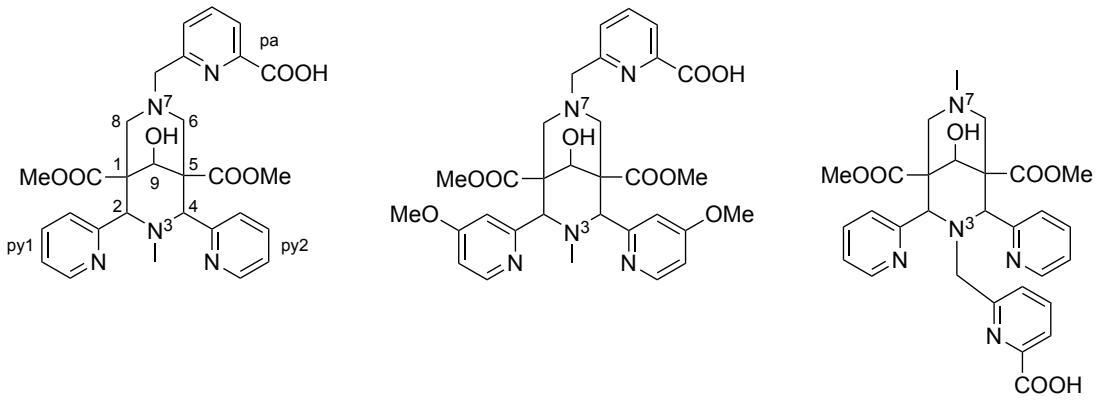

B1a, Hbispa[1a] **(*p*-MeO)B1a**, (*p*-MeO)Hbispa[1a] **B1b**, Hbispa[1b]

Figure 30. Hexadentate bispa ligands.

3.1.1 Synthesis of Hbispa[1a]

In Hbispa[1a] (**B1a**) the picolinic acid moiety is connected to N7 of the bispidine scaffold and the numbering scheme for this ligand is shown in **Figure 30**. The synthesis of **B1a** was developed within the frame of a master thesis[359] and is therefore only briefly reviewed here. Standard piperidone **P1**[361] and bispidone **B8**[296] were synthesized by slightly modified literature procedures.[317] The piperidone **P1** is obtained as a mixture of its keto and its enol form, but only the main keto tautomer is depicted in the reaction scheme. Previous attempts in the COMBA group to introduce a secondary amine directly at N7 of the bispidine backbone, by using ammonia in the second Mannich reaction, failed. For this reason, a benzyl protected amine was inserted in step (i) of the synthetic route.[362] To prevent ligand decomposition by a *retro* Michael reaction, the bispidone **B8** was reduced with sodium borohydride to the alcohol **B9**.[298,363] The benzyl protecting group was then removed by hydrogenation with palladium on activated charcoal.[309,362] In the next step, bispidol **B10** was coupled to the picolinic acid derivative **11** *via* nucleophilic substitution yielding the ester-protected ligand precursor (*t*Bu)bispa[1a], **(*t*Bu)B1a**. By hydrolysis of this

intermediate with trifluoroacetic acid H(TFA), **B1a** was obtained as trifluoroacetate (TFA) salt.[359]

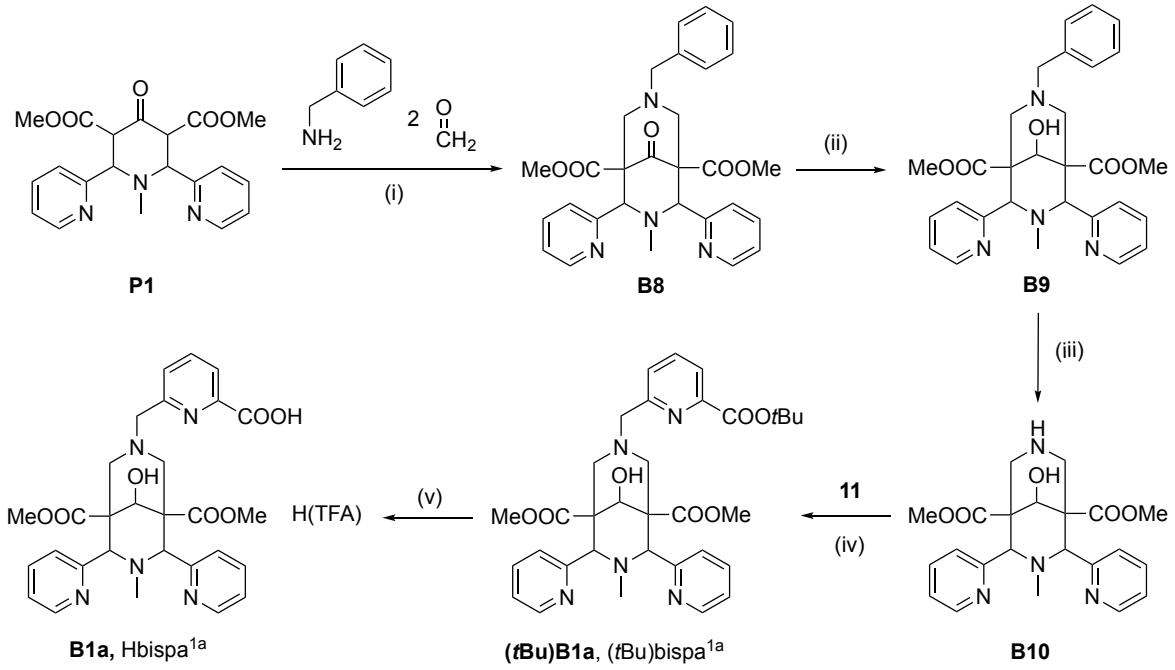

Figure 31. Synthesis of Hbispa[1a] (**B1a**). (i) THF, reflux, 30 min; (ii) $NaBH_4$, 1,4-dioxane / water (3:1), –5 °C, 30 min, 0 °C, overnight; (iii) 1 bar H_2, Pd/C, EtOAc, 90 °C, overnight; (iv) Na_2CO_3, MeCN, reflux, 24 h; (vii) H(TFA), CH_2Cl_2, rt, 24 h.

After repeated bispa syntheses crystals of **B1a**•H(TFA) suitable for solid state X-ray analysis were obtained from one batch. The general notation **ligand**•H(TFA) indicates that one molecule trifluoroacetic acid is present per ligand. In the case of the bispa ligands, the bispidol framework is usually protonated and hence positively charged, and TFA acts as a counterion. The ligand crystallizes in a chair-chair conformation, where the pyridine donors adopt the favored equatorial position with respect to the six-membered N3 aza-cyclohexane (see **Figure 32**). Bispidines in general are highly preorganized for complexation to metal ions.[298,313] As the bispa ligand was isolated as TFA salt, one of the amine functions, namely N7, is protonated. It is probably for this reason and due to the carboxylate group, which allows for hydrogen bonding, that in the solid state structure of **B1a**•H(TFA) the pyridine donors and the picolinate point towards the putative metal binding site. The distance between the nitrogen donors N3 and N7 of the bispidine backbone is a measure for the size of the metal coordination site and is roughly 2.9 Å for most bispidines.[298] For **B1a** the N3-N7 distance is 2.684(2) Å in the solid state structure.

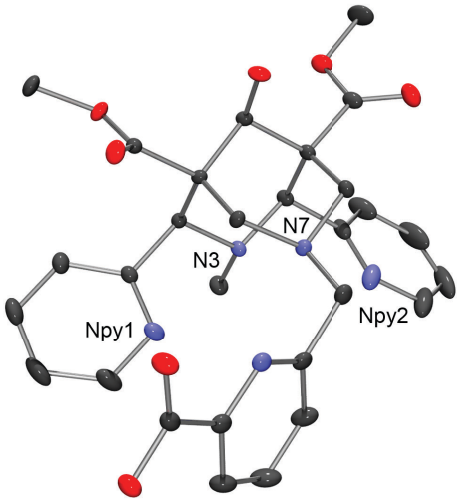

Figure 32. ORTEP plot of **B1a**•H(TFA). Ellipsoids are shown at the 50 % probability level; co-crystallized solvent molecules, counterions, and hydrogen atoms are omitted for clarity.[256]

The hydrogenation of **B9** to **B10** in step (iii) was only feasible in small scales and upscaling to more than 3 grams led to incomplete conversion. For this reason, the reduction of the C9 keto function and the removal of the benzyl protecting group, steps (ii) and (iii) in **Figure 31**, were carried out in reverse order. This allowed for the conversion of higher amounts of **B8** (up to 10 grams) with consistent yields in both steps in comparison to the previous reported procedure.[359] Compounds **B11**[309] and **B10**[359] are literature-known.

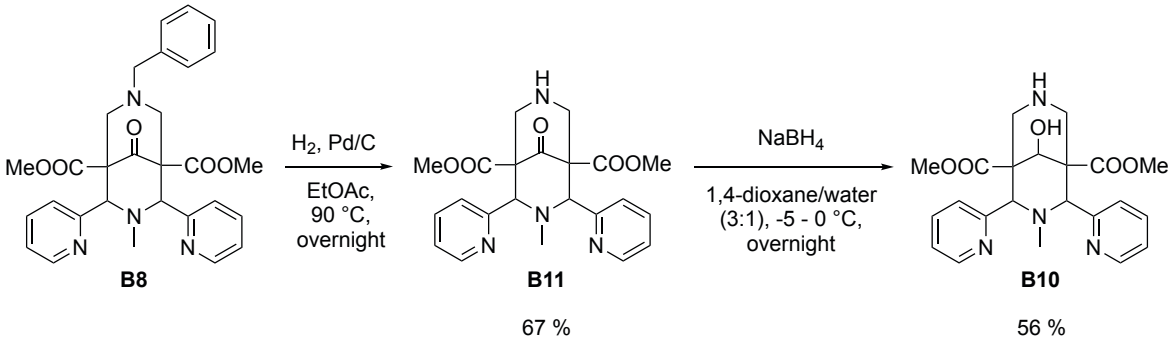

Figure 33. Optimized sequence in the synthesis of Hbispa[1a] (**B1a**).

3.1.2 Synthesis of (*p*-MeO)Hbispa[1a]

COMBA *et al.* found that the stability of bispidine metal complexes is increased by introducing a methoxy group in the *para*-position of the pyridines at C2 and C4 of the bispidine backbone.[317] Inspired by these findings, a *para*-methoxy substituted derivative of Hbispa[1a] (**B1a**) was synthesized. To this end, 4-methoxypicolinaldehyde **16** was prepared in a four-step sequence, shown in **Figure 34**.[317] First, picoline-*N*-oxide **12** was nitrated in position 4 with sulfuric acid and fuming nitric acid yielding 4-nitropicoline-*N*-oxide **13**.[364,365] In a Boekelheide rearrangement, using trifluoroacetic anhydride, **13** was subsequently converted to the corresponding alcohol **14**,[366-370] which was then reacted with sodium methoxide to afford **15** *via* nucleophilic *ipso*-substitution.[371] In the last step, **15** was oxidized by selenium dioxide to the 4-substituted picolinaldehyde **16**.[317]

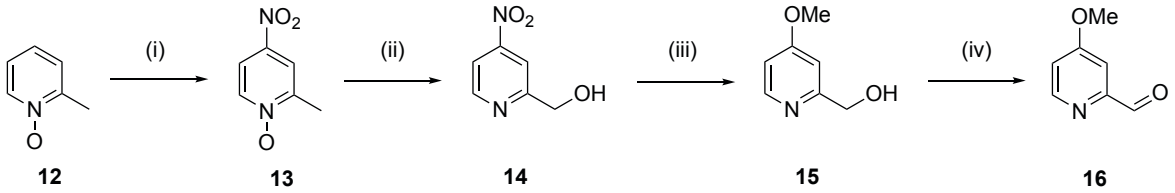

Figure 34. Synthesis of 4-methoxypicolinaldehyde **16**. (i) H_2SO_4 / HNO_3, 120 °C, 3 h; (ii) $(CF_3COO)_2O$, CH_2Cl_2, rt, 3 d; (iii) NaOMe, MeOH, 80 °C, 24 h, (iv) SeO_2, 1,4-dioxane, 85 °C, 3 h.[317]

The other starting materials for the synthesis of the *para*-methoxy substituted piperidone **P2**, *i.e.* dimethyl-1,3-acetonedicarboxylate and methylamine, are commercially available. Piperidone **P2** is literature-known and was mainly obtained as the enol-tautomer.[317]

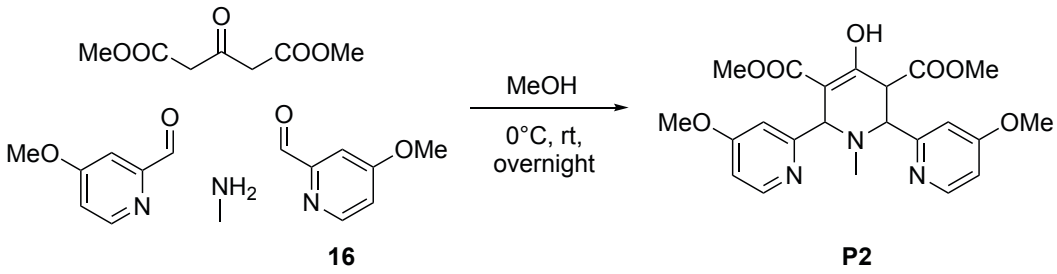

Figure 35. Synthesis of the *para*-methoxy substituted piperidone **P2**.[317]

In analogy with the synthesis of **B1a**, described in the previous chapter, the substituted derivative (*p*-MeO)Hbispa[1a] (**(*p*-MeO)B1a**) was prepared according to the synthetic

scheme depicted in **Figure 36**. All intermediates as well as the TFA salt of the final ligand **(*p*-MeO)B1a**•H(TFA) were characterized by standard analytical methods, *i.e.* ^{1}H- and ^{13}C-NMR spectroscopy, high resolution mass spectrometry (HR-MS) and elemental analysis (EA). For the compounds **B12**, **B13**, **B14**, and **(*p*-MeO)(*t*Bu)B1a**, a solid state structure could be determined by X-ray analysis. Bispidone **B12** crystallized in the chair-chair conformation, required for metal ion complexation, with the two pyridine donors in equatorial position (endo-endo). The following transformations did not influence this orientation and the preorganization of the bispidine scaffold was thus preserved. Also in the case of **(*p*-MeO)B1a**, performing steps (ii) and (iii) in reverse order would probably improve the synthesis, but this has not yet been tested.

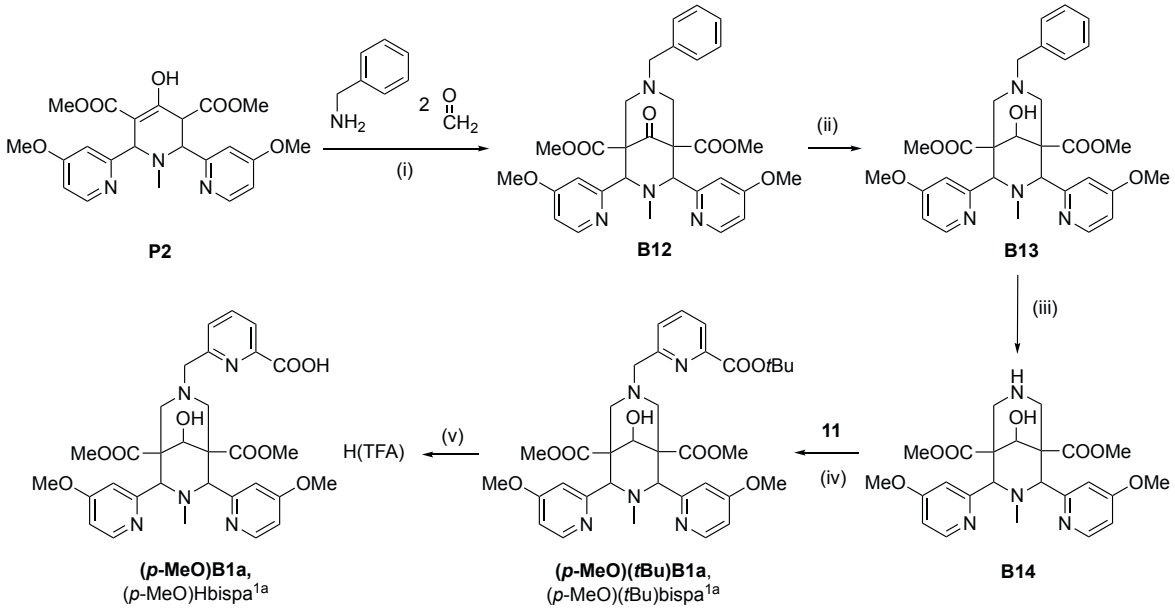

Figure 36. Synthesis of (*p*-MeO)Hbispa[1a] (**(*p*-MeO)B1a**). (i) THF, reflux, 30 min; (ii) $NaBH_4$, 1,4-dioxane / water (3:1), –5 °C, 30 min, 0 °C, overnight; (iii) 8 bar H_2, Pd/C, EtOAc, 95 °C, overnight; (iv) Na_2CO_3, MeCN, reflux, 24 h; (vii) H(TFA), CH_2Cl_2, rt, overnight.

3.1.3 Synthesis of Hbispa[1b]

Different structural isomers of bispidines are accessible by simply exchanging the substituents at N3 and N7 of the ligand backbone with each other. An example are pentadentate bispidones possessing a picolyl pendent arm at either N3 or N7.[326] Metal complexes of these isomers display surprisingly different properties with respect to stability and reactivity.[303,372] Due to these findings, the hexadentate bispa ligand Hbispa[1b] (**B1b**) was prepared for comparison with Hbispa[1a] (**B1a**). In **B1a**, the picolinic acid group

is attached to N7 of the bispidine scaffold, whereas in **B1b**, the additional group is introduced at N3.

In the case of **B1b**, the secondary amine for coupling to the picolinic acid fragment is required at position N3 and could be directly introduced by using ammonia in the synthesis of piperidone **P3**.[296] In the second Mannich reaction bispidone **B15**[373] is build up and then subsequently reduced with sodium borohydride to afford bispidol **B16**.[300] The protected picolinic acid fragment *tert*-butyl 6-(bromomethyl)picolinate **11** is then coupled *via* nucleophilic substitution to **B16** yielding (*t*Bu)bispa[1b], **(*t*Bu)B1b**. This step is followed by hydrolysis of the ligand precursor to the TFA salt of **B1b** using trifluoroacetic acid.

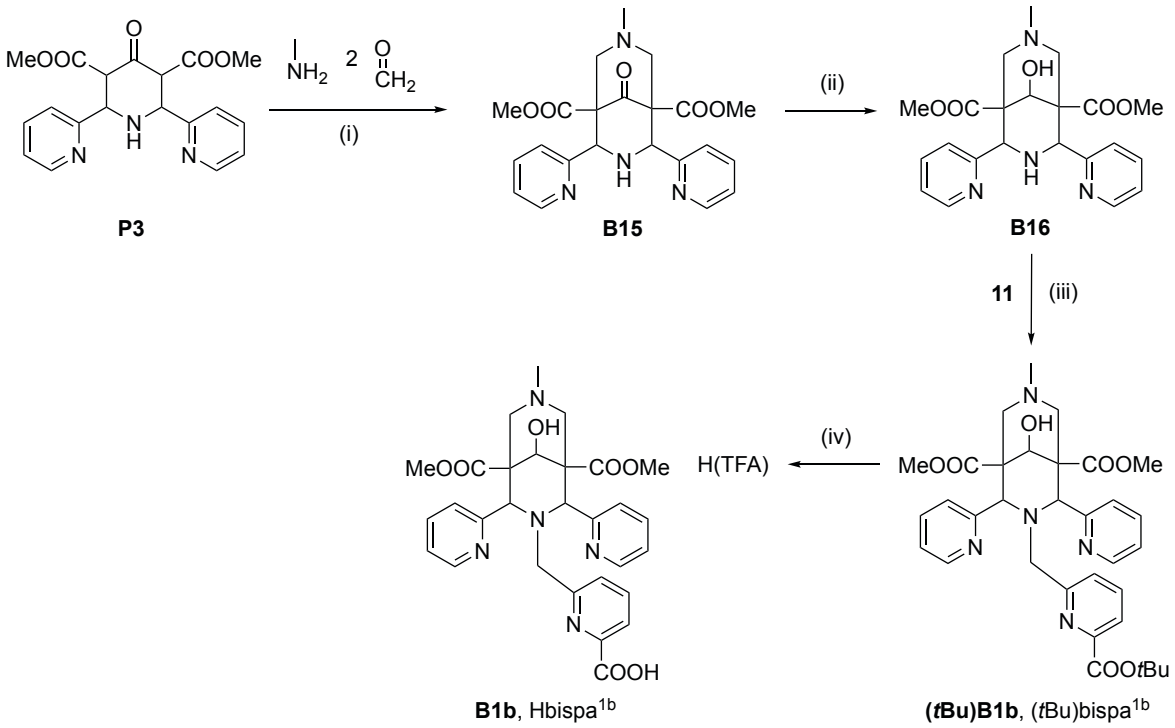

Figure 37. Synthesis of Hbispa[1b] (**B1b**). (i) THF, reflux, 3 h; (ii) $NaBH_4$, 1,4-dioxane / water (3:1), –5 °C, 30 min, 0 °C, overnight; (iii) Na_2CO_3, MeCN, reflux, 24 h; (iv) H(TFA), CH_2Cl_2, rt, 24 h.

The newly synthesized compounds **(*t*Bu)B1b** and **B1b**•H(TFA) were investigated by ^{1}H- and ^{13}C-NMR spectroscopy, high resolution mass spectrometry (HR-MS), and elemental analysis (EA). **B1b**•H(TFA) was further characterized by solid state X-ray analysis and the obtained structure is depicted in **Figure 38**. Similar to **B1a**, the isomer **B1b** adopts the required chair-chair conformation with the pyridine donors in the equatorial position, only the picolinic acid moiety is not yet pointing towards the metal coordination site. According to the solid state structure the protonation of **B1b** also occurs at N7 of the bispidine

backbone. The distance between the nitrogen donors N3 and N7 is 2.664(2) Å in **B1b** and hence similar to the N3-N7 distance determined for **B1a** (2.684(2) Å).

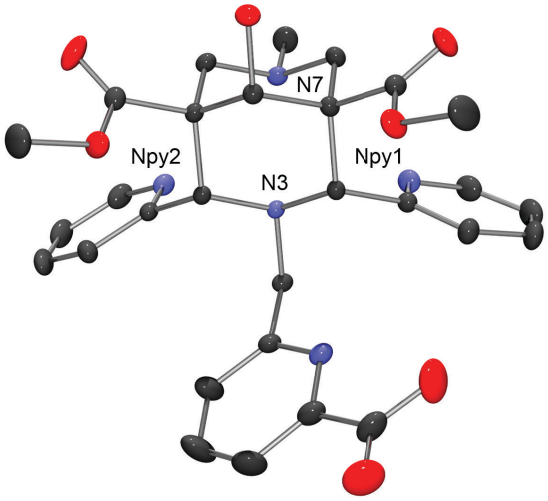

Figure 38. ORTEP plot of **B1b**•H(TFA). Ellipsoids are shown at the 50 % probability level; co-crystallized solvent molecules, counterions, and hydrogen atoms are omitted for clarity.[256]

3.2 Synthesis and characterization of an octadentate bispa ligand

In addition to the hexadentate bispa ligands discussed so far, an octadentate derivative can be synthesized by attaching picolinic acid groups at both, N3 (pa3) and N7 (pa7) of the bispidine scaffold. The structure of the octadentate bispa ligand H_2bispa^2 (**B2**) is shown in **Figure 39** together with the corresponding numbering scheme.

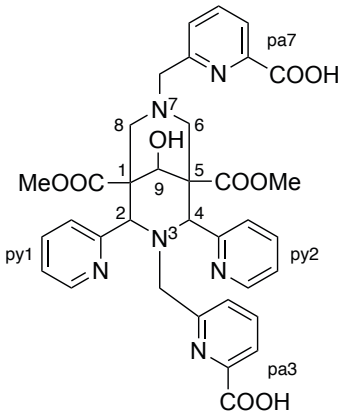

Figure 39. Structure of the octadentate bispa ligand H_2bispa^2 (**B2**).

In the first step of the synthesis of the octadentate ligand **B2**, two consecutive double Mannich reactions lead to the formation of the bispidine scaffold **B17** (**Figure 40**). As a secondary amine at N7 of the bispidine backbone cannot be introduced directly, a protecting group is needed. Benzyl amine, which was used in the syntheses of **B1a** and **(*p*-MeO)B1a**, proved to be unsuitable for the preparation of **B2**, as the subsequent removal of the benzyl moiety with hydrogen (1 bar) in the presence of palladium on charcoal support only led to partial conversion. Additionally, the desired product could not be isolated from the reaction mixture. An increase of the hydrogen pressure to 7 bar did not lead to full conversion, but resulted in an inseparable mixture of various side products. Instead of the benzyl protecting group, 2,4-dimethoxybenzyl (DMB) was then chosen for the synthesis of **B2**. The DMB moiety had already been used successfully for the preparation of bispidones by Kolanowski *et al.* [311]

Using commercially available starting materials, the literature-known piperidone **P3**[296] was synthesized and subsequently reacted with formaldehyde and 2,4-dimethoxy-benzylamine to afford the protected bispidone **B17**.[374] In order to prevent ring opening by a *retro* Michael reaction, the C9 keto group of **B17** was reduced with sodium borohydride, yielding bispidol **B18**. Straightforward deprotection with trifluoroacetic acid led to intermediate **B19**, which was isolated as a trifluoroacetate (TFA) salt. Fragment **B19**

possesses two secondary amines suitable for coupling *via* nucleophilic substitution to *tert*-butyl 6-(bromomethyl)picolinate **11**. The *tert*-butyl ester groups of the resulting precursor (*t*Bu)$_2$bispa^2, **(*t*Bu)$_2$B2**, were consequently removed by treatment with trifluoroacetic acid to obtain **B2**•H(TFA).

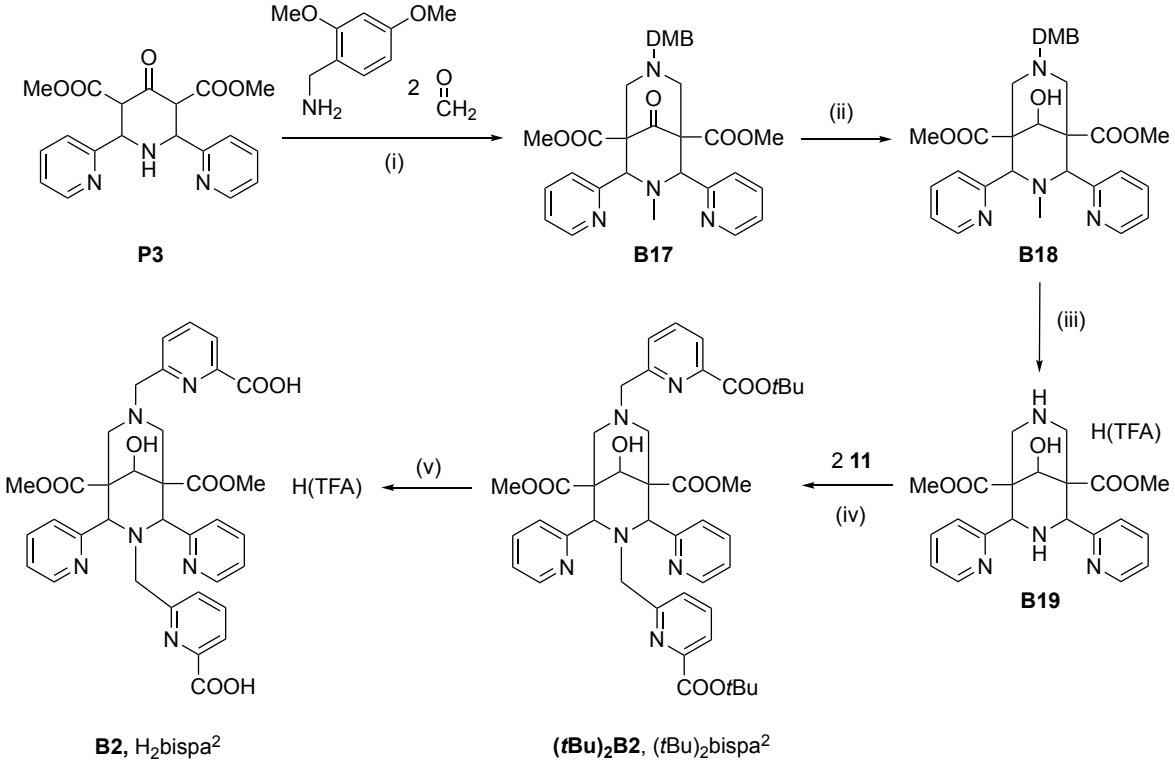

Figure 40. Synthesis of H_2bispa^2 (**B2**). (i) THF, reflux, overnight (DMB = dimethoxybenzyl); (ii) $NaBH_4$, 1,4-dioxane / water (3:1), –5 °C, 30 min, 0 °C, overnight; (iii) H(TFA), CH_2Cl_2, reflux, 2 d; (iv) Na_2CO_3, MeCN, reflux, overnight; (v) H(TFA), CH_2Cl_2, rt, overnight.

Compounds **B19**•H(TFA), **(*t*Bu)$_2$B2**, and **B2**•H(TFA) were characterized by ^{1}H- and ^{13}C-NMR spectroscopy, high resolution mass spectrometry (HR-MS), elemental analysis (EA), and solid state X-ray analysis. The solid state structure of intermediate **B19**•H(TFA) shows protonation at N7 of the bispidine scaffold, as observed for **B1a** and **B1b**. In addition to the synthesis of **B2**, the bispidol fragment **B19**•H(TFA) might present a versatile building block for other bispidine systems. Due to the two secondary amines in the ligand backbone, simultaneous attachment of similar residues at N3 and N7 can be performed easily by nucleophilic substitution. This is especially interesting in cases in which the direct introduction *via* Mannich reaction is difficult.

Crystallization of the *tert*-butyl ester protected ligand precursor **(*t*Bu)$_2$B2** from ethyl acetate delivered crystals suitable for X-ray analysis. The solid state structure shows the

sodium complex of **(*t*Bu)$_2$B2** with a bromide as counterion. The protected picolinic acid moiety at N3 (pa3) is disorderd at the ester group, which is not depicted in **Figure 41** for improved clarity. Without considering the disordered oxygen atoms, the bond lengths between the central sodium cation and ligand donor atoms are in a range of 2.394(5) Å (Na-Npa3) to 2.793(5) Å (Na-Opa7). The Na-Npy1 distance, in contrast, is with 3.2154(35) Å significantly elongated. The solid state structure is in agreement with the EA, which confirms the presence of one molecule sodium bromide per **(*t*Bu)$_2$B2**.

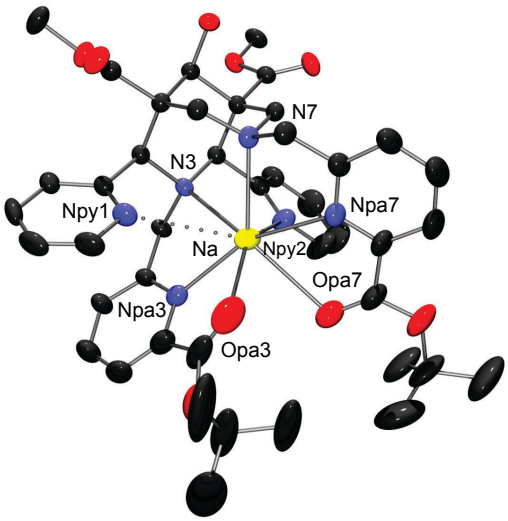

Figure 41. ORTEP plot of the complex cation of [Na^{I}((*t*Bu)$_2$B2)]Br. Ellipsoids are shown at the 50 % probability level; disorders, co-crystallized solvent molecules, counterions, and hydrogen atoms are omitted for clarity.[256]

Crystals of **B2**•H(TFA) suitable for solid state X-ray analysis were obtained by slow evaporation from a methanolic solution. The ligand crystallizes as a zwitterion with seven water molecules in the asymmetric unit, forming an extensive hydrogen-bonded network. The solid state structure further reveals that the tertiary nitrogen atoms N7 and Npa3 are protonated, and that the two azacyclohexane rings of the bispidine scaffold are oriented in chair-chair conformations with an N3-N7 distance of 2.766(3) Å. In contrast, the elemental analysis indicates the presence of one molecule of trifluoroacetic acid and thus three acidic protons. The stoichiometry was verified by potentiometric titration of the ligand, which determined an average of 2.93 equivalents of acidic protons per ligand (see Experimental Section for details). The non-stoichiometric number of protons is explained by the presence of a small amount of ligand in zwitterionic form.

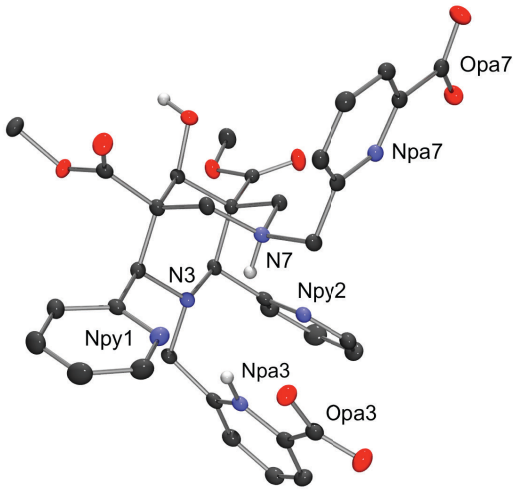

Figure 42. ORTEP plot of **B2**. Ellipsoids are shown at the 50 % probability level; co-crystallized solvent molecules and all hydrogen atoms on carbon atoms are omitted for clarity.[256]

3.3 Acid-base properties of the bispa ligands

With regard to potential nuclear medicine applications, the stabilities of metal-ligand complexes were investigated. To this end, potentiometric acid-base titrations are performed to measure complex formation constants. Therefore, the pKa values of the respective ligands must be determined initially. In order to measure the protonation constants of the hexadentate bispa ligands Hbispa[1a] (**B1a**) and Hbispa[1b] (**B1b**), potentiometric titrations in aqueous solution at 25 °C and at an ionic strength of 0.1 M (KNO_3) were performed. Hexadentate bispa ligands have six basic centers consisting of five nitrogen donors (two tertiary amines and three pyridines) and one carboxylate group. Therefore, the compounds possess six pKa values but, as the fully protonated ligands are expected to be very strong acids, not all of these constants are accessible by potentiometric titration. The pKa values are 7.73, 3.94 and ~1.83 for **B1a**, and 9.05 and 6.10 for **B1b**. The first protonation of the ligand occurs at a pKa value of about 8 for **B1a** and 9 for **B1b** and is associated with proton addition to one of the tertiary amines of the bispidine scaffold. This is confirmed by the solid state structures of the protonated bispa ligands. The species distribution for **B1a** and **B1b** as a function of the pH is depicted in **Figure 43**. L denotes the respective ligand with completely deprotonated basic centers and the charges of the species are generally omitted for clarity. The diagrams clearly demonstrate the different protonation properties of the isomeric bispa ligands **B1a** and **B1b**: At physiological pH of 7.4 **B1b** almost exclusively exists in its single protonated form, whereas at the same pH the species distribution of **B1a** already displays a significant amount of completely deprotonated ligand. As the deprotonated form is required for metal ion coordination, this might have an impact on the complexation behavior of the two bispa ligands.

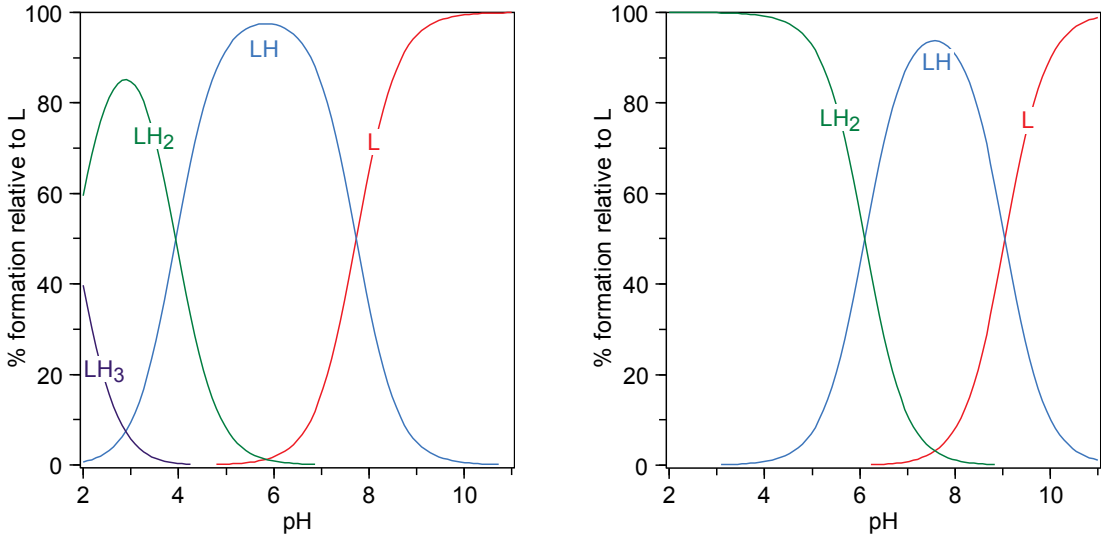

Figure 43. Species distribution diagrams of **B1a** (left) and **B1b** (right) in aqueous solution for c(L) = 10^{-3} M.

The protonation constants of H_2bispa^2 (**B2**) were also determined by potentiometric titration of aqueous ligand solutions (25 °C, 0.1 M KCl). The pKa values for **B2** are 7.45, 5.62, and 3.31. The highest pKa value of 7.45 is assigned to the protonation of a tertiary amine of the bispidine backbone. A comparison of different bispidine systems shows that the first protonation generally occurs in the pKa range of 6.68(8) to 9.13(7),[302,303] where the value for **B2** is at the lower end of the scale. The proton addition to the tertiary amine is presumably followed by protonation of the carboxylates of the two picolinic acid moieties (pKa values of 5.62 and 3.31). Additional ligand protonation constants, *i.e.* more acidic pKa values, were not accessible.

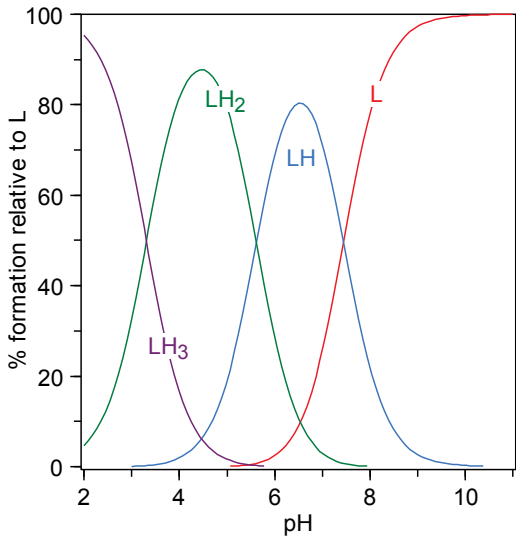

Figure 44. Species distribution diagram of **B2** in aqueous solution for c(**B2**) = 10^{-3} M.

Table 5. Overall (β_x) and stepwise (K_x) protonation constants in log units for **B1a**, **B1b** and **B2**.

equilibrium reaction[(a)]	**B1a**	**B1b**	**B2**
		log β_x	
$L + H \rightleftharpoons LH$	7.73(3)	9.05(7)	7.45(1)
$L + 2\ H \rightleftharpoons LH_2$	11.68(5)	15.15(14)	13.07(2)
$L + 3\ H \rightleftharpoons LH_3$	13.50(12)		16.37(3)
		pKa_x	
$L + H \rightleftharpoons LH$	7.73	9.05	7.45
$LH + H \rightleftharpoons LH_2$	3.95	6.10	5.62
$LH_2 + H \rightleftharpoons LH_3$	1.82		3.31

[(a)] L denotes the respective ligand with completely deprotonated basic centers; the charges of the species are omitted for clarity.

4 Investigation of the hexadentate bispa ligands

Building on the promising results obtained for bispidines regarding the application with copper(II)-64,[172,173,218,346] the new hexadentate bispa ligands were also investigated using this diagnostic radiometal ion. Additionally, studies with gallium(III)-68, another versatile PET nuclide, were conducted. The corresponding radiochemical measurements are presented in detail in Chapter 4.2. Prior to the experiments with radionuclides, the suitability of the bispa ligands for the metal ions copper(II) and gallium(III) was investigated in studies with the respective non-radioactive isotopes (see Chapter 4.1). In addition, the coordination chemistry of the bispa systems with other transition metal ions, *i.e.* cobalt(II), nickel(II) and zinc(II) was studied.

4.1 Coordination chemistry of the hexadentate bispa ligands[v]

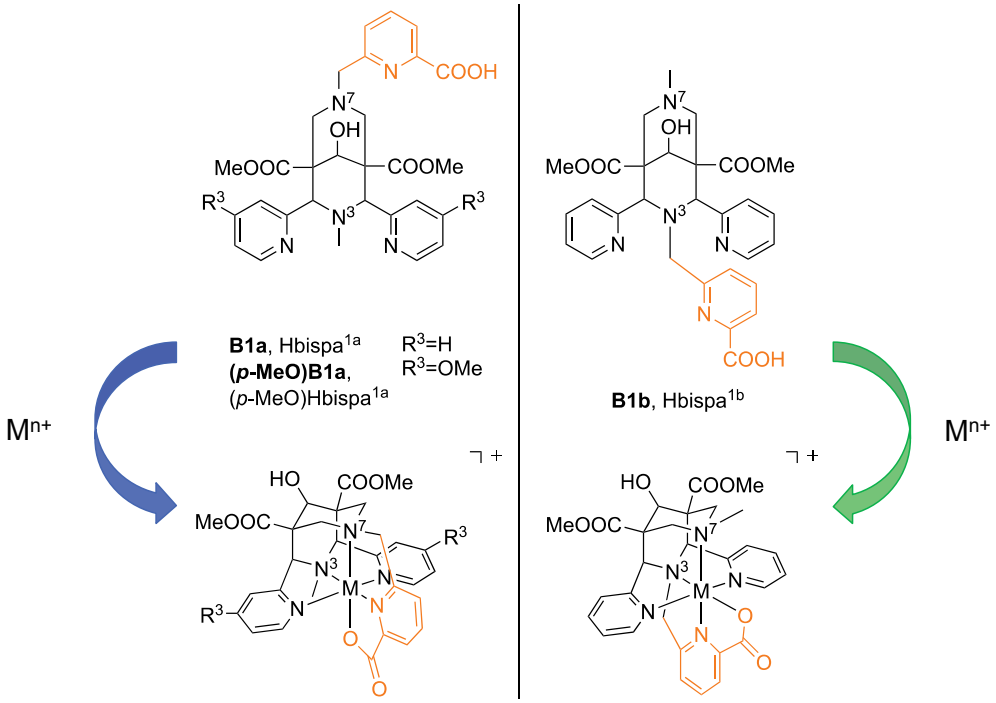

Figure 45. Complexation reactions of the hexadentate bispa ligands **B1a**, **(*p*-MeO)B1a**, and **B1b** with the metal ions Co^{2+}, Ni^{2+}, Cu^{2+}, Zn^{2+}, and Ga^{3+}, respectively (M^{n+}).

[v] Reproduced in part with permission from P. Comba, L. Grimm, C. Orvig, K. Rück, H. Wadepohl, *Inorg. Chem.* **2016**, *55*, 12531-12543, Copyright 2016 American Chemical Society.

Complexation reactions of the hexadentate bispa ligands **B1a**, **(*p*-MeO)B1a**, and **B1b** were carried out with cobalt(II), nickel(II), copper(II), zinc(II), and gallium(III). Equimolar solutions of the TFA salts of **B1a**, **(*p*-MeO)B1a**, or **B1b** and the respective metal salt in methanol (Co^{II}, Ni^{II}, Cu^{II}, Zn^{II}) or in a mixture of methanol and water (Ga^{III}) were combined and stirred at room temperature (Co^{II}, Ni^{II}, Cu^{II}, Zn^{II}) or at 60 °C (Ga^{III}). In the case of the colored complexes, an immediate color change was observed upon addition of the ligand solutions to the dissolved metal salts. The formation of the metal complexes was confirmed by high resolution mass spectrometry (HR-MS). The isolated metal complexes were investigated by elemental analysis (EA), solid state X-ray analysis, NMR spectroscopy, UV-vis-NIR spectroscopy, ESR spectroscopy, cyclic voltammetry, and potentiometric titrations where appropriate.

The formation of the gallium(III) complex of **(*p*-MeO)B1a** was confirmed by HR-MS, but the purification of [Ga^{III}**(*p*-MeO)B1a**]$(X)_2$ (Ga^{III}-**(*p*-MeO)B1a**) was not successful and hence no further characterization could be performed. The gallium(III) complex based on **B1b** was not stable under the conditions of electrospray ionization (ESI) MS. However, the formation of [Ga^{III}**B1b**]$(NO_3)_2$ (Ga^{III}-**B1b**) was confirmed by X-ray analysis, NMR spectroscopy, and EA (see Experimental Section). As mentioned before, the bispa ligand **B1a** was developed within the scope of a master thesis as potential chelator for copper(II)-64 and gallium(III)-68.[359] In this previous study **B1a** was reacted with non-radioactive Cu^{II} and Ga^{III} as a proof of concept and the respective metal complexes could be isolated and identified. However, a detailed characterization of the complexes as well as the radiochemical investigation of **B1a** were conducted as part of the present thesis.

4.1.1 Solid state X-ray analysis

For all metal complexes of **B1a** and **B1b**, as well as for the copper(II) and zinc(II) complex of **(*p*-MeO)B1a** crystals suitable for solid state X-ray analysis could be obtained. The single crystals were either prepared by diffusion of diethyl ether into complex solutions of methanol or acetonitrile, or by slow evaporation of the solvent consisting of a mixture of methanol and water (2:1). As expected the structures of the metal complexes show distorted octahedral coordination geometries (see **Table 6** and **Table 7**). Because of the frequent presence of different types and amounts of crystal solvent, there is no unique packing motif for the complexes even with the same type of ligand.

Table 6. Selected bond distances and angles of **B1a**, $[Co^{II}(\mathbf{B1a})]^+$, $[Ni^{II}(\mathbf{B1a})]^+$, $[Cu^{II}(\mathbf{B1a})]^+$, $[Cu^{II}((\mathbf{p\text{-}MeO})\mathbf{B1a})]^+$, $[Zn^{II}(\mathbf{B1a})]^+$, $[Zn^{II}((\mathbf{p\text{-}MeO})\mathbf{B1a})]^+$, and $[Ga^{III}(\mathbf{B1a})]^{2+}$.

	B1a	$[Co^{II}(\mathbf{B1a})]^+$	$[Ni^{II}(\mathbf{B1a})]^+$	$[Cu^{II}(\mathbf{B1a})]^+$	$[Cu^{II}((\mathbf{p\text{-}MeO})\mathbf{B1a})]^+$	$[Zn^{II}(\mathbf{B1a})]^+$	$[Zn^{II}((\mathbf{p\text{-}MeO})\mathbf{B1a})]^+$	$[Ga^{III}(\mathbf{B1a})]^{2+}$
distances [Å]								
M-N7		2.2503(17)	2.1625(11)	2.3280(13)	2.4013(11)	2.3465(17)	2.4301(15)	2.189(2)
M-N3		2.1203(18)	2.0850(12)	2.0097(13)	2.0358(12)	2.1477(16)	2.1965(15)	2.0529(19)
M-Npy1		2.1203(18)	2.0936(11)	2.0229(14)	2.0177(11)	2.1516(18)	2.1061(17)	2.068(2)
M-Npy2		2.1398(18)	2.0798(11)	2.0347(13)	2.0180(11)	2.1314(18)	2.1042(18)	2.077(2)
M-Npa		2.0209(18)	1.9660(12)	1.9893(13)	2.0329(12)	2.0444(17)	2.0495(15)	1.962(2)
M-Opa		2.0912(16)	2.1359(10)	2.3127(12)	2.3502(11)	2.1441(15)	2.0891(14)	1.9830(17)
N3···N7	2.684(2)	2.952(2)	2.934(2)	2.954(2)	2.9699(15)	2.958(2)	2.9835(20)	2.893(2)
Npy1···Npy2	4.922(3)	4.142(3)	4.088(2)	3.999(2)	3.9668(18)	4.148(3)	4.0869(25)	4.052(3)
angles [°]								
N3-M-N7		84.92(6)	87.36(4)	85.53(5)	83.60(4)	82.18(6)	80.14(5)	85.92(7)
N3-M-Npy1		78.15(7)	79.69(4)	81.89(5)	80.43(4)	76.98(6)	77.17(6)	79.14(8)
N3-M-Npy2		77.89(7)	79.71(4)	81.70(5)	81.37(4)	77.18(6)	77.02(6)	79.43(8)
N3-M-Npa		162.95(7)	168.75(4)	165.43(5)	160.68(4)	158.82(7)	155.26(6)	166.01(8)
N7-M-Npy1		95.68(7)	95.34(5)	94.95(5)	93.39(5)	98.23(6)	91.38(6)	95.23(8)
N7-M-Npy2		94.47(7)	94.46(5)	94.16(5)	95.31(4)	90.64(6)	94.25(6)	94.61(8)
Npy1-M-Npy2		152.97(7)	156.70(4)	160.52(6)	158.79(4)	151.20(7)	152.19(6)	155.67(8)
N7-M-Npa		78.73(7)	81.84(4)	80.25(5)	77.38(4)	76.82(6)	75.14(5)	80.15(8)

Table 7. Selected bond distances and angles of **B1b**, $[Co^{II}(\mathbf{B1b})]^{+}$, $[Ni^{II}(\mathbf{B1b})]^{+}$, $[Cu^{II}(\mathbf{B1b})]^{+}$, $[Zn^{II}(\mathbf{B1b})]^{+}$, and $[Ga^{III}(\mathbf{B1b})]^{2+}$.

	B1b	$[Co^{II}(\mathbf{B1b})]^{+}$	$[Ni^{II}(\mathbf{B1b})]^{+}$	$[Cu^{II}(\mathbf{B1b})]^{+}$	$[Zn^{II}(\mathbf{B1b})]^{+}$	$[Ga^{III}(\mathbf{B1b})]^{2+}$
distances [Å]						
M-N7		2.0271(17)	2.0941(11)	2.0077(11)	2.1032(16)	2.0622(18)
M-N3		2.0060(18)	2.0731(11)	2.0738(11)	2.2507(14)	2.1045(18)
M-Npy1		2.1973(18)	2.1255(12)	2.4192(13)	2.1979(16)	2.0667(17)
M-Npy2		2.1928(18)	2.1235(12)	2.3789(13)	2.2655(15)	2.1179(17)
M-Npa		1.8749(17)	1.9578(11)	1.9129(11)	2.0509(14)	1.9868(18)
M-Opa		2.0020(16)	2.0664(10)	2.0119(11)	2.0358(13)	1.9149(16)
N3···N7	2.664(2)	2.855(2)	2.921(2)	2.882(2)	2.963(2)	2.907(3)
Npy1···Npy2	4.805(2)	4.313(3)	4.181(2)	4.642(2)	4.327(2)	4.121(3)
angles [°]						
N3-M-N7		90.12(7)	89.01(4)	89.83(4)	85.70(5)	88.46(7)
N3-M-Npy1		80.08(7)	80.39(4)	76.39(5)	76.73(5)	80.97(7)
N3-M-Npy2		80.34(7)	80.61(4)	76.76(5)	75.87(5)	79.74(7)
N3-M-Npa		85.29(8)	83.58(4)	83.73(4)	77.59(5)	80.91(7)
N7-M-Npy1		94.57(7)	93.60(4)	95.73(5)	95.29(6)	93.12(7)
N7-M-Npy2		94.40(7)	93.85(4)	95.82(4)	90.20(5)	91.75(7)
Npy1-M-Npy2		158.44(7)	159.45(4)	150.65(4)	151.53(5)	159.96(6)
N7-M-Npa		175.15(8)	172.43(4)	173.38(4)	162.64(5)	169.11(6)

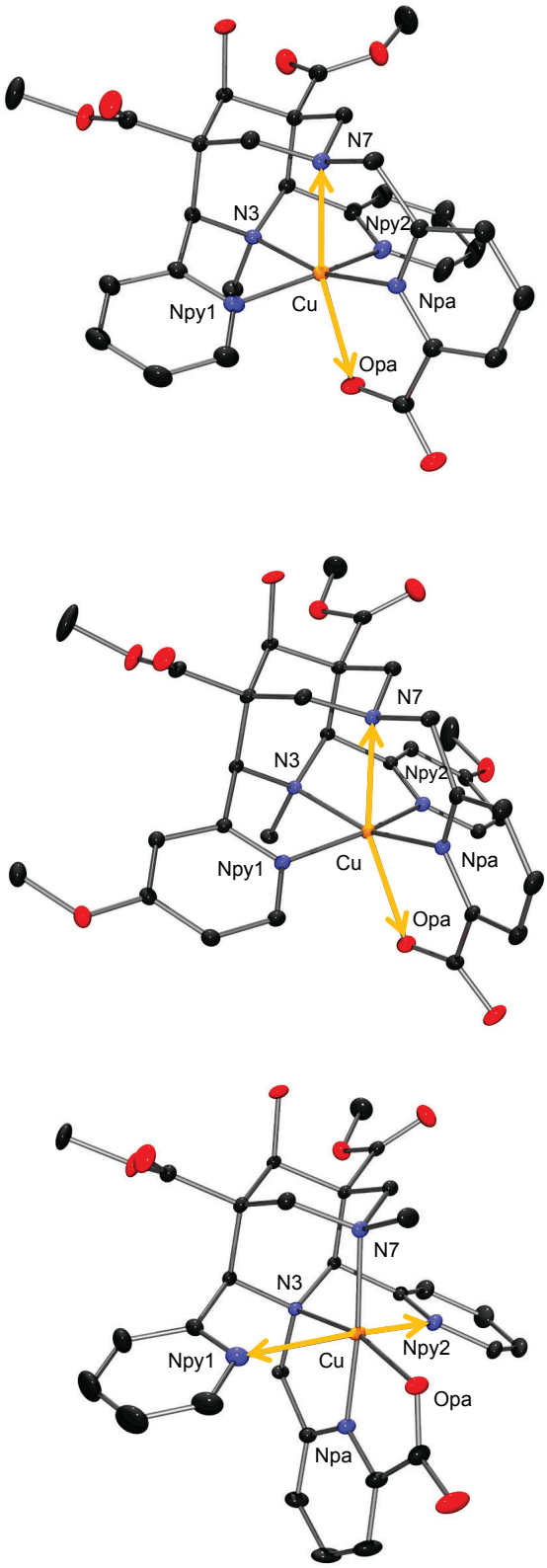

Figure 46. From top to bottom: ORTEP plots of the complex cations of [Cu^{II}(**B1a**)](TFA), [Cu^{II}((***p*-MeO**)**B1a**)](TFA), and [Cu^{II}(**B1b**)](TFA). Ellipsoids are shown at the 50 % probability level; co-crystallized solvent molecules, counterions, and hydrogen atoms are omitted for clarity. The *pseudo* JAHN-TELLER elongated axes are highlighted as orange arrows.[256]

Figure 46 shows the molecular cations of the Cu^{II} complexes of **B1a**, **(*p*-MeO)B1a**, and **B1b**. All three d^9 systems display the expected *pseudo* JAHN-TELLER elongation. In the case of $[Cu^{II}(\mathbf{B1a})]^+$ (Cu^{II}-**B1a**) and $[Cu^{II}(\mathbf{(p\text{-}MeO)B1a})]^+$ (Cu^{II}-**(*p*-MeO)B1a**) the distortion is along the N7-Cu-Opa axis, whereas in $[Cu^{II}(\mathbf{B1b})]^+$ (Cu^{II}-**B1b**) the axis Nyp1-Cu-Npy2 is elongated. The structural data of the other metal-bispa complexes are also given in **Table 6** and **Table 7**.

Similar to the tetra-, penta- and hexadentate bispidines studied by COMBA *et al.* so far, the bispa-type ligands are very rigid and preorganized for tetragonally distorted complexes, in particular for JAHN-TELLER active systems such as Cu^{II}.[298,302,303,375] In general, the bond from the metal center to N7 is more flexible (part of two six-membered chelates) than that to N3 (part of two rigid five-membered chelates), and this usually leads to a longer and more flexible bond for M-N7 compared to M-N3. For the **B1a**- and the **(*p*-MeO)B1a**-based complexes, as well as for the corresponding pentadentate all-N ligands,[298,302,303,375] the flexibility of the M-N7 bond is restricted by a five-membered chelate ring to the third pyridine group (picolinate-pyridine in **B1a** and **(*p*-MeO)B1a**). However, the elongation along M-N7 is clearly shown for all structures of **B1a** and **(*p*-MeO)B1a** as depicted in **Table 6**. Obviously, for Cu^{II} this leads to an electronic stabilization, for Co^{II}, this is not unfavorable but for Ni^{II}, Zn^{II}, and Ga^{III} it is. For the pentadentate bispidines it was observed that the Cu^{II} complex exhibits the highest stability, followed by the Co^{II} complex and the respective Ni^{II} system.[303] This finding is in contrast to the predictions from the Irving-Williams series.[376,377] The structural analyses of the all-N pentadentate and hexadentate bispidines were accompanied by computational modeling.[302,303] Comparing the thus obtained stabilities and overall shapes with the structures of **B1a** and **(*p*-MeO)B1a**, it appears that for these bispa ligands the situation is very similar to the bispidine systems.

For **B1b**, the situation is somewhat different, *i.e.* for all five structures of the metal complexes, the differences of bond distances from the metal center to N3 and N7 are smaller than for both **B1a** and **(*p*-MeO)B1a**. In the case of the copper(II), zinc(II), and gallium(III) complexes of **B1b**, the bond to N3 is even larger than that to N7 (see **Figure 46**). This binding motif has been observed and discussed in detail for bispidine ligands, *i.e.* there are two potential locations for the metal ion in the rigid bispidine cavity, and the stability of the two isomers depends on the size and electronic structure of the metal ion.[375] Also, for the Cu^{II} complexes of the pentadentate bispidines, JAHN-TELLER isomers have been reported.[329,378] The solid state structure of Cu^{II}-**B1b** shows an elongation along py1-Cu-py2 and similar bonds from Cu^{II} to N3 and N7. This structural

trend, as well as the similar overall shapes of **B1b** with the other metal ions Co^{II}, Ni^{II}, Zn^{II}, and Ga^{III}, indicate that **B1b** is also highly preorganized and complementary for Cu^{II}.

4.1.2 NMR spectroscopy

The newly synthesized bispa ligands as well as the respective zinc(II) and gallium(III) complexes were studied by ^{1}H- and ^{13}C-NMR spectroscopy (see Experimental Section and Appendix A). Two-dimensional correlation experiments (^{1}H-^{1}H and ^{1}H-^{13}C) were performed to allow the accurate assignment of all signals. Comparison of the NMR spectra of the metal-free ligands and the respective metal complexes shows significant changes of the proton chemical shifts associated with coordination of the ligands to the metal ions. The spectra confirm the formation of a single complex in solution with Zn^{II} and Ga^{III}, and these spectra are in accordance with the structures determined by solid state X-ray analysis. In **Figure 47** the spectral changes in the ^{1}H-NMR spectrum of bispa ligand **B1a** upon complexation of zinc(II) are depicted.

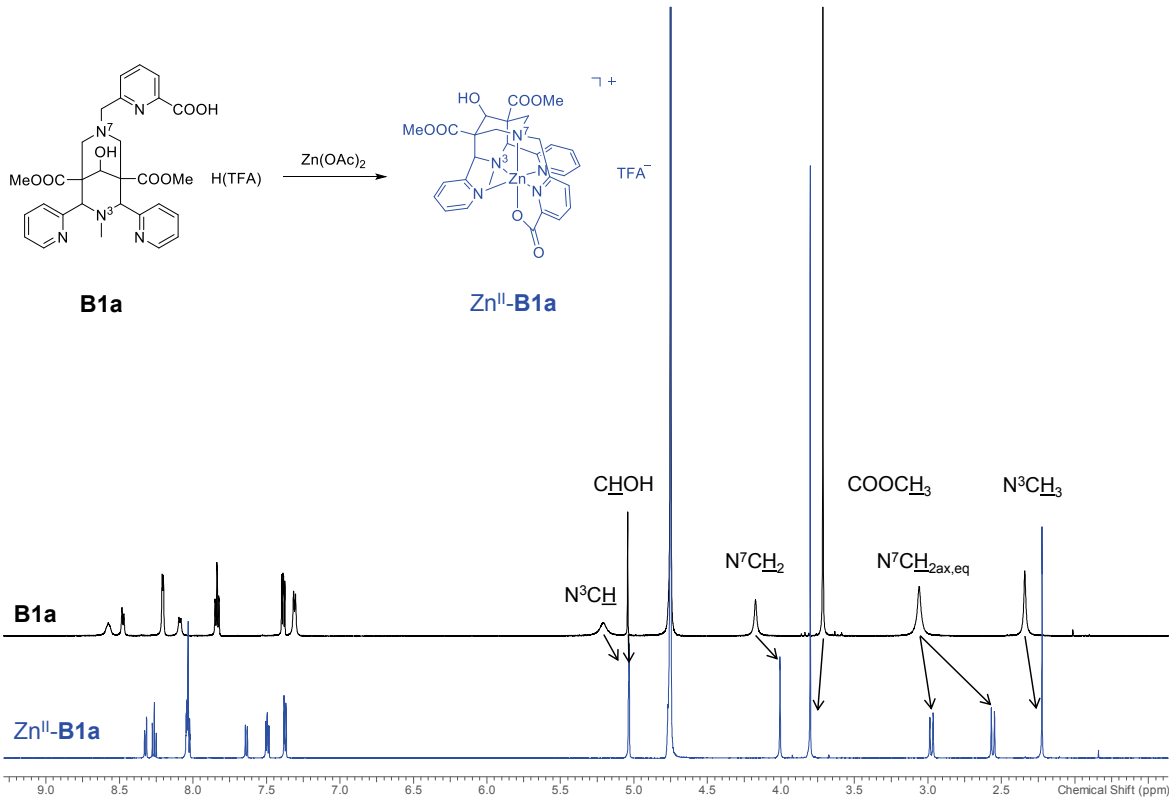

Figure 47. Overlay of the ^{1}H-NMR (600.13 MHz, 22 °C, D_2O) spectra of **B1a**·H(TFA) and [Zn^{II}(**B1a**)](TFA).

Except for [Ga^{III}(**B1b**)]$(NO_3)_2$, all metal complexes, as well as the bispa ligands have a trifluoroacetate (TFA) as counterion. In proton decoupled ^{13}C-NMR spectra of these compounds, signals for the two carbon atoms of TFA coupling to the three fluorine nuclei (I = 1/2) are expected. However, these signals are often too weak to be observed, but are resolved in the ^{13}C-NMR spectra of **(*p*-MeO)B1a**•H(TFA) and [Zn^{II}(**(*p*-MeO)B1a**)](TFA).

4.1.3 UV-vis-NIR spectroscopy

The spectroscopic data of the bispa complexes in the ultraviolet (UV), visible (vis) and near-infrared (NIR) region of the electromagnetic spectrum are given in **Table 8**, together with reported values for complexes of the known hexadentate bispidine N_2py_4 (**B3**).[302] The solution electronic spectra were measured at room temperature in MeOH (Ni^{II} and Cu^{II}) or dimethyl sulfoxide (DMSO; Co^{II}). The experimental spectra and the deconvolution of unresolved transitions with Gaussian fits are summarized in Appendix D. For each metal center, the spectra of the complexes of the four ligands are as similar as expected, showing the higher asymmetry for the bispa compared to the **B3** systems. The bispidine ligand **B3** comprises only pyridines and tertiary amines as donor groups and those possess very similar ligand field parameters.[140,379] Because of the significant π donation of the carboxylates, the ligand field emerging from the three bispa ligands is smaller than that of **B3**.

Table 8. Spectroscopic data of the metal complexes of **B1a**, **(*p*-MeO)B1a**, **B1b**, and **B3**.

	UV-vis-NIR (dd transitions)[(a)]	ref.
[Co^{II}(**B1a**)](TFA)	470 (123), 557 (43), 993 (5)	
[Co^{II}(**(*p*-MeO)B1a**)](TFA)	467 (173), 541 (37), 1030 (6)	
[Co^{II}(**B1b**)](TFA)	475 (117), 516 (9), 544 (23), 584 (7), 677 (6), 920 (6)	
[Co^{II}(**B3**)]$(PF_6)_2$	397 (170), 493 (67), 551 (27) sh	[302]
[Ni^{II}(**B1a**)](TFA)	515 (12), 558 (11), 819 (20), 923 (25)	
[Ni^{II}(**(*p*-MeO)B1a**)](TFA)	521 (12), 585 (10), 866 (38)	
[Ni^{II}(**B1b**)](TFA)	512 (18), 796 (13), 877 (36)	
[Ni^{II}(**B3**)]$(ClO_4)_2$	304 (443) sh, 532 (18), 815 (30)	[302]
[Cu^{II}(**B1a**)](TFA)	672 (93), 1284 (34)	
[Cu^{II}(**(*p*-MeO)B1a**)](TFA)	673 (106), 1227 (36)	

$[Cu^{II}$(**B1b**)](TFA)	651 (78), 904 (18)	
$[Cu^{II}$(**B3**)]$(ClO_4)_2$	620 (110)	[302]

[(a)] Measurements at 25 °C in MeOH (Ni^{II} and Cu^{II} complexes of **B1a**, **(*p*-MeO)B1a**, and **B1b**), DMSO (Co^{II} complexes of **B1a**, **(*p*-MeO)B1a** and **B1b**), or in MeCN (**B3**).

For an octahedral cobalt(II) complex three dd-transitions are expected, *i.e.* $^4T_{1g}\rightarrow{}^4T_{2g}$, $^4T_{1g}\rightarrow{}^4A_{2g}$, and $^4T_{1g}(F)\rightarrow{}^4T_{1g}(P)$. Metal bispa complexes are less symmetrical than O_h and this leads to further splitting of the terms. Due to limited resolution, not all transitions can be distinguished. For Co^{II}-**B1a** and Co^{II}-**(*p*-MeO)B1a** three transitions can be resolved, whereas the spectrum of Co^{II}-**B1b** shows six maxima in the absorbance spectra.

As a rough approximation the metal ion in bispa complexes is coordinated in a slightly distorted tetragonal geometry. For a nickel(II) complex with O_h symmetry transitions from the electronic $^3A_{2g}$ ground state to the three excited states $^3T_{2g}$, $^3T_{1g}$ (F), and $^3T_{1g}$ (P) are expected. Often there is an additional spin-forbidden transition to the ^1E_g state observable. If only the coordinating ligand atoms are considered in the nickel(II) bispa complex cations, *i.e.* five similar nitrogen donors and one negatively charged oxygen, a *pseudo* C_{4v} symmetry can be deduced. The transition from O_h to C_{4v} symmetry results in a splitting of the excited electronic states. For Ni^{II}-**B1a** and Ni^{II}-**B1b** there are two signals around 900 nm in the absorbance spectra and this might be associated with a splitting of the $^3A_{2g}\rightarrow{}^3T_{2g}$ transition. However, the assignment in this region is difficult due to the often relatively intense band resulting from the spin-forbidden transition (~900-1000 nm). For Ni^{II}-**(*p*-MeO)B1a** there is only one broad band at 866 nm, which is not further resolved. The same applies for the $^3A_{2g}\rightarrow{}^3T_{1g}$ (F) transition, which can either be observed as two separate signals or as one broad band around 500 nm. The third transition is obscured by strong ligand-metal charge transfer (CT) bands occurring at wavelengths below 400 nm.

A d^9 metal ion such as copper(II) possesses an electronic gap or "hole" on its d level and can hence be treated as an "inverse" d^1 ion. For systems with only one d electron (or one electronic "hole") the orbital model can be applied.[380] For tetragonal copper(II) complexes, a d orbital splitting as depicted in **Figure 48** can be derived. Due to the *pseudo* JAHN-TELLER effect, one axis in the Cu^{II}-bispa systems is elongated and this axis is usually designated as the z axis. Because of the elongation of the z axis all orbitals with z character are lowered energetically. For the copper(II) bispa complexes two signals around 651-672 nm and 904-1284 nm, respectively, were observed. According to the d orbital splitting in **Figure 48** the broad band at lower energy (higher wavelength) can be assigned to the $d_{z2}\rightarrow d_{x2-y2}$ transition. Further electronic transitions are possible from the

d_{xy}, d_{xz} and d_{yz} orbitals to the $d_{x^2-y^2}$ level, but those are not resolved in the UV-vis-NIR spectra of the complexes and thus only one additional signal was detected.

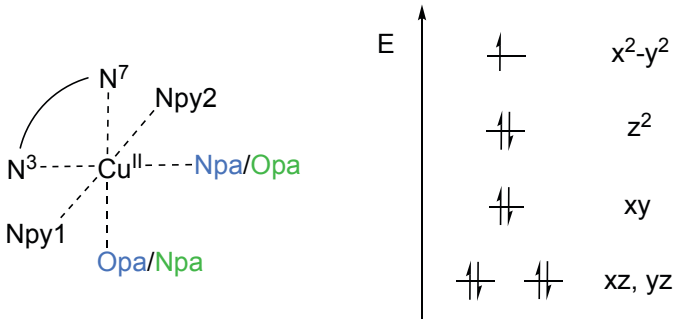

Figure 48. Coordination geometry of the copper(II) complexes based on the bispa ligands **B1a** and **B1b** (left) and the corresponding scheme of the d orbital splitting (right). Adapted from reference [381].

4.1.4 ESR spectroscopy

The ESR spectra of the copper(II) complexes based on **B1a**, **(*p*-MeO)B1a**, and **B1b** were recorded and simulated as frozen solutions. The experimental spectra depicted in Appendix E show the characteristic hyperfine coupling to copper with a nuclear spin of I = 3/2. The form of ESR signals of metal complexes depends on their coordination geometry. The dependency of the anisotropic g tensors of axial symmetric Cu^{II} compounds is for example as follows: $g_x = g_y$ and $g_z > g_x, g_y$. The same considerations apply for the corresponding A tensors. An axial ESR spectrum hence indicates a tetragonal symmetry of the copper(II) complex.[382] The Spin Hamiltonian parameters derived by simulation of the ESR spectra using the software package XSophe[383,384] are listed in **Table 9**.

Table 9. Results of the simulation of the ESR spectra of the copper(II) complexes based on **B1a**, **(*p*-MeO)B1a**, **B1b**, and **B3**.

	simulated ESR parameters[(a)]		
	g_x, g_y, g_z	A_x, A_y, A_z [10^{-4} cm]	ref.
$[Cu^{II}$(**B1a**)](TFA)	2.059, 2.059, 2.243	13, 13, 145	
$[Cu^{II}$((***p*-MeO)B1a**)](TFA)	2.057, 2.057, 2.244	10, 10, 170	
$[Cu^{II}$(**B1b**)](TFA)	2.016, 2.068, 2.236	27, 21, 145	
$[Cu^{II}$(**B3**)]$(ClO_4)_2$	2.069, 2.069, 2.208	-, -, 169	[302]

[(a)] Measurements at 8 K in MeOH (**B1a**, **(*p*-MeO)B1a**, and **B1b**) or at 130 K in DMF / water 2:1 (**B3**).

In agreement with the solid state structures and the analysis of the UV-vis-NIR spectra, the simulated ESR parameters indicate that the solution structures are similar to those in the solid state. The coordination geometries derived from the solid state structures of the copper(II) complexes based on **B3**,[302] **B1a**, and **B1b** are depicted schematically in **Figure 49**. In the case of $[Cu^{II}$(**B3**)$]^{2+}$ (Cu^{II}-**B3**) there are only tertiary amine and pyridine donors which possess very similar ligand field properties.[140,379] One of the three coordination axes in Cu^{II}-**B3** is elongated due to the JAHN-TELLER effect and this results in identical g_x and g_y parameters and a higher value for g_z.[302] Axial symmetry is also observed for Cu^{II}-**B1a** and Cu^{II}-**(*p*-MeO)B1a**) where the axis N7-Cu-Opa is elongated. Similar g_x and g_y parameters are again obtained for the nitrogen donors in the x,y plane. The *para*-substitution in Cu^{II}-**(*p*-MeO)B1a**) does not have a big influence on the Spin Hamiltonian parameters (see **Table 9**). The simulation of the ESR spectrum of the copper(II) complex based on **B1b** reveals different g parameters ($g_x \neq g_y \neq g_z$) and hence points to a rhombic site geometry. The obtained value of g_z is higher than g_x and g_y due to the elongation of the Npy1-Cu-Npy2 axis. Furthermore, the carboxylate in the x,y plane leads to a larger asymmetry and hence to different g_x and g_y parameters.

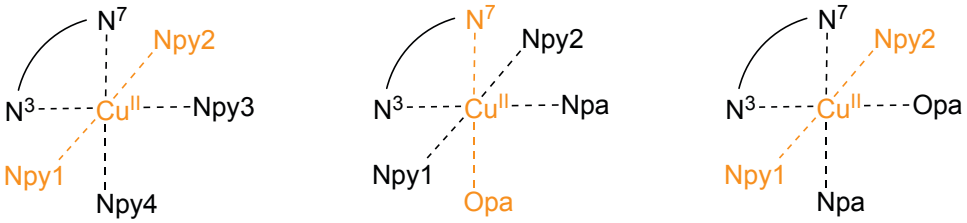

$[Cu^{II}(\mathbf{B3})]^{2+}$ $[Cu^{II}(\mathbf{B1a})]^{+}$ $[Cu^{II}(\mathbf{B1b})]^{+}$

Figure 49. From left to right: Coordination geometries derived from the solid state structures of the copper(II) complexes based on **B3**, **B1a**, and **B1b** with the *pseudo* JAHN-TELLER elongated axes highlighted in orange.

4.1.5 AOM analysis

For the copper(II) complexes of the bispa ligands **B1a** and **B1b** an angular overlap model (AOM) based ligand field analysis of the electronic and ESR spectra has been carried out. This study was performed for a detailed comparison of the solid state structures and the structures in solution as well as to understand differences in the degree of preorganization of the two isomeric ligands for the JAHN-TELLER labile Cu^{II} ion.

Term energies of transition metal complexes are governed by the metal center, the donor atoms and the coordination geometry.[385] The AOM uses a simplified molecular orbital (MO) approach to calculate the spectroscopic properties of such complexes.[386-388] In this model metal-ligand (M-L) bonds are described by covalent σ, π and δ interactions using two-atom overlap integrals of the metal d orbitals and the donor orbitals. Each M-L interaction has to be parameterized individually with the respective e_σ, e_π and e_δ values. These parameters are positive for donor atoms and negative for acceptors, and their values decrease in the order $|e_\sigma| > |e_\pi| > |e_\delta|$. The interaction between a free electron pair at the ligand and a metal orbital with suitable symmetry has a destabilizing effect resulting in an upward shift in energy of the metal atomic orbital and e_σ is thus always positive. The π parameter, on the other hand, can adopt both signs, depending on the character of the bond with respect to π-forward and π-backward donation. In the case of an anisotropic π bond, e_π is divided into two parts, *i.e.* $e_{\pi x}$ and $e_{\pi y}$. Due to the minor overlap integral of δ bonds, the values for e_δ are relatively small and are hence often neglected. Moreover, the ligand systems investigated here do not possess orbitals suitable for the formation of δ bonds. The AOM parameters depend on the metal-ligand distance r in a way that their values approximately decrease with the sixth power of r.[386-389] In tetragonally distorted copper(II) complexes the energy of the d_{z2} orbital is decreased by configurational

interaction with the metal 4s orbital. This effect, known as ds mixing, is considered in the AOM by assigning each ligand an additional bonding parameter e_{ds} with e_{ds} = 1/4 e_{σ}.[330,390]

The AOM calculations reported here were performed with the computer program CAMMAG.[391] The coordinates of the Cu^{II} center and the donor atoms were taken from the X-ray structures of Cu^{II}-**B1a** and Cu^{II}-**B1b**. In both cases, the z axis was defined along the *pseudo* JAHN-TELLER elongated axis (see also **Figure 49**). Details of the AOM analysis together with examples of input-files are given in Appendix F. AOM e_{σ}, e_{π} and e_{ds} parameters are not transferable in principle but in a series of studies, it has been shown that the error made by assuming transferability generally is acceptable.[315,379,392] However, with published parameters for Cu^{II}-amine, Cu^{II}-pyridine and Cu^{II}-carboxylate bonds, adjusted to the observed Cu^{II}-donor distances with $1/r^6$,[385,390,393] the computed and experimentally determined electronic transitions are only in fair agreement. Thus, modifications of the ligand field parameters were introduced and led to acceptable predictions of the dd transitions and EPR g tensor parameters as shown in **Table 10**. One reason for the discrepancy between the published and moderately adjusted AOM parameters is that those for the carboxylates are merely the result of an *ad-hoc* parameterization for one particular set of complexes,[393] while the parameterization for amines and pyridines were deduced from a larger set of spectroscopic studies.[385] Also, transferability is an assumption with limited applicability, and electron transfer from anionic ligands may be problematic in this context.[394] In addition and most importantly, small structural changes upon dissolution of the complexes, in particular along the JAHN-TELLER vibration, may lead to significant changes of the ligand field. However, while the adjustments to the AOM parameters seemed to be necessary for esthetic reasons, the qualitative interpretation that there are only minor structural changes upon dissolution of the complexes does not change with the two sets of parameters used.

The structural data suggest that Cu^{II}-**B1a** is elongated along the N7-Cu-Opa axis, while the elongation observed for Cu^{II}-**B1b** is along Npy1-Cu-Npy2. Based on both sets of AOM parameters, the solid state structure is confirmed to also be the structure in solution and this has some implication for the relative stabilities (see below). The splitting of the three d_{π} orbitals is not resolved for either isomer but, from the relative line width of the $d_{xy,xz,yz} \rightarrow d_{x^2-y^2}$ transitions, it appears that the splitting is slightly larger for Cu^{II}-**B1a**, and this agrees with the geometry observed in the solid state structures, which for Cu^{II}-**B1a** suggests interaction of the carboxylate π donor with the Cu^{II} $d_{xz,yz}$ orbitals. The in-plane carboxylate in Cu^{II}-**B1b** leads to a relative destabilization of the d_{π} orbitals and a

stabilization of the d_{x2-y2} orbital with respect to Cu^{II}-**B1a** with an axial carboxylate, emerging in a generally lower ligand field but a higher energy $d_{z2} \rightarrow d_{x2-y2}$ transition.

The conservation of the solid state structures in solution, *i.e.* the different orientations of the *pseudo* JAHN-TELLER axes, is also well supported by the g values resulting from simulation of the frozen solution X-band ESR spectra. As already discussed in Chapter 4.1.4, tertiary amines and pyridine donors exhibit very similar ligand field parameters,[140,379] while those for carboxylate are significantly different and therefore lead to a larger in-plane asymmetry in Cu^{II}-**B1b**.

In metal complexes the donor atoms N7 and N3 of the bispidine scaffold are part of rather flexible six- and very rigid five-membered chelate rings, respectively.[375] This structural difference in general leads to long M-N7 and shorter M-N3 bonds and therefore to a rigid bispidine ligand shape that is highly complementary for copper(II). For the N_2py_3-type isomers similar to **B1a** and **B1b** this results in distinct stability differences between the two corresponding isomeric Cu^{II} complexes and an interesting Cu^{II} selectivity for one of the two isomers.[303] However, "JAHN-TELLER isomerism" was observed for the Cu^{II} complexes of a number of bispidine derivatives,[329,378] and the ligand field properties of the two isomers Cu^{II}-**B1a** and Cu^{II}-**B1b** as well as the stronger Cu^{II}-Opa interaction in Cu^{II}-**B1b** suggest that this isomer might lead to a slightly more stable Cu^{II} complex.

Table 10. Comparison of experimental and calculated (AOM) spectroscopic data of the copper(II) complexes based on **B1a** and **B1b**.

		UV-vis-NIR (dd transitions)	ESR
		λ [cm^{-1}]	g_x, g_y, g_z
[Cu^{II}(**B1a**)](TFA)	exp.	14880, 7790	2.059, 2.059, 2.243
	AOM_{pub} [(a)]	17870, 17330, 15640, 9110	2.029, 2.038, 2.136
	AOM_{adj} [(b)]	16131, 15668, 13421, 8114	2.028, 2.046, 2.154
[Cu^{II}(**B1b**)](TFA)	exp.	15360, 11060	2.016, 2.068, 2.236
	AOM_{pub} [(a)]	18530, 18260, 17440, 11200	2.014, 2.055, 2.120
	AOM_{adj} [(b)]	17306, 16978, 15713, 10681	2.015, 2.060, 2.128

[(a)] For AOM_{pub} published AOM parameters were used.[385,390,393] [(b)] AOM_{adj} gives data based on moderately adjusted parameters offering improved matching to the spectroscopic data (see Appendix F).

4.1.6 Cyclic voltammetry

The electrochemical measurements of the metal complexes were performed at ambient temperature in dimethylformamide. The obtained redox potentials are summarized in **Table 11** and the corresponding cyclovoltammograms are depicted in Appendix G. With the bispa complexes of Ni^{II} and Co^{II} two signals corresponding to the $Ni^{II/I}$ ($Co^{II/I}$) and $Ni^{III/II}$ ($Co^{III/II}$) couples were detected, and for the Cu^{II} systems a single wave for $Cu^{II/I}$ was observed in the measurable range as permitted by the solvent. It is known that the stability constants of Cu^{I} complexes are relatively uniform, while those of Cu^{II} vary over a wide range.[168] Therefore, $Cu^{II/I}$ redox potentials are linearly correlated to the thermodynamic stability of the corresponding Cu^{II} complexes,[167] and this correlation has been used to predict approximate stability constants of Cu^{II} bispidine complexes.[303,395] In comparison to other Cu^{II} bispidine systems only bearing nitrogen donors, the reversible redox potentials of Cu^{II}-**B1a**, Cu^{II}-**(*p*-MeO)B1a**, and Cu^{II}-**B1b** are significantly lower, indicating higher Cu^{II} complex stabilities, in particular compared to the hexadentate Cu^{II}-**B3** system.[302] The reason for these strongly negative redox potentials is the coordination of the carboxylate group to the copper(II) center. The anionic oxygen donor transfers electron density to the metal ion and this results in a decrease of the $Cu^{II/I}$ redox potential. According to the obtained potentials listed in **Table 11**, Cu^{II}-**B1b** is predicted to be slightly more stable than Cu^{II}-**B1a**, which is in agreement with the spectroscopic analysis.

Comparing the bispidine complexes of all three investigated metal ions there is a general trend observed with the **B3** complexes having significantly higher redox potentials than the bispa systems, whereas the values for the **B1b** isomer are slightly more negative than that for the respective **B1a** and **(*p*-MeO)B1a** complexes, *i.e.* M-**B3** > M-**B1a** > M-**(*p*-MeO)B1a** > M-**B1b**. This order can be explained by means of structural and electronic considerations: The *para*-methoxy groups in M-**(*p*-MeO)B1a** increase the electron density at the pyridine nitrogens and hence on the copper(II) center, which leads to a more negative redox potential in comparison to M-**B1a**. A structural difference between the **B1a** and **(*p*-MeO)B1a** metal complexes on the one hand and M-**B1b** on the other hand is the distinct orientation of the elongated *pseudo* JAHN-TELLER axes. Due to the elongation of the N7-Cu-Opa axis in the **B1a** and **(*p*-MeO)B1a** complexes, the metal-carboxylate bond in M-**B1b** is slightly shorter and this consequently decreases the redox potential.

Table 11. Electrochemical data of the metal complexes based on **B1a**, **(*p*-MeO)B1a**, **B1b**, and **B3**.

	redox potentials $E_{1/2}$ *vs.* fc/fc^+ [V] [(a)]		
	$M^{II/I}$	$M^{III/II}$	ref.
$[Co^{II}$(**B1a**)](TFA)	–1.94	–0.37	
$[Co^{II}$((**(*p*-MeO)B1a**)](TFA)	–1.97	–0.41	
$[Co^{II}$(**B1b**)](TFA)	–2.09	–0.52	
$[Co^{II}$(**B3**)]$(PF_6)_2$	-	0.22	[302]
$[Ni^{II}$(**B1a**)](TFA)	–2.18	0.76 (irrev.)	
$[Ni^{II}$((**(*p*-MeO)B1a**)](TFA)	–2.24	0.71 (irrev.)	
$[Ni^{II}$(**B1b**)](TFA)	–2.27 (irrev.)	0.71	
$[Ni^{II}$(**B3**)]$(ClO_4)_2$	–1.28 (irrev.)	1.39 (irrev.)	[302]
$[Cu^{II}$(**B1a**)](TFA)	–1.02	-	
$[Cu^{II}$((**(*p*-MeO)B1a**)](TFA)	–1.08	-	
$[Cu^{II}$(**B1b**)](TFA)	–1.17	-	
$[Cu^{II}$(**B3**)]$(ClO_4)_2$	–0.66	-	[302]

[(a)] Measurements at 25 °C in DMF and 0.1 M (n-Bu_4N)(ClO_4) (**B1a**, **(*p*-MeO)B1a**, and **B1b**) or in MeCN and 0.1 M (n-Bu_4N)(PF_6) (**B3**).

4.1.7 Potentiometric titrations

The stability constants of the isomeric Cu^{II}-bispa complexes Cu^{II}-**B1a** and Cu^{II}-**B1b** were determined under similar experimental conditions as those used in the protonation experiments (see Chapter 3.3). As the stability constants were not accessible *via* direct potentiometry, ligand-ligand competition titrations were performed in a ratio of 1:1:1 (Cu^{II} / L / L', with L = **B1a** or **B1b** and L' = EDTA (**L9**)). Back-titrations were carried out in order to screen for complete equilibration of the system. When titrating the metal-ligand solutions up to a pH of 11, a shift between the titration curve and the back-titration was observed. By lowering the final pH value to 10, both curves became congruent, which indicates decomposition processes in basic media (pH > 10). Therefore, only data points in the pH range of 2-10 were considered in the fitting procedures. The main species formed in solution are CuL and CuLH (see Appendix C for species distribution plots). Only the 1:1 complexation was modeled, which is in agreement with the spectroscopic and structural data. Logarithmic complex stability constants of 18.9 for Cu^{II}-**B1a** and 19.4 for

Cu^{II}-**B1b** were obtained, *i.e.* the Cu^{II}-**B1b** complex is slightly more stable than its isomer and this is in accordance with the structural, spectroscopic and electrochemical analyses. Both ligands lead to significantly larger Cu^{II} complex stabilities than the known hexadentate ligand **B3** by around three orders of magnitude (16.3).[302] The species distribution diagrams of copper(II) in the presence of **B1a** and **B1b** are shown in Appendix C.

Table 12. Copper(II) complex stability constants and $pM_{7.4}$ values of **B1a** and **B1b** (H_2O, 25 °C, 0.1 M KNO_3).

equilibrium reaction [(a)]	stability constant log β	**B1a**	**B1b**
Cu + L ⇌ CuL	log β_{CuL}	18.88(10)	19.44(18)
Cu + L + H ⇌ CuLH	log β_{CuLH}	21.07(6)	21.77(21)
	$pM_{7.4}$ value [(b)]	19.3	18.7

[(a)] L denotes the respective ligand with completely deprotonated basic centers; the charges of the species are omitted for clarity. [(b)] Calculated for 10 µM total ligand and 1 µM total metal ion concentration at pH 7.4 and 25 °C.

The pM values at pH 7.4 (pM = -log $[M^{n+}]$) are also given in **Table 12**. These define the complex stabilities at a particular pH value and for PET chelators the pM values at physiological pH are of particular relevance. Interestingly, based on the log β values and spectroscopic as well as electrochemical data, **B1b** is a slightly better ligand than **B1a** (19.4 *vs.* 18.9). However, at pH = 7.4 this is reversed according to the calculated pM values of 18.7 and 19.3, respectively. The species distributions of the metal-free ligands, given in **Figure 43** of Chapter 3.3, indicate that this is related to the relevant pKa values. These findings are therefore an excellent example for the importance of pM values to directly assess different ligands for a given metal ion. In **Table 13** the stability parameters determined for the copper(II) bispa complexes are compared to various literature-known Cu^{II} chelators. To avoid the release of the radioisotope, the metal complex has to be stable in the presence of competing metal ions. In this context, stability studies of similar bispidine systems have already shown high stability of the corresponding Cu^{II} complexes and good selectivity of the ligands for Cu^{II} in comparison to Co^{II}, Ni^{II}, and Zn^{II}.[218,302,303]

Table 13. Comparison of the pKa, log β_{CuL} and $pCu_{7.4}$ values of bispa ligands and selected chelators from literature.

ligand	pKa	log β_{CuL}	$pCu_{7.4}$ [(a)]	ref
Hbispa[1a] (**B1a**)	7.73(3), 3.95(5), 1.82(12)	18.88(10)	19.3	
Hbispa[1b] (**B1b**)	9.05(7), 6.10(14)	19.44(18)	18.7	
N_2py_4 (**B3**)	6.68, 11.40	16.28	17.6	[302]
Diol of **B5**	>12, 10.6(6), 4.5(1), 2.0(2), 0.82(1), <0.82	19.2(2)	17.0	[218]
TETA (**L6**)	10.82(1), 10.10(2), 4.15(1), 3.21(1)	21.87(6)	16.7	[396]
TE1PA (**L18**)	11.55(1), 10.11(1), 2.71(1), 1.7(1)	25.5(1)	19.6	[124]
DOTA (**L5**)	11.14(1), 9.69(2), 4.85(2), 3.95(1)	22.72(4)	17.6	[396]
DO1PA (**L14**)	10.46(1), 9.26(1), 3.23(1)	24.01(1)	20.0	[124]
NOTA (**L4**)	11.73(2), 5.74(1), 3.16	21.63(2)	18.2	[116]

[(a)] L denotes the respective ligand with completely deprotonated basic centers; the charges of the species are omitted for clarity.

The comparison of copper(II) complexes based on different ligand systems reveals a certain deviation with regard to the bispa ligands (see **Figure 50**). The potentials of the copper(II) bispidine and bispa complexes were referenced against the redox couple ferrocene/ferrocenium (fc/fc^+) by default.[303] To be able to directly compare these values with the redox potentials used by RORABACHER *et al.* for their potential-stability correlation,[167] the corresponding potentials were also referenced *vs.* fc/fc^+. Therefore, an fc/fc^+ redox potential of –0.4 V *vs.* the standard hydrogen electrode (SHE) was assumed based on the approximation that this value is invariant with solvent.[397,398] However, there are reports indicating that this assumption is not entirely correct.[399-401] A detailed list of redox potentials and stability constants used for the plot in **Figure 50** is compiled in Appendix G. It is important to note that the potentials were determined in different solvents. For reasons of comparability the cyclovoltammetric measurements of bispidine ligands are usually performed in acetonitrile, but it was shown that the redox potentials assessed in water are in the same range for the investigated compounds (see Appendix G).[303] Due to solubility problems of the cobalt(II) and nickel(II) bispa complexes, dimethyl formamide was used as solvent for the electrochemical analyses of the bispa systems. However, it was observed that the $Cu^{II/I}$ potentials of Cu^{II}-**B1a** measured in dimethyl formamide and in acetonitrile are comparable.[359] The presentation of the values in **Figure 50** shows that the RORABACHER-correlation can be applied to the

neutral all-N bispidine ligands as indicated by the linear fit. The bispa ligands, in contrast, are considerably shifted from this line and this is probably due to their anionic character. For this reason, RORABACHER *et al.* only considered ligands uncharged in their deprotonated form in order to eliminate electrostatic effects.[167] The analysis of further monoanionic ligands might provide a similar correlation as that found for neutral systems.

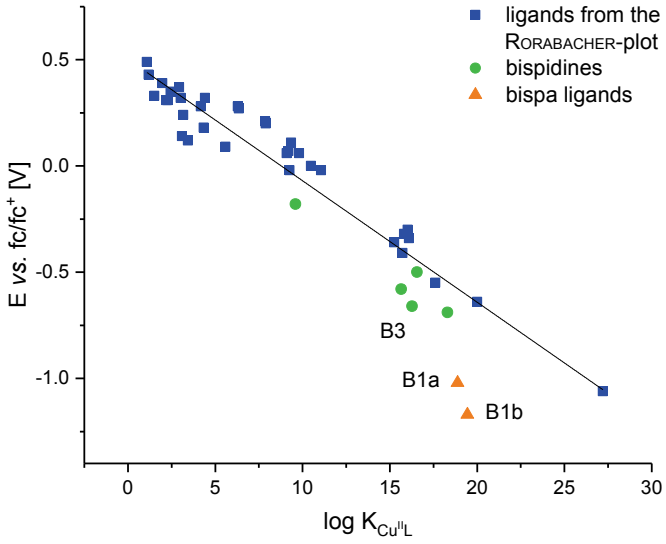

Figure 50. Plot of the potentials of $Cu^{II/I}L$ redox couples as a function of the logarithmic values of the $Cu^{II}L$ formation constants. Blue squares represent various ligand systems used by RORABACHER *et al.*[167] Green circles represent bispidines investigated by COMBA *et al*.[303] Orange triangles represent the bispa ligands **B1a** and **B1b**. Linear fit including the ligands from the original RORABACHER-plot and the bispidines: y = –0.05718 ± 0.00262; R^2: 0.92609.

In summary, the copper(II) complexes of **B1a** and **B1b** were shown to display high complex stabilities, which is an important prerequisite for radiopharmaceutical applications. In the light of the planned investigation of the bispa ligands with radioactive gallium(III) isotopes, the stability of the Ga^{III}-bispa complexes is of crucial importance as well. A thorough discussion of the stability of these complexes in challenge experiments and biodistribution studies will be presented in Chapter 4.2.2.

4.2 Radiochemical investigations of the hexadentate bispa ligands

In the previous chapter the hexadentate bispa ligands were shown to form complexes with the metal ions copper(II) and gallium(III). Therefore, the bispa ligands were investigated for potential radiopharmaceutical applications with the PET isotopes copper-64 and gallium-68. In the scope of the present thesis only the isomeric bispa ligands **B1a** and **B1b** were examined. The results of these studies are presented in the following.

4.2.1 Radiochemistry with copper(II)-64

The radiochemical investigations with copper(II)-64 were performed at the Institute of Radiopharmaceutical Cancer Research of the Helmholtz Zentrum Dresden-Rossendorf (HZDR). Radiolabeling experiments, *in vitro* competition assays and the determination of the partition coefficients log $D_{o/w}$ were carried out in the group of Dr. Holger STEPHAN by Karin LANDROCK and Janine PARTSCH. The biodistribution studies were performed by Prof. Dr. Jens PIETZSCH and coworkers.

Radiolabeling experiments

Prior to the experiments, the radiochemical purity of the $^{64}Cu^{II}$-radiolabeled bispa ligands **B1a** and **B1b** was determined by radio-high performance liquid chromatography (radio-HPLC) to be > 99 %. The radiolabeling efficiency of **B1a** and **B1b** with copper(II)-64 was investigated as a function of time and concentration. Therefore, sample solutions with different amounts of the respective ligand and $^{64}CuCl_2$ were prepared and allowed to radiolabel at ambient temperature. If not stated otherwise, the ligands were used in their protonated form with one trifluoroacetate (TFA) as the counterion. The experimental setup was carried out in a way to obtain final ligand concentrations of ~10^{-4} to 10^{-6} M and the studies were performed with starting activities of 10 and 100 MBq $^{64}CuCl_2$, respectively. Depending on the molar activity of different $^{64}Cu^{II}$ production runs, and the time of $^{64}Cu^{II}$ use after the end of bombardment (EOB), different aliquots of $^{64}CuCl_2$ were added to obtain the desired starting activity. The degree of radiolabeling was assessed by radio-thin layer chromatography (radio-TLC) at 5, 30 and 60 minutes after addition of $^{64}CuCl_2$. The radio-TLC conditions described in the Experimental Section allowed for the clear separation of “free” copper(II)-64 and the two radiolabeled bispa ligands. While $^{64}CuCl_2$ remains at the origin, both $^{64}Cu^{II}$-bispa complexes move with an R_f-value of 0.8. The

radiochemical yield (RCY) was determined by integrating the peaks in the radio-thin layer chromatograms. In the case of **B1a** and **B1b** a total amount of 0.5 µg ligand per 100 µL (~5•10^{-6} M) could be radiolabeled quantitatively (RCY > 99%) within 5 minutes at room temperature using 100 MBq $^{64}CuCl_2$. After decreasing the amount of ligand to 0.1 µg (~10^{-6} M) under the same conditions, only partial radiolabeling was observed, *i.e.* 15 % RCY for $^{64}Cu^{II}$-**B1a** and 30 % RCY for $^{64}Cu^{II}$-**B1b**.

The specific or molar activity of a compound is a measure of its ability to be radiolabeled by a certain amount of radioactivity and is given in detected activity per gram or mole of the substance.[135] Radiolabeling of **B1a** and **B1b** with copper(II)-64 yielded molar activities of ~100 GBq/µmol and ~200 GBq/µmol, respectively. Such high activities are desirable for nuclear medicine applications, as this means that a small quantity of ligand can be radiolabeled with a high amount of activity. As a consequence, the drug dose required for the patient is minimized. Altogether, a very efficient and rapid $^{64}Cu^{II}$ complexation of the bispa ligands was found under mild conditions. The other bispidine systems studied so far also displayed fast radiolabeling kinetics with $^{64}Cu^{II}$, but they were not investigated with activities as high as 100 MBq.[172,173] For this reason the maximum molar activity of these compounds could not be determined.

Competition assays

The stability of a radiolabeled metal complex towards transchelation is usually tested in challenge experiments with competing compounds or mixtures thereof. The standard procedure involves labeling of the ligand with the respective radiometal ion followed by incubation with the chosen competitor. After a certain time period, the amount of stable complex is then determined using a suitable analytical method.

The first challenge experiments with the $^{64}Cu^{II}$-bispa complexes were performed in the presence of the competing ligands cyclam (**L3**) and EDTA (**L9**). Complete radiolabeling of **B1a** and **B1b** with copper(II)-64 (RCY > 99 %) was initially checked by radio-TLC analysis. The radiolabeled complexes were then incubated with a 100-fold molar excess of cyclam and EDTA, respectively. After incubation at room temperature for 2 and 24 hours, the samples were assayed by radio-HPLC. The radio-HPLC protocol applied revealed well-separated signals for the metal complexes, hence providing information on the degree of transchelation. As expected, both $^{64}Cu^{II}$-**B1a** and $^{64}Cu^{II}$-**B1b** were stable by more than 99 % after 2 and 24 hours in the presence of cyclam as well as of EDTA.

To further study the kinetic stability of the $^{64}Cu^{II}$-bispa complexes, superoxide dismutase (SOD) challenge experiments were carried out. The copper / zinc enzyme SOD is mostly abundant in kidney and liver cells as well as erythrocytes. The major function of SOD is the cellular defense against oxidative damage, as it catalyzes the disproportionation of superoxide radicals to oxygen and hydrogen peroxide. This catalytic conversion takes place at the active site of the enzyme, which embeds the metal ions copper and zinc.[402,403] Several stability studies of $^{64}Cu^{II}$-labeled BFC-protein conjugates have shown transchelation of $^{64}Cu^{II}$ to SOD.[207,208] For this reason, STEPHAN and coworkers developed a new SOD stability assay,[182] which was also used in the study presented here. Briefly, a 3-fold excess of human SOD was added to the bispa complexes $^{64}Cu^{II}$-**B1a** and $^{64}Cu^{II}$-**B1b** and the samples were then incubated for 1 hour at 37 °C. The subsequent analysis was performed using non-reducing and non-denaturing polyacrylamide gel electrophoresis (native PAGE). After electrophoresis, the gel was examined by electronic autoradiography with a radioluminography laser scanner. The different blackening intensities of the bands correlate with the amount of copper-64, which dissociates from the ligand upon incubation with SOD and is subsequently bound to the enzyme.[182] Following autoradiography, the gels were stained with colloidal Coomassie G-250 to visualize the protein bands. A representative gel is depicted in **Figure 51** and the results obtained for $^{64}Cu^{II}$-**B1a** and $^{64}Cu^{II}$-**B1b** are given in **Table 14**. The results are compared to prominent literature-known copper(II) chelators studied by STEPHAN *et al.* to show the potential of the newly-developed SOD assay.[182] The corresponding experiments were carried out under the same conditions applied in this study and the results can hence be directly compared. The $^{64}Cu^{II}$-bispa complexes displayed high resistance towards transchelation to human SOD with less than 1 % of incorporation. These values are in the same range as those observed for N_2py_4 (**B3**) and all macrocyclic ligands under investigation. However, $^{64}Cu^{II}$-(***p*-MeO)B4** shows 4.3 ± 0.1 % transchelation ratio, which means that it is slightly less stable against SOD than the bispa complexes. In contrast, the acyclic radiolabeled chelator EDTA underwent an almost complete transchelation (85.4 ± 13.6 %) in the presence of SOD.[182]

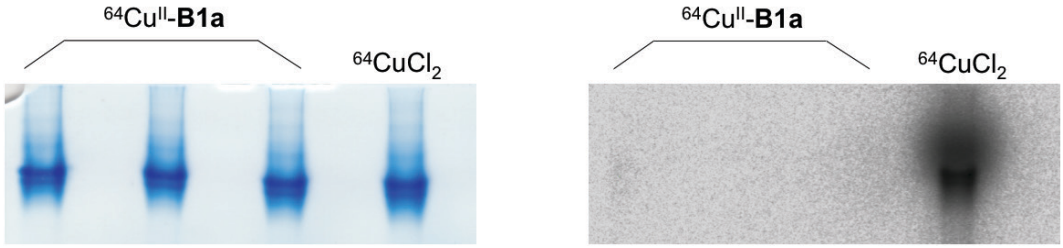

Figure 51. Analysis of $^{64}Cu^{II}$ transchelation to human erythrocyte superoxide dismutase (SOD) for $^{64}Cu^{II}$-**B1a**. Colloidal Coomassie stained native polyacrylamide gel (left) and autoradiography showing $^{64}Cu^{II}$-labeled bands of SOD (right). The respective analysis for $^{64}Cu^{II}$-**B1b** is shown in Appendix H.

Table 14. $^{64}Cu^{II}$ transchelation [% of control] to human erythrocyte superoxide dismutase (SOD) for various $^{64}Cu^{II}$-labeled ligands after 1 h. Each value is given as mean ± standard deviation of three measurements.

complex	transchelation [% of control]	ref
$^{64}Cu^{II}$-**B1a**	0.2 ± 0.1	
$^{64}Cu^{II}$-**B1b**	0.4 ± 0.1	
$^{64}Cu^{II}$-**B3**	0.7 ± 0.3	[173,177]
$^{64}Cu^{II}$-(***p*-MeO)B4**	4.3 ± 0.1	[172,177]
$^{64}Cu^{II}$-TETA	1.3 ± 0.6	[182]
$^{64}Cu^{II}$-DOTA	1.7 ± 1.3	[182]
$^{64}Cu^{II}$-NOTA	1.4 ± 0.7	[182]
$^{64}Cu^{II}$-cyclam	1.0 ± 0.5	[182]
$^{64}Cu^{II}$-DIAMSAR	0.6 ± 0.1	[182]
$^{64}Cu^{II}$-EDTA	85.4 ± 13.6	[182]

The ultimate *in vitro* stability test for radiometal ion complexes is the incubation of the compound in the presence of blood serum. In addition to the SOD challenge experiment described above, STEPHAN *et al.* also developed a complementary serum stability assay.[182] Instead of SOD, the radiolabeled ligands **B1a** and **B1b** were incubated with aliquots of human serum and the samples were analyzed by non-reducing sodium dodecyl sulfate (SDS) PAGE. The stained gels as well as the autoradiographic scans for $^{64}Cu^{II}$-**B1a** and $^{64}Cu^{II}$-**B1b** are shown in **Figure 52** and Appendix H. The prominent protein band in the size range of approximately 65 kDa most likely corresponds to $^{64}Cu^{II}$-labeled serum albumin. Other serum proteins with high affinity for copper(II) are not visible,

possibly due to their predominantly low abundance in human serum and the rather low activities of $^{64}CuCl_2$ used in the experiments.[182] Quantitative analysis of the band intensities revealed 17.8 ± 1.1 % transchelation to human serum proteins for $^{64}Cu^{II}$-**B1a** and 6.0 ± 1.1 % for $^{64}Cu^{II}$-**B1b**. These high values were surprising, considering that the stability of radiolabeled ligands in SOD is usually observed to be in the same range as that in human serum.[182] Furthermore, the bands in the autoradiography were considerably smeared and this made the integration difficult. The autoradiography corresponding to the serum stability assay of $^{64}Cu^{II}$-**B1b** additionally shows a band at the top of the scan that cannot be assigned.

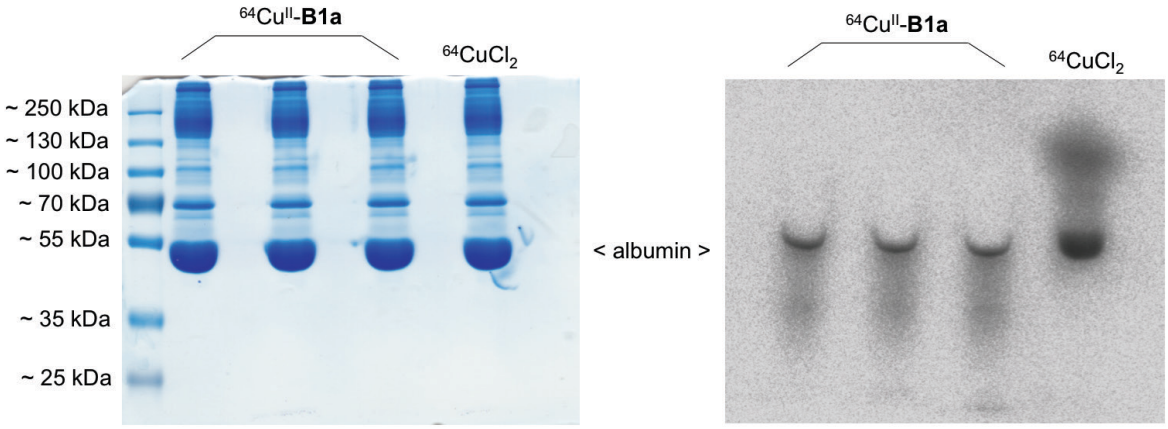

Figure 52. Analysis of $^{64}Cu^{II}$ transchelation to human serum proteins for $^{64}Cu^{II}$-**B1a**. Colloidal Coomassie stained native polyacrylamide gel (left) and autoradiography showing $^{64}Cu^{II}$-labeled bands of human serum proteins (right).

To validate the serum stability of $^{64}Cu^{II}$-**B1a** and $^{64}Cu^{II}$-**B1b** the respective experiments were repeated and then analyzed by radio-size exclusion chromatography (SEC) instead of gel electrophoresis. In both cases, the completely intact radiometal complexes (> 99 %) were eluted from the SEC column and no serum bound activity could be detected. This contradicts the results of the above-described serum challenge assays evaluated by gel electrophoresis. Finally, biodistribution studies were performed with the bispa-based complexes to provide clarity about their stability (see below).

Lipophilicity studies

Information about the lipophilicity of the $^{64}Cu^{II}$-labeled bispa ligands **B1a** and **B1b** were obtained using the shake-flask procedure.[189,190] The distribution ratio $D_{o/w}$ was determined as the concentration ratio of the respective $^{64}Cu^{II}$-bispa complexes between 1-octanol and

an aqueous phase at different pH. The distribution ratios are given as log $D_{o/w}$ values in **Table 15**. Similar to previously investigated bispidine systems,[172,173] the complexes $^{64}Cu^{II}$-**B1a** and $^{64}Cu^{II}$-**B1b** are quite hydrophilic. Therefore, comparative biodistribution behavior, *i.e.* fast blood clearance and renal excretion, are expected for the $^{64}Cu^{II}$-labeled bispa ligands. The log $D_{o/w}$ values of $^{64}Cu^{II}$-**B1b** with a positive overall charge of one and of the twice positively charged $^{64}Cu^{II}$-**B3** are in the same range.[173] Reduction of the C9 keto group leads to a slight increase of hydrophilicity, which can be seen by comparison of the $^{64}Cu^{II}$-bispidine complexes based on **B3** and **B6**.[173] The *para*-methoxy substitution of the pyridine groups in **(*p*-MeO)B4**, on the other hand, decreases the hydrophilicity.[172] Note that an efficient QSPR model was developed by COMBA *et al.* for the prediction of lipophilicities / hydrophilicities.[188,404]

The distribution ratios of $^{64}Cu^{II}$-**B1a** are clearly more negative than those of $^{64}Cu^{II}$-**B1b**. This can be explained by the structural differences of the two copper(II) complexes, thoroughly discussed in Chapter 4.1. The lipophilic behavior of compounds is correlated to the respective charge distributions. The copper(II)-carboxylate bond length in the solid state structure of Cu^{II}-**B1a** is 2.3127(12) Å and therefore significantly larger than the respective distance in Cu^{II}-**B1b** with 2.0119(11) Å. In several spectroscopic studies it could be shown that the structures determined by X-ray analysis are preserved in solution. The positive charge at the central copper(II) ion and the negative charge of the carboxylate are apparently more separated in Cu^{II}-**B1a** resulting in a more hydrophilic complex.

Table 15. Distribution ratios log $D_{o/w}$ of $^{64}Cu^{II}$-bispidine complexes at different pH.

bispidine ligand	log $D_{o/w}$ at pH			ref
	7.2	7.4	7.6	
Hbispa^{1a} (**B1a**) [(a)]	-3.79 ± 0.02	-3.78 ± 0.02	-3.77 ± 0.02	
Hbispa^{1b} (**B1b**) [(a)]	-2.70 ± 0.02	-2.74 ± 0.02	-2.74 ± 0.02	
N_2py_4 (**B3**)	-2.73	-2.77	-2.69	[173]
B6	-2.89	-2.88	-2.85	[173]
(*p*-MeO)B4	-2.49	-2.44	-2.42	[172]

[(a)] Values are given as mean ± standard deviation of four measurements.

Biodistribution

The stability of the $^{64}Cu^{II}$-bispa complexes $^{64}Cu^{II}$-**B1a** and $^{64}Cu^{II}$-**B1b** was additionally tested in biodistribution studies on male Wistar Kyoto rats. The radiolabeled bispa ligands were injected into the tail vain of the rats and the animals were sacrificed 5 minutes, 30 minutes, and 24 hours post injection (p.i.). Organs and tissues of interest were rapidly excised, weighed, and the accumulated radioactivity determined using a γ counter. When uncomplexed copper(II) ions in the form of $^{64}CuCl_2$ are injected, an accumulation of radioactive species is observed in the liver, intestine and kidneys.[173] The biodistribution pattern of $^{64}Cu^{II}$-**B1a** and $^{64}Cu^{II}$-**B1b**, in contrast, show fast elimination *via* the kidney and no significant accumulation in other organs or tissues. The $^{64}Cu^{II}$ radioactivity concentration was calculated as either the percentage of the injected dose per gram (%ID/g) or, for stomach, intestine, feces and urine, the percentage of injected dose (%ID). The biodistribution and elimination data of $^{64}Cu^{II}$-**B1a** and $^{64}Cu^{II}$-**B1b** are depicted in **Figure 53** and **Figure 54**, and additionally given in Appendix H. Except for the kidneys, the activity uptake was less than 1 %ID/g tissue and this activity was eliminated after 24 hours. As expected from the lipophilicity studies the $^{64}Cu^{II}$-bispa complexes are rapidly excreted *via* the renal pathway, *i.e.* kidneys and urine. Furthermore, the biodistribution shows no signs for demetalation of the complexes *in vivo*. On the contrary, they appear to be highly stable and this is in agreement with the results of the serum assays analyzed by radio-SEC.

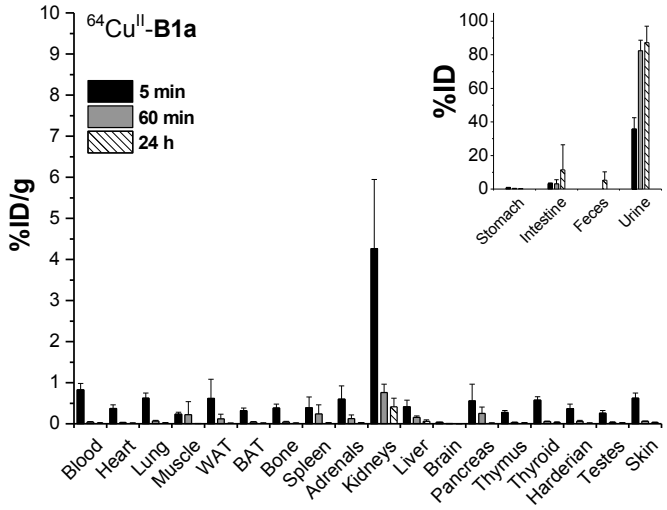

Figure 53. Biodistribution pattern of the $^{64}Cu^{II}$ complex based on **B1a** at 5 min, 60 min, and 24 h p.i. (four Wistar Kyoto rats per time point and compound, mean value ± standard deviation); graphs provided by Prof. Dr. Jens PIETZSCH.

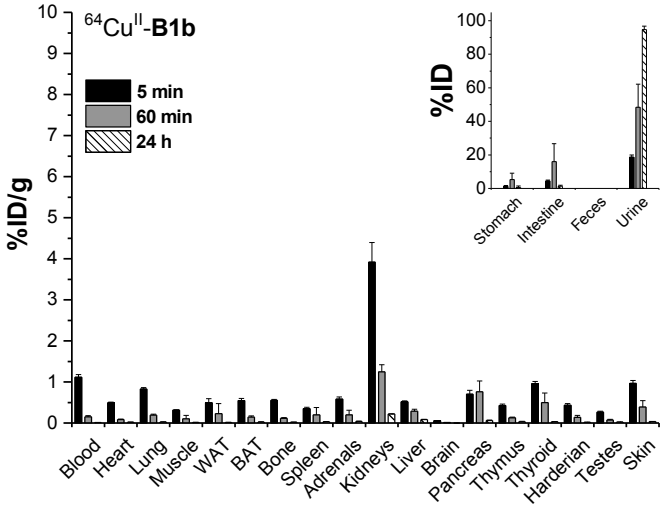

Figure 54. Biodistribution pattern of the $^{64}Cu^{II}$ complex based **B1b** at 5 min, 60 min, and 24 h p.i. (four Wistar Kyoto rats per time point and compound, mean value ± standard deviation); graphs provided by Prof. Dr. Jens PIETZSCH.

4.2.2 Radiochemistry with gallium(III)-68

The radiochemical studies with gallium(III)-68 were also performed at the Institute of Radiopharmaceutical Cancer Research of the Helmholtz Zentrum Dresden-Rossendorf (HZDR). Except for the animal studies, the experiments were carried out in the group of Dr. Holger STEPHAN by Madlen MATTERNA and Dr. Kristof ZARSCHLER with assistance of Miriam STARKE. The biodistribution studies were performed by Prof. Dr. Jens PIETZSCH and coworkers.

Radiolabeling experiments

Initial radiochemical investigations with gallium(III)-68 were performed using the bispa ligand **B1a**. In the course of the radiolabeling studies different temperatures, ligand concentrations and activities were tested. The degree of radiolabeling was monitored by radio-TLC, allowing the clear separation of uncomplexed $^{68}Ga^{III}$ and $^{68}Ga^{III}$-**B1a**. As **B1a** could not be radiolabeled with $^{68}Ga^{III}$ at room temperature, the experiments were performed at 37 °C while mixing the samples with 750 revolutions per minute (rpm) in a thermomixer. It was found that 30 µg ligand per 300 µL buffer solution (~10^{-4} M) were quantitatively radiolabeled with ~65 MBq $^{68}GaCl_3$ within 30 minutes. At lower ligand concentrations of ~5•10^{-4} to 5•10^{-6} M only incomplete radiolabeling was observed under the described conditions and with 0.3 µg **B1a** (~10^{-6} M) the radiochemical yield (RCY) dropped to 0 %. The molar activity of **B1a** was calculated based on an experiment with 1.5 µg ligand (~5•10^{-6} M) and 47.6 MBq $^{68}GaCl_3$. After 15 minutes 55 % RCY were determined and this corresponds to a molar activity of ~12 GBq/µmol for **B1a**. For radiolabeling with starting activities of 80 MBq and higher, the reaction temperature had to be increased to 50 °C.

Competition assays

The stability of $^{68}Ga^{III}$-**B1a** was investigated in the presence of either EDTA (**L9**) or human serum. For the EDTA challenge experiment, **B1a** was first radiolabeled with $^{68}GaCl_3$ and then incubated with a 10-fold molar excess of EDTA at ambient temperature. The degree of transchelation was determined by radio-TLC after 1, 2 and 4 hours. At all time points the amount of radioactivity bound to EDTA was less than 1 %, which shows that $^{68}Ga^{III}$-**B1a** is stable against EDTA.

A serum stability assay similar to those described for $^{64}Cu^{II}$ complexes was also performed with $^{68}Ga^{III}$-**B1a**.[182] Radiolabeled **B1a** was incubated in the presence of human serum for 1 hour at 37 °C and the samples were then analyzed by gel electrophoresis and subsequent autoradiography. The stained gel and the autoradiographic scan are depicted in **Figure 55**. Blood serum contains the glycoprotein transferrin which possesses two iron binding sites. Due to the close similarity of Fe^{III} and Ga^{III}, transferrin also displays high affinity to the latter metal ion.[223,224] The intense band in the autoradiography of the gel can be assigned to human transferrin, which has a molecular weight of about 73 kDa.[405] Quantitative analysis of the bands revealed that 56.2 ± 2.6% of the gallium(III)-68 activity initially coordinated to **B1a** was now bound to transferrin. Even though $^{68}Ga^{III}$-**B1a** showed no transchelation in the presence of EDTA, the complex is not stable against human serum.

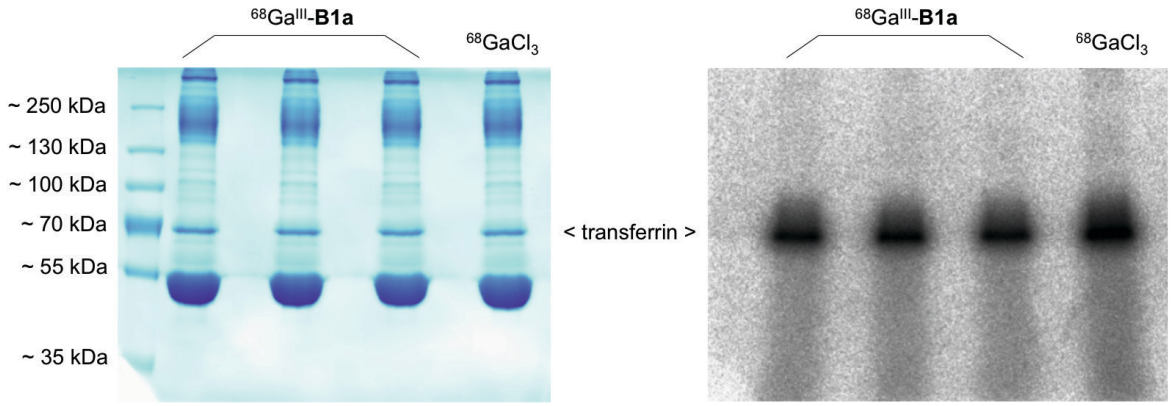

Figure 55. Analysis of $^{68}Ga^{III}$ transchelation to human serum proteins for $^{68}Ga^{III}$-**B1a**. Colloidal Coomassie stained native polyacrylamide gel (left) and autoradiography showing $^{68}Ga^{III}$-labelled bands of human serum proteins (right).

Biodistribution

Analogous to the experiments described above for copper-64, a biodistribution study was performed with $^{68}Ga^{III}$-**B1a**. The amount of activity in the organs and tissues was determined 5 and 60 minutes after intravenous application of the radiolabeled ligand. The values were calculated in %ID/g or %ID and are given in **Figure 56** and Appendix H. In contrast to the biodistribution pattern of the $^{64}Cu^{II}$-bispa complexes, the data collected for $^{68}Ga^{III}$-**B1a** show substantial activity uptake in most tissues. In addition, the activity is not significantly eliminated from the organism, but rather increases in some parts, for example in the white adipose tissue (WAT) and the bone. The biodistribution and elimination behavior of $^{68}Ga^{III}$-**B1a** is in agreement with the low stability of the complex in the

presence of human serum (see above). Due to these results no further stability studies with gallium(III) bispa complexes were performed and the isomeric bispa ligand **B1b** was also not investigated in radiochemical studies.

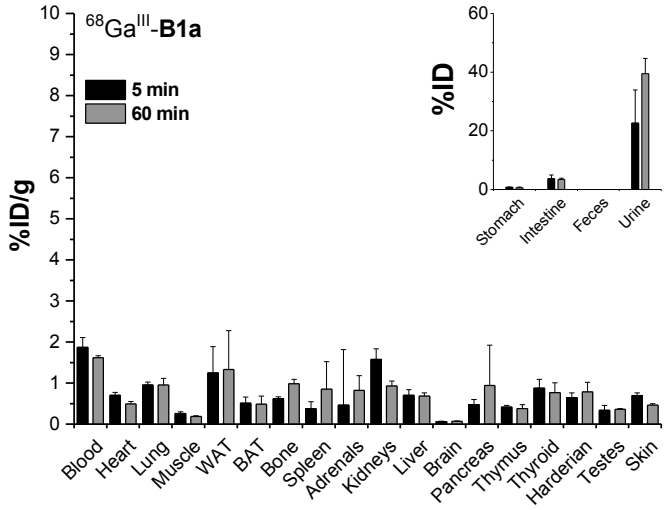

Figure 56. Biodistribution pattern of the $^{68}Ga^{III}$ complex based on **B1a** at 5 min and 60 min p.i. (four Wistar Kyoto rats per time point and compound, mean value ± standard deviation); graphs provided by Prof. Dr. Jens PIETZSCH.

4.3 Conclusion

In Chapter 4.1 the coordination chemistry of the hexadentate bispa ligands **B1a**, **(*p*-MeO)B1a**, and **B1b** was investigated with the metal ions cobalt(II), nickel(II), copper(II), zinc(II), and gallium(III). Extensive structural and spectroscopic studies of the metal bispa complexes were performed and discussed with regard to nuclear medicine applications. The isomeric bispa ligands **B1a** and **B1b** were then further examined with the PET nuclides copper-64 and gallium-68.

Bispa ligand **B1a** could not be radiolabeled with gallium(III)-68 at room temperature, but a labeling procedure at 37 °C was developed, which is compatible with the use of biological vectors. Challenge experiments with $^{68}Ga^{III}$-**B1a** revealed that the complex is stable in the presence of EDTA (**L9**). However, incubation of $^{68}Ga^{III}$-**B1a** with human serum resulted in 56.2 ± 2.6% transchelation to transferrin after 1 h at 37 °C. The low stability of $^{68}Ga^{III}$-**B1a** was also confirmed by biodistribution studies in rats. The bispa system hence proved to be inadequate for application as a $^{68}Ga^{III}$-chelating unit in nuclear medicine. Due to these results no further studies with the bispa ligands and gallium(III)-68 were performed. Because the presence of only one oxygen donor seems to be insufficient for stable complexation of gallium(III), our group is currently working on improved bispidine ligands for this specific metal ion.

The $^{64}Cu^{II}$-bispa complexes, on the other hand, showed very promising properties including fast radiolabeling, high stability, and favorable biodistribution behavior. In radiolabeling experiments, molar activities as high as ~100 and ~200 GBq/µmol were determined for $^{64}Cu^{II}$-**B1a** and $^{64}Cu^{II}$-**B1b**, respectively. Stability assays in the presence of EDTA, cyclam (**L3**), SOD and human serum revealed no transchelation of $^{64}Cu^{II}$ to the competing ligands or proteins. The results of these *in vitro* studies were confirmed by biodistribution experiments showing very rapid blood and normal-tissue clearance of both $^{64}Cu^{II}$-bispa complexes. The high stability of the complexes *in vitro* and *in vivo* is in agreement with their formation constants determined by potentiometric titration. The thermodynamic stability constants log β are 18.9 for Cu^{II}-**B1a** and 19.4 for Cu^{II}-**B1b** and this correlates with the respective $Cu^{II/I}$ redox potentials of –1.02 and –1.17 V *vs.* fc/fc^{+}. Based on these results, **B1b** appears to be a slightly better ligand than **B1a**. However, a parameter more relevant for *in vivo* applications than log β is the pM value at pH 7.4 (pM = –log $[M^{n+}]$). According to the calculated pM values of 19.3 and 18.7 for Cu^{II}-**B1a** and Cu^{II}-**B1b**, respectively, the stability order is reversed. Furthermore, the lipohilicity studies showed that $^{64}Cu^{II}$-**B1a** is slightly more hydrophilic than $^{64}Cu^{II}$-**B1b** and this is preferable

with regard to radiopharmaceutical applications. In summary, the hexadentate bispa system was shown to be a promising platform for the development of new $^{64}Cu^{II}$ PET tracers.

5 Investigation of the octadentate bispa ligand[vi]

Bispidines represent an emerging ligand family for radiopharmaceutical applications, whereby the focus so far has been on acyclic hexadentate and macrocyclic tetradentate ligand systems and their Cu^{II} complexes.[172,173,218,346] In Chapter 3.2 the synthesis and characterization of the potentially octadentate bispa ligand H_2bispa^2 (**B2**) was reported. In this chapter studies on the complexation behavior of the N_6O_2-type ligand **B2** with non-radioactive In^{III}, Lu^{III}, and La^{III} are presented. The corresponding metal complexes were studied by nuclear magnetic resonance (NMR) spectroscopy, high resolution mass spectrometry (HR-MS), elemental analysis (EA), solid state X-ray analysis and potentiometric titrations. The coordination chemistry of **B2** with La^{III} was thought to be of interest due to some similarities of La^{III} and Ac^{III}, which does not have any stable isotope.[284] However, in terms of covalency, *i.e.* electronics and donor preference, there is a significant difference between lanthanides and actinides.[285-287] In addition to the "cold chemistry", radiolabeling and radiostability studies were performed with $^{111}In^{III}$, $^{177}Lu^{III}$, and $^{225}Ac^{III}$ to evaluate the potential of **B2** for the application as a chelator in nuclear medicine.

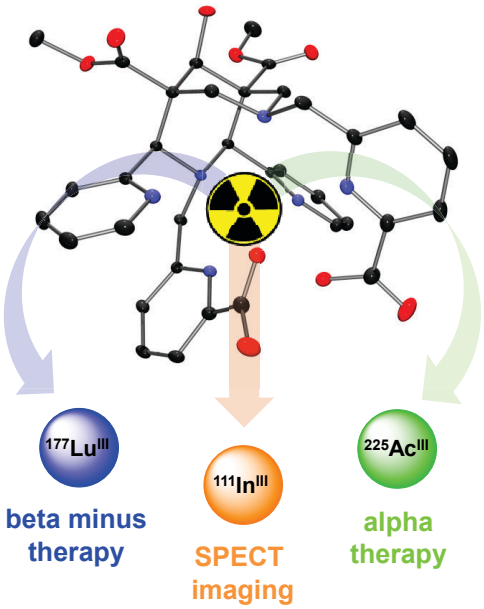

Figure 57. Representation of the radiochemical investigation of bispa ligand **B2** with the radioactive metal ions $^{111}In^{III}$, $^{177}Lu^{III}$, and $^{225}Ac^{III}$.

[vi] Parts of this chapter will be published in P. Comba, U. Jermilova, C. Orvig, B. O. Patrick, C. F. Ramogida, K. Rück, C. Schneider, M. Starke, *Chem. Eur. J.*, *submitted manuscript.*

5.1 Coordination chemistry of the octadentate bispa ligand

5.1.1 Characterization of metal-bispa^2 complexes

In the light of potential radiopharmaceutical applications, the coordination chemistry of H_2bispa^2 (**B2**) with In^{III}, Lu^{III}, and La^{III} was studied. To this end, equimolar solutions of the ligand and the respective metal salts in methanol (Lu^{III} and La^{III}) or in a mixture of methanol and water (In^{III}) were combined. With In^{III} and Lu^{III} the respective metal acetates were used, where acetate acts as a base for the deprotonation of the ligand. For the synthesis of the La^{III} complex, the chloride was used instead of the acetate salt and, therefore, diluted sodium hydroxide solution was added. The formation of the metal complexes was confirmed by HR-MS as well as ^{1}H- and ^{13}C-NMR spectroscopy. Two-dimensional NMR correlation experiments (^{1}H-^{1}H and ^{1}H-^{13}C) were used to assign the signals unambiguously.

The picolinate and pyridine donors of the ligand can rotate freely, leading to a simple ^{1}H-NMR spectrum (see Experimental Section and Appendix A). Upon coordination of the free ligand to the metal ions, significant changes in chemical shifts and coupling patterns of the NMR spectra are observed. The ^{1}H-NMR spectrum of the $[La^{III}(\mathbf{B2})]^+$ (La^{III}-**B2**) complex displays sharp and well-resolved diastereotopic splitting of the methylene protons associated with the picolinic acid arms. In addition, all previously equivalent sets of protons show different chemical shifts. A slightly different but altogether similar splitting pattern can be observed in the ^{1}H-NMR spectrum of the corresponding Lu^{III} complex. In contrast, the ^{1}H-NMR of the $[In^{III}(\mathbf{B2})]^+$ (In^{III}-**B2**) complex reveals changes in chemical shifts but shows no additional splitting of the signals. Furthermore, some peaks in the spectra of the complex become broad in comparison to the free ligand, suggesting some sort of fluxional behavior in solution.

Crystals of the In^{III} complex suitable for solid state X-ray analysis were obtained by slow evaporation from a methanolic solution. The complex cation $[In^{III}(\mathbf{B2})]^+$ crystallizes with one trifluoroacetate (TFA) as counterion and four molecules of water in the asymmetric unit. The central In^{III} ion is coordinated by seven donor atoms of the doubly deprotonated N_6O_2-type ligand, with bond lengths between 2.200(1) Å for In-Npa3 and 2.486(1) Å for In-N3. The pyridine nitrogen Npy1 has an In-Npy1 distance of 3.1073(11) Å and might hence be described as semi-coordinating since the pyridine lone pair is oriented towards the metal ion and efficiently shields the metal center from other donor groups, such as coordinating solvents or anions. The solid state structure of the complex cation $[In^{III}(\mathbf{B2})]^+$

is depicted in **Figure 58** and the corresponding structural and crystallographic data are presented in **Table 16** and Appendix B.

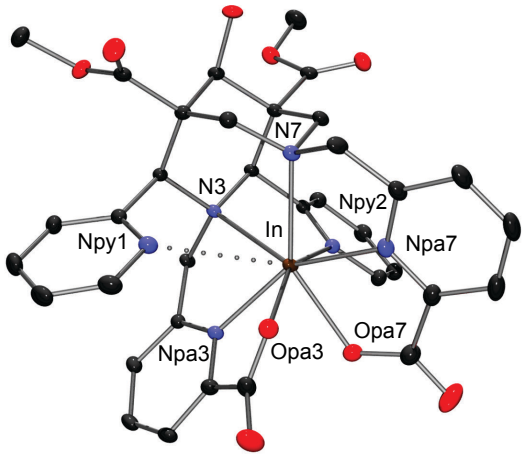

Figure 58. ORTEP plot of the complex cation of [In^{III}(**B2**)](TFA). Ellipsoids are shown at the 50 % probability level; co-crystallized solvent molecules, counterions, and hydrogen atoms are omitted for clarity.[256]

Table 16. Selected bond distances of H_2bispa^2 (**B2**) and [In^{III}(**B2**)](TFA).

	H_2bispa^2 (**B2**)	[In^{III}(**B2**)](TFA)
distance [Å]		
In-N7		2.3867(10)
In-N3		2.4859(10)
In···Npy1		3.1073(11)
In-Npy2		2.3784(10)
In-Npa7		2.2201(10)
In-Opa7		2.2599(9)
In-Npa3		2.2000(10)
In-Opa3		2.2270(9)
N3···N7	2.766(3)	2.9355(14)
Npy1···Npy2	4.679(3)	5.0052(15)

The elemental analysis of the In^{III}-**B2** complex confirms the presence of water molecules in the solid sample. For the corresponding Lu^{III} and La^{III} complexes, no crystals suitable

for X-ray crystallography were obtained. However, NMR and HR-MS as well as the elemental analyses of the compounds confirm structures similar to the corresponding In^{III} complex, *i.e.* a 1:1 metal ion to ligand complex with TFA as a counterion and several water molecules.

5.1.2 Potentiometric titrations

The thermodynamic stabilities of the In^{III}-, Lu^{III}- and La^{III}-complexes based on **B2** were measured by potentiometric titration (H_2O, 25 °C, 0.1 M KCl), and the respective constants are listed in **Table 17**. While for Lu^{III} and La^{III} the stability constants were accessible by direct titration of equimolar ligand / metal ion solutions, a competing ligand was needed to determine the stability of the In^{III}-**B2** complex. The acyclic chelator EDTA (**L9**) was used for the ligand-ligand competition titrations (see Experimental Section for details).

Table 17. Metal complex stability constants (log β) and $pM_{7.4}$ values of **B2** (H_2O, 25 °C, 0.1 M KCl).

model [a]	In^{III} [b]	Lu^{III}	La^{III}
ML	24.39(6)	8.51(3)	11.42(6)
MLH		12.60(22)	15.49(13)
MLH_2		16.35(11)	
MLH_{-1}			0.50(4)
$pM_{7.4}$ [c]	25.0	9.1	12.0

[a] L denotes the respective ligand with completely deprotonated basic centers; the charges of the species are omitted for clarity. [b] Formation of InL was determined by ligand-ligand competition titrations. [c] Calculated for 10 µM total ligand and 1 µM total metal ion concentration at pH 7.4 and 25 °C.

The formation constants $\log \beta_{ML}$ and pM values ($pM = -\log [M^{n+}]$ at pH 7.4) for In^{III} complexes with several selected chelators are summarized in **Table 18**. The logarithmic stability constant of the In^{III}-**B2** complex is 24.4 and therefore significantly larger than the respective stability constant observed for the In^{III}-transferrin complex (18.3). The iron-binding human serum protein is a main *in vivo* competitor for In^{III}.[406] Compared to other ligand systems relevant for nuclear medicine, In^{III}-**B2** was found to have a higher stability constant than $[In^{III}(DOTA)]^-$ (23.9),[250] but to be less stable than $[In^{III}(DTPA)]^{2-}$ (29.0)[407] and $[In^{III}(octapa)]^-$ (26.8).[158] In this context, it is interesting to note

that In^{III}-DOTA is significantly more stable *in vivo* than In^{III}-DTPA, even though the log β_{ML} and $pM_{7.4}$ values for In^{III}-DTPA are much higher than for the corresponding DOTA complex.[48] This demonstrates that these thermodynamic parameters can provide initial insight into the stability of metal ion complexes, but cannot be correlated directly with their *in vivo* behavior, where inertness rather than stability are of importance (kinetics *vs.* thermodynamics). In addition, hydrolysis plays a major role considering the nM to pM concentrations of the complexes in comparison to the relatively high concentrations of hydroxides at physiological pH. The complex stabilities log β_{ML} of the complexes Lu^{III}-**B2** and La^{III}-**B2** were also determined and are relatively small (8.5 and 11.4 respectively) in comparison to the corresponding complexes with other chelators (see Appendix C). The species distribution diagrams of **B2** in the presence of the investigated metal ions are shown in Appendix C.

Table 18. Stability constants (log β_{ML}) and $pM_{7.4}$ values for selected In^{III} complexes.

ligand	log β_{ML}	$pM_{7.4}$ [(a)]	ref
DOTA (**L5**)	23.9(1)	18.8	[158,250]
DTPA (**L10**)	29.0	25.7	[158,407]
H_4octapa (**L35**)	26.8(1)	26.5	[158]
transferrin	18.30	18.7	[158,406]
H_2bispa^2 (**B2**)	24.39(6)	25.0	

[(a)] Calculated for 10 µM total ligand and 1 µM total metal ion concentration at pH 7.4 and 25 °C.

5.2 Radiochemical investigations of the octadentate bispa ligand

The novel bispidine ligand H_2bispa^2 (**B2**) was investigated with the radioactive metal ions $^{111}In^{III}$, $^{177}Lu^{III}$, and $^{225}Ac^{III}$. These radiometal ions typically form complexes with chelators of high denticity, *i.e.* 7-12 coordinate, and are used for either diagnostic ($^{111}In^{III}$) or therapeutic ($^{177}Lu^{III}$ and $^{222}Ac^{III}$) purposes.[21,48] The radiochemical studies were carried out at the Tri University Meson Facility (TRIUMF), Canada's national laboratory for particle and nuclear physics and accelerator-based science in Vancouver. The radiolabeling and challenge experiments were performed by Dr. Caterina RAMOGIDA with assistance of Una JERMILOVA.

5.2.1 Radiolabeling experiments

Initial radiolabeling studies with $^{111}In^{III}$, $^{177}Lu^{III}$, and $^{225}Ac^{III}$ with **B2** were performed to assess the potential of the new octadentate bispidine as a ligand scaffold in nuclear medicine applications. The degree of radiolabeling was analyzed by radio-high performance liquid chromatography (radio-HPLC) or radio-thin layer chromatography (radio-TLC). Stringent mild and fast radiolabeling procedures were enforced throughout the initial experiments with all three nuclides in order to mimic the most favorable conditions employed in a radiopharmacy setting and which would be amenable to "kit-type" labeling. Room temperature, rapid labeling at low ligand concentrations is an important condition for new ligands under investigation in radiopharmaceutical applications, and would present a particular advantage compared to the "gold standard" macrocyclic ligand DOTA (**L5**), which often requires heating samples at elevated temperatures for extended periods of time. For example, many of the aforementioned "pa" ligands like H_2dedpa (**L30**) and H_4octapa (**L35**) have the ability to quantitatively complex several radiometal ions in 10 minutes at ambient temperature.

B2 was successfully radiolabeled with the commercially available SPECT isotope $^{111}In^{III}$ ($t_{1/2}$ = 2.8 d[27]) within 10 minutes at room temperature at ligand concentrations of ~10^{-4} to 10^{-7} M. The radiochemical yield (RCY) was determined by radio-HPLC to be > 99 %. A representative chromatogram is shown in **Figure 59**. Radiolabeling of $[^{111}In^{III}(\mathbf{B2})]^+$ ($^{111}In^{III}$-**B2**) yielded molar activities as high as ~70 GBq/µmol or 89 MBq/µg in 10 minutes at ambient temperature, when radiolabeled with 8.9 MBq $^{111}In^{III}$ at 10^{-7} M ligand. At **B2** ligand concentrations of 10^{-8} M, the radiolabeling yield dropped to 0 % after 10 minutes at ambient temperature. Note that the molar activity is usually determined under conditions

yielding RCYs of less than 99 %, otherwise the observed activity is typically underestimated. As no radiolabeling was observed when decreasing the ligand concentration to 10^{-8} M, this error should be negligibly small. The results for **B2** are comparable to those obtained for H_4octapa, which quantitatively complexes $^{111}In^{III}$ at ligand concentrations as low as 10^{-7} M.[158] Conversely, $[^{111}In^{III}(DOTA)]^-$ ($^{111}In^{III}$-DOTA) labeling at identical conditions resulted in only 40 % RCY.[158]

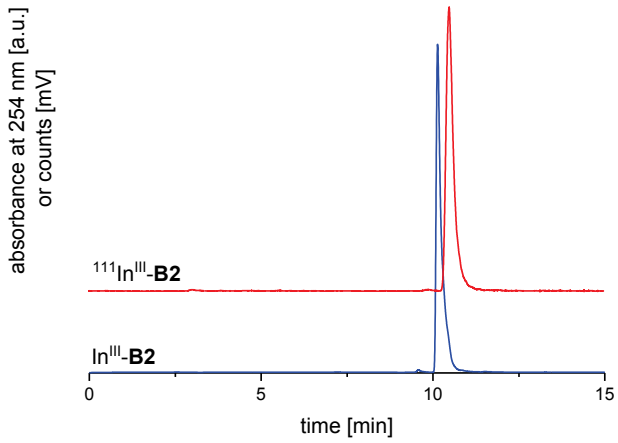

Figure 59. Representative HPLC radiochromatogram of $^{111}In^{III}$-**B2** (t_R = 10.5 min, red line) reacted for 10 minutes at ambient temperature (0.1 µg ligand, ~10^{-7} M, 8.9 MBq, pH 4), and corresponding UV chromatogram of non-radioactive In^{III}-**B2** (t_R = 10.1 min, blue line). Small differences in retention times of radioactive and non-radioactive complex are caused by the instrument setup, *i.e.* sequential arrangement of UV-vis detector followed by radiation detector.

Unlike the facile labeling kinetics observed for $^{111}In^{III}$, radiolabeling at 10^{-4} M **B2** with the β^- and γ emitter $^{177}Lu^{III}$ ($t_{1/2}$ = 6.7 d[27]) required gentle heating to 40 °C for 1 hour to obtain quantitative labeling (RCY > 99 %). Quantitative radiolabeling of DOTA was also achieved under analogous conditions (40 °C, 1 h). With the same ligand concentration of 10^{-4} M **B2** the RCY was 49 % after 15 minutes at room temperature (see **Figure 60**). Under these conditions, radiolabeling with 3.7 MBq $^{177}Lu^{III}$ yielded a molar activity of 10 MBq/µmol. Due to the inability of **B2** to quantitatively complex $^{177}Lu^{III}$ at ambient temperature at the highest ligand concentration, $^{177}Lu^{III}$ radiolabeling at lower ligand concentrations was not attempted.

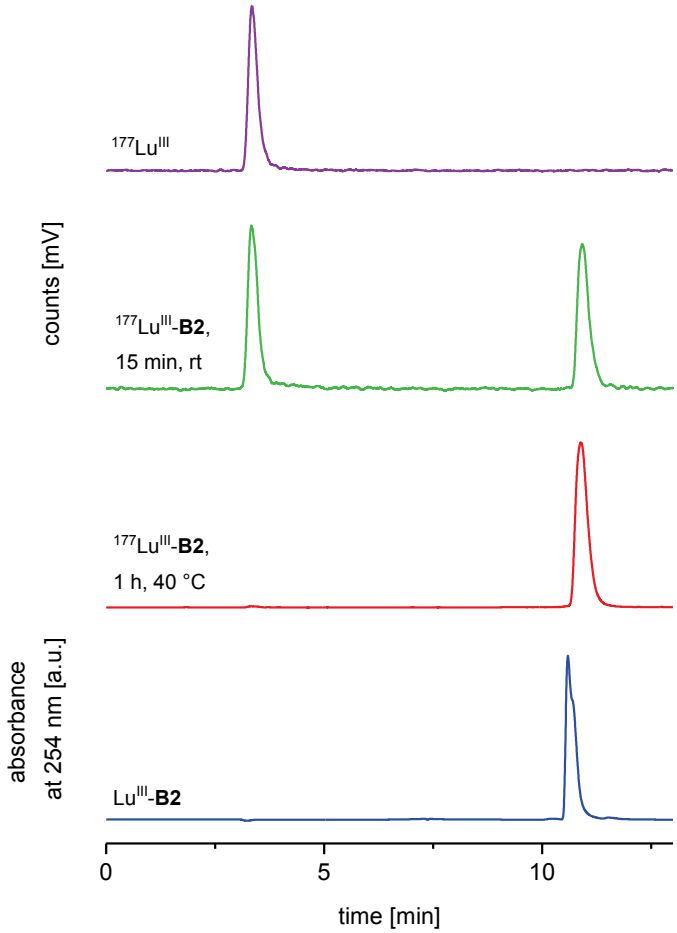

Figure 60. HPLC radiochromatograms of $^{177}Lu^{III}$-**B2** (t_R = 10.9 min). Reaction conditions: 100 µg of **B2**, 1 h, 40 °C (red line, RCY > 99 %); 100 µg of **B2**, 15 min, room temperature (green line, RCY = 49 %); 100 µg of **B2** as control (purple line, t_R of $^{177}Lu^{3+}$ = 3.3 min). Corresponding UV chromatogram of non-radioactive Lu^{III}-**B2** (t_R = 10.6 min, blue line). Small differences in retention times of radioactive and non-radioactive complex are caused by the instrument setup, *i.e.* sequential arrangement of UV-vis detector followed by radiation detector.

The α emitter ^{225}Ac ($t_{1/2}$ = 10.0 d[27]) is a promising candidate for labeling biomolecules in targeted α therapy (TAT). The high linear energy transfer (LET) of alpha particles renders their emitters ideal for treating small tumors with minimal chance of harming surrounding healthy tissue.[21] ^{225}Ac radiolabeling chemistry is further complicated by its decay scheme which goes through predominantly six daughters, including ^{221}Fr ($t_{1/2}$ = 4.9 min[27]) and ^{213}Bi ($t_{1/2}$ = 45.6 min[27]), meaning a chelator suitable for $^{225}Ac^{III}$ pharmaceuticals must stably bind the nuclide as well as control the fate of the daughters.[281] Preliminary room temperature $^{225}Ac^{III}$ labeling of **B2** was attempted at ligand concentrations of ~10^{-4} to 10^{-8} M in ammonium acetate buffer, pH 6. The radiochemical yield of $[^{225}Ac^{III}(\mathbf{B2})]^+$ ($^{225}Ac^{III}$-**B2**) was determined after 30 minutes by spotting an aliquot on TLC plates,

developing in an appropriate solvent (see Experimental Section), and counting the activity on the plates immediately and the following day. Measuring the TLC plates the following day was necessary in order to allow any initial $^{213}Bi^{III}$ to decay and calculate corrected $^{225}Ac^{III}$ radiolabeling yields. At ligand concentrations of ~10^{-4}, 10^{-5}, 10^{-6} and 10^{-8} M, $^{225}Ac^{III}$ RCYs were 98, 94, 64 and 2 %, respectively (see **Figure 61**). Radiolabeling of **B2** with 40 kBq $^{225}Ac^{III}$ hence yielded a molar activity of 20 MBq/µmol. These results present a substantial advantage over the current "gold standard" DOTA, which required heating samples above 60 °C in order to initiate $^{225}Ac^{III}$ labeling, even at the highest ligand concentration.

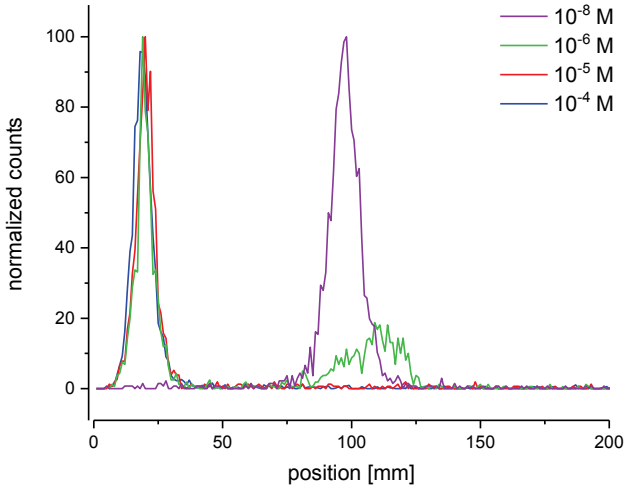

Figure 61. TLC radiochromatograms of $^{225}Ac^{III}$ labeling reactions at **B2** ligand concentrations of 10^{-4} (blue line), 10^{-5} (red line), 10^{-6} (green line), and 10^{-8} (purple line), reacted for 30 min at ambient temperature, pH 6. Peaks centered at 20 mm correspond to $^{225}Ac^{III}$-labeled species; peaks above 60 mm correspond to uncomplexed $^{225}Ac^{III}$.

5.2.2 Competition assays

Serum contains many endogenous proteins, such as transferrin and metallothionein, which can compete for and displace chelator-bound metal ions *in vivo*. As such, any radiometal-ligand complex must be able to withstand transchelation to such proteins in order to successfully deliver the radiotracer to the desired molecular target. To investigate the stability of the $^{111}In^{III}$-, $^{177}Lu^{III}$- and $^{225}Ac^{III}$-**B2** complexes, a competition experiment was performed in the presence of excess human serum. This assay is a popular method to predict the *in vivo* inertness of radiometal ion complexes.

In addition to human serum, the $^{225}Ac^{III}$-**B2** complex was challenged *via* a La^{III} competition experiment. Because of their similar ionic radii, La^{III} (103-116 ppm, CN = 6-9) and Ac^{III} (112 ppm, CN = 6)[148] are often considered chemical surrogates.[284] Despite fundamental differences in coordination chemistry among trivalent actinides and lanthanides,[285-287] using non-radioactive metal ions such as La^{III} as a competitor is a straightforward and widely used method to probe the kinetic off-rate of a pre-formed actinium(III) complex,[288,408] since many ligands that bind Ac^{III} may also efficiently complex La^{III}.

For the serum stability assays the radiolabeled ligands were incubated in the presence of human serum at 37 °C. The degree of radiometal ion loss to serum proteins was then assayed by either size exclusion using PD-10 columns ($^{111}In^{III}$ and $^{177}Lu^{III}$ experiments) or by radio-TLC ($^{225}Ac^{III}$). The $^{111}In^{III}$-**B2** complex showed respectable stability with 88, 87, and 87 % of $^{111}In^{III}$ remaining chelate bound after 1 hour, 1 and 5 days against human serum at 37 °C (**Table 19**). These results suggest a small amount (~12 %) of the $^{111}In^{III}$ has been transchelated from the ligand to serum rapidly after one hour, but then the remaining $^{111}In^{III}$-**B2** complex remains stable over the following 1 and 5 day time points. Literature compounds $[^{111}In^{III}(octapa)]^-$ ($^{111}In^{III}$-octapa) and $^{111}In^{III}$-DOTA exhibited similar stabilities of 92 and 89 %, respectively, after 1 day.[158] Sampling after 5 days was not conducted in these experiments. $[^{177}Lu^{III}(\mathbf{B2})]^+$ ($^{177}Lu^{III}$-**B2**) was incubated and analyzed in human serum over 7 days, where the complex remained moderately stable after 1 hour and 1 day, with 89 and 86 % intact, respectively. Thereafter, a small drop in stability was seen at later time points, where 69 % of the $^{177}Lu^{III}$ complex remained intact after 7 days. The $[^{177}Lu^{III}(octapa)]^-$ ($^{177}Lu^{III}$-octapa) and $[^{177}Lu^{III}(DOTA)]^-$ ($^{177}Lu^{III}$-DOTA) complexes were previously found to be comparably stable to $^{177}Lu^{III}$-**B2** after 1 day in human serum (~87 % for both literature compounds).[409] Later time points of either the DOTA or octapa complexes were not analyzed. Therefore, it is unknown whether their respective $^{177}Lu^{III}$ complexes would also decline in stability over the course of 7 days. Finally, $^{225}Ac^{III}$-**B2** and "gold standard" $[^{225}Ac^{III}(DOTA)]^-$ ($^{225}Ac^{III}$-DOTA) were incubated with human serum for one week, and the complex stability was assayed at several stages. The $^{225}Ac^{III}$-**B2** complex was exceptionally stable over the course of 7 days remaining 89 % intact and this value is comparable to the 7 day stability of the "gold standard" $^{225}Ac^{III}$-DOTA (85 % intact).

Table 19. Radiometal ion complex stability in human serum (n = 3 for each $^{111}In^{III}$ complex and for $^{225}Ac^{III}$-**B2** , n = 2 for each $^{177}Lu^{III}$ complex and for $^{225}Ac^{III}$-DOTA).

complex	1 h [%]	1 d [%]	5 d [%]	7 d [%]	ref
$^{111}In^{III}$-**B2**	88.4 ± 1.2	87.4 ± 0.6	87.4 ± 1.5	ND [(a)]	
$^{111}In^{III}$-octapa	93.8 ± 3.6	92.3 ± 0.04	ND [(a)]	ND [(a)]	[158]
$^{111}In^{III}$-DOTA	89.6 ± 2.1	89.4 ± 2.2	ND [(a)]	ND [(a)]	[158]
$^{177}Lu^{III}$-**B2**	88.9 ± 1.1	86.1 ± 0.5	76.7 ± 0.01	68.8 ± 0.7	
$^{177}Lu^{III}$-octapa	88.1 ± 1.2	87.7 ± 0.7	ND [(a)]	ND [(a)]	[409]
$^{177}Lu^{III}$-DOTA	87.7 ± 0.7	87.4 ± 2.1	ND [(a)]	ND [(a)]	[409]
$^{225}Ac^{III}$-**B2**	97.4 ± 0.5	92.3 ± 0.7	90.7 ± 0.5 [(b)]	88.9 ± 2.8	
$^{225}Ac^{III}$-DOTA	93.9 ± 4.5	90.9 ± 5.6	91.1 ± 6.1	84.7 ± 8.1	

[(a)] ND = not determined. [(b)] Stability data at 3 days.

The La^{III} exchange competition experiment (**Table 20**) serves as an additional stability assay of the $^{225}Ac^{III}$-**B2** complex and is compared directly to the results obtained for $^{225}Ac^{III}$-DOTA, analyzed under equivalent conditions. The stability of the $^{225}Ac^{III}$-**B2** complex shows a very similar trend to the $^{225}Ac^{III}$-DOTA complex, *i.e.* 72 and 77 % of the initial complex remained intact after one week, respectively. Results of both the human serum and La^{III} exchange competition assays of the $^{225}Ac^{III}$ complex coupled with the mild and efficient radiolabeling protocol, suggest that **B2** is a promising chelator for Ac^{III} pharmaceuticals.

Table 20. $^{225}Ac^{III}$-ligand competition against La^{III} exchange with the values represented as % intact complex (5:1 La^{III} to ligand ratio added, n = 2).

complex	0.2 d [%]	1 d [%]	2 d [%]	3 d [%]	6 d [%]	7 d [%]
$^{225}Ac^{III}$-**B2**	95.5 ± 0.2	91.5 ± 0.7	88.8 ± 2.5	85.2 ± 1.7	74.4 ± 1.4	71.7 ± 2.7
$^{225}Ac^{III}$-DOTA	94.5 ± 3.5 [(a)]	94.9 ± 2.9	86.2 ± 3.1	ND [(b)]	ND [(b)]	77.1 ± 3.6

[(a)] Stability data at 0.08 days. [(b)] ND = not determined.

5.3 Conclusion

In this chapter the non-radioactive coordination chemistry of the novel octadentate bispidine ligand H_2bispa^2 (**B2**) was described, as well as its evaluation for radiopharmaceutical applications. Therefore, **B2** was reacted with the "cold" metal ions In^{III}, Lu^{III}, and La^{III} for structural and solution studies, after which the radiolabeling efficiencies and radiostabilities of **B2** with $^{111}In^{III}$, $^{177}Lu^{III}$, and $^{225}Ac^{III}$ were determined. The stability constants of the In^{III}-, Lu^{III}- and La^{III}-**B2** complex assessed by potentiometric titration are quite different from one another. However, the *in vitro* studies in the presence of human serum reveal similar stabilities for all radioactive metal-**B2** complexes. These findings show once again that thermodynamic parameters like complex stability constants cannot always be correlated with the behavior in such competition assays, especially considering the different experimental conditions.[158] Stabilities *vs.* human serum comparable or better to those of the corresponding metal-DOTA complexes were observed. Besides showing respectable stabilities, the complexes $^{111}In^{III}$-**B2** and $^{225}Ac^{III}$-**B2** can additionally be formed quantitatively at room temperature. This is particularly important, because long-lived radioisotopes like $^{111}In^{III}$ and $^{225}Ac^{III}$ are often used in combination with heat-sensitive antibodies as targeting vectors. The next steps towards the development of a bispa-based radiopharmaceutical will be the introduction of a suitable vector moiety into the bispidine scaffold and the *in vivo* evaluation of the resulting conjugate.

6 Conclusion and outlook

In the course of the present thesis various picolinic acid-based bispidine ligands were synthesized and evaluated regarding their putative application in nuclear medicine. By the introduction of picolinic acid groups into the bispidine scaffold, it was intended to improve the thermodynamic stability of the respective copper(II) bispidine complexes and to extend the spectrum of the bispidines to other radiopharmaceutically relevant metal ions. The bispidine ligands studied for $^{64}Cu^{II}$ PET imaging so far solely contained nitrogen donor atoms, as for example N_2py_4 (**B3**).[172,173] The incorporation of an anionic oxygen donor was hence meant to enable the new bispa ligands to also stably bind hard metal cations. Through the attachment of one or two picolinic acid moieties at the bispidine backbone, hexa- and octadentate bispa ligands were prepared (see **Figure 62** and **Figure 64**).

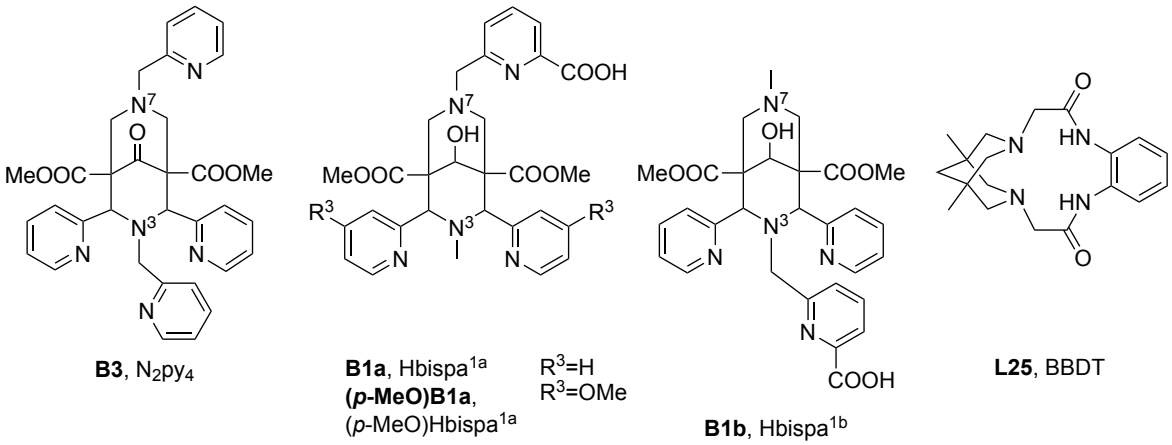

B3, N_2py_4 **B1a**, Hbispa[1a] **(*p*-MeO)B1a**, (*p*-MeO)Hbispa[1a] **B1b**, Hbispa[1b] **L25**, BBDT

Figure 62. Portfolio of bispidine-based ligand systems for nuclear medicine applications.[173,177]

First, the coordination chemistry of the isomeric hexadentate bispa ligands Hbispa[1a] (**B1a**) and Hbispa[1b] (**B1b**), as well as of the *para*-methoxy substituted **B1a** derivative (*p*-MeO)Hbispa[1a] (**(*p*-MeO)B1a**) was investigated with non-radioactive metal ions. To this end, the N_5O-type bispa ligands were reacted in complexation studies with cobalt(II), nickel(II), copper(II), zinc(II), and gallium(III). The resulting metal complexes were then characterized using standard structural and spectroscopic methods.

Due to the favorable nuclear properties of gallium(III)-68 ($t_{1/2}$ = 1.1 h[27], β^+ emission), the bispa ligand **B1a** was evaluated in initial radiolabeling and stability studies with this radionuclide. Quantitative radiolabeling of **B1a** with $^{68}Ga^{III}$ was achieved after increasing

the reaction temperature from 25 °C to 37 °C. In addition, the radiolabeled complex $^{68}Ga^{III}$-**B1a** was shown to be unstable in the presence of human serum as well as in biodistribution experiments in rats. As a consequence of the inadequate stability of the $^{68}Ga^{III}$-bispa complex no further studies with gallium(III)-68 were performed. The presence of one hard donor group is obviously insufficient for the stable coordination of the hard metal ion Ga^{III}. Therefore, novel bispidine ligands are currently being developed for this specific metal ion. There are several possible approaches including the evaluation of other substituents like carboxylic acids and phosphonic acids at the bispidine backbone as well as the preparation of heptadentate ligand systems.

Building on the promising results obtained for the all-N bispidine systems,[172,173] the hexadentate bispa ligands were also evaluated with the PET nuclide copper(II)-64 ($t_{1/2}$ = 12.7 h[27], β^+ emission). Prior to the radiochemical studies, the non-radioactive copper(II) bispa complexes were investigated using X-ray crystallography, UV-vis-NIR and ESR spectroscopy, cyclovoltammetry, and potentiometry. These analyses pointed to a high preorganization of the bispa ligands for copper(II) complexation as well as to a high stability of the resulting complexes. The formation constants $\log \beta_{CuL}$ determined by potentiometric titrations were ~19 for the copper(II) complexes based on **B1a** and **B1b** and hence roughly three orders of magnitude larger than the value for Cu^{II}-**B3** of 16.3.[302] The high complex stability was confirmed by *in vitro* challenge experiments with the respective radiolabeled ligands. No demetallation was observed, neither after incubation with an excess of the competing ligands cyclam (**L3**) and EDTA (**L9**) nor in the presence of SOD or human serum. In addition, biodistribution studies with the $^{64}Cu^{II}$-bispa complexes in rats revealed excellent *in vivo* stability as well as favorable clearance behavior. Furthermore, the bispa ligands could be radiolabeled with copper(II)-64 in only 5 minutes at ambient temperature with molar activities as high as ~100-200 GBq/µmol. These results are very promising regarding the putative application of bispa ligands as part of radiopharmaceuticals. As the $^{64}Cu^{II}$ complex based on **B1a** was found to be the most hydrophilic, the focus of future research will be on this specific bispa ligand. The next crucial step towards the development of a bispa-based radiopharmaceutical should now be the functionalization of the ligand scaffold with a suitable group for coupling to biological vectors like peptides and antibodies. Current work concentrates on the introduction of a *p*-isothiocyanatobenzyl group *via* the C9 alcohol of the bispidine scaffold, which can subsequently be conjugated to an amine group of the respective vector moiety (see **Figure 63**). The resulting radiolabeled bispa-vector conjugate then needs to be further investigated in studies on tumor-bearing animals in order to evaluate its targeting and accumulation properties.

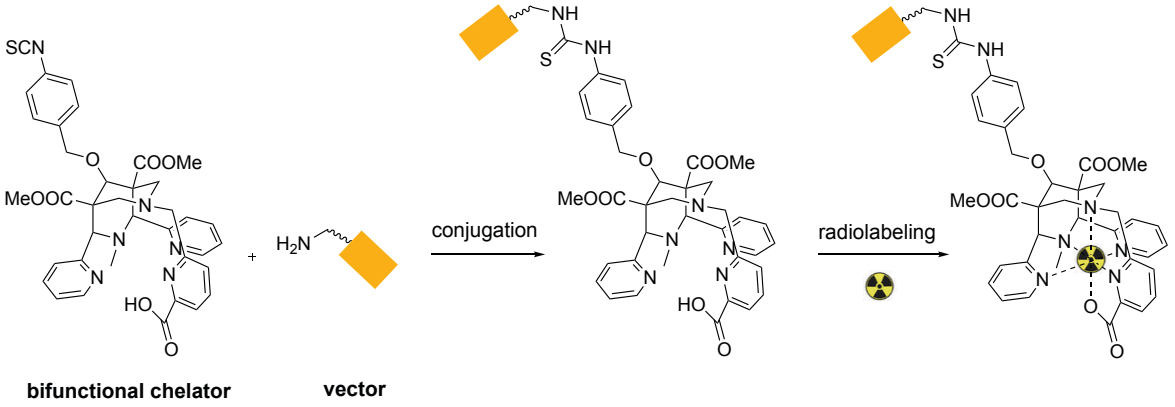

Figure 63. Illustration of the conjugation of a potential bifunctional bispa ligand to a vector moiety followed by labeling of the conjugate with a radiometal ion.

With the novel hexadentate bispa ligands, the portfolio of bispidine-based compounds now includes neutral chelators (**B3** and others[172,173]) as well as systems with negative charges of –1 (bispa ligands) and –2 (macrocycle **L25**, BBDT[177]) in their deprotonated form (see **Figure 62**). The corresponding copper(II) complexes consequently display overall charges of +2, +1, and 0, respectively. As the hydrophilicity and the charge of a substance strongly influence the *in vivo* behavior, it is highly convenient for radiopharmaceutical applications to have the possibility to choose from such a broad ligand spectrum.

The octadentate bispa ligand H_2bispa^2 (**B2**) was studied with radionuclides relevant for therapeutic and diagnostic purposes, *i.e.* $^{111}In^{III}$ ($t_{1/2}$ = 2.8 d[27], emission of γ rays and AUGER electrons), $^{177}Lu^{III}$ ($t_{1/2}$ = 6.7 d[27], β^- particles and γ rays), and $^{225}Ac^{III}$ ($t_{1/2}$ = 10.0 d[27], α particles). The coordination chemistry of the N_6O_2-type bispa ligand was first investigated with the non-radioactive metal ions indium(III), lutetium(III), and lanthanum(III). In **Figure 64** the complexation reaction of **B2** and In^{III} to [In^{III}(bispa^2)](TFA) (In^{III}-**B2**) is shown. The central indium(III) ion is coordinated by eight ligand donor atoms, whereby one metal-donor distance is elongated.

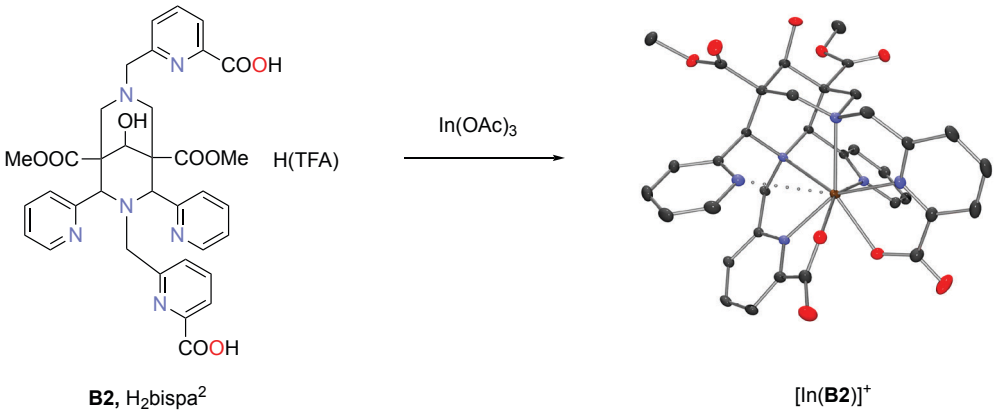

B2, H_2bispa^2 [In(**B2**)]$^+$

Figure 64. Complexation reaction of the octadentate ligand H_2bispa^2 (**B2**) to the respective indium(III) complex.[256]

The complex stability constants of In^{III}-, Lu^{III}- and La^{III}-**B2** were determined by potentiometric titrations. Although the values obtained varied greatly, the challenge experiments with the radioactive metal-**B2** complexes in the presence of human serum gave similar stabilities. The radiolabeled bispa complexes were comparably or even more stable under these conditions than the respective complexes of the "gold standard" DOTA (**L5**) with the same radiometal ions. After an incubation time of 1 hour for example, 89 and 88 % of $^{177}Lu^{III}$-**B2** and $^{177}Lu^{III}$-DOTA remain intact, respectively. Unlike DOTA, **B2** could be quantitatively radiolabeled with $^{111}In^{III}$ and $^{225}Ac^{III}$ under ambient conditions, which is very important for applications involving monoclonal antibodies as vector moieties. In the case of $^{111}In^{III}$, room temperature radiolabeling yielded a high molar activity of ~70 GBq/µmol within 10 minutes.

Recently, hole size calculations have been performed to understand the steric part of the different thermodynamic stabilities of the **B2**-metal complexes.[410] Furthermore, the theoretical determination of log D values for these systems based on calculated charge distributions, as previously reported for copper(II) complexes,[188,404] is in the focus of ongoing research. The promising results of the presented radiochemical studies of bispa ligand **B2** will certainly promote the development of a bifunctional derivative similar to that currently in preparation for **B1a** (see above). With the new octadentate bispa ligand, the scope of bispidine chelators is now extended to nuclear medicine applications beyond $^{64}Cu^{II}$ PET imaging.

7 Experimental Section[vii]

7.1 Materials and methods

Chemicals and procedures

Chemicals and solvents were purchased from Sigma-Aldrich Chemie GmbH, Fisher Scientific GmbH, Merck KGaA, ABCR GmbH & Co., and Tokyo Chemical Industry Co. Ltd. and were of the highest available purity. Dry solvents were used as delivered without further purification. For HPLC separations, potentiometric titrations, and radiochemical studies, Milli-Q water was used. Some of the reactions reported were carried out under an inert gas atmosphere of argon or nitrogen by means of standard SCHLENK- or glovebox techniques. Glassware was heated and dried under vacuum prior to usage.

Nuclear magnetic resonance (NMR) spectroscopy

NMR spectra were recorded on Bruker Avance I 200, Bruker Avance II 400, Bruker Avance III 600 (Heidelberg University), Bruker Avance 400inv and Bruker Avance 400dir (University of British Columbia, Vancouver) spectrometers. The ^{13}C-NMR spectra were measured with ^{1}H decoupling. DEPT-135 as well as two-dimensional correlation spectroscopy like COSY, HSQC, and HMBC were used to assign the signals. ^{1}H- and ^{13}C-NMR chemical shifts δ are reported in ppm values relative to the known solvent peak references: δ_H = 7.27 ppm and δ_C = 77.0 ppm for $CDCl_3$, δ_H = 3.31 ppm and δ_C = 49.2 ppm for MeOH-d^4, δ_H = 1.94 ppm and δ_C = 1.4 ppm for MeCN-d^3, and δ_H = 4.75 ppm for D_2O. The following abbreviations were used to describe the multiplicity of the signals: s = singlet, bs = broad singlet, d = doublet, bd = broad doublet, t = triplet, dd = doublet of doublet, ddd = doublet of doublet of doublet, td = triplet of doublet, and m = multiplet. The software package ACD/Labs was used for data processing and to create the figures in Appendix A.[411]

[vii] Reproduced in part with permission from P. Comba, L. Grimm, C. Orvig, K. Rück, H. Wadepohl, *Inorg. Chem.* **2016**, *55*, 12531-12543, Copyright 2016 American Chemical Society.; Parts of this chapter will be published in P. Comba, U. Jermilova, C. Orvig, B. O. Patrick, C. F. Ramogida, K. Rück, C. Schneider, M. Starke, *Chem. Eur. J.*, *submitted manuscript.*

Mass spectrometry (MS)

High resolution (HR) mass spectra were either recorded on a Bruker ApexQe FT-ICR instrument by Dr. Jürgen GROSS and coworkers (Heidelberg University) or on a Waters/Micromass LCT TOF-MS spectrometer by Dr. Yun LING and coworkers (University of British Columbia, Vancouver).

Elemental analysis (EA)

Elemental analyses were performed on a CHN-O-vario EL by the "Microanalysis Laboratory", Institute of Organic Chemistry, Heidelberg University.

High performance liquid chromatography (HPLC)

A HPLC system consisting of a Waters 600 controller, a Waters 2487 dual wavelength absorbance detector, and a Waters delta 600 pump was used. The purification of the metal ion complexes [In^{III}(**B2**)](TFA) and [La^{III}(**B2**)](TFA) was carried out using a semipreparative Phenomenex Synergi Hydro-RP column (250 mm x 21.2 mm, 80 Å, 4 µm).

Solid state X-ray analysis

At Heidelberg University crystallographic data were collected and solved by Prof. Dr. Hubert WADEPOHL and coworkers. Data collection was performed on a Bruker AXS Smart 1000 CCD diffractometer (Mo-K_α radiation, sealed X-ray tube, graphite monochromator) or on an Agilent Technologies Supernova-E CCD diffractometer (Mo- or Cu-Kα radiation, microfocus X-ray tube, multilayer mirror optics). The solid state structures of **B2** and [In^{III}(**B2**)](TFA) were determined at the University of British Columbia, Vancouver, by Dr. Brian PATRICK. These measurements were performed on a Bruker APEX DUO diffractometer (Cu-Kα radiation) or a Bruker X8 APEX II diffractometer (Mo-Kα radiation) with cross-coupled multilayer optics, respectively. The experimental structures reported in this thesis are or will be deposited at the Cambridge Crystallographic Data Centre (CCDC) and can thus be obtained free of charge *via* https://www.ccdc.cam.ac.uk/structures/. The corresponding CCDC-reference codes are given in Appendix B. The plots of the solid state structures were created using the programs ORTEP and POV-Ray.[412,413]

UV-vis-NIR spectroscopy

UV-vis-NIR spectra were recorded at 25 °C on a Jasco V-570 spectrophotometer equipped with a Jasco ETC-505T cryostat or on an Agilent 8453 spectrophotometer equipped with an Unisoku USP-203-A cryostat. Prior to each measurement the baseline was recorded using pure solvents and subtracted automatically. In the spectra device-related noise was smoothed using Origin (OriginLab). Unresolved transitions were fitted with Gaussian envelopes as shown in Appendix C.

Electron spin resonance (ESR) spectroscopy

ESR measurements were performed on a Bruker ELEX-SYS-E-500 instrument at 8 K, using methanol as solvent. The Spin Hamiltonian parameters were obtained by simulation of the experimental data with the XSophe software package.[383,384] Fourier filtering (HAMMING function) and SAVITZKY-GOLAY filtering were undertaken to increase the spectral resolution. The cutoff of the HAMMING function was adjusted so that the high frequency noise was minimized without distorting the spectrum.

Angular overlap model (AOM) analysis

Ligand field calculations were performed with the computer program CAMMAG.[391] The used published and adjusted parameters as well as examples of input-files are given in Appendix F.

Cyclic voltammetry

Cyclovoltammetric measurements were performed on a CH Instruments CHI660D electro-chemical workstation, equipped with a CH Instruments Picoamp Booster and Faraday Cage. A three-electrode setup consisting of a glassy-carbon working electrode, a platinum wire auxiliary electrode and an Ag/AgCl reference electrode (3 M NaCl) was used. The complexes to be measured were dissolved in dry DMF with 0.1 M (*n*-Bu_4N)(ClO_4) as the electrolyte salt. The solutions were degassed, and a slight argon stream was set above the solution during the measurement (scan rate of 0.1 V/s). All values were referenced against the potential of ferrocene as an external standard ($E_{1/2}$ (fc/fc^+) = 0.55 V).

Potentiometric titrations

All potentiometric measurements were carried out using a Metrohm Titrando 905 device, equipped with a BlueLine 17 pH electrode (Schott instruments) and dosing systems (Dosino 800, Metrohm) containing the respective titrants. The addition of titrant as well as the data collection were automatically carried out by the software package *tiamo* 2.3 (Metrohm). The potentiometric setup consisted of a water-jacketed glass vessel maintained at 25 °C using a Lauda ecoline E300 thermostat. To exclude atmospheric CO_2 from the titration cell, a slight argon stream was passed over the sample solution during the measurement. All pH titrations were performed at a constant ionic strength of μ = 0.1 M electrolyte salt and the solutions were prepared with Milli-Q water.

The investigations of the hexadentate bispa ligands **B1a** and **B1b** as well as their copper(II) complexes were performed with KNO_3 as the electrolyte salt. As titrants 0.1 M KOH and 0.1 M HNO_3 were used, respectively. Prior to and after each measurement, the standard potential of the electrode (E_0) was determined by titration of a HNO_3 solution and subsequent analysis of the titration curve using the computer program TITKURVE.[414] Aqueous stock solutions of the ligands were prepared at a concentration of 2 mM. The samples (20 mL, 0.04 mmol ligand) were placed in the glass vessel and 0.1 M HNO_3 was used to adjust the initial pH value. Measurements were carried out in the absence of metal ions and with a metal-to-ligand ratio of 1:1. Each titration curve consisted of 50-65 titration points at the 2-11 pH range and three replicate titrations were performed for each system. Backtitrations were always carried out to ensure that equilibrium was attained at each point. A measuring time of 120 s (determination of protonation constants) and 300 s (determination of copper(II) stability constants) per titration point proved to be sufficient to avoid hysteresis. For the determination of the stability constants with Cu^{II}, 1:1 ligand-ligand competition titrations were performed. K_2H_2EDTA was used as the competing ligand with known pKa values and complex stability constants (μ = 0.1 M, 25 °C; pKa: 10.19, 6.13, 2.69, 2.0; log K_{CuL}: 18.78, log K_{CuLH}: 3.1, log K_{CuLH-1}: 11.4).[415]

Potentiometric titrations of bispa ligand **B2** and the corresponding metal complexes were performed with KCl as the electrolyte salt. Titrants used were 0.1 M KOH and 0.1 M HCl. Before each measurement, the standard potential of the electrode (E_0) was determined by titration of a HCl solution and subsequent analysis with the computer program GLEE.[416] The ligand and metal ion concentrations were in the range of 0.5 to 2.0 mM for potentiometric titrations. Equilibrium times were 5 min for pKa titrations and 15 min for metal complex titrations. For determination of the acid dissociation constants of **B2**, the

initial pH of the ligand solution was adjusted by addition of 0.1 M HCl. The required metal ions indium(III), lutetium(III), and lanthanum(III) were purchased as atomic absorption standard (AAS) solutions. The exact amount of acid present in the AAS solution was determined by titration of equimolar solutions of the respective metal ion and K_2H_2EDTA. The complex stability constants of lutetium(III) and lanthanum(III) with **B2** were accessible *via* direct potentiometric titration of sample solutions with a metal-to-ligand ratio of 1:1. In case of indium(III), ligand-ligand competition titrations were performed in a ratio of 1:1:0.5 (In^{III} / **B2**•H(TFA) / competing ligand). K_2H_2EDTA was used as the competing ligand with known protonation and complex stability constants (μ = 0.1 M, 25 °C; log K_{InL}: 25.0, log K_{InLH}: 1.7, log K_{InLH-1}: 8.43).[415] The formation constants corresponding to the hydrolysis of the metal ions in solution were taken from the literature.[162,417] In the case of all three metal complex titrations, precipitations were observed at a pH > 10 and the respective data points were thus excluded from the analysis.

Protonation constants and complex stability constants were calculated from the experimental data with the computer program HYPERQUAD (version hq2008).[160] The total concentrations of the compounds and the pKw value (13.78) were not refined. The values given in parentheses are the standard deviation of three measurements. Species distributions were plotted from the obtained constants using the HySS program (version 4.0.31).[418]

7.2 Syntheses of picolinic acid-based bispidine ligands

Synthesis of the protected picolinic acid

The *tert*-butyl substituted picolinic acid derivative **11** was prepared in a two-step synthesis,[360] whereby AIBN was used as the radical initiator for bromination of **10** instead of benzoyl peroxide.[359]

General procedure 1 (GP1) for the coupling of the bispidine scaffold and the protected picolinic acid

The respective bispidol fragment (1.0 eq) was dissolved in MeCN. To this solution *tert*-butyl 6-(bromomethyl)picolinate **11** (1.0-2.4 eq depending on the synthesis) and an excess of Na_2CO_3 (6.0-6.1 eq) were added. The suspension was heated to reflux overnight or for 24 h, and then the excess of Na_2CO_3 was removed by filtration. The filtrate was concentrated *in vacuo* and the yellow residue partitioned between equal volumes (100 mL) of water and CH_2Cl_2. In the next step the combined organic phases were dried over Na_2SO_4, filtered, and concentrated under reduced pressure. The purification of the crude product was performed as described in the individual synthesis instructions.

General procedure 2 (GP2) for the removal of the *tert*-butyl ester protecting group

To the *tert*-butyl ester protected ligand precursor dissolved in CH_2Cl_2 an equivalent volume of trifluoroacetic acid, H(TFA), was added and the solution was stirred overnight or for 24 h at room temperature. The solvent was then evaporated and the crude product was purified to afford the final ligand as the corresponding TFA salt.

7.2.1 Synthesis of Hbispa[1a]

The syntheses of the following compounds were performed according to slightly modified literature procedures and are thus not reported in this thesis: piperidone **P1**,[317,361] bispidone **B8**,[296,317] bispidols **B9** and **B10**, **(*t*Bu)B1a** and **B1a**•H(TFA).[359]

7.2.2 Synthesis of (*p*-MeO)Hbispa[1a]

The following compounds were synthesized corresponding to a literature-known procedure: **13**, **14**, **15**, **16**, and **P2**.[317]

Dimethyl 7-benzyl-2,4-bis(4-methoxypyridin-2-yl)-3-methyl-9-oxo-3,7-diazabicyclo[3.3.1]-nonane-1,5-dicarboxylate

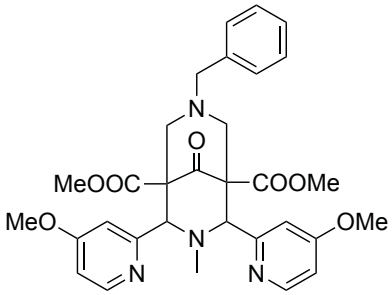

B12

$C_{31}H_{34}N_4O_7$

574.63 g/mol

Piperidone **P2** (34.0 g, 76.8 mmol, 1.0 eq) was dissolved in 100 mL tetrahydrofuran and heated to 50 °C. Benzylamine (2.96 mL, 9.87 g, 92.1 mmol, 1.2 eq) and formaldehyde (13.9 mL, 37 % in MeOH / H_2O, 184 mmol, 2.4 eq) were added successively *via* a dropping funnel. The reaction mixture was heated under reflux for 30 minutes. After cooling to room temperature the solvent was removed under reduced pressure and the remaining solid was recrystallized from hot MeOH yielding **B12** as colorless crystals (31.3 g, 54.5 mmol, 71 %).

^{1}H-NMR (600.13 MHz, 25 °C, $CDCl_3$): δ = 2.06 (s, 3 H, $N^3C\underline{H}_3$), 2.58 (d, $^2J_{H,H}$ = 11.9 Hz, 2 H, $N^7C\underline{H}_{2ax,eq}$), 3.15 (d, $^2J_{H,H}$ = 11.9 Hz, 2 H, $N^7C\underline{H}_{2ax,eq}$), 3.48 (s, 2 H, $N^7C\underline{H}_2$), 3.81 (s, 6 H, $COOC\underline{H}_3$), 3.86 (s, 6 H, p-$C\underline{H}_3O$), 4.64 (s, 2 H, $N^3C\underline{H}$), 6.68-6.69 (m, 2 H, H_{ar}), 7.25-7.26 (m, 1 H, H_{ar}), 7.31-7.34 (m, 4 H, H_{ar}), 7.55 (s, 2 H, H_{ar}), 8.30 (d, $^3J_{H,H}$ = 5.7 Hz, 2 H, H_{ar}) ppm.

^{13}C-NMR (150.92 MHz, 25 °C, $CDCl_3$): δ = 43.4, 52.4, 55.0, 58.7, 62.1, 62.5, 73.5, 107.8, 110.7, 127.1, 128.4, 129.7, 136.1, 150.5, 159.9, 166.1, 168.7, 203.6 ppm.

HR-ESI MS (pos, MeOH): [**B12**+Na]$^+$ calcd. 597.23197, obsd. 597.23361; [**B12**+H]$^+$ calcd. 575.25003, obsd. 575.25165.

Elemental analysis (report no. 36927): [**B12**] calcd. C, 63.80, H 6.04, N 9.60 %; obsd. C, 64.07, H 6.02, N 9.56 %.
Solid state X-ray structure: co_kr14 (CCDC 1547413).

Dimethyl 7-benzyl-9-hydroxy-2,4-bis(4-methoxypyridin-2-yl)-3-methyl-3,7-diazabicyclo-[3.3.1]nonane-1,5-dicarboxylate

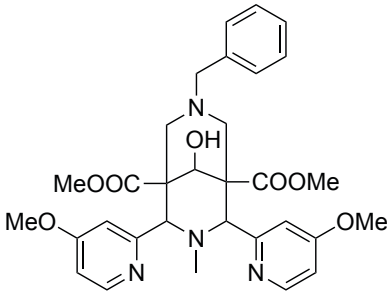

B13
$C_{31}H_{36}N_4O_7$
576.65 g/mol

Bispidone **B12** (1.86 g, 3.24 mmol, 1.0 eq) was dissolved in 80 mL of a 1,4-dioxane-water mixture (3:1) and cooled to –5 °C. A solution of sodium borohydride (61.2 mg, 1.62 mmol, 0.5 eq) in 40 mL of a 1,4-dioxane-water mixture (3:1) was added dropwise within 30 min and the solution was stirred overnight at 0 °C. Concentrated sulfuric acid was added and the solution (pH 2) was stirred for 1 h at room temperature. An aqueous solution of sodium hydroxide (20 wt%) was added to adjust a pH of 10 and the solution was stirred for 1 h at room temperature before filtering off the precipitate, washing carefully with CH_2Cl_2. The liquid layers were separated and the aqueous phase was extracted with CH_2Cl_2 (3 x 50 mL). The combined organic layers were dried over Na_2SO_4, filtered and the solvent was removed *in vacuo*. The crude product was recrystallized from hot MeOH yielding **B13** as colorless crystals (460 mg, 798 µmol, 43 %).

^{1}H-NMR (600.13 MHz, 25 °C, MeOH-d^4): δ = 1.85 (s, 3 H, $N^3C\underline{H}_3$), 2.38 (d, $^2J_{H,H}$ = 12.3 Hz, 2 H, $N^7C\underline{H}_{2ax,eq}$), 2.64 (d, $^2J_{H,H}$ = 12.3 Hz, 2 H, $N^7C\underline{H}_{2ax,eq}$), 3.42 (s, 2 H, $N^7C\underline{H}_2$), 3.63 (s, 6 H, $COOC\underline{H}_3$), 3.88 (s, 6 H, p-$C\underline{H}_3O$), 3.98 (s, 2 H, $N^3C\underline{H}$), 4.65 (s, 1 H, $C\underline{H}OH$), 6.87 (dd, $^3J_{H,H}$ = 5.9 Hz, $^3J_{H,H}$ = 2.5 Hz, 2 H, H_{ar}), 7.28-7.31 (m, 1 H, H_{ar}), 7.34-7.39 (m, 4 H, H_{ar}), 7.52 (s, 2 H, H_{ar}), 8.19 (d, $^3J_{H,H}$ = 5.8 Hz, 2 H, H_{ar}) ppm.

^{13}C-NMR (150.92 MHz, 25 °C, MeOH-d^4): δ = 44.6, 50.2, 52.7, 54.2, 56.1, 65.8, 73.3, 76.1, 109.6, 112.0, 128.3, 129.7, 131.2, 138.6, 150.8, 162.4, 168.4, 173.7 ppm.
HR-ESI MS (pos, MeOH): [**B13**+Na]$^+$ calcd. 599.24762, obsd 599.24846; [**B13**+H]$^+$ calcd. 577.26568, obsd. 577.26618.
Elemental analysis (report no. 36950): [**B13**•0.5(1,4-dioxane)] calcd. C, 63.86, H 6.50, N 9.03 %; obsd. C, 63.77, H 6.52, N 9.03 %.
Solid state X-ray structure: co_kr15 (CCDC 1547414).

Dimethyl 9-hydroxy-2,4-bis(4-methoxypyridin-2-yl)-3-methyl-3,7-diazabicyclo[3.3.1]-nonane-1,5-dicarboxylate

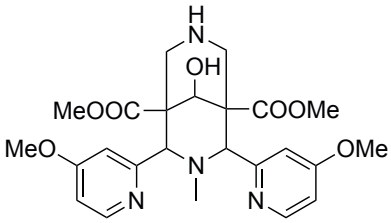

B14
$C_{24}H_{30}N_4O_7$
486.53 g/mol

To a solution of **B13** (2.02 g, 3.50 mmol, 1.0 eq) in 60 mL EtOAc palladium on activated charcoal (202 mg, 10 wt%) was added and the suspension was stirred at 95 °C and 8 bar hydrogen overnight in an autoclave. Subsequently, the reaction mixture was concentrated under reduced pressure, the residue was diluted in CH_2Cl_2 and the catalyst was removed by filtration over a celite pad. After evaporation of the solvent, the crude product was recrystallized from hot MeOH to afford **B14** as colorless crystals (730 mg, 1.50 mmol, 43 %).

^{1}H-NMR (600.13 MHz, 25 °C, MeOH-d^4): δ = 1.84 (s, 3 H, N^{3}C$\underline{H}_3$), 2.95-3.15 (m, 4 H, N^{7}C$\underline{H}_{2ax,eq}$), 3.60 (s, 6 H, COOC$\underline{H}_3$), 3.92 (bs, 6 H, p-C$\underline{H}_3$O), 4.03 (s, 2 H, N^{3}C$\underline{H}$), 4.78 (s, 1 H, C$\underline{H}$OH), 6.80 (bs, 1 H, H_{py}), 6.95 (bs, 2 H, H_{py}), 7.54 (bs, 1 H, H_{py}), 8.24 (bs, 1 H, H_{py}), 8.51 (bs, 1 H, H_{py}) ppm.
^{13}C-NMR (150.92 MHz, 25 °C, MeOH-d^4): δ = 42.5, 44.1, 52.3, 52.6, 56.4, 74.4, 76.4, 77.3, 110.4, 111.5, 112.7, 160.0, 152.1, 160.5, 161.4, 168.7, 173.5 ppm.

HR-DART MS (pos, CH_2Cl_2): [2**B14**+H]$^+$ calcd. 973.43018, obsd 973.43388; [**B14**+H]$^+$ calcd. 487.21873, obsd. 487.21949.
Elemental analysis (report no. 37093): [**B14**•MeOH] calcd. C, 57.90, H 6.61, N 10.80 %; obsd. C, 57.81, H 6.62, N 10.92 %.
Solid state X-ray structure: co_kr17a (CCDC 1547415).

Dimethyl 7-((6-(tert-butoxycarbonyl)pyridin-2-yl)methyl)-9-hydroxy-2,4-bis(4-methoxy-pyridin-2-yl)-3-methyl-3,7-diazabicyclo[3.3.1]nonane-1,5-dicarboxylate

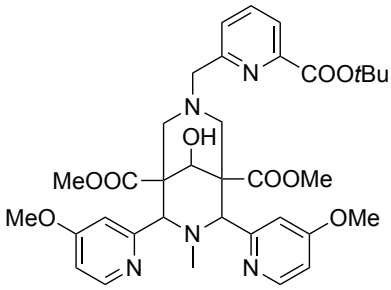

(*p*-MeO)(*t*Bu)B1a
$C_{35}H_{43}N_5O_9$
677.76 g/mol

According to **GP1** the bispidol fragment **B14** (1.21 g, 2.49 mmol, 1.0 eq) was dissolved in 80 mL MeCN. To this solution *tert*-butyl 6-(bromomethyl)picolinate **11** (680 mg, 2.49 mmol, 1.0 eq) and Na_2CO_3 (1.58 g, 14.9 mmol, 6.0 eq) were added. The work up was carried out after 24 h and recrystallization of the orange crude product from hot MeCN delivered **(*p*-MeO)(*t*Bu)B1a** as colorless crystals (1.11 g, 2.49 mmol, 66 %).

^{1}H-NMR (600.13 MHz, 25 °C, MeCN-d^3): δ = 1.54 (s, 9 H, COOC(C$\underline{H}_3$)$_3$), 1.83 (s, 3 H, N^{3}C$\underline{H}_3$), 2.40 (d, $^2J_{H,H}$ = 11.9 Hz, 2 H, N^{7}C$\underline{H}_{2ax,eq}$), 2.56 (d, $^2J_{H,H}$ = 11.9 Hz, 2 H, N^{7}C$\underline{H}_{2ax,eq}$), 3.55 (s, 2 H, N^{7}C$\underline{H}_2$), 3.58 (s, 6 H, COOC$\underline{H}_3$), 3.78 (d, $^2J_{H,H}$ = 5.8 Hz, 1 H, CHO$\underline{H}$), 3.85 (s, 6 H, p-C$\underline{H}_3$O), 3.95 (bs, 2 H, N^{3}C$\underline{H}$), 4.60 (d, $^2J_{H,H}$ = 5.8 Hz, 1 H, C$\underline{H}$OH), 6.70 (dd, $^3J_{H,H}$ = 5.7 Hz, $^4J_{H,H}$ = 2.6 Hz, 2 H, H_{py}), 7.51 (d, $^3J_{H,H}$ = 7.7 Hz, 1 H, H_{py}), 7.57 (d, $^4J_{H,H}$ = 2.6 Hz, 2 H, H_{py}), 7.82 (t, $^3J_{H,H}$ = 7.7 Hz, 1 H, H_{py}), 7.99 (dd, $^3J_{H,H}$ = 7.7 Hz, $^4J_{H,H}$ = 0.9 Hz, 1 H, H_{py}), 8.17 (d, $^3J_{H,H}$ = 5.7 Hz, 2 H, H_{py}) ppm.
^{13}C-NMR (150.92 MHz, 25 °C, MeCN-d^3): δ = 28.3, 44.5, 49.9, 52.4, 53.6, 56.1, 66.0, 73.1, 75.8, 82.2, 109.3, 110.7, 124.1, 127.9, 138.1, 150.6, 151.2, 158.7, 162.6, 165.5, 167.2, 173.0 ppm.

HR-ESI MS (pos, MeCN-d^3 / MeOH): [(***p*-MeO)(*t*Bu)B1a**+Na]$^+$ calcd. 700.29530, obsd. 700.29629; [(***p*-MeO)(*t*Bu)B1a**+H]$^+$ calcd. 678.31335, obsd. 678.31466.

Elemental analysis (report no. 37163): [(***p*-MeO)(*t*Bu)B1a**] calcd. C, 62.03, H 6.40, N 10.33 %; obsd. C, 62.00, H 6.44, N 10.71 %.

Solid state X-ray structure: co_kr20 (1547416).

Trifluoroacetate salt of 6-((9-hydroxy-1,5-bis(methoxycarbonyl)-6,8-bis(4-methoxypyridin-2-yl)-7-methyl-3,7-diazabicyclo[3.3.1]nonan-3-yl)methyl)picolinic acid

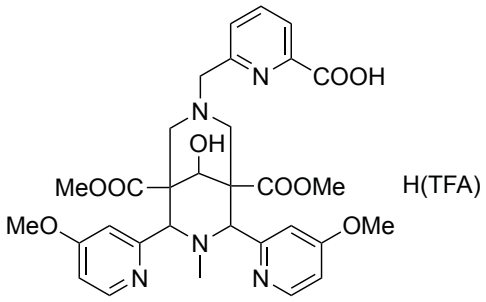

(*p*-MeO)B1a•H(TFA)

$C_{33}H_{36}F_3N_5O_{11}$

735.67 g/mol

According to **GP2** 5 mL H(TFA) were added to **(*p*-MeO)(*t*Bu)B1a** (211 mg, 311 µmol) in 5 mL CH_2Cl_2. Upon addition of H(TFA) the reaction mixture turned purple. The work up was carried out after stirring at room temperature overnight. The crude product was recrystallized from an ethanolic solution, which was overlaid with Et_2O, yielding **(*p*-MeO)B1a**•H(TFA) as colorless solid (183 mg, 249 µmol, 80 %).

^{1}H-NMR (600.13 MHz, 25 °C, D_2O): δ = 2.08 (s, 3 H, N^3CH_3), 2.52 (s, 2 H, $N^7CH_{2ax,eq}$), 2.87 (s, 2 H, $N^7CH_{2ax,eq}$), 3.74 (s, 6 H, $COOCH_3$), 3.81 (s, 2 H, N^7CH_2), 3.93 (s, 6 H, p-CH_3O), 4.75 (s, 2 H, N^3CH), 4.85 (s, 1 H, $CHOH$), 7.06 (s, 2 H, H_{py}), 7.51 (d, $^3J_{H,H}$ = 7.7 Hz, 1 H, H_{py}), 7.88 (bs, 2 H, H_{py}), 8.03 (d, $^3J_{H,H}$ = 7.7 Hz, 1 H, H_{py}), 8.10 (d, $^3J_{H,H}$ = 7.7 Hz, 1 H, H_{py}) ppm.

^{13}C-NMR (150.92 MHz, 25 °C, D_2O): δ = 43.0, 49.0, 53.3, 57.3, 61.3, 69.0, 69.9, 111.8, 112.3, 116.3, 123.6, 126.5, 140.5, 144.0, 151.7, 152.3, 156.4, 162.9, 170.7, 171.6 ppm.

HR-ESI MS (pos, MeOH): [(***p*-MeO)B1a**+Na]$^+$ calcd. 644.23270, obsd. 644.23327; [(***p*-MeO)B1a**+H]$^+$ calcd. 622.25075, obsd. 622.25191.

Elemental analysis (report no. 37387): [**(*p*-MeO)B1a**•H(TFA)] calcd. C, 53.88, H 4.93, N 9.52 %; obsd. C, 53.70, H 4.95, N 9.43 %.

7.2.3 Synthesis of Hbispa[1b]

The syntheses of the piperidone **P3**,[296] the bispidone **B15**,[373] and the bispidol **B16**[300] were performed with minor changes with respect to literature-known procedures.[317]

Dimethyl 3-((6-(tert-butoxycarbonyl)pyridin-2-yl)methyl)-9-hydroxy-7-methyl-2,4-di(pyridin-2-yl)-3,7-diazabicyclo[3.3.1]nonane-1,5-dicarboxylate

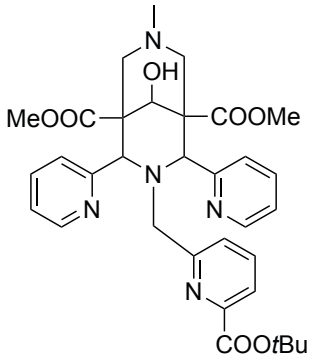

(*t*Bu)B1b

$C_{33}H_{39}N_5O_7$

617.70 g/mol

According to **GP1** the bispidol fragment **B16** (620 mg, 2.28 mmol, 1.0 eq) was dissolved in 50 mL of MeCN. To this solution *tert*-butyl 6-(bromomethyl)picolinate **11** (972 mg, 2.28 mmol, 1.0 eq) and Na_2CO_3 (1.44 g, 13.67 mmol, 6.0 eq) were added. The work up was carried out after 24 h to obtain **(*t*Bu)B1b** as an orange solid (4.58 g, 7.25 mmol, 92 %). The product was used without further purification.

^{1}H-NMR (600.13 MHz, 22 °C, MeCN-d^3): δ = 1.65 (s, 9 H, COOC(C$\underline{H}_3$)$_3$), 2.15 (s, 3 H, N^{7}C$\underline{H}_3$) 2.20 (s, 2 H, N^{7}C$\underline{H}_{2ax,eq}$), 2.30 (bs, 2 H, N^{7}C$\underline{H}_{2ax,eq}$), 3.57 (s, 6 H, COOC$\underline{H}_3$), 3.59 (s, 2 H, N^{3}C$\underline{H}_2$), 4.64 (d, $^2J_{H,H}$ = 3.2 Hz, 1 H, C$\underline{H}$OH), 4.86 (s, 2 H, N^{3}C$\underline{H}$), 6.83 (d, $^3J_{H,H}$ = 7.7 Hz, 1 H, H_{py}), 7.16 (dd, $^3J_{H,H}$ = 6.7 Hz, $^3J_{H,H}$ = 5.3 Hz, 2 H, H_{py}), 7.55 (t, $^3J_{H,H}$ = 7.7 Hz, 1 H, H_{py}), 7.69-7.72 (m, 3 H, H_{py}), 8.03 (bd, $^3J_{H,H}$ = 5.3 Hz, 2 H, H_{py}), 8.36 (d, $J_{H,H}$ = 4.3 Hz, 2 H, H_{py}) ppm.

^{13}C-NMR (150.92 MHz, 22 °C, MeCN-d^3): δ = 28.5, 46.2, 52.0, 52.4, 53.9, 59.3, 72.0, 72.3, 82.4, 123.4, 123.5, 125.3 127.8, 136.8, 137.6, 149.2, 149.8, 159.0, 161.1, 165.5, 173.3 ppm.

HR-ESI MS (pos, MeCN-d^3 / MeOH): [**(*t*Bu)B1b**+Na]$^+$ calcd. 640.27536, obsd. 640.27445; [**(*t*Bu)B1b**+H]$^+$ calcd. 618.29223, obsd. 618.29217.

Trifluoroacetate salt of 6-((9-hydroxy-1,5-bis(methoxycarbonyl)-7-methyl-2,4-di(pyridin-2-yl)-3,7-diazabicyclo[3.3.1]nonan-3-yl)methyl)picolinic acid

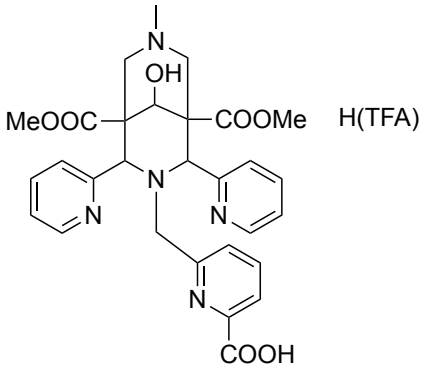

B1b•H(TFA)

$C_{31}H_{32}F_3N_5O_9$

675.62 g/mol

According to **GP2** 70 mL H(TFA) were added to **(*t*Bu)B1b** (3.57 g, 5.78 mmol) in 70 mL CH_2Cl_2. Upon addition of H(TFA) the reaction mixture turned purple. The work up was carried out after 24 h and the crude product was washed with EtOAc to give **B1b**•H(TFA) as a colorless solid (2.93 g, 5.22 mmol, 90 %). Crystals suitable for X-ray diffraction were obtained by recrystallization from hot MeOH.

^{1}H-NMR (600.13 MHz, 22 °C, D_2O): δ = 3.09 (s, 3 H, $N^7C\underline{H}_3$), 3.47 (d, $^2J_{H,H}$ = 13.0 Hz, 2 H, $N^7C\underline{H}_{2ax,eq}$), 3.66 (s, 6 H, $COOCH_3$), 3.80 (d, $^2J_{H,H}$ = 13.0 Hz, 2 H, $N^7C\underline{H}_{2ax,eq}$), 3.89 (s, 2 H, $N^3C\underline{H}_2$), 5.03 (s, 1 H, C<u>H</u>OH), 5.06 (s, 2 H, $N^3C\underline{H}$), 6.75 (d, $^3J_{H,H}$ = 7.9 Hz, 1 H, H_{py}), 7.26 (dd, $^3J_{H,H}$ = 7.6 Hz, $^3J_{H,H}$ = 4.9 Hz, 2 H, H_{py}), 7.35 (d, $^3J_{H,H}$ = 7.6 Hz, 2 H, H_{py}), 7.79 (td, $^3J_{H,H}$ = 7.6 Hz, $^4J_{H,H}$ = 1.6 Hz, 2 H, H_{py}), 7.97 (t, $^3J_{H,H}$ = 7.9 Hz, 1 H, H_{py}), 8.04 (d, $^3J_{H,H}$ = 7.9 Hz, 1 H, H_{py}), 8.31 (d, $^3J_{H,H}$ = 4.9 Hz, 2 H, H_{py}) ppm.

^{13}C-NMR (150.92 MHz, 22 °C, D_2O): δ = 43.1, 50.6, 53.0, 53.5, 55.5, 69.4, 70.5, 123.9, 125.1, 125.2, 125.9, 139.1, 145.3, 146.9, 150.0, 152.6, 153.3, 163.2, 170.1 ppm.

HR-ESI MS (pos, MeOH): [**B1b**+Na]$^+$ calcd. 584.21157, obsd. 584.21216; [**B1b**+H]$^+$ calcd. 562.22962, obsd. 562.22994.
Elemental analysis (report no. 37961): [**B1b**•H(TFA)] calcd. C, 55.11; H, 4.77; N, 10.37; obsd. C, 55.08; H, 4.82; N, 10.42 %.
Solid state X-ray structure: co_kr23 (CCDC 1481465).

7.2.4 Synthesis of H_2bispa^2

The piperidone **P3**,[296,317] the bispidone **B17**, and the bispidol **B18**[374] were synthesized according to literature-known procedures.

Trifluoroacetate salt of dimethyl 9-hydroxy-2,4-di(pyridin-2-yl)-3,7-diazabicyclo[3.3.1]-nonane-1,5-dicarboxylate

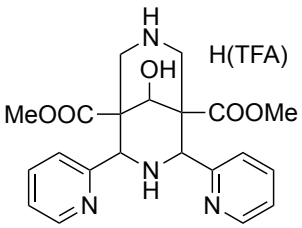

B19•H(TFA)
$C_{23}H_{25}F_3N_4O_7$
526.47 g/mol

To **B18** (2.31 g, 4.11 mmol) in 25 mL of CH_2Cl_2 25 mL H(TFA) were slowly added and the solution was refluxed for 2 d. After 30 min the reaction mixture turned purple. In the next step the solvent was removed *in vacuo* and the residue was refluxed in MeOH followed by hot filtration. The TFA salt of **B19** was obtained as colorless crystals (1.82 g, 3.46 mmol, 84 %) from the concentrated filtrate.

^{1}H-NMR (600.13 MHz, 25 °C, MeOH-d^4): δ = 3.48 (dd, $^2J_{H,H}$ = 13.2 Hz, $^3J_{H,H}$ = 1.2 Hz, 2 H, $N^7C\underline{H}_{2ax,eq}$), 3.62 (bd, $^2J_{H,H}$ = 13.2 Hz, 2 H, $N^7C\underline{H}_{2ax,eq}$), 3.69 (s, 6 H, $COOC\underline{H}_3$), 4.76 (d, $^3J_{H,H}$ = 1.4 Hz, 2 H, $N^3C\underline{H}$), 4.89 (s, 1 H, $C\underline{H}OH$), 7.40 (ddd, $^3J_{H,H}$ = 7.7 Hz, $^3J_{H,H}$ = 4.8 Hz, $^4J_{H,H}$ = 1.2 Hz, 2 H, H_{py}), 7.49 (d, $^3J_{H,H}$ = 7.7 Hz, 2 H, H_{py}), 7.85 (td, $^3J_{H,H}$ = 7.7 Hz, $^4J_{H,H}$ = 1.8 Hz, 2 H, H_{py}), 8.63 (ddd, $^3J_{H,H}$ = 4.8 Hz, $^3J_{H,H}$ = 1.8 Hz, $^4J_{H,H}$ = 0.9 Hz, 2 H, H_{py}) ppm.

^{13}C-NMR (150.92 MHz, 25 °C, MeOH-d^4): δ = 41.4, 51.9, 53.2, 67.6, 73.3, 124.7, 125.3, 139.0, 150.8, 158.2, 171.6 ppm.

HR-ESI MS (pos, MeOH): [**B19**+H]$^+$ calcd. 413.18195, obsd. 413.18221.

Elemental analysis (report no. 39141): [**B19**•H(TFA)] calcd. C, 52.47; H, 4.79; N, 10.64 %; obsd. C, 52.72; H, 4.93; N, 10.57 %.

Solid state X-ray structure: co_kr32 (CCDC 1547417).

Dimethyl 3,7-bis((6-(tert-butoxycarbonyl)pyridin-2-yl)methyl)-9-hydroxy-2,4-di(pyridin-2-yl)-3,7-diazabicyclo[3.3.1]nonane-1,5-dicarboxylate

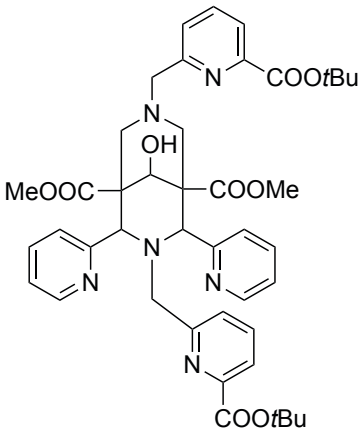

(*t*Bu)$_2$B2

$C_{43}H_{50}N_6O_9$

794.91 g/mol

According to **GP1** the bispidol fragment **B19**•H(TFA) (1.21 g, 2.49 mmol, 1.0 eq) was dissolved in 80 mL of MeCN. To this solution *tert*-butyl 6-(bromomethyl)picolinate **11** (2.07 g, 7.61 mmol, 2.4 eq) and Na_2CO_3 (2.02 g, 19.1 mmol, 6.1 eq) were added. The work up was carried out after heating to reflux overnight. The residue was dissolved in ethyl acetate and the solution was overlaid with Et_2O to obtain **(*t*Bu)$_2$B2** as a colorless solid (1.57 g, 1.98 mmol, 63 %) at –18 °C.

^{1}H-NMR (600.13 MHz, 25 °C, MeCN-d^3): δ = 1.63 (s, 9 H, COOC(C$\underline{H}_3$)$_3$), 1.65 (s, 9 H, COOC(C$\underline{H}_3$)$_3$), 2.47 (d, $^2J_{H,H}$ = 11.8 Hz, 2 H, N^{7}C$\underline{H}_{2ax,eq}$), 2.87 (d, $^2J_{H,H}$ = 11.8 Hz, 2 H, N^{7}C$\underline{H}_{2ax,eq}$), 3.55 (s, 6 H, COOC$\underline{H}_3$), 3.64 (s, 2 H, N^{3}C$\underline{H}_2$), 3.78 (bs, 2 H, N^{7}C$\underline{H}_2$), 4.26 (d, $^2J_{H,H}$ = 6.0 Hz, 1 H, CHO$\underline{H}$), 4.49 (s, 2 H, N^{3}C$\underline{H}$), 4.65 (d, $^2J_{H,H}$ = 6.0 Hz, 1 H, C$\underline{H}$OH), 6.78 (d, $^3J_{H,H}$ = 7.8 Hz, 1 H, H_{py}), 7.04-7.08 (m, 4 H, H_{py}), 7.48 (t, $^3J_{H,H}$ = 7.8 Hz, 1 H, H_{py}), 7.53-

7.58 (m, 3 H, H_{py}), 7.61 (d, $^3J_{H,H}$ = 7.8 Hz, 1 H, H_{py}), 7.97 (t, $^3J_{H,H}$ = 7.9 Hz, 1 H, H_{py}), 8.13 (d, $^3J_{H,H}$ = 7.9 Hz, 1 H, H_{py}), 8.24 (d, $^3J_{H,H}$ = 4.9 Hz, 2 H, H_{py}) ppm.

^{13}C-NMR (150.92 MHz, 25 °C, MeCN-d^3): δ = 28.4, 28.5, 49.9, 52.9, 55.2, 63.6, 66.2, 73.1, 74.1, 83.4, 84.2, 123.7, 124.3, 125.3, 126.1, 126.8, 128.8, 138.3, 138.7, 140.2, 149.1, 149.3, 150.4, 158.0, 158.7, 159.0, 164.7, 165.2, 172.4 ppm.

HR-ESI MS (pos, MeOH): [**(*t*Bu)$_2$B2**+H]$^+$ calcd. 795.37120, obsd. 795.37184.

Elemental analysis (report no. 39927): [**(*t*Bu)$_2$B2**•NaBr•H_2O] calcd. C, 56.39; H, 5.72; N, 9.18 %; obsd. C, 56.67; H, 5.61; N, 8.93 %.

Solid state X-ray structure: co_kr33_sq (CCDC 1547418).

Trifluoroacetate salt of 6,6'-((9-hydroxy-1,5-bis(methoxycarbonyl)-2,4-di(pyridin-2-yl)-3,7-diazabicyclo[3.3.1]nonane-3,7-diyl)bis(methylene))dipicolinic acid

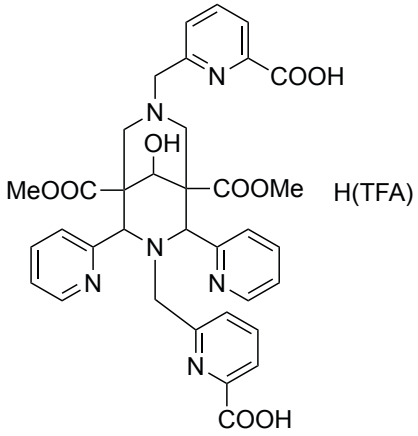

B2•H(TFA)

$C_{37}H_{35}F_3N_6O_{11}$

796.71 g/mol

According to **GP2** 10 mL H(TFA) were added to **(*t*Bu)$_2$B2** (900 mg, 1.13 mmol) in 10 mL CH_2Cl_2. Upon addition of H(TFA) the reaction mixture turned purple. The work up was carried out after stirring at room temperature overnight. The crude product was recrystallized from hot MeOH yielding **B2**•H(TFA) as colorless crystals (642 mg, 806 µmol, 71 %).

^{1}H-NMR (400.19 MHz, 25 °C, D_2O): δ = 3.66 (d, $^2J_{H,H}$ = 13.1 Hz, 2 H, $N^7C\underline{H}_{2ax,eq}$), 3.69 (s, 6 H, $COOC\underline{H}_3$), 3.87 (s, 2 H, $N^3C\underline{H}_2$), 4.02 (d, $^2J_{H,H}$ = 13.1 Hz, 2 H, $N^7C\underline{H}_{2ax,eq}$), 4.73 (s, 2 H, $N^7C\underline{H}_2$), 5.01 (s, 2 H, $N^3C\underline{H}$), 5.08 (s, 1 H, $C\underline{H}OH$), 6.77 (bd, $^3J_{H,H}$ = 7.7 Hz, 1 H, H_{py}),

7.23 (ddd, $^{3}J_{H,H}$ = 7.5 Hz, $^{3}J_{H,H}$ = 5.0 Hz, $^{4}J_{H,H}$ = 0.9 Hz, 2 H, H_{py}), 7.36 (bd, $^{3}J_{H,H}$ = 7.9 Hz, 2 H, H_{py}), 7.80 (td, $^{3}J_{H,H}$ = 7.7 Hz, $^{3}J_{H,H}$ = 1.7 Hz, 2 H, H_{py}), 7.90 (bd, $^{3}J_{H,H}$ = 4.4 Hz, 2 H, H_{py}), 7.98 (t, $^{3}J_{H,H}$ = 7.9 Hz, 1 H, H_{py}), 8.05-8.10 (m, 2 H, H_{py}), 8.18 (t, $^{3}J_{H,H}$ = 7.7 Hz, 1 H, H_{py}), 8.21-8.23 (m, 1 H, H_{py}) ppm.

^{13}C-NMR (100.64 MHz, 25 °C, D_2O): δ = 49.2, 53.2, 53.8, 56.2, 61.6, 69.8, 71.0, 124.4, 125.3, 125.5, 126.3, 126.7, 130.3, 139.3, 140.3, 145.5, 147.2, 148.6, 149.4, 150.1, 152.9, 153.6, 163.2, 168.4, 170.3 ppm.

HR-ESI MS (pos, MeOH): [**B2**+H]$^{+}$ calcd. 683.2460, obsd. 683.2452.

Elemental analysis (report no. 39971): [**B2**•H(TFA)] calcd. C, 55.78; H, 4.43; N, 10.55 %; obsd. C, 55.52; H, 4.08; N, 10.77 %.

Solid state X-ray structure: co498 (CCDC 1550809).

7.3 Metal complexes

7.3.1 Metal complexes based on the hexadentate bispa ligands

Cobalt(II) bispa complexes

*[Co^{II}(**B1a**)](TFA) ($C_{31}H_{30}F_3N_5CoO_9$, 732.54 g/mol).*

B1a•H(TFA) (150 mg, 222 µmol, 1.0 eq) was dissolved in 10 mL of dry MeOH under inert gas atmosphere. $Co(OAc)_2$•$4H_2O$ (55.3 mg, 222 µmol, 1.0 eq) was added, and the resulting red solution was stirred for 2 h at room temperature. After evaporation of the solvent, the residue was taken up in MeOH and subjected to Et_2O diffusion at room temperature yielding [Co^{II}(**B1a**)](TFA)•$0.5H_2O$ as red crystals (55.8 mg, 71.9 µmol, 32 %).

HR-ESI MS (pos, MeOH): [Co^{II}(**B1a**)]$^+$ calcd. 619.14717, obsd. 619.14725.
Elemental analysis (report no. 38721): [[Co^{II}(**B1a**)](TFA)•$0.5H_2O$] calcd. C, 50.54; H, 4.31; N, 9.36 %; obsd. C, 50.65; H, 4.51; N, 9.64 %.
UV-vis-NIR (DMSO, rt): λ [nm] (ε [$M^{-1}cm^{-1}$]) = 470 (123), 557 (43), 993 (5).
CV (DMF, rt): $E_{1/2}$ = –0.37 V, –1.94 V (*vs.* fc/fc^+).
Solid state X-ray structure: co_kr30 (CCDC 1481460).

*[Co^{II}(**(*p*-MeO)B1a**)](TFA) ($C_{33}H_{34}CoF_3N_5O_{11}$, 792.59 g/mol)*

(*p*-MeO)B1a•H(TFA) (150 mg, 204 µmol, 1.0 eq) was dissolved in 10 mL of dry MeOH under inert gas atmosphere. $Co(OAc)_2$•$4H_2O$ (50.8 mg, 204 µmol, 1.0 eq) was added and the resulting pink solution was stirred for 2 h at room temperature. After evaporation of the solvent, the residue was redissolved in MeOH and subjected to Et_2O diffusion at room temperature yielding [Co^{II}(**(*p*-MeO)B1a**)](TFA)•$3H_2O$ as dark red crystals (110 mg, 130 µmol, 64 %).

HR-ESI MS (pos, MeOH): [Co^{II}(**(*p*-MeO)B1a**)]$^+$ calcd. 679.16830, obsd. 679.16855.
Elemental analysis (report no. 38722): [[Co^{II}(**(*p*-MeO)B1a**)](TFA)•$3H_2O$] calcd. C, 46.82; H, 4.76; N, 8.27 %; obsd. C, 46.98; H, 4.76; N, 8.27 %.
UV-vis-NIR (DMSO, rt): λ [nm] (ε [$M^{-1}cm^{-1}$]) = 467 (173), 541 (37), 1030 (6).
CV (DMF, rt): $E_{1/2}$ = –0.41 V, –1.97 V (*vs.* fc/fc^+).

*[Co^{II}(**B1b**)](TFA) ($C_{31}H_{30}F_3N_5CoO_9$, 732.54 g/mol).*

B1b•H(TFA) (150 mg, 222 µmol, 1.0 eq) was dissolved in 10 mL of dry MeOH under inert gas atmosphere. $Co(OAc)_2$•$4H_2O$ (55.3 mg, 222 µmol, 1.0 eq) was added and the resulting orange solution was stirred for 2 h at room temperature. After evaporation of the solvent, the residue was taken up in MeOH and subjected to Et_2O diffusion at room temperature yielding [Co^{II}(**B1b**)](TFA)•$0.5H_2O$ as brown crystals (116 mg, 150 µmol, 67 %).

HR-ESI MS (pos, MeOH): [Co^{II}(**B1b**)]$^+$ calcd. 619.14717, obsd. 619.14728.
Elemental analysis (report no. 38723): [[Co^{II}(**B1b**)](TFA)•$0.5H_2O$] calcd. C, 50.54; H, 4.47; N, 9.36 %; obsd. C, 50.40; H, 4.51; N, 9.53 %.
UV-vis-NIR (DMSO, rt): λ [nm] (ε [$M^{-1}cm^{-1}$]) = 475 (117), 516 (9), 544 (23), 584 (7), 677 (6), 920 (6).
CV (DMF, rt): $E_{1/2}$ = –0.52 V, –2.09 V (*vs.* fc/fc$^+$).
Solid state X-ray structure: co_kr31 (CCDC 1481466).

Nickel(II) bispa complexes

*[Ni^{II}(**B1a**)](TFA) ($C_{31}H_{30}F_3N_5NiO_9$, 732.30 g/mol)*.

Solutions of **B1a**•H(TFA) (100 mg, 150 µmol, 1.0 eq) and $Ni(OAc)_2$•$4H_2O$ (37.3 mg, 150 µmol, 1.0 eq) in 5 mL MeOH, respectively, were combined and the resulting violet solution was stirred overnight at room temperature. After evaporation of the solvent, the residue was taken up in MeOH and subjected to Et_2O diffusion at 5 °C yielding [Ni^{II}(**B1a**)](TFA)•$2H_2O$ as violet crystals (110 mg, 150 µmol, 85 %). Some of the crystals were redissolved in a mixture of MeOH and H_2O (2:1) and violet plates suitable for X-ray diffraction were obtained by slow evaporation of the solvent mixture.

HR-ESI MS (pos, MeOH): [Ni^{II}(**B1a**)]$^+$ calcd. 618.14932, obsd. 618.14926.
Elemental analysis (report no. 36295): [[Ni^{II}(**B1a**)](TFA)•$2H_2O$] calcd. C, 48.46; H, 4.46; N, 9.12 %; obsd. C, 48.36; H, 4.51; N, 9.24 %.
UV-vis-NIR (MeOH, rt): λ [nm] (ε [$M^{-1}cm^{-1}$]) = 515 (12), 558 (11), 819 (20), 923 (25).
CV (DMF, rt): $E_{1/2}$ = 0.76 V irrev., –2.18 V (*vs.* fc/fc$^+$).
Solid state X-ray structure: co_kr12 (CCDC 1481461).

*[Ni^{II}(**(p-MeO)B1a**)](TFA) ($C_{33}H_{34}F_3N_5NiO_{11}$, 792.35 g/mol)*

Solutions of **(*p*-MeO)B1a**•H(TFA) (120 mg, 163 µmol, 1.0 eq) and $Ni(OAc)_2$•$4H_2O$ (40.6 mg, 163 µmol, 1.0 eq) in 5 mL MeOH, respectively, were combined and gave a violet solution, which was stirred overnight at room temperature. After evaporation of the solvent, the residue was redissolved in MeOH and subjected to Et_2O diffusion at 5 °C yielding [Ni^{II}(**(*p*-MeO)B1a**)](TFA)•MeOH as a violet solid (123 mg, 149 µmol, 91 %).

HR-ESI MS (pos, MeOH): [Ni^{II}(**(*p*-MeO)B1a**)]$^+$ calcd. 678.1705, obsd. 678.108.
Elemental analysis (report no. 37275): [[Ni^{II}(**(*p*-MeO)B1a**)](TFA)•MeOH] calcd. C, 49.54; H, 4.65; N, 8.50 %; obsd. C, 49.34; H, 4.53; N, 8.36 %.
UV-vis-NIR (MeOH, rt): λ [nm] (ε [$M^{-1}cm^{-1}$]) = 521 (12), 585 (10), 866 (38).
CV (DMF, rt): $E_{1/2}$ = 0.71 V irrev., –2.24 V (*vs.* fc/fc$^+$).

*[Ni^{II}(**B1b**)](TFA) ($C_{31}H_{30}F_3N_5NiO_9$, 732.30 g/mol)*.

Solutions of **B1b**•H(TFA) (100 mg, 148 µmol, 1.0 eq) and $Ni(OAc)_2$•$4H_2O$ (36.8 mg, 148 µmol, 1.0 eq) in 5 mL MeOH, respectively, were combined and the resulting brown solution was stirred for 2 h at room temperature. After evaporation of the solvent, the residue was taken up in MeOH and subjected to Et_2O diffusion at 5 °C yielding [Ni^{II}(**B1b**)](TFA)•0.5MeOH as brown crystals (77.6 mg, 106 µmol, 72 %).

HR-ESI MS (pos, MeOH): [Ni^{II}(**B1b**)]$^+$ calcd. 618.14932, obsd. 618.14908.
Elemental analysis (report no. 37469): [[Ni^{II}(**B1b**)](TFA)•0.5MeOH] calcd. C, 50.56; H, 4.31; N, 9.36 %; obsd. C, 50.43; H, 4.35; N, 9.47 %.
UV-vis-NIR (MeOH, rt): λ [nm] (ε [$M^{-1}cm^{-1}$]) = 512 (18), 796 (13), 877 (36).
CV (DMF, rt): $E_{1/2}$ = 0.71 V, –2.27 V irrev. (*vs.* fc/fc$^+$).
Solid state X-ray structure: co_kr27 (CCDC 1481467).

Copper(II) bispa complexes

*[Cu^{II}(**B1a**)](TFA) ($C_{31}H_{30}CuF_3N_5O_9$, 737.15 g/mol)*.[359]

Solutions of **B1a**•H(TFA)•MeOH•H_2O (107 mg, 147 µmol, 1.0 eq) in 4 mL MeOH and $Cu(OAc)_2$•H_2O (29.3 mg, 147 µmol, 1.0 eq) in 6 mL MeOH were combined and the resulting turquoise solution was stirred for 2 h at room temperature. After evaporation of the solvent, the residue was redissolved in MeOH and subjected to Et_2O diffusion at 5 °C yielding [Cu^{II}(**B1a**)](TFA)•1.5MeOH•1.5H_2O as turquoise crystals (100 mg, 123 µmol, 84 %).

HR-ESI MS (pos, MeOH): $[Cu^{II}(\mathbf{B1a})]^+$ calcd. 623.14358, obsd. 623.14326.

Elemental analysis (report no. 34995): $[[Cu^{II}(\mathbf{B1a})](TFA)\bullet 1.5MeOH\bullet 1.5H_2O]$ calcd. C, 48.06; H, 4.84; N, 8.62 %; obsd. C, 47.83; H, 4.62; N, 8.77 %.

UV-vis-NIR (MeOH, rt): λ [nm] (ε $[M^{-1}cm^{-1}]$) = 672 (93), 1284 (34).

CV (DMF, rt): $E_{1/2}$ = –1.02 V (*vs.* fc/fc^+).

Solid state X-ray structure: co_kr08 (CCDC 1481462).

*$[Cu^{II}$**((p-MeO)B1a**$)](TFA)$ ($C_{33}H_{34}CuF_3N_5O_{11}$, 797.20 g/mol)*

Solutions of **(*p*-MeO)B1a**•H(TFA) (120 mg, 163 µmol, 1.0 eq) in 5 mL MeOH and $Cu(OAc)_2\bullet H_2O$ (32.6 mg, 163 µmol, 1.0 eq) in 5 mL MeOH were combined and the resulting blue solution was stirred overnight at room temperature. After evaporation of the solvent, the residue was taken up in MeOH and subjected to Et_2O diffusion at 5 °C yielding $[Cu^{II}($**(*p*-MeO)B1a**$)](TFA)\bullet 1.5H_2O$ as blue crystals (128 mg, 155 µmol, 95 %).

HR-ESI MS (pos, MeOH): $[Cu^{II}($**(*p*-MeO)B1a**$)]^+$ calcd. 683.1647, obsd. 683.1649.

Elemental analysis (report no. 34995): $[[Cu^{II}($**(*p*-MeO)B1a**$)](TFA)\bullet 1.5H_2O]$ calcd. C, 48.09; H, 4.52; N, 8.50 %; obsd. C, 48.16; H, 4.61; N, 8.41 %.

UV-vis-NIR (MeOH, rt): λ [nm] (ε $[M^{-1}cm^{-1}]$) = 673 (106), 1227 (36).

CV (DMF, rt): $E_{1/2}$ = –1.08 V (*vs.* fc/fc^+).

Solid state X-ray structure: co_kr22.

*$[Cu^{II}$**(B1b)**$](TFA)$ ($C_{31}H_{30}CuF_3N_5O_9$, 737.15 g/mol)*.

Solutions of **B1b**•H(TFA) (100 mg, 148 µmol, 1.0 eq) and $Cu(OAc)_2\bullet H_2O$ (29.6 mg, 148 µmol, 1.0 eq) in 5 mL MeOH, respectively, were combined and the resulting blue solution was stirred for 2 h at room temperature. After evaporation of the solvent, the residue was redissolved in MeOH and subjected to Et_2O diffusion at 5 °C yielding $[Cu^{II}($**B1b**$)](TFA)\bullet H_2O$ as dark blue crystals (100 mg, 123 µmol, 84 %).

HR-ESI MS (pos, MeOH): $[Cu^{II}($**B1b)**$]^+$ calcd. 623.14358, obsd. 623.14372.

Elemental analysis (report no. 37467): $[[Cu^{II}($**B1b**$)](TFA)\bullet H_2O]$ calcd. C, 49.31; H, 4.27; N, 9.27 %; obsd. C, 49.02; H, 4.43; N, 9.40 %.

UV-vis-NIR (MeOH, rt): λ [nm] (ε $[M^{-1}cm^{-1}]$) = 651 (78), 904 (18).

CV (DMF, rt): $E_{1/2}$ = -1.17 V (*vs.* fc/fc^+).

Solid state X-ray structure: co_kr24 (CCDC 1481468).

Zinc(II) bispa complexes

*[Zn^{II}(**B1a**)](TFA) ($C_{31}H_{30}F_3N_5O_9Zn$, 738.98 g/mol)*.

Solutions of **B1a**•H(TFA) (100 mg, 150 µmol, 1.0 eq) and $Zn(OAc)_2$•$2H_2O$ (32.9 mg, 150 µmol, 1.0 eq) in 5 mL MeOH, respectively, were combined and the reaction mixture was stirred overnight at room temperature. After evaporation of the solvent, the residue was taken up in methanol and subjected to Et_2O diffusion at 5 °C yielding [Zn^{II}(**B1a**)](TFA)•$2H_2O$ as colorless crystals (100 mg, 147 µmol, 98 %). Some of the crystals were redissolved in a mixture of MeOH and H_2O (2:1) and colorless plates suitable for X-ray diffraction were obtained by slow evaporation of the solvent mixture.

^{1}H-NMR (600.13 MHz, 22 °C, D_2O): δ = 2.22 (s, 3 H, N^3CH_3), 2.56 (d, $^2J_{H,H}$ = 12.9 Hz, 2 H, $N^7CH_{2ax,eq}$), 2.98 (d, $^2J_{H,H}$ = 12.9 Hz, 2 H, $N^7CH_{2ax,eq}$), 3.80 (s, 6 H, $COOCH_3$), 4.01 (s, 2 H, N^7CH_2), 5.03 (s, 2 H, N^3CH), 5.04 (s, 1 H, CHOH), 7.37-7.38 (m, 2 H, H_{py}), 7.48-7.51 (m, 2 H, H_{py}), 7.64 (d, $^3J_{H,H}$ = 7.8 Hz, 1 H, H_{py}), 8.02-8.05 (m, 4 H, H_{py}), 8.26 (d, $^3J_{H,H}$ = 7.8 Hz, 1 H, H_{py}), 8.33 (d, $^3J_{H,H}$ = 7.8 Hz, 1 H, H_{py}) ppm.
^{13}C-NMR (150.92 MHz, 22 °C, D_2O): δ = 43.5, 50.3, 53.5, 61.6, 68.7, 68.8, 123.4, 124.9, 126.2, 126.3, 141.8, 142.8, 146.5, 148.5, 152.1, 153.6, 169.3, 171.3 ppm.
HR-ESI MS (pos, MeOH): $[Zn^{II}(\mathbf{B1a})]^+$ calcd. 624.14312, obsd. 624.14336.
Elemental analysis (report no. 36296): [[Zn^{II}(**B1a**)](TFA)•$2H_2O$] calcd. C, 48.04; H, 4.42; N, 9.04 %; obsd. C, 48.06; H, 4.25; N, 9.35 %.
Solid state X-ray structure: co_kr11 (CCDC 1481463).

*[Zn^{II}(**(*p*-MeO)B1a**)](TFA) ($C_{33}H_{34}F_3N_5O_{11}Zn$, 799.03 g/mol)*

Solutions of **(*p*-MeO)B1a**•H(TFA) (120 mg, 163 µmol, 1.0 eq) and $Zn(OAc)_2$•$2H_2O$ (35.8 mg, 163 µmol, 1.0 eq) in 5 mL MeOH, respectively, were combined and the reaction mixture was stirred overnight at room temperature. After evaporation of the solvent, the residue was taken up in MeOH and subjected to Et_2O diffusion at 5 °C yielding [Zn^{II}(**(*p*-MeO)B1a**)](TFA)•$2H_2O$ as colorless crystals (120 mg, 144 µmol, 88 %).

^{1}H-NMR (600.13 MHz, 22 °C, D_2O): δ = 2.21 (s, 3 H, N^3CH_3), 2.55 (d, $^2J_{H,H}$ = 12.9 Hz, 2 H, $N^7CH_{2ax,eq}$), 2.93 (d, $^2J_{H,H}$ = 12.9 Hz, 2 H, $N^7CH_{2ax,eq}$), 3.79 (s, 6 H, $COOCH_3$), 3.85 (s, 6 H, p-OCH_3), 3.97 (s, 2 H, N^7CH_2), 4.88 (s, 2 H, N^3CH), 4.97 (s, 1 H, CHOH), 6.83 (d, $^4J_{H,H}$ = 2.5 Hz, 2 H, H_{py}), 6.97 (d, $^3J_{H,H}$ = 6.3 Hz, $^4J_{H,H}$ = 2.5 Hz, 2 H, H_{py}), 7.62 (d, $^3J_{H,H}$ = 7.8 Hz, 1 H, H_{py}), 7.81 (d, $^3J_{H,H}$ = 6.3 Hz, 1 H, H_{py}), 8.24 (t, $^3J_{H,H}$ = 7.8 Hz, 1 H, H_{py}), 8.28 (d, $^3J_{H,H}$ = 7.8 Hz, 1 H, H_{py}) ppm.

^{13}C-NMR (150.92 MHz, 22 °C, D_2O): δ = 43.3, 50.4, 53.3, 53.4, 56.2, 61.6, 68.5, 68.6, 111.0, 111.4, 116.3, 123.3, 126.1, 126.3, 142.7, 146.6, 149.7, 153.5, 153.9, 162.8, 169.0, 169.2, 171.3 ppm.

HR-ESI MS (pos, MeOH): $[Zn^{II}$(**(*p*-MeO)B1a**)$]^+$ calcd. 684.1643, obsd. 684.1643.

Elemental analysis (report no. 39847): [$[Zn^{II}$(**(*p*-MeO)B1a**)](TFA)•$2H_2O$] calcd. C, 47.46; H, 4.59; N, 8.39 %; obsd. C, 47.27; H, 4.73; N, 8.41 %.

Solid state X-ray structure: co_kr19.

*[Zn^{II}(**B1b**)](TFA) ($C_{31}H_{30}F_3N_5O_9Zn$, 738.98 g/mol)*.

Solutions of **B1b**•H(TFA) (100 mg, 148 µmol, 1.0 eq) and $Zn(OAc)_2$•$2H_2O$ (32.5 mg, 148 µmol, 1.0 eq) in 5 mL MeOH, respectively, were combined and the reaction mixture was stirred overnight at room temperature. After evaporation of the solvent, the residue was redissolved in MeCN and subjected to Et_2O diffusion at 5 °C yielding [Zn^{II}(**B1b**)](TFA)•H_2O•0.5MeCN as colorless crystals (66.9 mg, 90.5 µmol, 61 %).

^{1}H-NMR (600.13 MHz, 22 °C, D_2O): δ = 2.75 (d, $^2J_{H,H}$ = 13.3 Hz, 2 H, $N^7C\underline{H}_{2ax,eq}$), 2.79 (s, 3 H, $N^7C\underline{H}_3$), 3.04 (d, $^2J_{H,H}$ = 13.3 Hz, 2 H, $N^7C\underline{H}_{2ax,eq}$), 3.70 (s, 6 H, $COOCH_3$), 4.28 (s, 2 H, $N^3C\underline{H}_2$), 5.08 (s, 1 H, C<u>H</u>OH), 5.29 (s, 2 H, $N^3C\underline{H}$), 6.98 (d, $^3J_{H,H}$ = 7.8 Hz, 1 H, H_{py}), 7.31 (dd, $^3J_{H,H}$ = 7.6 Hz, $^3J_{H,H}$ = 5.4 Hz, 2 H, H_{py}), 7.37 (d, $^3J_{H,H}$ = 7.6 Hz, 2 H, H_{py}), 7.65 (t, $^3J_{H,H}$ = 7.8 Hz, 1 H, H_{py}), 7.74 (d, $^3J_{H,H}$ = 7.8 Hz, 1 H, H_{py}), 7.81 (td, $^3J_{H,H}$ = 7.6 Hz, $^4J_{H,H}$ = 1.6 Hz, 2 H, H_{py}), 8.33 (d, $^3J_{H,H}$ = 5.4 Hz, 2 H, H_{py}) ppm.

^{13}C-NMR (150.92 MHz, 22 °C, D_2O): δ = 46.7, 52.5, 53.4, 53.9, 60.1, 68.9, 70.8, 122.5, 124.6, 125.2, 126.3, 140.7, 141.1, 143.3, 147.7, 149.7, 151.6, 170.1, 170.9 ppm.

HR-ESI MS (pos, MeOH): $[Zn^{II}$(**B1b**)$]^+$ calcd. 624.14312, obsd. 624.14347.

Elemental analysis (report no. 3574): [$[Zn^{II}$(**B1b**)](TFA)•H_2O•0.5MeCN] calcd. C, 49.43; H, 4.34; N, 9.91 %; obsd. C, 49.63; H, 4.00; N, 9.84 %.

Solid state X-ray structure: co_kr25 (CCDC 1481469).

Gallium(III) bispa complexes

*[Ga^{III}(**B1a**)](TFA)(NO_3) ($C_{31}H_{30}F_3GaN_6O_{12}$, 805.33 g/mol)*.[359]

Solutions of **B1a**•H(TFA) (100 mg, 148 µmol, 1.0 eq) in 10 mL of a MeOH-H_2O mixture (1:2) and $Ga(NO_3)$ (37.9 mg, 148 µmol, 1.0 eq) in 5 mL of a MeOH-H_2O mixture (1:2) were combined and the pH was adjusted to 5 by addition of 0.1 M NaOH. The reaction mixture was then stirred at 60 °C for 2 h and after evaporation of the solvent, the residue was

taken up in a mixture of MeOH and H_2O (2:1). By slow evaporation of the solvent mixture, [Ga^{III}(**B1a**)](TFA)(NO_3)•3H_2O was obtained as colorless crystals (83.0 mg, 96.6 µmol, 65 %).

^{1}H-NMR (200.13 MHz, 27 °C, D_2O): δ = 2.67 (s, 3 H, N^3CH_3), 2.89 (d, $^2J_{H,H}$ = 13.7 Hz, 2 H, $N^7CH_{2ax,eq}$), 3.57 (d, $^2J_{H,H}$ = 13.7 Hz, 2 H, $N^7CH_{2ax,eq}$), 3.86 (s, 6 H, $COOCH_3$), 4.60 (s, 2 H, N^7CH_2), 5.21 (s, 1 H, CHOH), 5.70 (s, 1 H, N^3CH), 7.73-7.81 (m, 4 H, H_{py}), 7.99 (d, $^3J_{H,H}$ = 5.3 Hz, 2 H, H_{py}), 8.10 (dd, $^3J_{H,H}$ = 7.3 Hz, $^4J_{H,H}$ = 1.3 Hz, 1 H, H_{py}), 8.38 (td, $^3J_{H,H}$ = 7.8 Hz, $^4J_{H,H}$ = 1.5 Hz, 2 H, H_{py}), 8.66-8.78 (m, 2 H, H_{py}) ppm.
^{13}C-NMR (150.92 MHz, 22 °C, D_2O): δ = 44.4, 52.1, 52.1, 53.2, 54.1, 62.1, 67.3, 67.6, 125.1, 125.1, 125.8, 128.3, 128.3, 128.4, 142.9, 145.8, 147.4, 147.6, 148.7, 151.5, 151.6, 164.6, 168.7 ppm.
HR-ESI MS (pos, MeOH): [Ga^{III}(**B1a**)]$^{2+}$ calcd. 314.56950, obsd 314.56964; [**B1a**+H]$^+$ calcd. 562.22941, obsd. 562.22962; [Ga^{III}(**B1a**)-H]$^+$ calcd. 628.13173, obsd. 628.13167.
Elemental analysis (report no. 36368): [[Ga^{III}(**B1a**)](TFA)(NO_3)•3H_2O] calcd. C, 43.33; H, 4.22; N, 9.78 %; obsd. C, 43.33; H, 4.40; N, 9.71 %.
Solid state X-ray structure: co_kr07 (CCDC 1481464).

*[Ga^{III}(**(p-MeO)B1a**)](X)$_2$*

Solutions of **(*p*-MeO)B1a**•H(TFA) (100 mg, 136 µmol, 1.0 eq) in 10 mL of a MeOH-H_2O mixture (1:2) and Ga(NO_3)•6H_2O (49.5 mg, 136 µmol, 1.0 eq) in 5 mL of a MeOH-H_2O mixture (1:2) were combined and the pH was adjusted to 5 by addition of 0.1 M NaOH. The reaction mixture was stirred at 60 °C for 2 h and after evaporation of the solvent, the crude product was obtained as colorless solid. Attempts to purify the compound by recrystallization from different solvents were not successful.

HR-ESI MS (pos, MeOH): [Ga^{III}(**(*p*-MeO)B1a**)]$^{2+}$ calcd. 344.5801, obsd. 344.5804.

*[Ga^{III}(**B1b**)](NO_3)$_2$ ($C_{29}H_{30}GaN_7O_{13}$, 754.32 g/mol).*

Solutions of **B1b**•H(TFA) (100 mg, 148 µmol, 1.0 eq) in 5 mL of a MeOH-H_2O mixture (1:2) and Ga(NO_3)•6H_2O (37.9 mg, 148 µmol, 1.0 eq) in 5 mL of a MeOH-H_2O mixture (1:2) were combined and the pH was adjusted to 5 by addition of 0.1 M NaOH. The reaction mixture was stirred at 60 °C for 3 h and after evaporation of the solvent, the residue was taken up in MeOH and subjected to Et_2O diffusion at 5 °C yielding [Ga^{III}(**B1b**)](NO_3)$_2$•2H_2O as colorless crystals (62.6 mg, 83.0 µmol, 56 %).

^{1}H-NMR (600.13 MHz, 22 °C, D_2O): δ = 3.05 (s, 3 H, $N^7C\underline{H}_3$), 3.08 (d, $^{2}J_{H,H}$ = 14.1 Hz, 2 H, $N^7C\underline{H}_{2ax,eq}$), 3.27 (d, $^{2}J_{H,H}$ = 14.1 Hz, 2 H, $N^7C\underline{H}_{2ax,eq}$), 3.77 (s, 6 H, $COOC\underline{H}_3$), 4.95 (s, 2 H, $N^3C\underline{H}_2$), 5.23 (s, 1 H, C<u>H</u>OH), 5.97 (s, 2 H, $N^3C\underline{H}$), 7.42 (d, $^{3}J_{H,H}$ = 7.9 Hz, 1 H, H_{py}), 7.67 - 7.71 (m, 4 H, H_{py}), 8.05 (t, $^{3}J_{H,H}$ = 7.9 Hz, 2 H, H_{py}), 8.11 (d, $^{3}J_{H,H}$ = 7.9 Hz, 1 H, H_{py}), 8.19 (td, $^{3}J_{H,H}$ = 8.0 Hz, $^{4}J_{H,H}$ = 1.2 Hz, 2 H, H_{py}), 8.60 (d, $^{3}J_{H,H}$ = 5.3 Hz, 2 H, H_{py}) ppm.

^{13}C-NMR (150.92 MHz, 22 °C, D_2O): δ = 46.7, 53.8, 53.8, 54.1, 62.1, 67.4, 70.1, 124.9, 126.3, 126.9, 128.9, 139.3, 144.9, 145.0, 146.2, 146.4, 147.9, 165.6, 168.5 ppm.

Elemental analysis (report no. 37566): [[Ga^{III}(**B1b**)]$(NO_3)_2$•$2H_2O$] calcd. C, 44.07; H, 4.34; N, 12.41 %; obsd. C, 43.75; H, 4.23; N, 12.26 %.

Solid state X-ray structure: co_kr26 (CCDC 1481470).

7.3.2 Metal complexes based on the octadentate bispa ligand

*[In^{III}(**B2**)](TFA) ($C_{37}H_{32}F_3InN_6O_{11}$, 908.51 g/mol)*.

Solutions of **B2**•H(TFA) (52.9 mg, 66.4 µmol, 1.0 eq) in 5 mL MeOH and $In(OAc)_3$•$5H_2O$ (27.9 mg, 73.0 µmol, 1.1 eq) in 30 mL H_2O were combined and the colorless solution was stirred for 2 h at room temperature. After evaporation of the solvent, the crude product was purified by reverse phase (RP)-HPLC using eluents: A: 0.1 % H(TFA) in H_2O and B: MeCN with a linear gradient of 5 to 100 % B over a period of 25 min and a flow rate set to 1 mL/min. The retention time of the metal complex was t_R ([In^{III}(**B2**)]$^+$) = 12.9 min. The HPLC fractions were combined and concentrated *in vacuo* yielding [In^{III}(**B2**)](TFA)•$5H_2O$ as a colorless solid (58.5 mg, 58.6 µmol, 88 %). Crystals suitable for X-ray analysis were obtained by slow evaporation from a methanolic solution.

^{1}H-NMR (400.19 MHz, 25 °C, D_2O): δ = 3.24 (d, $^{2}J_{H,H}$ = 12.0 Hz, 2 H, $N^7C\underline{H}_{2ax,eq}$), 3.46 (d, $^{2}J_{H,H}$ = 12.0 Hz, 2 H, $N^7C\underline{H}_{2ax,eq}$), 3.66 (s, 6 H, $COOC\underline{H}_3$), 4.54 (bs, 2 H, $N^7C\underline{H}_2$), 4.63 (s, 2 H, $N^3C\underline{H}_2$), 5.19 (s, 1 H, C<u>H</u>OH), 5.46 (bs, 2 H, $N^3C\underline{H}$), 7.31-7.34 (m, 2 H, H_{py}), 7.38 (d, $^{3}J_{H,H}$ = 7.7 Hz, 1 H, H_{py}), 7.43 (bd, $^{3}J_{H,H}$ = 7.5 Hz, 1 H, H_{py}), 7.84-7.90 (m, 3 H, H_{py}), 7.92-7.96 (m, 1 H, H_{py}), 7.98 (dd, $^{3}J_{H,H}$ = 6.9 Hz, $^{4}J_{H,H}$ = 2.0 Hz, 1 H, H_{py}), 8.35 (bs, $^{3}J_{H,H}$ = 5.1 Hz, 2 H, H_{py}), 8.48-8.54 (m, 2 H, H_{py}) ppm.

^{13}C-NMR (100.64 MHz, 25 °C, D_2O): δ = 51.3, 53.8, 54.4, 61.5, 62.8, 70.0, 71.1, 124.4, 125.8, 126.0, 126.2, 126.7, 128.1, 141.7, 143.9, 145.1, 145.5, 146.9, 149.8, 150.1, 150.6, 150.7, 167.2, 167.2, 170.1 ppm.

HR-ESI MS (pos, MeOH): [In^{III}(**B2**)]$^+$ calcd. 795.1264, obsd. 795.1268.

Elemental analysis (report no. 39940): [[In^{III}(**B2**)](TFA)•$5H_2O$] calcd. C, 44.50; H, 4.24; N, 8.42 %; obsd. C, 44.41; H, 4.08; N, 8.77 %.

Solid state X-ray structure: co500 (CCDC 1550810).

*[Lu^{III}(**B2**)](TFA) ($C_{37}H_{32}F_3LuN_6O_{11}$, 968.66 g/mol).*

Solutions of **B2**•H(TFA) (20.0 mg, 25.1 µmol, 1.0 eq) and $Lu(OAc)_3$•$4H_2O$ (10.7 mg, 25.1 µmol, 1.0 eq) in 3 mL MeOH each were combined and the colorless solution was stirred for 4 h at room temperature. After evaporation of the solvent, the residue was redissolved in MeOH and subjected to Et_2O diffusion yielding [Lu^{III}(**B2**)](TFA)•$3.5H_2O$ as a colorless solid (21.8 mg, 21.1 µmol, 84 %).

^{1}H-NMR (400.13 MHz, 25 °C, D_2O): δ = 2.77-2.85 (m, 2 H, $N^7CH_{2ax,eq}$), 3.09 (d, $^2J_{H,H}$ = 13.4 Hz, 1 H, $N^7CH_{2ax,eq}$), 3.36 (d, $^2J_{H,H}$ = 13.4 Hz, 1 H, $N^7CH_{2ax,eq}$), 3.72 (s, 3 H, $COOCH_3$), 3.77 (s, 3 H, $COOCH_3$), 3.84 (d, $^2J_{H,H}$ = 15.7 Hz, 1 H, N^7CH_2), 4.40-4.54 (m, 2 H, N^3CH_2), 4.86 (d, $^2J_{H,H}$ = 15.7 Hz, 1 H, N^7CH_2), 5.17 (s, 2 H, N^3CH), 5.19 (s, 1 H, CHOH), 6.98-7.00 (m, 1 H, H_{py}), 7.20 (ddd, $^3J_{H,H}$ = 7.9 Hz, $^3J_{H,H}$ = 3.9 Hz, $^4J_{H,H}$ = 1.2 Hz, 1 H, H_{py}), 7.33-7.37 (m, 2 H, H_{py}), 7.40 (bd, $^3J_{H,H}$ = 7.9 Hz, 1 H, H_{py}), 7.70-7.74 (m, 3 H, H_{py}), 7.81 (td, $^3J_{H,H}$ = 7.8 Hz, $^4J_{H,H}$ = 1.5 Hz, 1 H, H_{py}), 7.85 (td, $^3J_{H,H}$ = 7.8 Hz, $^4J_{H,H}$ = 1.7 Hz, 1 H, H_{py}), 8.09 (bd, $^3J_{H,H}$ = 7.6 Hz, 1 H, H_{py}), 8.16 (t, $^3J_{H,H}$ = 7.6 Hz, 1 H, H_{py}), 8.24 (dd, $^3J_{H,H}$ = 5.4 Hz, $^4J_{H,H}$ = 0.7 Hz, 1 H, H_{py}), 8.93 (dd, $^3J_{H,H}$ = 5.4 Hz, $^4J_{H,H}$ = 0.7 Hz, 1 H, H_{py}) ppm.

^{13}C-NMR (100.62 MHz, 25 °C, D_2O): δ = 48.2, 49.9, 53.4, 53.5, 53.6, 54.3, 67.4, 68.4, 70.4, 74.4, 74.6, 122.6, 122.9, 123.7, 124.8, 125.1, 125.6, 126.6, 140.5, 141.1, 141.5, 142.2, 150.1, 150.2, 150.8, 154.0, 155.2, 155.7, 156.2, 171.0, 171.1, 171.7, 172.2.

HR-ESI MS (pos, MeOH): [Lu^{III}(**B2**)]$^+$ calcd. 855.1633, obsd. 855.1641.

Elemental analysis (report no. 39879): [[Lu^{III}(**B2**)](TFA)•$3.5H_2O$] calcd. C, 43.07; H, 3.81; N, 8.15 %; obsd. C, 43.23; H, 4.11; N, 8.21 %.

*[La^{III}(**B2**)](TFA) ($C_{37}H_{32}F_3LaN_6O_{11}$, 932.60 g/mol)*.

Solutions of **B2**•H(TFA) (54.8 mg, 68.8 µmol, 1.0 eq) and $LaCl_3$•$7H_2O$ (25.5 mg, 68.8 µmol, 1.0 eq) in 10 mL MeOH each were combined and the pH was adjusted to 7 by addition of 10wt% NaOH. The colorless reaction mixture was stirred overnight at room temperature. After evaporation of the solvent, the crude product was purified by RP-HPLC using eluents: A: 0.1 % H(TFA) in H_2O and B: MeCN with a linear gradient of 5 to 100 % B over a period of 25 min and a flow rate set to 1 mL/min. The retention time of the metal complex was t_R ([La^{III}(**B2**)]$^+$) = 14.0 min. The HPLC fractions were combined and concentrated *in vacuo* yielding [La^{III}(**B2**)](TFA)•$5H_2O$ as a colorless solid (56.9 mg, 55.6 µmol, 81 %).

^{1}H-NMR (400.13 MHz, 25 °C, D_2O): δ = 2.55 (d, $^{2}J_{H,H}$ = 12.9 Hz, 1 H, $N^{7}C\underline{H}_{2ax,eq}$), 2.70 (d, $^{2}J_{H,H}$ = 12.9 Hz, 1 H, $N^{7}C\underline{H}_{2ax,eq}$), 2.76 (d, $^{2}J_{H,H}$ = 13.1 Hz, 1 H, $N^{7}C\underline{H}_{2ax,eq}$), 3.33 (d, $^{2}J_{H,H}$ = 13.1 Hz, 1 H, $N^{7}C\underline{H}_{2ax,eq}$), 3.56 (d, $^{2}J_{H,H}$ = 14.3 Hz, 1 H, $N^{7}C\underline{H}_{2}$), 3.63 (s, 3 H, $COOC\underline{H}_{3}$), 3.67 (s, 3 H, $COOC\underline{H}_{3}$), 4.32 (d, $^{2}J_{H,H}$ = 15.6 Hz, 1 H, $N^{3}C\underline{H}_{2}$), 4.48 (d, $^{2}J_{H,H}$ = 15.6 Hz, 1 H, $N^{3}C\underline{H}_{2}$), 4.68 (d, $^{2}J_{H,H}$ = 14.3 Hz, 1 H, $N^{7}C\underline{H}_{2}$), 4.92 (s, 1 H, $N^{3}C\underline{H}$), 4.99 (s, 1 H, $N^{3}C\underline{H}$), 5.04 (s, 1 H, $C\underline{H}OH$), 7.02 (d, $^{3}J_{H,H}$ = 7.8 Hz, 1 H, H_{py}), 7.16 (dd, $^{3}J_{H,H}$ = 6.9 Hz, $^{3}J_{H,H}$ = 5.6 Hz, 1 H, H_{py}), 7.32-7.46 (m, 4 H, H_{py}), 7.55 (td, $^{3}J_{H,H}$ = 7.8 Hz, $^{3}J_{H,H}$ = 1.4 Hz, 1 H, H_{py}), 7.67-7.72 (m, 2 H, H_{py}), 7.90 (td, $^{3}J_{H,H}$ = 7.8 Hz, $^{3}J_{H,H}$ = 1.4 Hz, 1 H, H_{py}), 8.13 (t, $^{3}J_{H,H}$ = 7.8 Hz, 1 H, H_{py}), 8.17 (dd, $^{3}J_{H,H}$ = 7.8 Hz, $^{4}J_{H,H}$ = 1.4 Hz, 1 H, H_{py}), 8.28 (bd, $^{3}J_{H,H}$ = 4.9 Hz, 1 H, H_{py}), 8.71 (bd, $^{3}J_{H,H}$ = 4.9 Hz, 1 H, H_{py}) ppm.

^{13}C-NMR (100.62 MHz, 25 °C, D_2O): δ = 50.0, 50.4, 53.3, 53.4, 53.9, 54.6, 66.0, 67.1, 70.5, 73.9, 75.1, 123.3, 124.3, 124.7, 125.0, 125.1, 125.3, 125.4, 127.2, 140.4, 140.5, 140.7, 141.4, 148.4, 149.5, 150.2, 151.3, 153.5, 155.3, 155.5, 155.8, 171.6, 171.7, 172.3, 173.1 ppm.

HR-ESI MS (pos, MeOH): $[La^{III}(\mathbf{B2})]^{+}$ calcd. 819.1289, obsd. 819.1311.

Elemental analysis (report no. 39880): $[[La^{III}(\mathbf{B2})](TFA)\cdot 5H_2O]$ calcd. C, 43.46; H, 4.14; N, 8.22 %; obsd. C, 43.41; H, 4.02; N, 8.07 %.

7.4 Details of the radiochemical investigations of the hexadentate bispa ligands

7.4.1 Materials and methods

Radionuclide production

The production of $^{64}Cu^{II}$ was performed at a PET cyclotron (Cyclone® 18/9, Helmholtz-Zentrum Dresden-Rossendorf) as described in detail elsewhere.[199] The yields of the nuclear reaction $^{64}Ni(p,n)^{64}Cu$ were between 3.6-5.2 GBq with molar activities of 150-250 GBq/µmol Cu^{II} diluted in 0.01 M HCl. The $^{68}Ga^{III}$ generator was purchased from Eckert & Ziegler (Berlin, Germany) with a nominal activity of 1100 MBq. The radionuclide $^{68}Ga^{III}$ was eluted as $[^{68}Ga]GaCl_3$ ($^{68}GaCl_3$) with 0.1 M HCl using the fractionated elution approach.[419]

Radio-thin layer chromatography (radio-TLC)

Neutral Al_2O_3 thin layer chromatography (TLC) plates (Merck, F_{254}) were used to assay the degree of $^{64}Cu^{II}$ radiolabeling, whereas instant TLC strips impregnated with silica gel (iTLC-SG, Agilent) were used to assay $^{68}Ga^{III}$ radiolabeling reaction progress and complex stability. After the development in an appropriate mobile phase (MP) the radio-TLC chromatograms were exposed to reusable imaging plates, which were then analyzed on the radioisotope thin layer analyzer BAS-1800II (Raytest). Radiochemical yields (RCY) were determined by integrating the peaks in the chromatograms.

Radio-high performance liquid chromatography (radio-HPLC) and radio-size exclusion chromatography (radio-SEC)

Radio-HPLC was performed on a Knauer WellChrom system equipped with the solvent organizer K-1500, the HPLC pump K-1001 (10 mL), a dynamic mixing chamber, the UV detector K-2501 and the gamma radioactivity detector Gabi Star (Raytest). A Phenomenex Aqua C18 column (250 mm x 4.6 mm, 125 Å, 5 µm) was used for separation and the injection volume was 10 µL. Radio-SEC was performed on the same Knauer WellChrom system with a self-packed Sephadex G25 size exclusion column (200 x 15 mm). Areas under the peaks observed in the HPLC and SEC radiotraces were integrated to determine complex stabilities.

Gel electrophoresis

Native polyacrylamide gel electrophoresis (PAGE) for the analysis of the SOD challenge experiments and sodium dodecyl sulfate (SDS)-PAGE for the analysis of the serum stability assays were performed according to the procedure described in reference [182].

7.4.2 Radiochemical studies with copper(II)-64 and gallium(III)-68

Radiolabeling experiments with bispa ligands

$^{64}Cu^{II}$ radiolabeling. Experiments were performed at final ligand concentrations of ~10^{-4}, $5 \cdot 10^{-5}$, 10^{-5}, $5 \cdot 10^{-6}$ and 10^{-6} M corresponding to 10, 5, 1, 0.5 and 0.1 µg of **B1a**•H(TFA) or **B1b**•H(TFA) in a total volume of 100 µL. In all radiochemical studies the ligands were used as TFA salts. The starting activities were 10 and 100 MBq, respectively, which corresponds to different volumes of $^{64}CuCl_2$ in 0.01 M HCl depending on the molar activity of different ^{64}Cu production runs and the time of ^{64}Cu use after end of bombardment (EOB). The aqueous sample solutions were diluted with 0.05 M 2-(*N*-morpholino)-ethanesulfonic acid (MES) / NaOH buffer (pH 5.5) such that the final volume was 100 µL after the addition of $^{64}CuCl_2$. Formation of the radiocopper(II) bispa complexes was quantified using radio-TLC after 5, 30 and 60 min. Small aliquots of the samples were spotted on neutral Al_2O_3 TLC plates and a 1:1 (v/v) mixture of 2 M NH_4OAc and MeOH was used as mobile phase (MP). At these conditions, the R_f-values of the radiolabeled compounds were R_f ($^{64}CuCl_2$) = 0, R_f (^{64}Cu-**B1a**) = 0.8, and R_f (^{64}Cu-**B1b**) = 0.8.

The molar activity of a compound can be calculated according to the following equation:

$$\text{molar activity} = \frac{\text{RCY [\%]} \cdot \text{starting activity}}{\text{amount of substance}} \qquad \text{Eq. 7}$$

In the case of $^{64}Cu^{II}$-**B1a** 0.1 µg (148 pmol) **B1a**•H(TFA) was reacted with 100 MBq $^{64}CuCl_2$. With a radiochemical yield (RCY) of 15 % after 5 min this leads to a molar activity of ~100 GBq/µmol. The molar activity of **B1b** was calculated based on a radiolabeling experiment under the same conditions with a RCY of 30 %.

$^{68}Ga^{III}$ radiolabeling. Experiments were carried out at final ligand concentrations of ~10^{-4}, $5 \cdot 10^{-5}$, 10^{-5}, $5 \cdot 10^{-6}$ and 10^{-6} M corresponding to 30, 15, 3, 1.5 and 0.3 µg of **B1a**•H(TFA) in a total volume of 300 µL. Therefore, a 1 mg/mL stock solution of **B1a**•H(TFA) in 1 M NaOAc buffer (pH 4.6) with 10 % EtOH was prepared. For example to obtain a ligand

concentration of ~10^{-4} M, 30 µL stock solution, 231 µL 1 M NaOAc buffer (pH 4.6) and 39 µL $^{68}GaCl_3$ in 0.1 M HCl (~65 MBq) were combined. The volume aliquots of $^{68}GaCl_3$ were chosen depending on the activity of the $^{68}Ga^{III}$-eluate. The samples were incubated at 37 °C and 750 rpm in the thermomixer. The degree of radiolabeling was monitored by radio-TLC after 5, 10, 15 and 30 min. Small aliquots of the samples were spotted on iTLC-SG plates and a 1:1 (v/v) mixture of 2 M NH_4OAc and MeOH was used as mobile phase (MP). At these conditions, the R_f-values were R_f ($^{68}GaCl_3$) = 0 and R_f ($^{68}Ga^{III}$-**B1a**) = 0.87. The molar activity of **B1a** was calculated based on a radiolabeling experiment using 0.5 µg ligand (~5•10^{-6} M) and 47.6 MBq $^{68}GaCl_3$ with a RCY of 55 % after 15 min.

Competition assays of radiolabeled bispa ligands

$^{64}Cu^{II}$ complex stability studies in cyclam and EDTA. For the challenge experiments 100 µg (148 nmol, 1.0 eq) **B1a**•H(TFA) or **B1b**•H(TFA) in 0.05 M MES / NaOH buffer (pH 5.5) was radiolabeled with 10 MBq $^{64}CuCl_2$. Quantitative formation of $^{64}Cu^{II}$-**B1a** and $^{64}Cu^{II}$-**B1b** was confirmed by radio-TLC as described above. Subsequently 2.97 mg (14.8 µmol, 100 eq) cyclam or 4.33 mg (14.8 µmol, 100 eq) EDTA in MES / NaOH buffer was added, resulting in a total volume of 200 µL. After 2 and 24 h the samples were analyzed by radio-HPLC using eluents A: 0.1 % H(TFA) in H_2O and B: 0.1 % H(TFA) in MeCN with a gradient of 0 to 70 % B over a period of 20 min, 70 to 100 % B over a period of 2 min, 100 % B for 5 min and a flow rate set to 1 mL/min. The retention times of the compounds were t_R ($^{64}Cu^{II}$-EDTA) = 4.8 min, t_R ($^{64}Cu^{II}$-cyclam) = 9.5 min, t_R ($^{64}Cu^{II}$-**B1a**) = 13.8 min, and t_R ($^{64}Cu^{II}$-**B1b**) = 14.4 min. All experiments were performed in triplicate and samples with the pure $^{64}Cu^{II}$-(competing ligand) complex and with $^{64}CuCl_2$, respectively, were always prepared as references and analyzed in parallel.

$^{64}Cu^{II}$ complex stability studies in superoxide dismutase (SOD) and human serum. The challenge assays of $^{64}Cu^{II}$-**B1a** and $^{64}Cu^{II}$-**B1b** were carried out according to the procedures described in reference [182]. The experiments were performed in triplicate and the amount of transchelation is given as mean value ± standard deviation. The Coomassie stained polyacrylamide gels and autoradiographies are depicted in Appendix H. The serum stability of $^{64}Cu^{II}$-**B1a** and $^{64}Cu^{II}$-**B1b** was additionally analyzed by radio-SEC. The $^{64}Cu^{II}$-bispa complexes were prepared by incubating 10.1 µL (15 nmol) **B1a**•H(TFA) or **B1b**•H(TFA), 130.9 µL 0.05 M MES / NaOH buffer (pH 5.5), and 9 µL $^{64}CuCl_2$ in 0.01 M HCl (~35 MBq) for 20 min at 25 °C. Quantitative formation was confirmed by radio-TLC as described above after which 100 µL of the samples were added to 50 µL 0.05 M 4-(2-

hydroxyethyl)-1-piperazine ethanesulfonic acid (HEPES) / NaOH buffer (pH 7.4) and 250 µL human serum. During incubation at 37 °C and 750 rpm in a thermomixer the samples were analyzed by radio-SEC at time points of 2 and 24 h. 150 mM PBS was used as eluent with a flow rate of 1 mL/min and these conditions allowed the clear separation of the relevant compounds with the following retention times: t_R ($^{64}Cu^{II}$-serum) = 6.8 min, t_R ($^{64}Cu^{II}$-**B1a**) = 14.2 min, and t_R ($^{64}Cu^{II}$-**B1b**) = 21.2 min.

$^{68}Ga^{III}$ complex stability studies in EDTA and human serum. For the EDTA challenge experiment the following stock solutions were prepared: 1 mg/mL **B1a**•H(TFA) in 1 M NaOAc buffer (pH 4.6) with 10 % EtOH and 14.8 M EDTA in 0.1 M MES / NaOH buffer (pH 5.5). In the first step 100 µL (100 µg, 148 nmol, 1.0 eq) **B1a** solution were radiolabeled with ~20 MBq $^{68}GaCl_3$. Prior to the addition of 100 µL (433 µg, 1.48 µmol, 10 eq) EDTA solution, quantitative formation of $^{68}Ga^{III}$-**B1a** was confirmed by radio-TLC as described above. The samples were subsequently incubated at 25 °C and 750 rpm in a thermomixer. At time points of 1, 2 and 4 h small aliquots were taken and analyzed by radio-TLC using iTLC-SG plates and 0.1 M citric acid as mobile phase (MP). With this MP $^{68}Ga^{III}$-**B1a** and $^{68}Ga^{III}$-EDTA can be separated chromatographically with R_f values of 0 and 0.93, respectively. The experiments were performed in duplicate. The human serum stability assay with $^{68}Ga^{III}$-**B1a** was carried out according to the procedure published for $^{64}Cu^{II}$ complexes in reference [182]. Aliquots of the **B1a** stock solution were first radiolabeled with $^{68}GaCl_3$ at 50 °C and 750 rpm for 30 min (10 µg ligand, 135 µL total volume, ~70 MBq). The samples were analyzed by radio-TLC as described above to confirm quantitative radiolabeling and then incubated with human serum for 1 h at 37 °C. The remaining analysis steps were performed as described in the literature.[182] The experiments were undertaken in triplicate and the resulting gel is depicted in Appendix H.

Lipophilicity studies of $^{64}Cu^{II}$-bispa complexes

Aqueous solutions containing 1 mM bispa ligand **B1a**•H(TFA) or **B1b**•H(TFA) and 100 µM $Cu(NO_3)_2$ spiked with 4 MBq $^{64}CuCl_2$ were prepared. Full complexation was checked by radio-TLC or radio-HPLC, which gave no evidence of free copper(II)-64 in the aqueous phase. Then, 50 µL of this solution was added to 450 µL of 0.05 M 4-(2-hydroxyethyl)-1-piperazine ethanesulfonic acid (HEPES) / NaOH (pH of 7.2, 7.4, 7.6). The distribution experiments in 1-octanol / buffer systems were carried out at 25 ± 1 °C in microcentrifuge tubes (2 mL) with mechanical shaking for 30 min. The phase ratio V (1-octanol) / V (aqueous solution) was 1:1 (0.5 mL each). All samples were centrifuged and the phases separated. The copper complex concentration in both phases was

determined radiometrically using γ radiation (^{64}Cu, NaI(Tl) scintillation counter automatic γ counter 1480, Wizard 3'', PerkinElmer). All experiments were performed four times to obtain an average value.

Biodistribution of $^{64}Cu^{II}$- and $^{68}Ga^{III}$-bispa^{1} complexes

The animal experiments were carried out in male Wistar rats (Wistar-Kyoto strain; aged 7-8 weeks, 140-195 g; Harlan Winkelmann GmbH, Borchen, Germany) according to the guidelines of the German Regulations for Animal Welfare. The protocol was approved by the local Ethical Committee for Animal Experiments. The biodistribution studies were performed by Prof. Dr. Jens PIETZSCH and coworkers as published in detail elsewhere.[172,393]

The preparation of the radiolabeled ligands $^{64}Cu^{II}$-**B1a** and $^{64}Cu^{II}$-**B1b** was carried out by Karin LANDROCK in the group of Dr. Holger STEPHAN. Therefore, 1 mg/mL stock solutions of the bispa ligands **B1a**•H(TFA) and **B1b**•H(TFA) in 0.05 M MES / NaOH buffer (pH 5.5) were prepared, respectively. In the next step 1.5 µL ligand solution, 136.5 µL MES buffer (see above) and 12 µL $^{64}CuCl_2$ in 0.01 M HCl (~50 MBq) were combined and incubated for 20 min at 25 °C. The samples were subsequently checked for quantitative radiolabeling by radio-TLC as described above and then used for the biodistribution studies. The $^{68}Ga^{III}$-**B1a** sample was prepared by Madlen MATTERNA in the group of Dr. Holger STEPHAN. **B1a**•H(TFA) was first dissolved in a 1 M NH_4OAc buffer (pH 7) with 10 % EtOH to obtain a ligand concentration of 1 mg/mL. A 100 µL ligand solution, 750 µL NH_4OAc buffer (see above), and 150 µL $^{68}GaCl_3$ in 1 M HCl were combined and incubated for 30 min at 50 °C and 750 rpm. Quantitative radiolabeling was checked by radio-TLC as described above.

The accumulated radioactivity in organs and tissues was calculated as either the percentage of the injected dose per gram (%ID/g) or, for stomach, intestine, feces, and urine, the percentage of injected dose (%ID). The corresponding data is given in Appendix H.

7.5 Details of the radiochemical investigations of the octadentate bispa ligand

7.5.1 Materials and methods

Radionuclide production

$^{111}InCl_3$ was cyclotron produced and provided by Nordion (Vancouver, BC, Canada) as a ~0.05 M HCl solution. $^{177}LuCl_3$ was purchased from Perkin-Elmer and received as ~0.05 M HCl solution. $^{225}Ac(NO_3)_3$ in 0.05 M HNO_3 was produced in-house (TRIUMF) by the spallation of a uranium carbide target and separated downstream from other radionuclides by a mass separator,[420,421] chemical purification of $^{225}Ac^{III}$ was accomplished by modifying previously published procedures on a *N,N,N',N'*-tetrakis-2-ethylhexylglycolamide (DGA) resin (branched, 50-100 µm, Eichrom Technologies LLC).[422,423]

Radio-thin layer chromatography (radio-TLC)

Instant thin layer chromatography paper strips impregnated with silica gel (iTLC-SG, Varian) were used to analyze $^{225}Ac^{III}$ radiolabeling reaction progress and complex stability and were counted on a BioScan System 200 imaging scanner equipped with a BioScan Autochanger 1000.

Radio-high performance liquid chromatography (radio-HPLC)

Analysis of $^{111}In^{III}$- and $^{177}Lu^{III}$-radiolabeled complexes was carried out using a Phenomenex Synergi 4 µ Hydro-RP analytical column (250 mm x 4.60 mm, 80 Å, 4 µm) using an Agilent HPLC system equipped with a model 1200 quaternary pump, a model 1200 UV absorbance detector (set at 254 nm), and a Raytest Gabi Star NaI(Tl) detector.

7.5.2 Radiochemical studies with indium(III)-111, lutetium(III)-177, and actinium(III)-225

Radiolabeling experiments with bispa ligand B2

$^{111}In^{III}$ and $^{177}Lu^{III}$ radiolabeling. The radiolabeling procedures followed closely those outlined previously.[58,424] Briefly, **B2**•H(TFA) and standard DOTA was made up as a stock solution (1 mg/mL, ~10^{-3} M) in deionized water. Using serial dilution, stock ligand solutions of **B2**•H(TFA) with concentrations of ~10^{-4}-10^{-6} M were also prepared. A 100 µL aliquot of each ligand stock solution (or 100 µL of deionized water as a blank) was added to a screw-cap mass spectrometry vial and diluted with sodium acetate buffer (10 mM, pH 4) such that the final volume was 1.0 mL after the addition of $^{111}InCl_3$ or $^{177}LuCl_3$, resulting in final ligand concentrations of 10^{-4}-10^{-7} M. An aliquot of $^{111}InCl_3$ or $^{177}LuCl_3$ (~3.7-18.5 MBq for labeling and ~111-333 MBq for serum competition) was added to the vials containing the ligand and buffer and allowed to react at ambient temperature for 10 min. The reaction mixture was analyzed by radio-HPLC to confirm radiolabeling and calculate yields. Areas under the peaks observed in the HPLC radiotrace were integrated to determine radiolabeling yields. For radio-HPLC the eluents A: 0.1 % H(TFA) in H_2O and B: MeCN were used with a linear gradient of 0 to 100 % B over a period of 20 min and a flow rate set to 1 mL/min. The retention times of the compounds were t_R ($^{111}In^{III}$-**B2**) = 10.5 min, t_R ($^{177}Lu^{III}$-**B2**) = 10.9 min, t_R ($^{111}InCl_3$) = ~5-7 min, and t_R ($^{177}LuCl_3$) = 3.3-3.5 min. The molar activity of **B2** with indium(III)-111 was calculated based on a radiolabeling experiment using 0.1 µg ligand (10^{-7} M) and 8.9 MBq $^{111}InCl_3$ at pH 4 resulting in a RCY of > 99 % after 10 min at room temperature. For the calculation of the molar activity of **B2** with lutetium(III)-177 an experiment with the following reaction conditions was used: 100 µg ligand (10^{-4} M), 3.7 MBq $^{177}LuCl_3$, pH 4, RCY = 49 % after 15 min at room temperature.

$^{225}Ac^{III}$ radiolabeling. A stock ligand solution of **B2** was prepared (10 mg/mL) in deionized water. A 10 µL (100 µg) aliquot of ligand stock was added to a screw-cap mass spectrometry vial and diluted with 140-150 µL ammonium acetate buffer (0.15 M, pH 6). To the vial containing ligand and buffer, $^{225}Ac(NO_3)_3$ (10 µL, 40 kBq) was added, and the reaction was left to react at ambient temperature. Radiolabeling reactions were analyzed by modifying previously published procedures.[120,288,408,425] Reaction progress was analyzed at 5, 30 and 60 min by spotting a small aliquot on iTLC-SG paper (1-5 µL, 2 x 10 cm strips), and developing the strips with mobile phase (MP) A: 10 mM NaOH / 9 % NaCl solution, or spotting an aliquot on aluminum backed silica TLC plates developed

in MP B: 0.4 M sodium citrate, pH 4 with 10 % methanol. With MP A, uncomplexed $^{225}Ac^{III}$ precipitates and sticks to the baseline (R_f = 0) while $^{225}Ac^{III}$-chelate species migrate up the plate (R_f > 0.5); with MP B, uncomplexed $^{225}Ac^{III}$ travels with the solvent front (R_f ~ 1) while $^{225}Ac^{III}$ complexes stick to the baseline (R_f = 0). Developed plates were counted immediately and the following day to allow for $^{213}Bi^{III}$ decay ($t_{1/2}$ = 45.6 min[27]), and corrected $^{225}Ac^{III}$ radiolabeling yields were calculated by integrating the peaks in the radiochromatogram. The molar activity of **B2** with actinium(III)-225 was calculated based on a radiolabeling experiment using 1 µg ligand (10^{-6} M) and 40 kBq $^{225}Ac(NO_3)_3$ at pH 6 resulting in 64 % RCY after 30 min at room temperature.

Competition assays of radiolabeled bispa ligand B2

$^{111}In^{III}$ and $^{177}Lu^{III}$ complex stability studies in human serum. $^{111}In^{III}$- or $^{177}Lu^{III}$-ligand human serum stability experiments were analyzed using GE Healthcare Life Sciences PD-10 desalting columns (size exclusion for MW < 5000 Da) and counted with a Capintec CRC 55t dose calibrator. The procedures closely followed those outlined previously.[58,424] The compounds $^{111}In^{III}$-**B2** and $^{177}Lu^{III}$-**B2** and corresponding blanks were prepared with the radiolabeling protocol described above. Solutions were prepared in vials with 1.0 mL of human serum, 325 µL of $^{111}In^{III}$ or $^{177}Lu^{III}$ complex, and 675 µL of phosphate buffered saline (PBS, pH 7.4) and incubated at 37 °C in a sand bath. The experiments were performed in triplicate for each $^{111}In^{III}$ and in duplicate for each $^{177}Lu^{III}$ complex. For $^{111}In^{III}$ competitions, at time points of 1 h, 1 and 5 d, 400 µL of the human serum competition mixture were removed from each vial (800 µL were removed for the last time point). For $^{177}Lu^{III}$ competitions, after 1 h, 1, 5 and 7 d, 330, 330, 660 and 660 µL of the human serum competition mixture were removed, respectively. The aliquot was diluted to a total of 2.5 mL with PBS, and then counted in a dose calibrator to obtain a value for the total activity to be loaded on the PD-10 column (*F*). The diluted human serum mixture (2.5 mL) was then loaded onto the PD-10 column (pre-conditioned with 20 mL of PBS) and the empty vial was counted in the dose calibrator to determine the residual activity left in the vial (*R*). The 2.5 mL of loading volume were eluted into a waste container, and then the PD-10 column was eluted with 3.5 mL of PBS and collected into a separate vial. The eluent that contained $^{111}In^{III}$ or $^{177}Lu^{III}$ bound / associated with serum proteins (size exclusion for MW < 5000 Da) was counted in the dose calibrator (*E*) and then compared to the total amount of activity that was loaded on the PD-10 column to obtain the percentage of $^{111}In^{III}$ or $^{177}Lu^{III}$ that was still ligand-bound and not transchelated to serum proteins using the equation: 1–[*E*(*F*–*R*)].

$^{225}Ac^{III}$ complex stability studies in human serum. The compound $^{225}Ac^{III}$-**B2** was prepared with the radiolabeling procedure described above. To the reaction vial containing the radiometal-ligand complex (160-170 µL), an equal volume of human serum was added and the competition mixture was incubated at room temperature. The experiments were performed in triplicate for $^{225}Ac^{III}$-**B2** and in duplicate for $^{225}Ac^{III}$-DOTA. At time points of 1 h, 1, 3, 5 and 7 d, aliquots (5 µL) were spotted on iTLC-SG plates and developed with MP A, as described above, or on aluminum backed silica TLC plates developed with MP C: 50 mM EDTA, pH 5. Using MP C, chelate-bound $^{225}Ac^{III}$ sticks to the baseline (R_f = 0), and any $^{225}Ac^{III}$ that has de-complexed from the chelate will travel with the solvent front (R_f ~ 1). The TLC gradient was validated by incubating "free" $^{225}Ac^{III}$ with human serum under analogous conditions, to ensure that all the activity is eluted with the solvent front (R_f ~1).

La^{III} exchange $^{225}Ac^{III}$ Complex Stability Studies. The compound $^{225}Ac^{III}$-**B2** was prepared according to the radiolabeling procedure as described above. An aliquot of lanthanum(III) nitrate solution (0.1 M, 6.3 µL, 5 eq compared to **B2**) was added to the preformed $^{225}Ac^{III}$ complex, and the mixture was allowed to react at ambient temperature. After 0.08, 0.2, 1, 3, 6, and 7 d, aliquots of the competition reactions (1-3 µL) were spotted on aluminum backed silica TLC plates and developed with MP B as described above.

8 Bibliography

[1] A. Werner, *Z. anorg. Chem.* **1893**, *3*, 267-330.
[2] L. H. Gade, *Koordinationschemie*, 2. korrigierter Nachdruck, Wiley-VCH, Weinheim, **2008**.
[3] E. C. Constable, C. E. Housecroft, *Chem. Soc. Rev.* **2013**, *42*, 1429-1439.
[4] A. Werner, *Lehrbuch der Stereochemie*, University of California Libraries, **1904**.
[5] G. Duca, *Homogeneous catalysis with metal complexes*, Springer, Berlin, Heidelberg, **2012**.
[6] S. J. Lippard, *Angew. Chem., Int. Ed.* **1988**, *27*, 344-361.
[7] M. Costas, K. Chen, L. Que Jr, *Coord. Chem. Rev.* **2000**, *200–202*, 517-544.
[8] T. R. Simmons, G. Berggren, M. Bacchi, M. Fontecave, V. Artero, *Coord. Chem. Rev.* **2014**, *270–271*, 127-150.
[9] Z. Guo, P. J. Sadler, *Angew. Chem.* **1999**, *111*, 1610-1630.
[10] K. D. Mjos, C. Orvig, *Chem. Rev.* **2014**, *114*, 4540-4563.
[11] B. Lippert, *Cisplatin: chemistry and biochemistry of a leading anticancer drug*, Wiley-VCH, Weinheim, **1999**.
[12] R. C. Blodgett Jr, M. A. Heuer, R. G. Pietrusko, *Sem. Arthr. Rheum.* **1984**, *13*, 255-273.
[13] D. H. Brown, W. E. Smith, *Chem. Soc. Rev.* **1980**, *9*, 217-240.
[14] H. L. DuPont, *Drug Intell. Clin. Pharm.* **1987**, *21*, 687-693.
[15] N. Yang, H. Sun, *Coord. Chem. Rev.* **2007**, *251*, 2354-2366.
[16] P. Caravan, J. J. Ellison, T. J. McMurry, R. B. Lauffer, *Chem. Rev.* **1999**, *99*, 2293-2352.
[17] S. Jurisson, D. Berning, W. Jia, D. Ma, *Chem. Rev.* **1993**, *93*, 1137-1156.
[18] K. Schwochau, *Angew. Chem., Int. Ed.* **1994**, *33*, 2258-2267.
[19] B. M. Zeglis, J. L. Houghton, M. J. Evans, N. Viola-Villegas, J. S. Lewis, *Inorg. Chem.* **2013**, *53*, 1880-1899.
[20] D. Brasse, A. Nonat, *Dalton Trans.* **2015**, *44*, 4845-4858.
[21] C. F. Ramogida, C. Orvig, *Chem. Commun.* **2013**, *49*, 4720-4739.
[22] P. J. Blower, *Dalton Trans.* **2015**, *44*, 4819-4844.
[23] A. Vértes, S. Nagy, Z. Klencsár, R. G. Lovas, F. Rösch, *Handbook of Nuclear Chemistry: Basics of Nuclear Science, volume 1*, Kluwer Academic Publishers, **2003**.
[24] J. T. Bushberg, J. M. Boone, *The essential physics of medical imaging*, 3rd edition, Lippincott Williams & Wilkins, **2011**.
[25] Y.-S. Kim, M. W. Brechbiel, *Tumor biology* **2012**, *33*, 573-590.
[26] A. I. Kassis, S. J. Adelstein, *J. Nucl. Med.* **2005**, *46*, 4S-12S.
[27] The LUND/LBNL nuclear data search, version 2.0, February 1999, http://nucleardata.nuclear.lu.se/toi/, accessed 24 February 2017.
[28] R. P. Baum, *Therapeutic nuclear medicine*, Springer, **2014**.
[29] M. N. Wernick, J. N. Aarsvold, *Emission tomography: the fundamentals of PET and SPECT*, Academic Press, **2004**.
[30] H. Herzog, F. Rösch, *Pharm. unserer Zeit* **2005**, *34*, 468-473.
[31] C. M. Gomes, A. J. Abrunhosa, P. Ramos, E. K. J. Pauwels, *Adv. Drug Delivery Rev.* **2011**, *63*, 547-554.
[32] M. Bauser, L. Lehmann, *Chem. unserer Zeit* **2012**, *46*, 80-99.
[33] I. Verel, G. W. M. Visser, G. A. van Dongen, *J. Nucl. Med.* **2005**, *46 Suppl 1*, 164S-171S.
[34] G. B. Saha, *Basics of PET imaging: physics, chemistry, and regulations*, Springer, **2015**.

[35] R. A. Pagnanelli, D. A. Basso, *J. Nucl. Med. Technol.* **2010**, *38*, 1-3.
[36] D. W. Jones, P. Hogg, E. Seeram, *Practical SPECT/CT in nuclear medicine*, Springer, London, **2013**.
[37] T. F. Brown, N. J. Yasillo, *J. Nucl. Med. Technol.* **1997**, *25*, 98-102.
[38] B. M. Zeglis, J. S. Lewis, *Dalton Trans.* **2011**, *40*, 6168-6195.
[39] K. Pant, O. Sedláček, R. A. Nadar, M. Hrubý, H. Stephan, *Adv. Healthcare Mater.* **2017**, DOI 10.1002/adhm.201601115.
[40] A. Vértes, S. Nagy, Z. Klencsár, R. G. Lovas, F. Rösch, *Handbook of Nuclear Chemistry: Radiochemistry and radiopharmaceutical chemistry in life sciences, volume 4*, Kluwer Academic Publishers, **2003**.
[41] T. J. Wadas, D. N. Pandya, K. K. Solingapuram Sai, A. Mintz, *Am. J. Roentgenol.* **2014**, *203*, 253-260.
[42] C. A. Boswell, M. W. Brechbiel, *J. Nucl. Med.* **2005**, *46*, 1946-1947.
[43] J. Schmaljohann, H. J. Biersack, S. Guhlke, *Pharm. unserer Zeit* **2005**, *34*, 498-504.
[44] C. S. Cutler, H. M. Hennkens, N. Sisay, S. Huclier-Markai, S. S. Jurisson, *Chem. Rev.* **2013**, *113*, 858-883.
[45] F. Rösch, R. P. Baum, *Dalton Trans.* **2011**, *40*, 6104-6111.
[46] S. S. Kelkar, T. M. Reineke, *Bioconjugate Chem.* **2011**, *22*, 1879-1903.
[47] S. C. Srivastava, *Semin. Nucl. Med.* **2012**, *42*, 151-163.
[48] E. W. Price, C. Orvig, *Chem. Soc. Rev.* **2014**, *43*, 260-290.
[49] A. Singh, H. R. Kulkarni, R. P. Baum, *PET Clinics* **2017**, *12*, 193-203.
[50] I. Novak-Hofer, A. P. Schubiger, *Eur. J. Nucl. Med. Mol. Imaging* **2002**, *29*, 821-830.
[51] H. Zhang, K. Abiraj, D. L. Thorek, B. Waser, P. M. Smith-Jones, M. Honer, J. C. Reubi, H. R. Maecke, *PLoS One* **2012**, *7*, e44046.
[52] C. Müller, M. Bunka, S. Haller, U. Köster, V. Groehn, P. Bernhardt, N. van der Meulen, A. Türler, R. Schibli, *J. Nucl. Med.* **2014**, *55*, 1658-1664.
[53] A. Jonkhoff, P. Huijgens, R. Versteegh, E. Van Dieren, G. Ossenkoppele, H. Martens, G. Teule, *Br. J. Cancer* **1993**, *67*, 693.
[54] S. R. Banerjee, M. G. Pomper, *Appl. Radiat. Isot.* **2013**, *76*, 2-13.
[55] H. Herzog, F. Rösch, G. Stöcklin, C. Lueders, S. M. Qaim, L. E. Feinendegen, *J. Nucl. Med.* **1993**, *34*, 2222-2226.
[56] S. Palm, R. M. Enmon, C. Matei, K. S. Kolbert, S. Xu, P. B. Zanzonico, R. L. Finn, J. A. Koutcher, S. M. Larson, G. Sgouros, *J. Nucl. Med.* **2003**, *44*, 1148-1155.
[57] M. Fani, H. Maecke, S. Okarvi, *Theranostics* **2012**, *2*, 481-501.
[58] E. W. Price, B. M. Zeglis, J. F. Cawthray, C. F. Ramogida, N. Ramos, J. S. Lewis, M. J. Adam, C. Orvig, *J. Am. Chem. Soc.* **2013**, *135*, 12707-12721.
[59] D. Hanahan, Robert A. Weinberg, *Cell* **2011**, *144*, 646-674.
[60] C. Sawyers, *Nature* **2004**, *432*, 294-297.
[61] M. Abercrombie, E. Ambrose, *Cancer Res.* **1962**, *22*, 525-548.
[62] H. Maeda, J. Wu, T. Sawa, Y. Matsumura, K. Hori, *J. Controlled Release* **2000**, *65*, 271-284.
[63] H. Koo, M. S. Huh, I.-C. Sun, S. H. Yuk, K. Choi, K. Kim, I. C. Kwon, *Acc. Chem. Res.* **2011**, *44*, 1018-1028.
[64] D.-E. Lee, H. Koo, I.-C. Sun, J. H. Ryu, K. Kim, I. C. Kwon, *Chem. Soc. Rev.* **2012**, *41*, 2656-2672.
[65] K. Zarschler, L. Rocks, N. Licciardello, L. Boselli, E. Polo, K. P. Garcia, L. De Cola, H. Stephan, K. A. Dawson, *Nanomedicine: NMB* **2016**, *12*, 1663-1701.
[66] G. Ting, C.-H. Chang, H.-E. Wang, *Anticancer Res.* **2009**, *29*, 4107-4118.
[67] T. Ido, C. N. Wan, J. S. Fowler, A. P. Wolf, *J. Org. Chem.* **1977**, *42*, 2341-2342.
[68] P. Som, H. L. Atkins, D. Bandoypadhyay, J. S. Fowler, R. R. MacGregor, K. Matsui, Z. H. Oster, D. F. Sacker, C. Y. Shiue, H. Turner, C.-N. Wan, A. P. Wolf, S. V. Zabinski, *J. Nucl. Med.* **1980**, *21*, 670-675.

[69] A. W. J. M. Glaudemans, R. H. Enting, M. A. A. M. Heesters, R. A. J. O. Dierckx, R. W. J. van Rheenen, A. M. E. Walenkamp, R. H. J. A. Slart, *Eur. J. Nucl. Med. Mol. Imaging* **2013**, *40*, 615-635.
[70] H.-J. Machulla, *Pharm. unserer Zeit* **2005**, *34*, 490-497.
[71] M. Fani, H. R. Maecke, *Eur. J. Nucl. Med. Mol. Imaging* **2012**, *39*, 11-30.
[72] J. C. Reubi, *Endocr. Rev.* **2003**, *24*, 389-427.
[73] D. M. Goldenberg, *J. Nucl. Med.* **2002**, *43*, 693-713.
[74] D. E. Milenic, E. D. Brady, M. W. Brechbiel, *Nat. Rev. Drug Discovery* **2004**, *3*, 488-499.
[75] C. A. Boswell, M. W. Brechbiel, *Nucl. Med. Biol.* **2007**, *34*, 757-778.
[76] E. Fischer, *Ber. Dtsch. Chem. Ges.* **1894**, *27*, 2985-2993.
[77] D. E. Koshland, *Angew. Chem., Int. Ed.* **1995**, *33*, 2375-2378.
[78] M. Patra, K. Zarschler, H.-J. Pietzsch, H. Stephan, G. Gasser, *Chem. Soc. Rev.* **2016**, *45*, 6415-6431.
[79] A. Janecka, M. Zubrzycka, T. Janecki, *J. Pept. Res.* **2001**, *58*, 91-107.
[80] G. Olias, C. Viollet, H. Kusserow, J. Epelbaum, W. Meyerhof, *J. Neurochem.* **2004**, *89*, 1057-1091.
[81] G. Weckbecker, I. Lewis, R. Albert, H. A. Schmid, D. Hoyer, C. Bruns, *Nat. Rev. Drug Discovery* **2003**, *2*, 999-1017.
[82] J. C. Reubi, L. Kvols, E. Krenning, S. W. J. Lamberts, *Metabolism* **1990**, *39*, 78-81.
[83] J. C. Reubi, J. Laissue, E. Krenning, S. W. J. Lamberts, *J. Steroid Biochem. Mol. Biol.* **1992**, *43*, 27-35.
[84] S. W. J. Lamberts, E. P. Krenning, R. Jean-Claude, *Endocr. Rev.* **1991**, *12*, 450-482.
[85] Y. C. Patel, T. Wheatley, *Endocrinology* **1983**, *112*, 220-225.
[86] A. G. Harris, *Gut* **1994**, *35*, S1-S4.
[87] E. Pohl, A. Heine, G. M. Sheldrick, Z. Dauter, K. S. Wilson, J. Kallen, W. Huber, P. J. Pfaffli, *Acta Cryst. Section D* **1995**, *51*, 48-59.
[88] Q. Wang, K. Graham, T. Schauer, T. Fietz, A. Mohammed, X. Liu, J. Hoffend, U. Haberkorn, M. Eisenhut, W. Mier, *Nucl. Med. Biol.* **2004**, *31*, 21-30.
[89] N. Iznaga-Escobar, *Nucl. Med. Biol.* **1998**, *25*, 441-447.
[90] P. O. Zamora, M. J. Marek, F. F. Knapp Jr, *Appl. Radiat. Isot.* **1997**, *48*, 305-309.
[91] H. Kolan, J. Li, M. Thakur, *Pept. Res.* **1995**, *9*, 144-150.
[92] M. M. Alauddin, L. A. Khawli, A. L. Epstein, *Int. J. Radiat. Appl. Instrum. Part B* **1992**, *19*, 445-454.
[93] B. A. Rhodes, *Int. J. Radiat. Appl. Instrum. Part B* **1991**, *18*, 667-676.
[94] G. L. Griffiths, D. M. Goldenberg, F. F. Knapp, A. P. Callahan, C.-H. Chang, H. J. Hansen, *Cancer Res.* **1991**, *51*, 4594-4602.
[95] V. Carroll, D. W. Demoin, T. J. Hoffman, S. S. Jurisson, *Radiochim. Acta* **2012**, *100*, 653-667.
[96] M. J. Heeg, S. S. Jurisson, *Acc. Chem. Res.* **1999**, *32*, 1053-1060.
[97] M. Brinkley, *Bioconjugate Chem.* **1992**, *3*, 2-13.
[98] T. L. Mindt, C. Müller, F. Stuker, J.-F. Salazar, A. Hohn, T. Mueggler, M. Rudin, R. Schibli, *Bioconjugate Chem.* **2009**, *20*, 1940-1949.
[99] C. A. G. N. Montalbetti, V. Falque, *Tetrahedron* **2005**, *61*, 10827-10852.
[100] V. D. Bock, H. Hiemstra, J. H. van Maarseveen, *Eur. J. Org. Chem.* **2006**, *2006*, 51-68.
[101] J. M. Baskin, C. R. Bertozzi, *QSAR Comb. Sci.* **2007**, *26*, 1211-1219.
[102] A. Y. Lebedev, J. P. Holland, J. S. Lewis, *Chem. Commun.* **2010**, *46*, 1706-1708.
[103] C. Camp, S. Dorbes, C. Picard, E. Benoist, *Tetrahedron Lett.* **2008**, *49*, 1979-1983.
[104] S. Knör, A. Modlinger, T. Poethko, M. Schottelius, H.-J. Wester, H. Kessler, *Chem. Eur. J.* **2007**, *13*, 6082-6090.
[105] J. C. Jewett, C. R. Bertozzi, *Chem. Soc. Rev.* **2010**, *39*, 1272-1279.

[106] C. R. Becer, R. Hoogenboom, U. S. Schubert, *Angew. Chem., Int. Ed.* **2009**, *48*, 4900-4908.
[107] M. Jamous, M. L. Tamma, E. Gourni, B. Waser, J. C. Reubi, H. R. Maecke, R. Mansi, *Nucl. Med. Biol.* **2014**, *41*, 464-470.
[108] J. C. Garrison, T. L. Rold, G. L. Sieckman, F. Naz, S. V. Sublett, S. D. Figueroa, W. A. Volkert, T. J. Hoffman, *Bioconjugate Chem.* **2008**, *19*, 1803-1812.
[109] C. J. Smith, H. Gali, G. L. Sieckman, C. Higginbotham, W. A. Volkert, T. J. Hoffman, *Bioconjugate Chem.* **2003**, *14*, 93-102.
[110] S. Liu, D. S. Edwards, *Bioconjugate Chem.* **2001**, *12*, 7-34.
[111] S. Liu, *Adv. Drug Delivery Rev.* **2008**, *60*, 1347-1370.
[112] C. A. Owen, *Am. J. Physiol.* **1965**, *209*, 900-904.
[113] A. Ando, I. Ando, T. Hiraki, K. Hisada, *Int. J. Radiat. Appl. Instrum. Part B* **1989**, *16*, 57-80.
[114] J. L. J. Dearling, B. M. Paterson, V. Akurathi, S. Betanzos-Lara, S. T. Treves, S. D. Voss, J. M. White, J. S. Huston, S. V. Smith, P. S. Donnelly, A. B. Packard, *Bioconjugate Chem.* **2015**, *26*, 707-717.
[115] R. Delgado, V. Felix, L. M. P. Lima, D. W. Price, *Dalton Trans.* **2007**, 2734-2745.
[116] A. Bevilacqua, R. I. Gelb, W. B. Hebard, L. J. Zompa, *Inorg. Chem.* **1987**, *26*, 2699-2706.
[117] M. Kodama, T. Koike, A. B. Mahatma, E. Kimura, *Inorg. Chem.* **1991**, *30*, 1270-1273.
[118] E. Kimura, H. Fujioka, A. Yatsunami, H. Nihira, M. Kodama, *Chem. Pharm. Bull.* **1985**, *33*, 655-661.
[119] K. A. Deal, I. A. Davis, S. Mirzadeh, S. J. Kennel, M. W. Brechbiel, *J. Med. Chem.* **1999**, *42*, 2988-2992.
[120] L. L. Chappell, K. A. Deal, E. Dadachova, M. W. Brechbiel, *Bioconjugate Chem.* **2000**, *11*, 510-519.
[121] I. A. Davis, K. A. Glowienka, R. A. Boll, K. A. Deal, M. W. Brechbiel, M. Stabin, P. N. Bochsler, S. Mirzadeh, S. J. Kennel, *Nucl. Med. Biol.* **1999**, *26*, 581-589.
[122] D. J. Stigers, R. Ferdani, G. R. Weisman, E. H. Wong, C. J. Anderson, J. A. Golen, C. Moore, A. L. Rheingold, *Dalton Trans.* **2010**, *39*, 1699-1701.
[123] R. Ferdani, D. J. Stigers, A. L. Fiamengo, L. Wei, B. T. Y. Li, J. A. Golen, A. L. Rheingold, G. R. Weisman, E. H. Wong, C. J. Anderson, *Dalton Trans.* **2012**, *41*, 1938-1950.
[124] L. M. P. Lima, D. Esteban-Gómez, R. Delgado, C. Platas-Iglesias, R. Tripier, *Inorg. Chem.* **2012**, *51*, 6916-6927.
[125] M. Roger, L. M. P. Lima, M. Frindel, C. Platas-Iglesias, J.-F. Gestin, R. Delgado, V. Patinec, R. Tripier, *Inorg. Chem.* **2013**, *52*, 5246-5259.
[126] E. H. Wong, G. R. Weisman, D. C. Hill, D. P. Reed, M. E. Rogers, J. S. Condon, M. A. Fagan, J. C. Calabrese, K.-C. Lam, I. A. Guzei, A. L. Rheingold, *J. Am. Chem. Soc.* **2000**, *122*, 10561-10572.
[127] E. P. Krenning, W. H. Bakker, P. P. M. Kooij, W. A. P. Breeman, H. Y. Oei, M. de Jong, J. C. Reubi, T. J. Visser, C. Bruns, D. J. Kwekkeboom, A. E. M. Reijs, P. M. van Hagen, J. W. Koper, S. W. J. Lamberts, *J. Nucl. Med.* **1992**, *33*, 652-658.
[128] E. P. Krenning, D. J. Kwekkeboom, W. H. Bakker, W. A. Breeman, P. P. Kooij, H. Y. Oei, M. van Hagen, P. T. Postema, M. de Jong, J. C. Reubi, T. J. Visser, A. E. M. Reijs, L. J. Hofland, J. W. Koper, S. W. J. Lamberts, *Eur. J. Nucl. Med.* **1993**, *20*, 716-731.
[129] J. B. Bomanji, N. D. Papathanasiou, *Eur. J. Nucl. Med. Mol. Imaging* **2012**, *39*, 113-125.
[130] L. Camera, S. Kinuya, K. Garmestani, C. Wu, M. W. Brechbiel, L. H. Pai, T. J. McMurry, O. A. Gansow, I. Pastan, C. H. Paik, J. A. Carrasquillo, *J. Nucl. Med.* **1994**, *35*, 882-889.

[131] C. Wu, H. Kobayashi, B. Sun, T. M. Yoo, C. H. Paik, O. A. Gansow, J. A. Carrasquillo, I. Pastan, M. W. Brechbiel, *Bioorg. Med. Chem.* **1997**, *5*, 1925-1934.
[132] P. Comba, W. Schiek, *Coord. Chem. Rev.* **2003**, *238–239*, 21-29.
[133] A. P. Wolf, *J. Nucl. Med.* **1981**, *22*, 392-393.
[134] A. P. Wolf, *J. Label. Compd. Rad.* **1981**, *18*, 1-2.
[135] Nomenclature guidelines ISRS2017, http://isrs2017.org/_medien/_content/files/nomenclature_guidelines.pdf, accessed on 24 February 2017.
[136] S. Liu, *Chem. Soc. Rev.* **2004**, *33*, 445-461.
[137] T. J. Wadas, E. H. Wong, G. R. Weisman, C. J. Anderson, *Chem. Rev.* **2010**, *110*, 2858-2902.
[138] R. G. Pearson, *J. Am. Chem. Soc.* **1963**, *85*, 3533-3539.
[139] R. G. Pearson, *J. Chem. Educ.* **1987**, *64*, 561.
[140] P. Comba, *Coord. Chem. Rev.* **2000**, *200–202*, 217-245.
[141] P. Comba, *Coord. Chem. Rev.* **1999**, *185–186*, 81-98.
[142] D. J. Cram, G. M. Lein, *J. Am. Chem. Soc.* **1985**, *107*, 3657-3668.
[143] P. Comba, A. Fath, A. Kuhner, B. Nuber, *J. Chem. Soc., Dalton Trans.* **1997**, 1889-1898.
[144] S. Bhattacharyya, M. Dixit, *Dalton Trans.* **2011**, *40*, 6112-6128.
[145] S. K. Bhattacharjee, K. K. Chako, *Tetrahedron* **1979**, *35*, 1999-2007.
[146] P. J. Blower, J. S. Lewis, J. Zweit, *Nucl. Med. Biol.* **1996**, *23*, 957-980.
[147] M. R. McDevitt, G. Sgouros, R. D. Finn, J. L. Humm, J. G. Jurcic, S. M. Larson, D. A. Scheinberg, *Eur. J. Nucl. Med.* **1998**, *25*, 1341-1351.
[148] R. Shannon, *Acta Cryst. Section A* **1976**, *32*, 751-767.
[149] J. R. Dilworth, S. J. Parrott, *Chem. Soc. Rev.* **1998**, *27*, 43-55.
[150] S. Liu, D. S. Edwards, *Chem. Rev.* **1999**, *99*, 2235-2268.
[151] A. Mahmood, A. G. Jones, *Technetium Radiopharmaceuticals* in *Handbook of Radiopharmaceuticals*. **2005**, John Wiley & Sons, Ltd. 323-362.
[152] T. Mindt, H. Struthers, E. Garcia-Garayoa, D. Desbouis, R. Schibli, *CHIMIA Int. J. Chem.* **2007**, *61*, 725-731.
[153] P. S. Donnelly, *Dalton Trans.* **2011**, *40*, 999-1010.
[154] U. Abram, R. Alberto, *J. Braz. Chem. Soc.* **2006**, *17*, 1486-1500.
[155] J. Bernard, K. Ortner, B. Spingler, H.-J. Pietzsch, R. Alberto, *Inorg. Chem.* **2003**, *42*, 1014-1022.
[156] A. E. Martell, R. J. Motekaitis, *Determination and use of stability constants*, 2nd edition, VCH publishers, **1992**.
[157] L. M. P. Lima, Z. Halime, R. Marion, N. Camus, R. Delgado, C. Platas-Iglesias, R. Tripier, *Inorg. Chem.* **2014**, *53*, 5269-5279.
[158] E. W. Price, J. F. Cawthray, G. A. Bailey, C. L. Ferreira, E. Boros, M. J. Adam, C. Orvig, *J. Am. Chem. Soc.* **2012**, *134*, 8670-8683.
[159] P. Comba, L. Grimm, C. Orvig, K. Rück, H. Wadepohl, *Inorg. Chem.* **2016**, *55*, 12531-12543.
[160] P. Gans, A. Sabatini, A. Vacca, *Talanta* **1996**, *43*, 1739-1753.
[161] D. C. Harris, *Lehrbuch der quantitativen Analyse*, 8th edition, Springer-Verlag, **2014**.
[162] C. F. Baes, R. E. Mesmer, *The Hydrolysis of Cations*, R.E. Krieger Publishing Company, Malabar, Florida, **1986**.
[163] H. Ackermann, G. Schwarzenbach, *Helv. Chim. Acta* **1949**, *32*, 1543-1554.
[164] K. N. Raymond, E. A. Dertz, *Biochemical and Physical Properties of Siderophores* in *Iron Transport in Bacteria*. **2004**, American Society of Microbiology.
[165] W. R. Harris, V. L. Pecoraro, *Biochemistry* **1983**, *22*, 292-299.
[166] M. J. Kappel, K. N. Raymond, *Inorg. Chem.* **1982**, *21*, 3437-3442.

[167] E. A. Ambundo, M.-V. Deydier, A. J. Grall, N. Aguera-Vega, L. T. Dressel, T. H. Cooper, M. J. Heeg, L. A. Ochrymowycz, D. B. Rorabacher, *Inorg. Chem.* **1999**, *38*, 4233-4242.
[168] D. B. Rorabacher, *Chem. Rev.* **2004**, *104*, 651-698.
[169] H. Rudolf, *dissertation* **2013**, Heidelberg University.
[170] C. J. Mathias, M. A. Green, *Nucl. Med. Biol.* **1998**, *25*, 585-587.
[171] D. Ma, F. Lu, T. Overstreet, D. E. Milenic, M. W. Brechbiel, *Nucl. Med. Biol.* **2002**, *29*, 91-105.
[172] P. Comba, S. Hunoldt, M. Morgen, J. Pietzsch, H. Stephan, H. Wadepohl, *Inorg. Chem.* **2013**, *52*, 8131-8143.
[173] S. Juran, M. Walther, H. Stephan, R. Bergmann, J. Steinbach, W. Kraus, F. Emmerling, P. Comba, *Bioconjugate Chem.* **2009**, *20*, 347-359.
[174] G. A. Bailey, E. W. Price, B. M. Zeglis, C. L. Ferreira, E. Boros, M. J. Lacasse, B. O. Patrick, J. S. Lewis, M. J. Adam, C. Orvig, *Inorg. Chem.* **2012**, *51*, 12575-12589.
[175] C. L. Ferreira, D. T. Yapp, E. Lamsa, M. Gleave, C. Bensimon, P. Jurek, G. E. Kiefer, *Nucl. Med. Biol.* **2008**, *35*, 875-882.
[176] W. Li, D. Ma, C. Higginbotham, T. Hoffman, A. Ketring, C. S. Cutler, S. Jurisson, *Nucl. Med. Biol.* **2001**, *28*, 145-154.
[177] P. Comba, M. Kubeil, J. Pietzsch, H. Rudolf, H. Stephan, K. Zarschler, *Inorg. Chem.* **2014**, *53*, 6698-6707.
[178] G. Thews, E. Mutschler, P. Vaupel, *Anatomie, Physiologie, Pathophysiologie des Menschen*, 4. Auflage, Wissenschaftliche Verlagsgesellschaft, Stuttgart, **1991**.
[179] H. Krebs, *Annu. Rev. Biochem.* **1950**, *19*, 409-430.
[180] H. Tapiero, D. Townsend, K. Tew, *Biomed. Pharmacother.* **2003**, *57*, 386-398.
[181] K. Pant, D. Gröger, R. Bergmann, J. Pietzsch, J. Steinbach, B. Graham, L. Spiccia, F. Berthon, B. Czarny, L. Devel, *Bioconjugate Chem.* **2015**, *26*, 906-918.
[182] K. Zarschler, M. Kubeil, H. Stephan, *RSC Advances* **2014**, *4*, 10157-10164.
[183] W. Kaim, B. Schwederski, *Bioanorganische Chemie*, 4. durchgesehene Auflage, Teubner Verlag, Wiesbaden, **2005**.
[184] D. Zeng, C. J. Anderson, *Chem. Commun.* **2013**, *49*, 2697-2699.
[185] D. Zeng, C. J. Anderson, *Solvent Extr. Ion Exch.* **2013**, *31*, 337-344.
[186] D. E. Mager, *Adv. Drug Delivery Rev.* **2006**, *58*, 1326-1356.
[187] A. Leo, C. Hansch, D. Elkins, *Chem. Rev.* **1971**, *71*, 525-616.
[188] P. Comba, B. Martin, A. Sanyal, H. Stephan, *Dalton Trans.* **2013**, *42*, 11066-11073.
[189] J. Sangster, *J. Phys. Chem. Ref. Data* **1989**, *18*, 1111-1229.
[190] H. Stephan, M. Kubeil, K. Gloe, K. Gloe, *Extraction methods* in *Analytical methods in supramolecular chemistry*, Schalley, C.A., Editor. **2012**, Wiley-VCH Verlag GmbH & Co. KGaA: Weinheim. 105-125.
[191] P. H. Hinderling, O. Schmidlin, J. K. Seydel, *J. Pharmacokinet. Biopharm.* **1984**, *12*, 263-287.
[192] M. Grover, B. Singh, M. Bakshi, S. Singh, *Pharm. Sci. Technol. Today* **2000**, *3*, 50-57.
[193] Monographie BIPM-5: Table of radionuclides, Volume 1, http://www.bipm.org/en/publications/scientific-output/monographie-ri-5.html, accessed 23 March 2017.
[194] T. W. Price, J. Greenman, G. J. Stasiuk, *Dalton Trans.* **2016**, *45*, 15702-15724.
[195] M. Shokeen, C. J. Anderson, *Acc. Chem. Res.* **2009**, *42*, 832-841.
[196] A. Obata, S. Kasamatsu, D. W. McCarthy, M. J. Welch, H. Saji, Y. Yonekura, Y. Fujibayashi, *Nucl. Med. Biol.* **2003**, *30*, 535-539.
[197] D. W. McCarthy, R. E. Shefer, R. E. Klinkowstein, L. A. Bass, W. H. Margeneau, C. S. Cutler, C. J. Anderson, M. J. Welch, *Nucl. Med. Biol.* **1997**, *24*, 35-43.

[198] M. A. Avila-Rodriguez, J. A. Nye, R. J. Nickles, *Appl. Radiat. Isot.* **2007**, *65*, 1115-1120.
[199] S. Thieme, M. Walther, H. J. Pietzsch, J. Henniger, S. Preusche, P. Mäding, J. Steinbach, *Appl. Radiat. Isot.* **2012**, *70*, 602-608.
[200] T. J. Wadas, E. H. Wong, G. R. Weisman, C. J. Anderson, *Curr. Pharm. Des.* **2007**, *13*, 3-16.
[201] H. A. Jahn, E. Teller, *Proc. R. Soc. London, A* **1937**, *161*, 220-235.
[202] A. L. Vavere, J. S. Lewis, *Dalton Trans.* **2007**, 4893-4902.
[203] J. L. Dearling, P. J. Blower, *Chem. Commun.* **1998**, 2531-2532.
[204] J. S. Lewis, R. Laforest, T. L. Buettner, S.-K. Song, Y. Fujibayashi, J. M. Connett, M. J. Welch, *Proc. Natl. Acad. Sci. USA* **2001**, *98*, 1206-1211.
[205] J. P. Holland, J. H. Giansiracusa, S. G. Bell, L.-L. Wong, J. R. Dilworth, *Phys. Med. Biol.* **2009**, *54*, 2103.
[206] G. R. Weisman, E. H. Wong, D. C. Hill, M. E. Rogers, D. P. Reed, J. C. Calabrese, *Chem. Commun.* **1996**, 947-948.
[207] L. A. Bass, M. Wang, M. J. Welch, C. J. Anderson, *Bioconjugate Chem.* **2000**, *11*, 527-532.
[208] C. A. Boswell, X. Sun, W. Niu, G. R. Weisman, E. H. Wong, A. L. Rheingold, C. J. Anderson, *J. Med. Chem.* **2004**, *47*, 1465-1474.
[209] B. M. Paterson, G. Buncic, L. E. McInnes, P. Roselt, C. Cullinane, D. S. Binns, C. M. Jeffery, R. I. Price, R. J. Hicks, P. S. Donnelly, *Dalton Trans.* **2015**, *44*, 4901-4909.
[210] E. Gourni, L. Del Pozzo, E. Kheirallah, C. Smerling, B. Waser, J.-C. Reubi, B. M. Paterson, P. S. Donnelly, P. T. Meyer, H. R. Maecke, *Mol. Pharm.* **2015**, *12*, 2781-2790.
[211] K. A. Lears, R. Ferdani, K. Liang, A. Zheleznyak, R. Andrews, C. D. Sherman, S. Achilefu, C. J. Anderson, B. E. Rogers, *J. Nucl. Med.* **2011**, *52*, 470-477.
[212] N. Di Bartolo, A. M. Sargeson, S. V. Smith, *Org. Biomol. Chem.* **2006**, *4*, 3350-3357.
[213] N. M. Di Bartolo, A. M. Sargeson, T. M. Donlevy, S. V. Smith, *J. Chem. Soc., Dalton Trans.* **2001**, 2303-2309.
[214] P. V. Bernhardt, R. Bramley, L. M. Engelhardt, J. M. Harrowfield, D. C. R. Hockless, B. R. Korybut-Daszkiewicz, E. R. Krausz, T. Morgan, A. M. Sargeson, *Inorg. Chem.* **1995**, *34*, 3589-3599.
[215] S. Liu, Z. Li, L. P. Yap, C. W. Huang, R. Park, P. S. Conti, *Chem. Eur. J.* **2011**, *17*, 10222-10225.
[216] S. Liu, D. Li, C.-W. Huang, L.-P. Yap, R. Park, H. Shan, Z. Li, P. S. Conti, *Theranostics* **2012**, *2*, 589-596.
[217] H. Cai, J. Fissekis, P. S. Conti, *Dalton Trans.* **2009**, 5395-5400.
[218] A. Roux, A. M. Nonat, J. Brandel, V. Hubscher-Bruder, L. J. Charbonnière, *Inorg. Chem.* **2015**, *54*, 4431-4444.
[219] L. R. Chervu, I. Sternlieb, *J. Nucl. Med.* **1974**, *15*, 1011-1013.
[220] M. D. Bartholomä, A. S. Louie, J. F. Valliant, J. Zubieta, *Chem. Rev.* **2010**, *110*, 2903-2920.
[221] C. L. Edwards, R. L. Hayes, *J. Nucl. Med.* **1969**, *10*, 103-105.
[222] F. Rösch, *Appl. Radiat. Isot.* **2013**, *76*, 24-30.
[223] M. Fani, J. P. André, H. R. Maecke, *Contrast Media Mol. Imaging* **2008**, *3*, 53-63.
[224] M. D. Bartholomä, *Inorg. Chim. Acta* **2012**, *389*, 36-51.
[225] A. E. Martell, R. J. Motekaitis, E. T. Clarke, R. Delgado, Y. Sun, R. Ma, *Supramol. Chem.* **1996**, *6*, 353-363.
[226] M. Hofmann, H. Maecke, A. Börner, E. Weckesser, P. Schöffski, M. Oei, J. Schumacher, M. Henze, A. Heppeler, G. Meyer, W. Knapp, *Eur. J. Nucl. Med.* **2001**, *28*, 1751-1757.

[227] P. Antunes, M. Ginj, H. Zhang, B. Waser, R. Baum, J.-C. Reubi, H. Maecke, *Eur. J. Nucl. Med. Mol. Imaging* **2007**, *34*, 982-993.
[228] J. Notni, J. Šimeček, P. Hermann, H. J. Wester, *Chem. Eur. J.* **2011**, *17*, 14718-14722.
[229] J. Notni, P. Hermann, J. Havlíčková, J. Kotek, V. Kubíček, J. Plutnar, N. Loktionova, P. J. Riss, F. Rösch, I. Lukeš, *Chem. Eur. J.* **2010**, *16*, 7174-7185.
[230] J. Šimeček, P. Hermann, H. J. Wester, J. Notni, *ChemMedChem* **2013**, *8*, 95-103.
[231] H. Stetter, W. Frank, R. Mertens, *Tetrahedron* **1981**, *37*, 767-772.
[232] W. D. Kim, G. E. Kiefer, F. Maton, K. McMillan, R. N. Muller, A. D. Sherry, *Inorg. Chem.* **1995**, *34*, 2233-2243.
[233] C. L. Ferreira, D. T. Yapp, D. Mandel, R. K. Gill, E. Boros, M. Q. Wong, P. Jurek, G. E. Kiefer, *Bioconjugate Chem.* **2012**, *23*, 2239-2246.
[234] C. L. Ferreira, E. Lamsa, M. Woods, Y. Duan, P. Fernando, C. Bensimon, M. Kordos, K. Guenther, P. Jurek, G. E. Kiefer, *Bioconjugate Chem.* **2010**, *21*, 531-536.
[235] B. P. Waldron, D. Parker, C. Burchardt, D. S. Yufit, M. Zimny, F. Roesch, *Chem. Commun.* **2013**, *49*, 579-581.
[236] Z. Baranyai, F. Uggeri, G. B. Giovenzana, A. Benyei, E. Brücher, S. Aime, *Chem. Eur. J.* **2009**, *15*, 1696-1705.
[237] R. Ferreirós-Martínez, D. Esteban-Gómez, C. Platas-Iglesias, A. de Blas, T. Rodríguez-Blas, *Dalton Trans.* **2008**, 5754-5765.
[238] M. Mato-Iglesias, E. Balogh, C. Platas-Iglesias, É. Tóth, A. de Blas, T. R. Blas, *Dalton Trans.* **2006**, 5404-5415.
[239] E. Balogh, M. Mato-Iglesias, C. Platas-Iglesias, É. Tóth, K. Djanashvili, J. A. Peters, A. de Blas, T. Rodríguez-Blas, *Inorg. Chem.* **2006**, *45*, 8719-8728.
[240] C. Platas-Iglesias, M. Mato-Iglesias, K. Djanashvili, R. N. Muller, L. V. Elst, J. A. Peters, A. de Blas, T. Rodríguez‐Blas, *Chem. Eur. J.* **2004**, *10*, 3579-3590.
[241] E. Boros, C. L. Ferreira, J. F. Cawthray, E. W. Price, B. O. Patrick, D. W. Wester, M. J. Adam, C. Orvig, *J. Am. Chem. Soc.* **2010**, *132*, 15726-15733.
[242] E. Boros, C. L. Ferreira, D. T. Yapp, R. K. Gill, E. W. Price, M. J. Adam, C. Orvig, *Nucl. Med. Biol.* **2012**, *39*, 785-794.
[243] E. Boros, C. L. Ferreira, B. O. Patrick, M. J. Adam, C. Orvig, *Nucl. Med. Biol.* **2011**, *38*, 1165-1174.
[244] A. Evers, R. D. Hancock, A. E. Martell, R. J. Motekaitis, *Inorg. Chem.* **1989**, *28*, 2189-2195.
[245] S. Kojima, M. Jay, *Eur. J. Nucl. Med. Mol. Imaging* **1987**, *13*, 366-370.
[246] D. J. Berry, Y. Ma, J. R. Ballinger, R. Tavaré, A. Koers, K. Sunassee, T. Zhou, S. Nawaz, G. E. Mullen, R. C. Hider, *Chem. Commun.* **2011**, *47*, 7068-7070.
[247] E. S. Delpassand, J. Sims-Mourtada, H. Saso, A. Azhdarinia, F. Ashoori, F. Torabi, G. Espenan, W. H. Moore, E. Woltering, L. Anthony, *Cancer Biother. Radiopharm.* **2008**, *23*, 292-300.
[248] J. O'Donoghue, T. Wheldon, *Phys. Med. Biol.* **1996**, *41*, 1973.
[249] A. Heppeler, S. Froidevaux, H. Mäcke, E. Jermann, M. Béhé, P. Powell, M. Hennig, *Chem. Eur. J.* **1999**, *5*, 1974-1981.
[250] E. T. Clarke, A. E. Martell, *Inorg. Chim. Acta* **1991**, *190*, 37-46.
[251] W. A. P. Breeman, M. de Jong, T. J. Visser, J. L. Erion, E. P. Krenning, *Eur. J. Nucl. Med. Mol. Imaging* **2003**, *30*, 917-920.
[252] A. Tatsi, T. Maina, R. Cescato, B. Waser, E. P. Krenning, M. de Jong, P. Cordopatis, J. C. Reubi, B. A. Nock, *EJNMMI Research* **2012**, *2*, 25.
[253] S. Chakraborty, J. Shi, Y.-S. Kim, Y. Zhou, B. Jia, F. Wang, S. Liu, *Bioconjugate Chem.* **2010**, *21*, 969-978.
[254] C. Decristoforo, I. Hernandez Gonzalez, J. Carlsen, M. Rupprich, M. Huisman, I. Virgolini, H.-J. Wester, R. Haubner, *Eur. J. Nucl. Med. Mol. Imaging* **2008**, *35*, 1507-1515.

[255] S. Liu, Z. He, W.-Y. Hsieh, P. E. Fanwick, *Inorg. Chem.* **2003**, *42*, 8831-8837.
[256] The following color code was used in the ORTEP plots of the solid state structures: C, gray; H, light gray; N, blue; O, red; Na; yellow, Cu, orange; In, brown; Lu, dark blue.
[257] A. Ilyukhin, M. Malyarik, S. Petrosyants, R. Davidovich, I. Samsonova, *Zhurnal Neorganicheskoj Khimii* **1995**, *40*, 1125-1136.
[258] H. R. Maecke, A. Riesen, W. Ritter, *J. Nucl. Med* **1989**, *30*, 1235-1239.
[259] S. Petrosyants, A. Ilyukhin, *Russ. J. Inorg. Chem.* **2011**, *56*, 2047-2069.
[260] M. J. Manyak, *Expert Rev. Anticancer Ther.* **2008**, *8*, 175-181.
[261] J. D. Petronis, F. Regan, K. Lin, *Clin. Nucl. Med.* **1998**, *23*, 672-677.
[262] L. Wei, X. Zhang, F. Gallazzi, Y. Miao, X. Jin, M. W. Brechbiel, H. Xu, T. Clifford, M. J. Welch, J. S. Lewis, *Nucl. Med. Biol.* **2009**, *36*, 345-354.
[263] A. M. R. Pillai, F. F Russ Knapp, *Curr. Radiopharm.* **2015**, *8*, 78-85.
[264] S. Banerjee, M. Pillai, F. Knapp, *Chem. Rev.* **2015**, *115*, 2934-2974.
[265] S. M. Kaminsky, O. Levy, C. Salvador, G. Dai, N. Carrasco, *Proc. Natl. Acad. Sci. USA* **1994**, *91*, 3789-3793.
[266] S. Aime, A. Barge, M. Botta, M. Fasano, J. Danilo Ayala, G. Bombieri, *Inorg. Chim. Acta* **1996**, *246*, 423-429.
[267] K. K. Agarwal, S. Singla, G. Arora, C. Bal, *Eur. J. Nucl. Med. Mol. Imaging* **2015**, *42*, 79-88.
[268] J. Yuan, C. Liu, X. Liu, Y. Wang, D. Kuai, G. Zhang, J. J. Zaknun, *Clin. Nucl. Med.* **2013**, *38*, 88-92.
[269] G. A. R. Solá, M. G. Argüelles, D. L. Bottazzini, J. C. Furnari, I. G. Parada, A. Rojo, H. V. Ruiz, *Radiochim. Acta* **2000**, *88*, 157-162.
[270] A. Ando, I. Ando, N. Tonami, S. Kinuya, K. Kazuma, A. Kataiwa, M. Nakagawa, N. Fujita, *Nucl. Med. Commun.* **1998**, *19*, 587-592.
[271] J. J. Zaknun, L. Bodei, J. Mueller-Brand, M. Pavel, R. Baum, D. Hörsch, M. O'Dorisio, T. O'Dorisiol, J. Howe, M. Cremonesi, *Eur. J. Nucl. Med. Mol. Imaging* **2013**, *40*, 800-816.
[272] D. J. Kwekkeboom, W. H. Bakker, P. P. Kooij, M. W. Konijnenberg, A. Srinivasan, J. L. Erion, M. A. Schmidt, J. L. Bugaj, M. de Jong, E. P. Krenning, *Eur. J. Nucl. Med. Mol. Imaging* **2001**, *28*, 1319-1325.
[273] J. Shi, Z. Liu, B. Jia, Z. Yu, H. Zhao, F. Wang, *Amino Acids* **2010**, *39*, 111-120.
[274] J. B. Stimmel, F. C. Kull, *Nucl. Med. Biol.* **1998**, *25*, 117-125.
[275] D. E. Milenic, K. Garmestani, L. L. Chappell, E. Dadachova, A. Yordanov, D. Ma, J. Schlom, M. W. Brechbiel, *Nucl. Med. Biol.* **2002**, *29*, 431-442.
[276] M. Hens, G. Vaidyanathan, X.-G. Zhao, D. D. Bigner, M. R. Zalutsky, *Nucl. Med. Biol.* **2010**, *37*, 741-750.
[277] M. Fani, P. Bouziotis, A. L. Harris, D. Psimadas, E. Gourni, G. Loudos, A. D. Varvarigou, H. R. Maecke, *Radiochim. Acta* **2007**, *95*, 351-357.
[278] F. Forrer, C. Oechslin-Oberholzer, B. Campana, R. Herrmann, H. R. Maecke, J. Mueller-Brand, A. Lohri, *J. Nucl. Med.* **2013**, *54*, 1045-1052.
[279] F. Forrer, J. Chen, M. Fani, P. Powell, A. Lohri, J. Müller-Brand, G. Moldenhauer, H. R. Maecke, *Eur. J. Nucl. Med. Mol. Imaging* **2009**, *36*, 1443-1452.
[280] M. M. Bernardo, R. R. Schroeder, D. Rorabacher, *Inorg. Chem.* **1991**, *30*, 1241-1247.
[281] M. Miederer, D. A. Scheinberg, M. R. McDevitt, *Adv. Drug Delivery Rev.* **2008**, *60*, 1371-1382.
[282] J. G. Jurcic, S. M. Larson, G. Sgouros, M. R. McDevitt, R. D. Finn, C. R. Divgi, Å. M. Ballangrud, K. A. Hamacher, D. Ma, J. L. Humm, *Blood* **2002**, *100*, 1233-1239.
[283] C. Apostolidis, R. Molinet, G. Rasmussen, A. Morgenstern, *Anal. Chem.* **2005**, *77*, 6288-6291.

[284] H. W. Kirby, L. R. Morss, *Actinium* in *The Chemistry of the Actinide and Transactinide Elements*, Morss, L.R.; Edelstein, N.M.Fuger, J., Editors. **2006**, Springer Netherlands: Dordrecht. 18-51.
[285] M. G. Ferrier, E. R. Batista, J. M. Berg, E. R. Birnbaum, J. N. Cross, J. W. Engle, H. S. La Pierre, S. A. Kozimor, J. S. L. Pacheco, B. W. Stein, S. C. E. Stieber, J. J. Wilson, *Nature Commun.* **2016**, *7*, 1-8.
[286] R. Diamond, K. Street Jr, G. T. Seaborg, *J. Am. Chem. Soc.* **1954**, *76*, 1461-1469.
[287] D. Manna, S. Mula, A. Bhattacharyya, S. Chattopadhyay, T. K. Ghanty, *Dalton Trans.* **2015**, *44*, 1332-1340.
[288] M. R. McDevitt, D. Ma, J. Simon, R. K. Frank, D. A. Scheinberg, *Appl. Radiat. Isot.* **2002**, *57*, 841-847.
[289] S. J. Kennel, L. L. Chappell, K. Dadachova, M. W. Brechbiel, T. K. Lankford, I. A. Davis, M. Stabin, S. Mirzadeh, *Cancer Biother. Radiopharm.* **2000**, *15*, 235-244.
[290] J. Schwartz, J. Jaggi, J. O'Donoghue, S. Ruan, M. McDevitt, S. Larson, D. Scheinberg, J. Humm, *Phys. Med. Biol.* **2011**, *56*, 721.
[291] M. Miederer, M. R. McDevitt, G. Sgouros, K. Kramer, N.-K. V. Cheung, D. A. Scheinberg, *J. Nucl. Med.* **2004**, *45*, 129-137.
[292] C. Mannich, P. Mohs, *Chem. Ber.* **1930**, *B63*, 608-612.
[293] P. W. Thies, *Pharm. unserer Zeit* **1986**, *15*, 172-176.
[294] N. Erdemoglu, A. Ozkan, F. Tosun, *Phytochem. Rev.* **2007**, *6*, 197-201.
[295] U. Holzgrabe, E. Erciyas, *Arch. Pharm.* **1992**, *325*, 657-663.
[296] A. Samhammer, U. Holzgrabe, R. Haller, *Arch. Pharm.* **1989**, *322*, 551-555.
[297] U. Holzgrabe, W. Friedrichsen, K.-F. Hesse, *Z. Naturforsch. B* **1991**, *46*, 1237-1250.
[298] P. Comba, M. Kerscher, W. Schiek, *Prog. Inorg. Chem.* **2007**, *55*, 613-704.
[299] A. Samhammer, U. Holzgrabe, R. Haller, *Arch. Pharm.* **1989**, *322*, 545-550.
[300] P. Comba, B. Kanellakopulos, C. Katsichtis, A. Lienke, H. Pritzkow, F. Rominger, *J. Chem. Soc., Dalton Trans.* **1998**, 3997-4002.
[301] P. Bischof, R. Gleiter, E. Müller, *Tetrahedron* **1976**, *32*, 2769-2773.
[302] C. Bleiholder, H. Börzel, P. Comba, R. Ferrari, M. Heydt, M. Kerscher, S. Kuwata, G. Laurenczy, G. A. Lawrance, A. Lienke, B. Martin, M. Merz, B. Nuber, H. Pritzkow, *Inorg. Chem.* **2005**, *44*, 8145-8155.
[303] K. Born, P. Comba, R. Ferrari, G. A. Lawrance, H. Wadepohl, *Inorg. Chem.* **2007**, *46*, 458-464.
[304] R. Haller, *Arch. Pharm.* **1969**, *302*, 113-118.
[305] H. Stetter, R. Merten, *Eur. J. Inorg. Chem.* **1957**, *90*, 868-875.
[306] P. Comba, S. Kuwata, G. Linti, M. Tarnai, H. Wadepohl, *Eur. J. Inorg. Chem.* **2007**, *2007*, 657-664.
[307] P. Comba, M. Kerscher, M. Merz, V. Müller, H. Pritzkow, R. Remenyi, W. Schiek, Y. Xiong, *Chem. Eur. J.* **2002**, *8*, 5750-5760.
[308] P. Comba, B. Kanellakopulos, C. Katsichtis, A. Lienke, H. Pritzkow, F. Rominger, *J. Chem. Soc., Dalton Trans.* **1998**, *23*, 3997-4002.
[309] P. Comba, H. Rudolf, H. Wadepohl, *Dalton Trans.* **2015**, *44*, 2724-2736.
[310] H. Börzel, P. Comba, K. S. Hagen, Y. D. Lampeka, A. Lienke, G. Linti, M. Merz, H. Pritzkow, L. V. Tsymbal, *Inorg. Chim. Acta* **2002**, *337*, 407-419.
[311] J. L. Kolanowski, E. Jeanneau, R. Steinhoff, J. Hasserodt, *Chem. Eur. J.* **2013**, *19*, 8839-8849.
[312] P. Comba, S. Kuwata, G. Linti, H. Pritzkow, M. Tarnai, H. Wadepohl, *Chem. Commun.* **2006**, 2074-2076.
[313] P. Comba, B. Nuber, A. Ramlow, *J. Chem. Soc., Dalton Trans.* **1997**, 347-352.
[314] P. Comba, B. Pokrandt, H. Wadepohl, *Aust. J. Chem.* **2017**, *70*, 576-580.
[315] M. Atanasov, P. Comba, S. Helmle, D. Müller, F. Neese, *Inorg. Chem.* **2012**, *51*, 12324-12335.

[316] H. Börzel, P. Comba, K. S. Hagen, M. Kerscher, H. Pritzkow, M. Schatz, S. Schindler, O. Walter, *Inorg. Chem.* **2002**, *41*, 5440-5452.
[317] P. Comba, M. Morgen, H. Wadepohl, *Inorg. Chem.* **2013**, *52*, 6481-6501.
[318] J. Benet-Buchholz, P. Comba, A. Llobet, S. Roeser, P. Vadivelu, H. Wadepohl, S. Wiesner, *Dalton Trans.* **2009**, 5910-5923.
[319] D. Pollak, R. Goddard, K.-R. Pörschke, *Inorg. Chem.* **2016**, *55*, 9424-9435.
[320] H. Cui, R. Goddard, K.-R. Pörschke, A. Hamacher, M. U. Kassack, *Inorg. Chem.* **2016**, *55*, 2986-2997.
[321] H. Cui, R. Goddard, K.-R. Pörschke, A. Hamacher, M. U. Kassack, *Inorg. Chem.* **2014**, *53*, 3371-3384.
[322] S. Norrehed, M. Erdelyi, M. E. Light, A. Gogoll, *Org. Biomol. Chem.* **2013**, *11*, 6292-6299.
[323] P. Comba, M. Kerscher, K. Rück, M. Starke, *manuscript in preparation*.
[324] K. Born, P. Comba, M. Kerscher, G. Linti, H. Pritzkow, H. Rohwer, *Dalton Trans.* **2009**, 362-367.
[325] P. Comba, A. Lienke, *Inorg. Chem.* **2001**, *40*, 5206-5209.
[326] P. Comba, M. Merz, H. Pritzkow, *Eur. J. Inorg. Chem.* **2003**, *9*, 1711-1718.
[327] P. Comba, A. Hauser, M. Kerscher, H. Pritzkow, *Angew. Chem., Int. Ed.* **2003**, *42*, 4536-4540.
[328] P. Comba, C. Lopez de Laorden, H. Pritzkow, *Helv. Chim. Acta* **2005**, *88*, 647-664.
[329] A. Bentz, P. Comba, R. J. Deeth, M. Kerscher, B. r. Seibold, H. Wadepohl, *Inorg. Chem.* **2008**, *47*, 9518-9527.
[330] P. Comba, N. Okon, R. Remenyi, *J. Comput. Chem.* **1999**, *20*, 781-785.
[331] I. Tomassoli, D. Gündisch, *Curr. Top. Med. Chem.* **2016**, *16*, 1314-1342.
[332] M. Breuning, M. Steiner, *Synthesis* **2008**, *2008*, 2841-2867.
[333] P. Comba, C. Lang, C. L. de Laorden, A. Muruganantham, G. Rajaraman, H. Wadepohl, M. Zajaczkowski, *Chem. Eur. J.* **2008**, *14*, 5313-5328.
[334] P. Comba, C. Haaf, A. Lienke, A. Muruganantham, H. Wadepohl, *Chem. Eur. J.* **2009**, *15*, 10880-10887.
[335] M. Haberberger, C. I. Someya, E. Irran, S. Enthaler, *Catal. Lett.* **2012**, *142*, 557-565.
[336] D. Scharnagel, A. Müller, F. Prause, M. Eck, J. Goller, W. Milius, M. Breuning, *Chem. Eur. J.* **2015**, *21*, 12488-12500.
[337] H. Börzel, P. Comba, C. Katsichtis, W. Kiefer, A. Lienke, V. Nagel, H. Pritzkow, *Chem. Eur. J.* **1999**, *5*, 1716-1721.
[338] H. Börzel, P. Comba, K. S. Hagen, C. Katsichtis, H. Pritzkow, *Chem. Eur. J.* **2000**, *6*, 914-919.
[339] H. Börzel, P. Comba, H. Pritzkow, *Chem. Commun.* **2001**, 97-98.
[340] K. Born, P. Comba, A. Daubinet, A. Fuchs, H. Wadepohl, *J. Biol. Inorg. Chem.* **2007**, *12*, 36-48.
[341] P. Comba, B. Martin, A. Muruganantham, J. Straub, *Inorg. Chem.* **2012**, *51*, 9214-9225.
[342] P. Comba, M. Kerscher, T. Krause, H. F. Schöler, *Environ. Chem.* **2015**, *12*, 381-395.
[343] P. Barman, A. K. Vardhaman, B. Martin, S. J. Wörner, C. V. Sastri, P. Comba, *Angew. Chem., Int. Ed.* **2015**, *54*, 2095-2099.
[344] H. Stephan, M. Walther, S. Fähnemann, P. Ceroni, J. K. Molloy, G. Bergamini, F. Heisig, C. E. Müller, W. Kraus, P. Comba, *Chem. Eur. J.* **2014**, *20*, 17011-17018.
[345] D. Brox, P. Comba, D.-P. Herten, E. Kimmle, M. Morgen, C. L. Ruehl, A. Rybina, H. Stephan, G. Storch, H. Wadepohl, *J. Inorg. Biochem.* **2015**, *148*, 78-83.
[346] A. Roux, R. Gillet, S. Huclier-Markai, L. Ehret-Sabatier, L. J. Charbonniere, A. M. Nonat, *Org. Biomol. Chem.* **2017**, *15*, 1475-1483.
[347] J. Culver, W. Akers, S. Achilefu, *J. Nucl. Med.* **2008**, *49*, 169-172.
[348] G. Singh, M. Gott, H.-J. Pietzsch, H. Stephan, *Nuklearmedizin* **2016**, *55*, 41-50.

[349] P. Comba, H. Pritzkow, W. Schiek, *Angew. Chem., Int. Ed.* **2001**, *40*, 2465-2468.
[350] C. Wagner, *master thesis* **2014**, Heidelberg University.
[351] S. König, *dissertation* **2016**, Heidelberg University.
[352] M. Regueiro-Figueroa, B. Bensenane, E. Ruscsák, D. Esteban-Gómez, L. J. Charbonnière, G. Tircsó, I. Tóth, A. d. Blas, T. Rodríguez-Blas, C. Platas-Iglesias, *Inorg. Chem.* **2011**, *50*, 4125-4141.
[353] E. Molnár, N. Camus, V. Patinec, G. A. Rolla, M. Botta, G. Tircsó, F. K. Kálmán, T. Fodor, R. Tripier, C. Platas-Iglesias, *Inorg. Chem.* **2014**, *53*, 5136-5149.
[354] A. Rodriguez-Rodriguez, Z. Garda, E. Ruscsak, D. Esteban-Gomez, A. de Blas, T. Rodriguez-Blas, L. M. P. Lima, M. Beyler, R. Tripier, G. Tircso, C. Platas-Iglesias, *Dalton Trans.* **2015**, *44*, 5017-5031.
[355] A. Nonat, C. Gateau, P. H. Fries, M. Mazzanti, *Chem. Eur. J.* **2006**, *12*, 7133-7150.
[356] A. Nonat, M. Giraud, C. Gateau, P. H. Fries, L. Helm, M. Mazzanti, *Dalton Trans.* **2009**, 8033-8046.
[357] A. M. Nonat, C. Gateau, P. H. Fries, L. Helm, M. Mazzanti, *Eur. J. Inorg. Chem.* **2012**, *2012*, 2049-2061.
[358] C. Guanci, G. Giovenzana, L. Lattuada, C. Platas-Iglesias, L. J. Charbonniere, *Dalton Trans.* **2015**, *44*, 7654-7661.
[359] K. Rübenacker, *master thesis* **2014**, Heidelberg University.
[360] E. W. Price, J. F. Cawthray, M. J. Adam, C. Orvig, *Dalton Trans.* **2014**, *43*, 7176-7190.
[361] K. W. Merz, K. Räuchle, *Arch. Pharm.* **1960**, *293*, 968-984.
[362] D. S. C. Black, M. A. Horsham, M. Rose, *Tetrahedron* **1995**, *51*, 4819-4828.
[363] R. Haller, H. Unholzer, *Arch. Pharm.* **1971**, *304*, 654-659.
[364] A. Ashimori, T. Ono, U. Takeshi, O. Yutaka, F. Chikara, W. Masahiro, Y. Kazumasa, *Chem. Pharm. Bull.* **1990**, *38*, 2446-2458.
[365] M. Tamura, Y. Urano, K. Kikuchi, T. Higuchi, M. Hirobe, T. Nagano, *Chem. Pharm. Bull.* **2000**, *48*, 1514-1518.
[366] N. Zaman, R. Guillot, K. Sénéchal-David, M.-L. Boillot, *Tetrahedron Lett.* **2008**, *49*, 7274-7275.
[367] C. Fontenas, E. Bejan, H. A. Haddou, G. Balavoine, *Synth. Commun.* **1995**, *25*, 629-633.
[368] S. Furukawa, *Yakugaku Zasshi* **1959**, *79*, 492-499.
[369] G. Kobayashi, S. Furukawa, Y. Kawada, *Yakugaku Zasshi* **1954**, *74*, 790-790.
[370] V. Boekelheide, W. Linn, *J. Am. Chem. Soc.* **1954**, *76*, 1286-1291.
[371] T. C. Kühler, M. Swanson, V. Shcherbuchin, H. Larsson, B. Mellgård, J.-E. Sjöström, *J. Med. Chem.* **1998**, *41*, 1777-1788.
[372] P. Comba, S. Fukuzumi, C. Koke, B. Martin, A. M. Löhr, J. Straub, *Angew. Chem.* **2016**, *128*, 11295-11299.
[373] R. Haller, *Arzneim.-Forsch.* **1965**, *15*, 1327-1330.
[374] C. Schneider, *master thesis* **2015**, Heidelberg University.
[375] P. Comba, M. Kerscher, M. Merz, V. Müller, H. Pritzkow, R. Remenyi, W. Schiek, Y. Xiong, *Chem. Eur. J.* **2002**, *8*, 5750-5760.
[376] H. Irving, R. J. P. Williams, *J. Chem. Soc. (Resumed)* **1953**, 3192-3210.
[377] H. Irving, R. J. P. Williams, *Nature* **1948**, *162*, 746-747.
[378] P. Comba, A. Hauser, M. Kerscher, H. Pritzkow, *Angew. Chem. Int. Ed.* **2003**, *42*, 4536-4540.
[379] P. V. Bernhardt, P. Comba, *Inorg. Chem.* **1993**, *32*, 2798-2803.
[380] J. Huheey, E. Keiter, R. Keiter, *Anorganische Chemie: Prinzipien von Struktur und Reaktivität*, Walter de Gruyter GmbH & Co KG, **2014**.
[381] M. Morgen, *dissertation* **2013**, Heidelberg University.
[382] M. Brustolon, E. Giamello, *Electron Paramagnetic Resonance*, Wiley, New York, **2009**.

[383] D. Wang, G. R. Hanson, *J. Magn. Reson. A* **1995**, *117*, 1-8.
[384] D. Wang, G. R. Hanson, *Appl. Magn. Reson.* **1996**, *11*, 401-415.
[385] P. Comba, *Coord. Chem. Rev.* **1999**, *182*, 343-371.
[386] E. Larsen, G. N. La Mar, *J. Chem. Educ.* **1974**, *51*, 633.
[387] C. E. Schäffer, C. K. Jørgensen, *Mol. Phys.* **1965**, *9*, 401-412.
[388] T. Schönherr, *Electronic and Vibronic Spectra of Transition Metal Complexes II* **1997**, 87-152.
[389] M. Gerloch, *Magnetism and ligand-field analysis*, CUP Archive, **1983**.
[390] P. Comba, B. Martin, A. Prikhod`ko, H. Pritzkow, H. Rohwer, *C. R. Chim.* **2005**, *8*, 1506-1518.
[391] M. Gerloch, Cammag, a Fortran program for AOM calculations, University of Cambridge, Cambridge, UK, **1991**.
[392] P. Comba, T. W. Hambley, M. A. Hitchman, H. Stratemeier, *Inorg. Chem.* **1995**, *34*, 3903-3911.
[393] P. Comba, F. Emmerling, M. Jakob, W. Kraus, M. Kubeil, M. Morgen, J. Pietzsch, H. Stephan, *Dalton Trans.* **2013**, *42*, 6142-6148.
[394] P. V. Bernhardt, P. Comba, *Inorg. Chem.* **1992**, *31*, 2638-2644.
[395] P. Comba, M. Morgen, H. Wadepohl, *Inorg. Chem.* **2013**, *52*, 6481-6501.
[396] E. T. Clarke, A. E. Martell, *Inorg. Chim. Acta* **1991**, *190*, 27-36.
[397] R. R. Gagne, C. A. Koval, G. C. Lisensky, *Inorg. Chem.* **1980**, *19*, 2854-2855.
[398] H. Koepp, H. Wendt, H. Strehlow, *Z. Elektrochem.* **1960**, *64*, 483-491.
[399] V. V. Pavlishchuk, A. W. Addison, *Inorg. Chim. Acta* **2000**, *298*, 97-102.
[400] M. R. McDevitt, A. W. Addison, *Inorg. Chim. Acta* **1993**, *204*, 141-146.
[401] R. Alexander, A. Parker, J. Sharp, W. Waghorne, *J. Am. Chem. Soc.* **1972**, *94*, 1148-1158.
[402] V. C. Culotta, M. Yang, T. V. O'Halloran, *Biochim. Biophys. Acta - Mol Cell Res.* **2006**, *1763*, 747-758.
[403] I. Fridovich, *Annu. Rev. Biochem.* **1995**, *64*, 97-112.
[404] P. Comba, B. Martin, A. Sanyal, *J. Comput. Chem.* **2013**, *34*, 1598-1608.
[405] R. C. Roberts, D. G. Makey, U. S. Seal, *J. Biol. Chem.* **1966**, *241*, 4907-4913.
[406] W. R. Harris, Y. Chen, K. Wein, *Inorg. Chem.* **1994**, *33*, 4991-4998.
[407] C. F. G. C. Geraldes, R. Delgado, A. M. Urbano, J. Costa, F. Jasanada, F. Nepveu, *J. Chem. Soc., Dalton Trans.* **1995**, 327-335.
[408] J. J. Wilson, M. Ferrier, V. Radchenko, J. R. Maassen, J. W. Engle, E. R. Batista, R. L. Martin, F. M. Nortier, M. E. Fassbender, K. D. John, E. R. Birnbaum, *Nucl. Med. Biol.* **2015**, *42*, 428-438.
[409] E. W. Price, B. M. Zeglis, J. F. Cawthray, J. S. Lewis, M. J. Adam, C. Orvig, *Inorg. Chem.* **2014**, *53*, 10412-10431.
[410] P. Comba, U. Jermilova, C. Orvig, B. O. Patrick, C. F. Ramogida, K. Rück, C. Schneider, M. Starke, *Chem. Eur. J., submitted manuscript*.
[411] ACD/Spectrus processor, version 2016.1, Advanced Chemistry Development, Inc., Toronto, ON, Canada, www.acdlabs.com, **2016**.
[412] C. K. Johnson, *ORTEP: A Thermal Ellipsoid Plotting Program*, Oak National Laboratories: Oak Ridge, TN, **1965**.
[413] C. Cason, T. Froehlich, N. Kopp, R. Parker, *POV-Ray for Windows*, Persistence of Vision Raytracer Pyt. Ltd, **2005**.
[414] K. Hegetschweiler, *TITKURVE Programm Titrationskurven Vers. 1.1 (unveröffentlicht)*, Zürich, **1993**.
[415] R. M. Smith, A. E. Martell, R. J. Motekaitis, *Critically Selected Stability Constants of Metal Complexes*, NIST Standard Reference Database 46, Version 8.0, Gaithersburg, MD, USA, **2004**.
[416] P. Gans, B. O'Sullivan, *Talanta* **2000**, *51*, 33-37.
[417] D. W. Barnum, *Inorg. Chem.* **1983**, *22*, 2297-2305.

[418] L. Alderighi, P. Gans, A. Ienco, D. Peters, A. Sabatini, A. Vacca, *Coord. Chem. Rev.* **1999**, *184*, 311-318.
[419] W. A. Breeman, M. de Jong, E. de Blois, B. F. Bernard, M. Konijnenberg, E. P. Krenning, *Eur. J. Nucl. Med. Mol. Imaging* **2005**, *32*, 478-485.
[420] J. Dilling, R. Krücken, L. Merminga, *ISAC and ARIEL: The TRIUMF Radioactive Beam Facilities and the Scientific Program*, Springer, **2014**.
[421] J. R. Crawford, P. Kunz, H. Yang, P. Schaffer, T. J. Ruth, *Appl. Radiat. Isot.* **2017**, *122*, 222-228.
[422] B. Zielinska, C. Apostolidis, F. Bruchertseifer, A. Morgenstern, *Solvent Extr. Ion Exch.* **2007**, *25*, 339-349.
[423] V. Radchenko, J. W. Engle, J. J. Wilson, J. R. Maassen, F. M. Nortier, W. A. Taylor, E. R. Birnbaum, L. A. Hudston, K. D. John, M. E. Fassbender, *J. Chrom. A* **2015**, *1380*, 55-63.
[424] C. F. Ramogida, J. F. Cawthray, E. Boros, C. L. Ferreira, B. O. Patrick, M. J. Adam, C. Orvig, *Inorg. Chem.* **2015**, *54*, 2017-2031.
[425] W. F. Maguire, M. R. McDevitt, P. M. Smith-Jones, D. A. Scheinberg, *J. Nucl. Med.* **2014**, *55*, 1492-1498.

9 Appendix[viii]

Appendix A: ^{1}H- and ^{13}C-NMR spectra

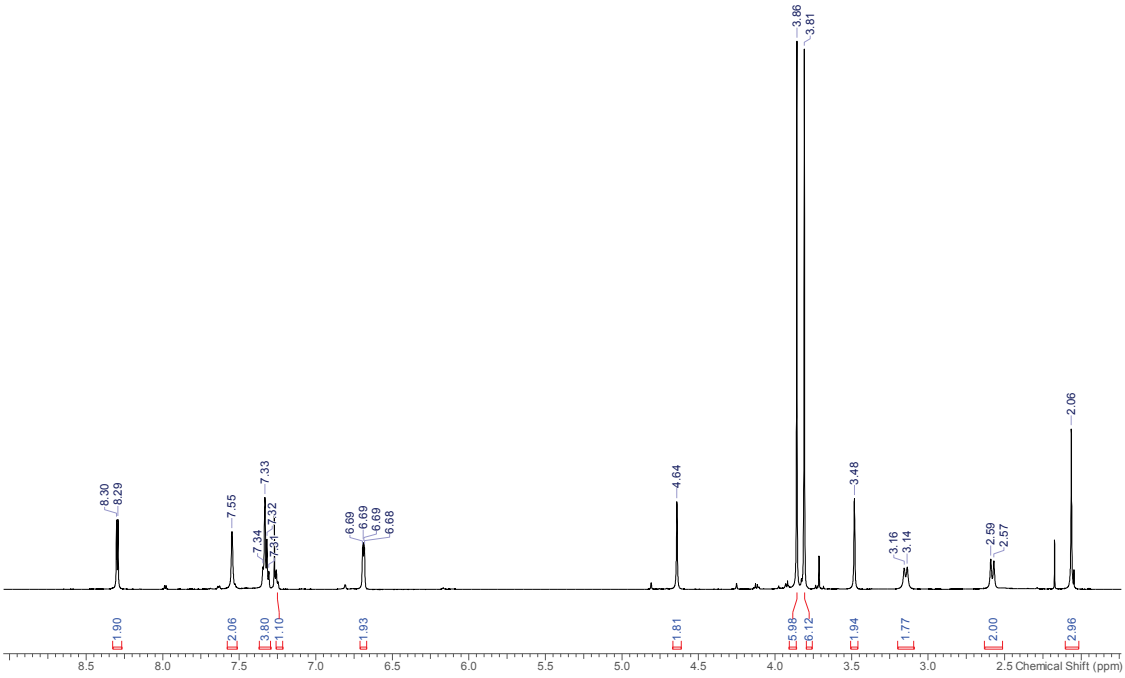

Figure A 1. ^{1}H-NMR (600.13 MHz, 25 °C, $CDCl_3$) spectrum of compound **B12**.

[viii] Reproduced in part with permission from P. Comba, L. Grimm, C. Orvig, K. Rück, H. Wadepohl, *Inorg. Chem.* **2016**, *55*, 12531-12543, Copyright 2016 American Chemical Society.; Parts of this chapter will be published in P. Comba, U. Jermilova, C. Orvig, B. O. Patrick, C. F. Ramogida, K. Rück, C. Schneider, M. Starke, *Chem. Eur. J.*, *submitted manuscript.*

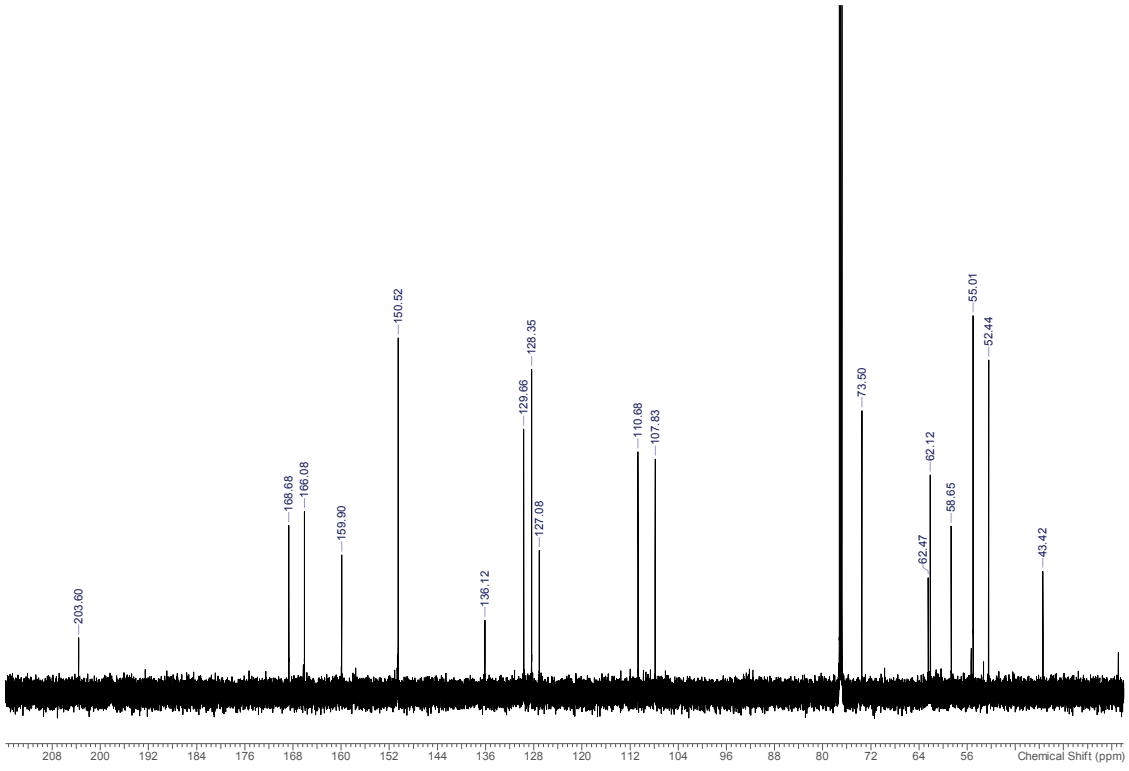

Figure A 2. ^{13}C-NMR (150.92 MHz, 25 °C, $CDCl_3$) spectrum of compound **B12**.

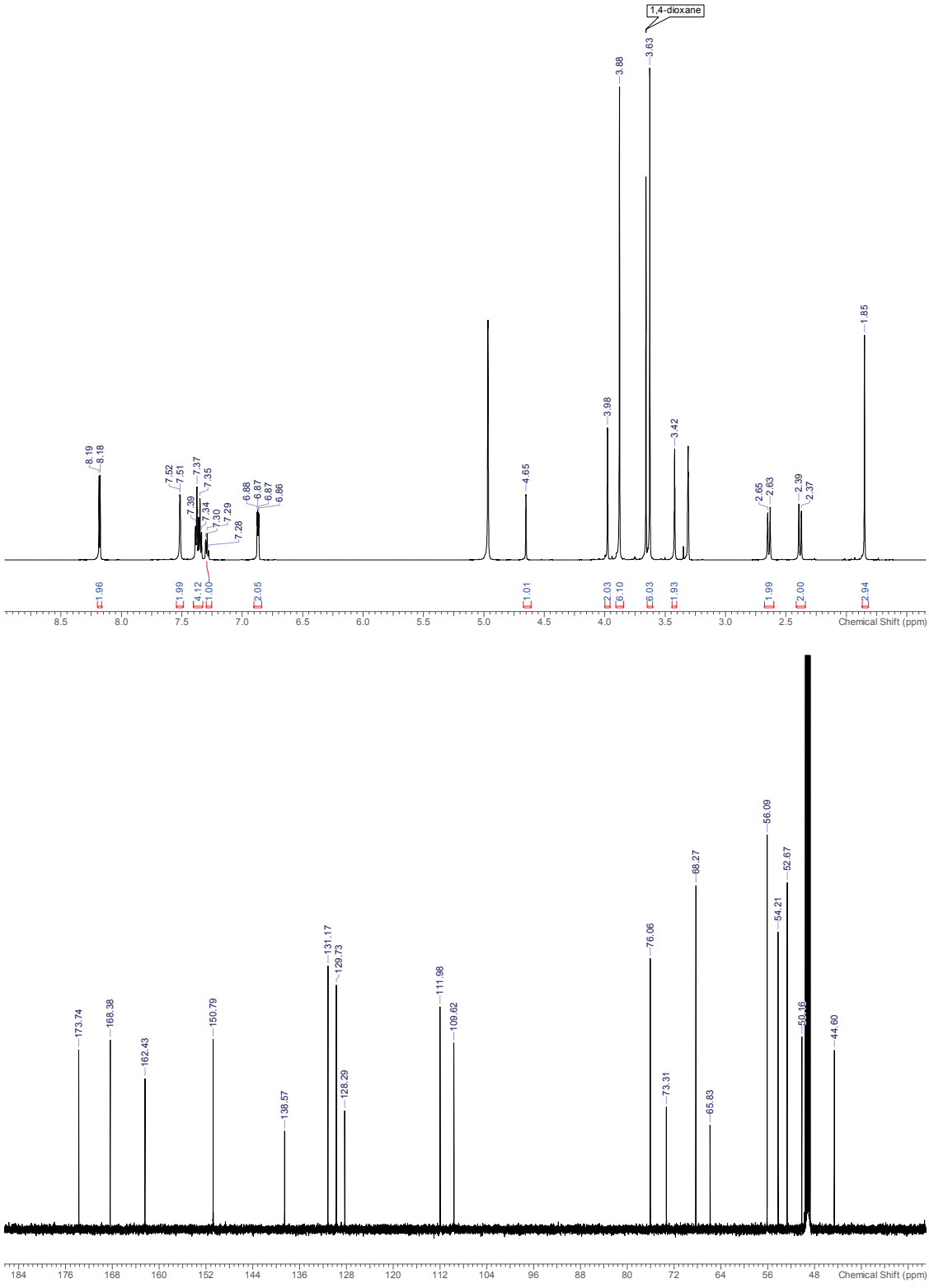

Figure A 3. ^{1}H-NMR (600.13 MHz, 25 °C, MeOH-d^{4}) spectrum (top) and ^{13}C-NMR (150.92 MHz, 25 °C, MeOH-d^{4}) spectrum (bottom) of compound **B13**.

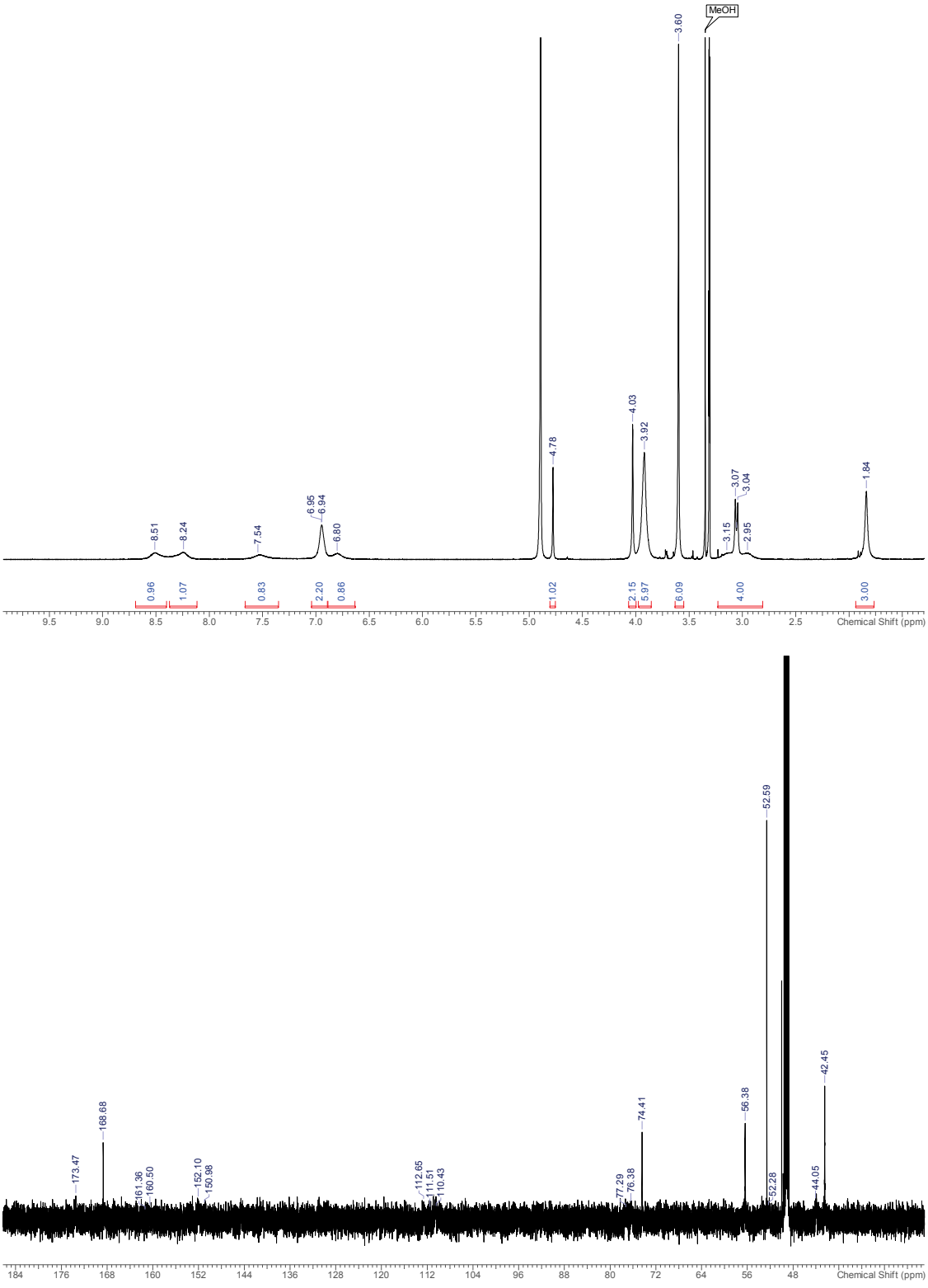

Figure A 4. ^{1}H-NMR (600.13 MHz, 25 °C, MeOH-d^{4}) spectrum (top) and ^{13}C-NMR (150.92 MHz, 25 °C, MeOH-d^{4}) spectrum (bottom) of compound **B14**.

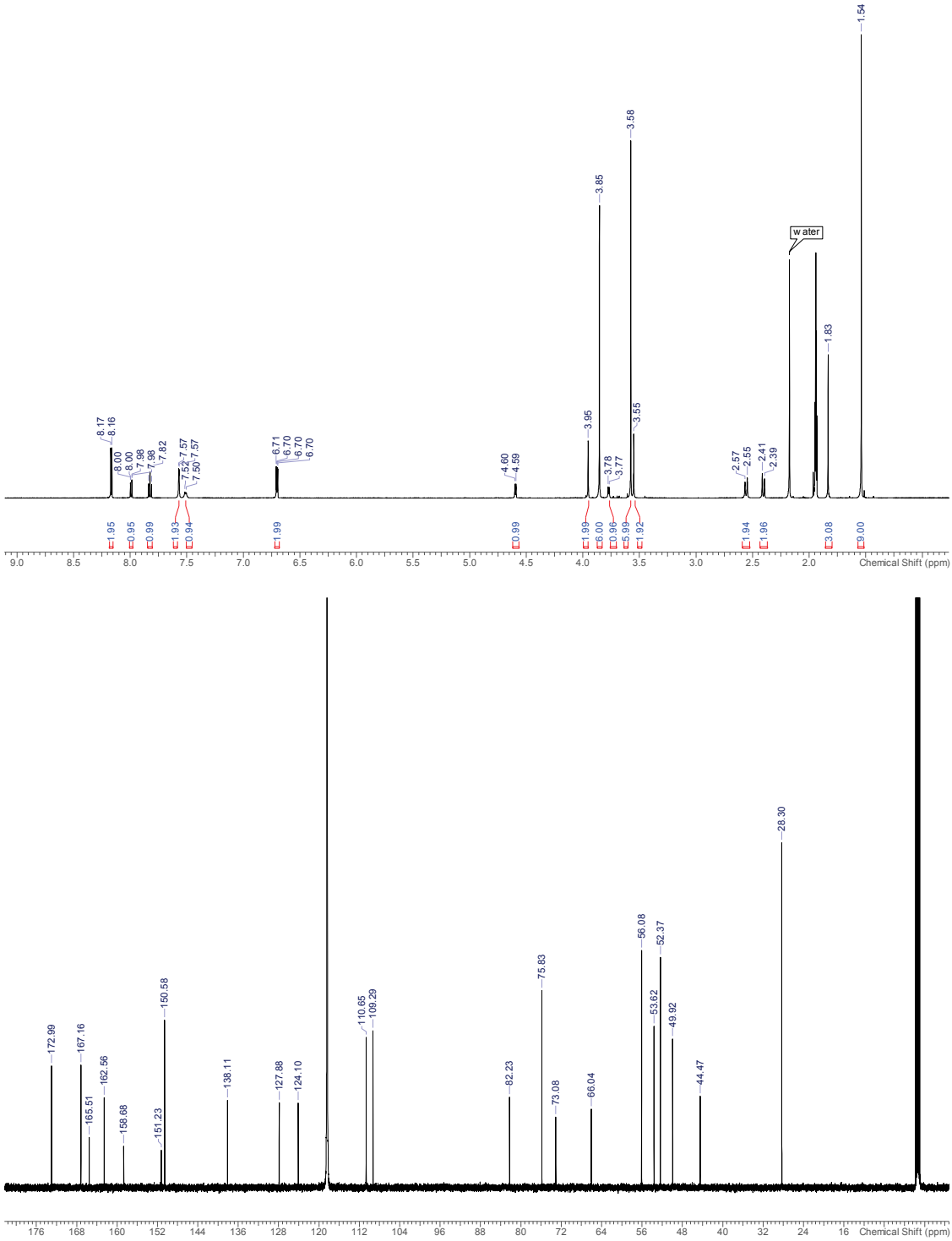

Figure A 5. ^{1}H-NMR (600.13 MHz, 25 °C, MeCN-d^{3}) spectrum (top) and ^{13}C-NMR (150.92 MHz, 25 °C, MeCN-d^{3}) spectrum (bottom) of compound **(*p*-MeO)(*t*Bu)B1a**. The water visible in the ^{1}H-NMR spectrum originates from the deuterated solvent.

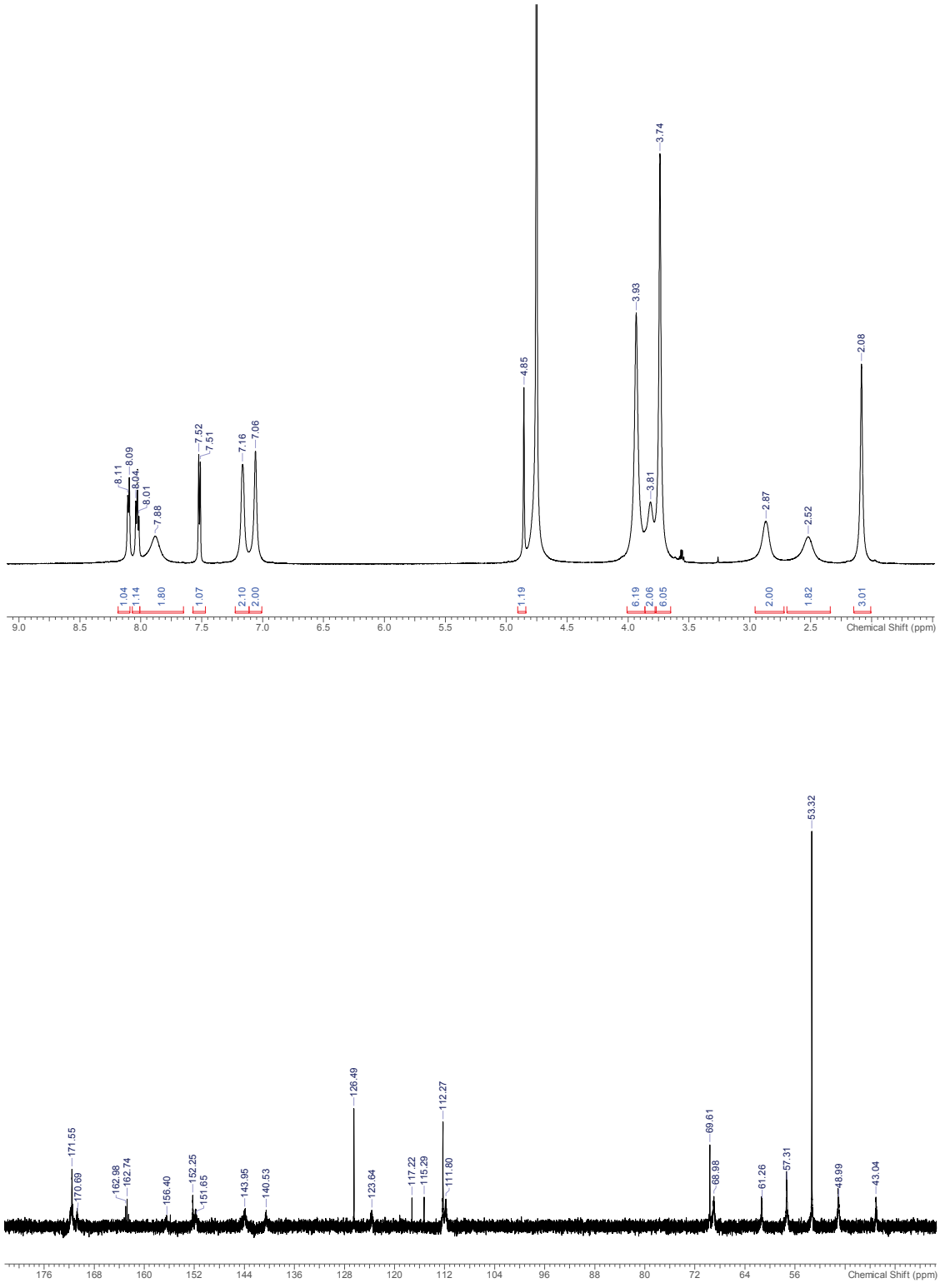

Figure A 6. ^{1}H-NMR (600.13 MHz, 25 °C, D_2O) spectrum (top) and ^{13}C-NMR (150.92 MHz, 25 °C, D_2O) spectrum (bottom) of compound **(*p*-MeO)B1a**•H(TFA).

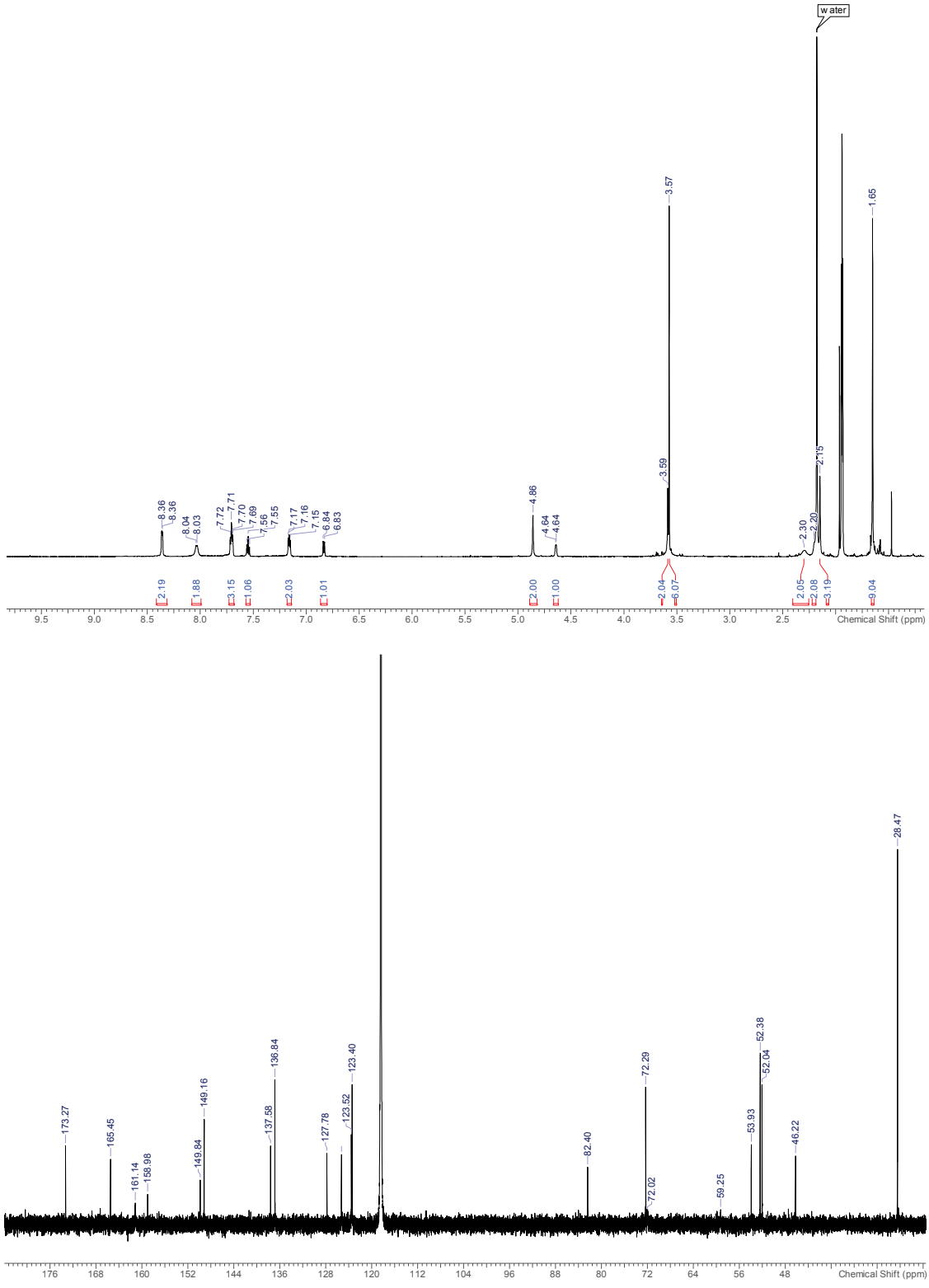

Figure A 7. ^{1}H-NMR (600.13 MHz, 22 °C, MeCN-d^{3}) spectrum (top) and ^{13}C-NMR (150.92 MHz, 22 °C, MeCN-d^{3}) spectrum (bottom) of compound ***(t*Bu)B1b**. The water visible in the ^{1}H-NMR spectrum originates from the deuterated solvent.

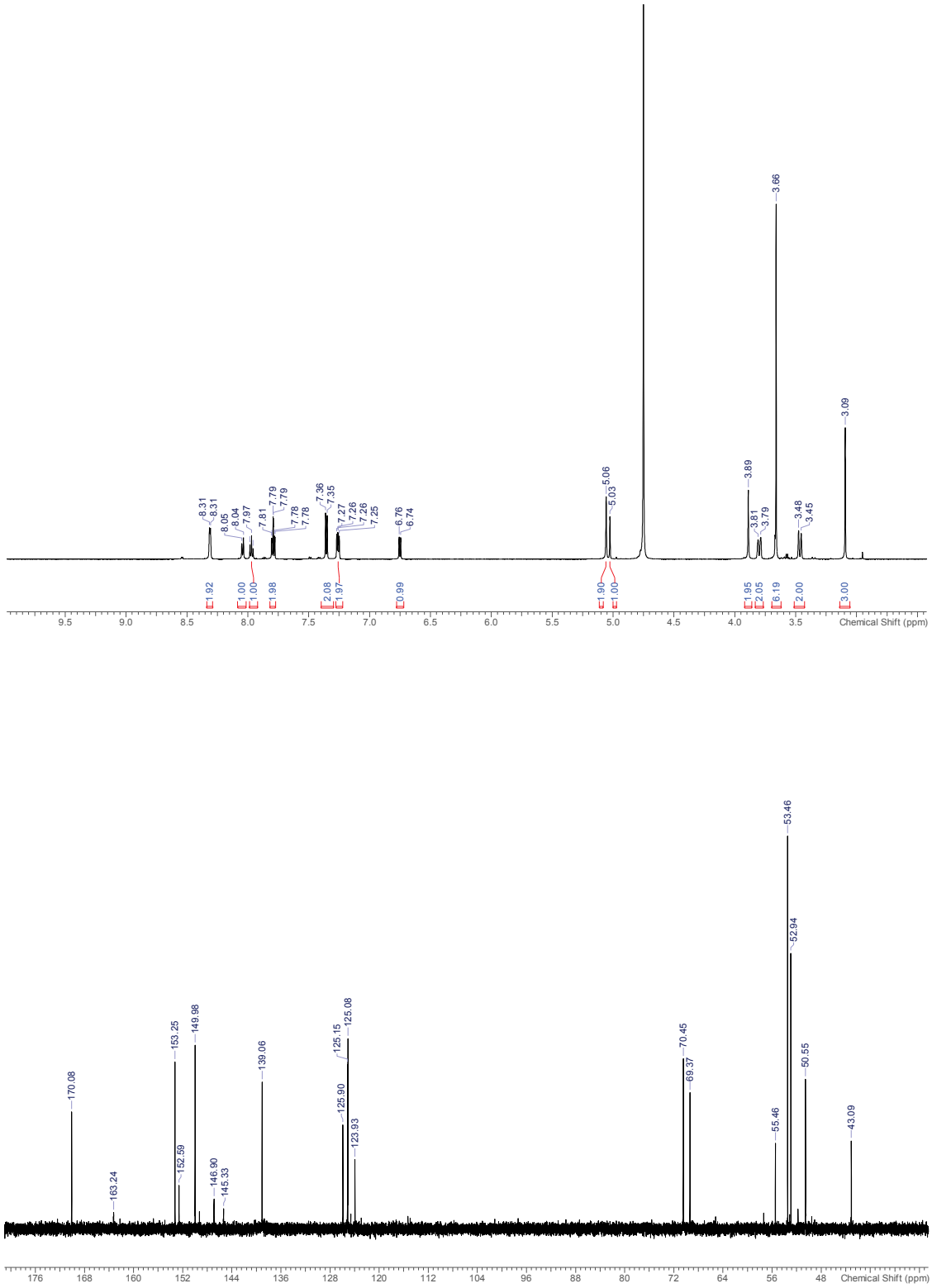

Figure A 8. ^{1}H-NMR (600.13 MHz, 22 °C, D_2O) spectrum (top) and ^{13}C-NMR (150.92 MHz, 22 °C, D_2O) spectrum (bottom) of compound **B1b**•H(TFA).

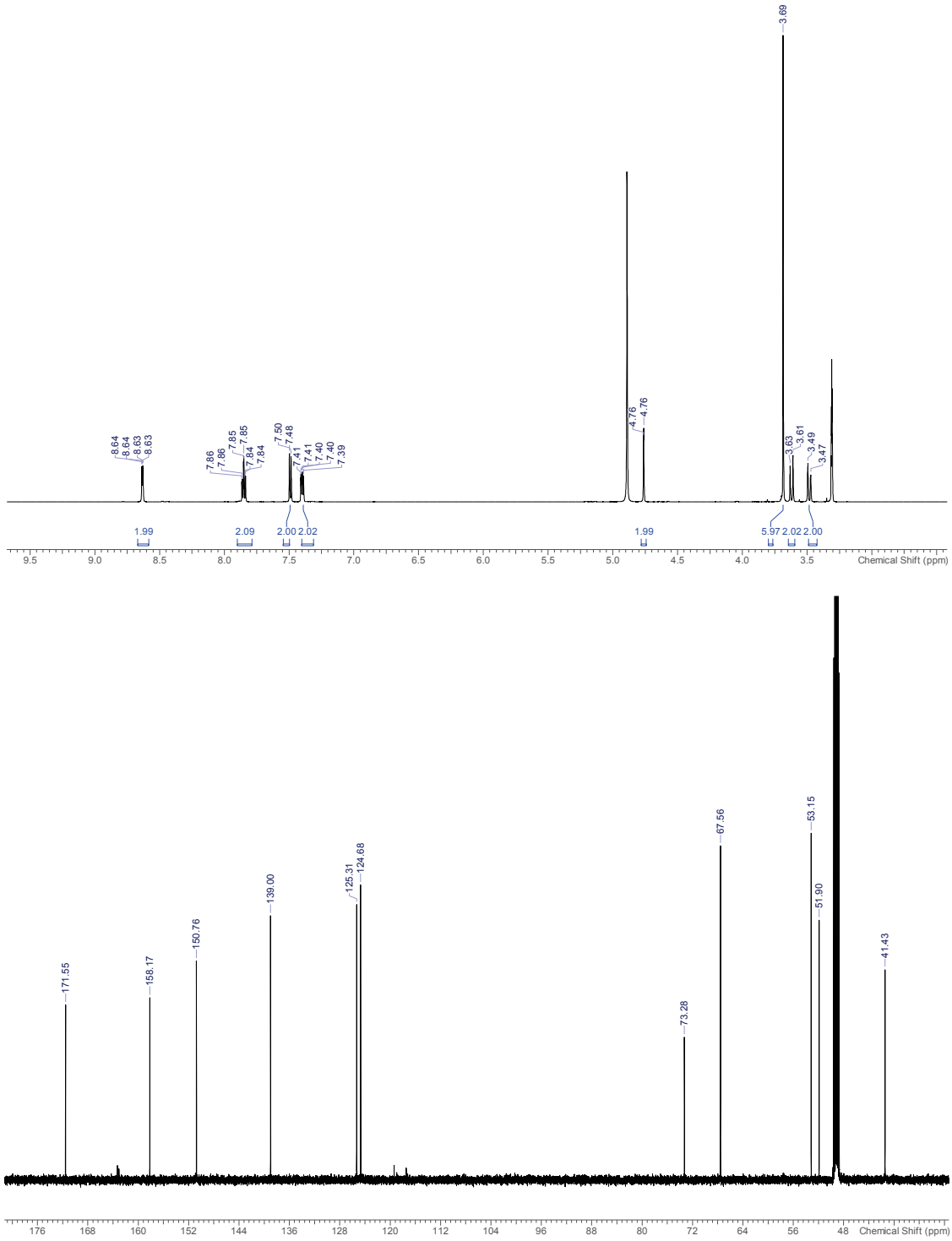

Figure A 9. ^{1}H-NMR (600.13 MHz, 25 °C, MeOH-d^{4}) spectrum (top) and ^{13}C-NMR (150.92 MHz, 25 °C, MeOH-d^{4}) spectrum (bottom) of compound **B19**•H(TFA).

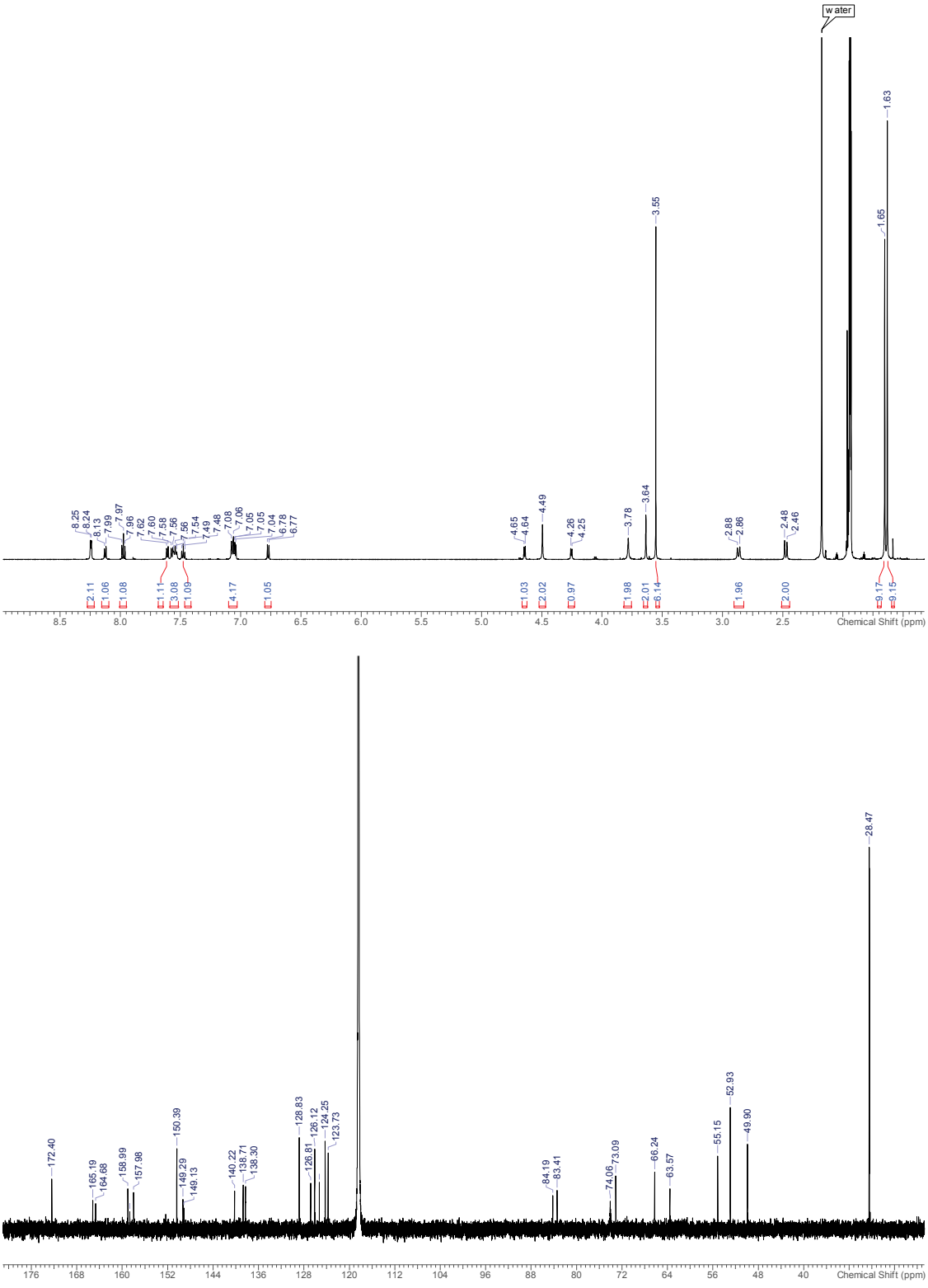

Figure A 10. ^{1}H-NMR (600.13 MHz, 25 °C, MeCN-d^{3}) spectrum (top) and ^{13}C-NMR (150.92 MHz, 25 °C, MeCN-d^{3}) spectrum (bottom) of compound **(*t*Bu)$_2$B2**. The water visible in the ^{1}H-NMR spectrum originates from the deuterated solvent.

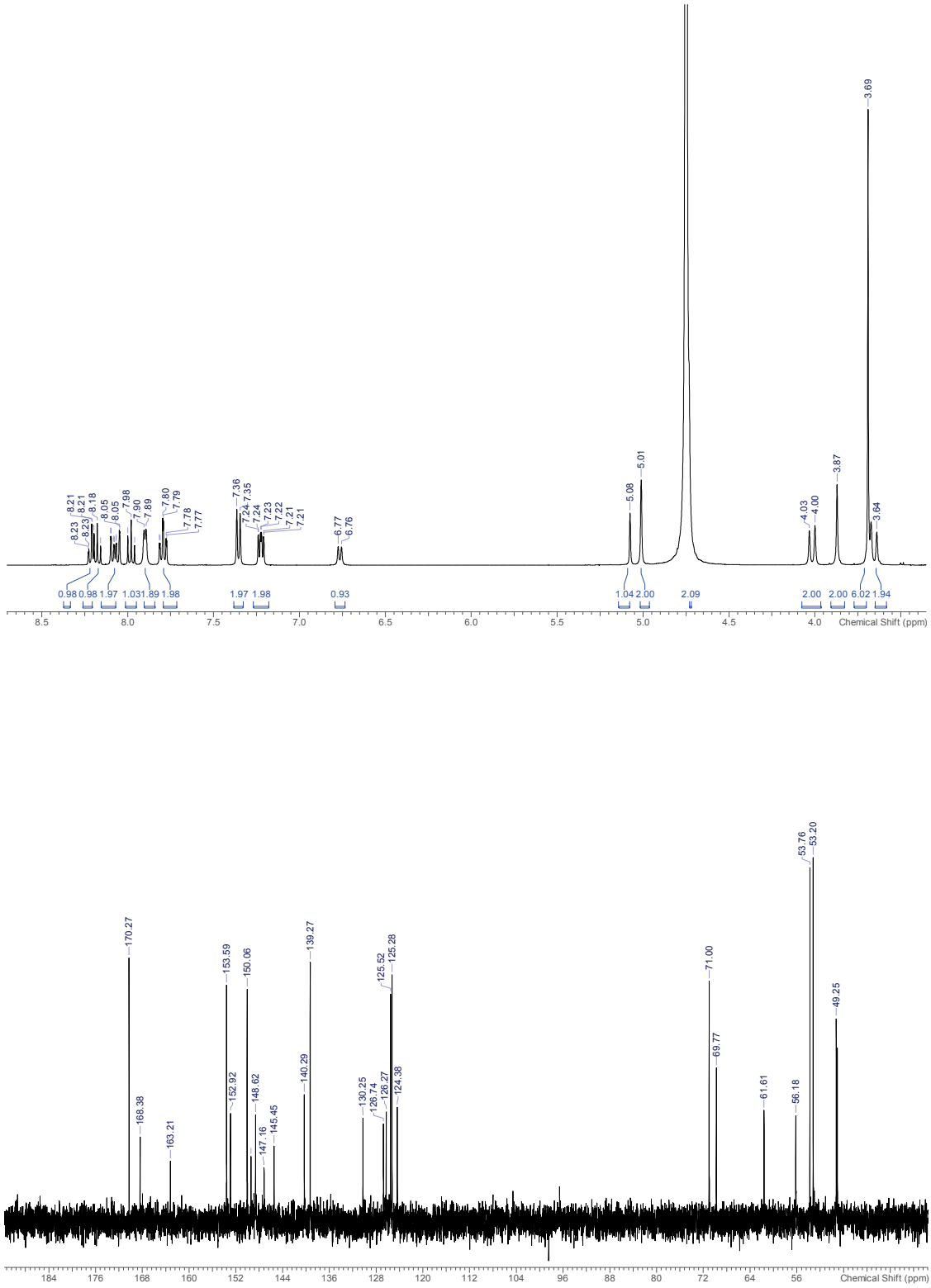

Figure A 11. ^{1}H-NMR (400.19 MHz, 25 °C, D_2O) spectrum (top) and ^{13}C-NMR (100.64 MHz, 25 °C, D_2O) spectrum (bottom) of compound **B2**•H(TFA).

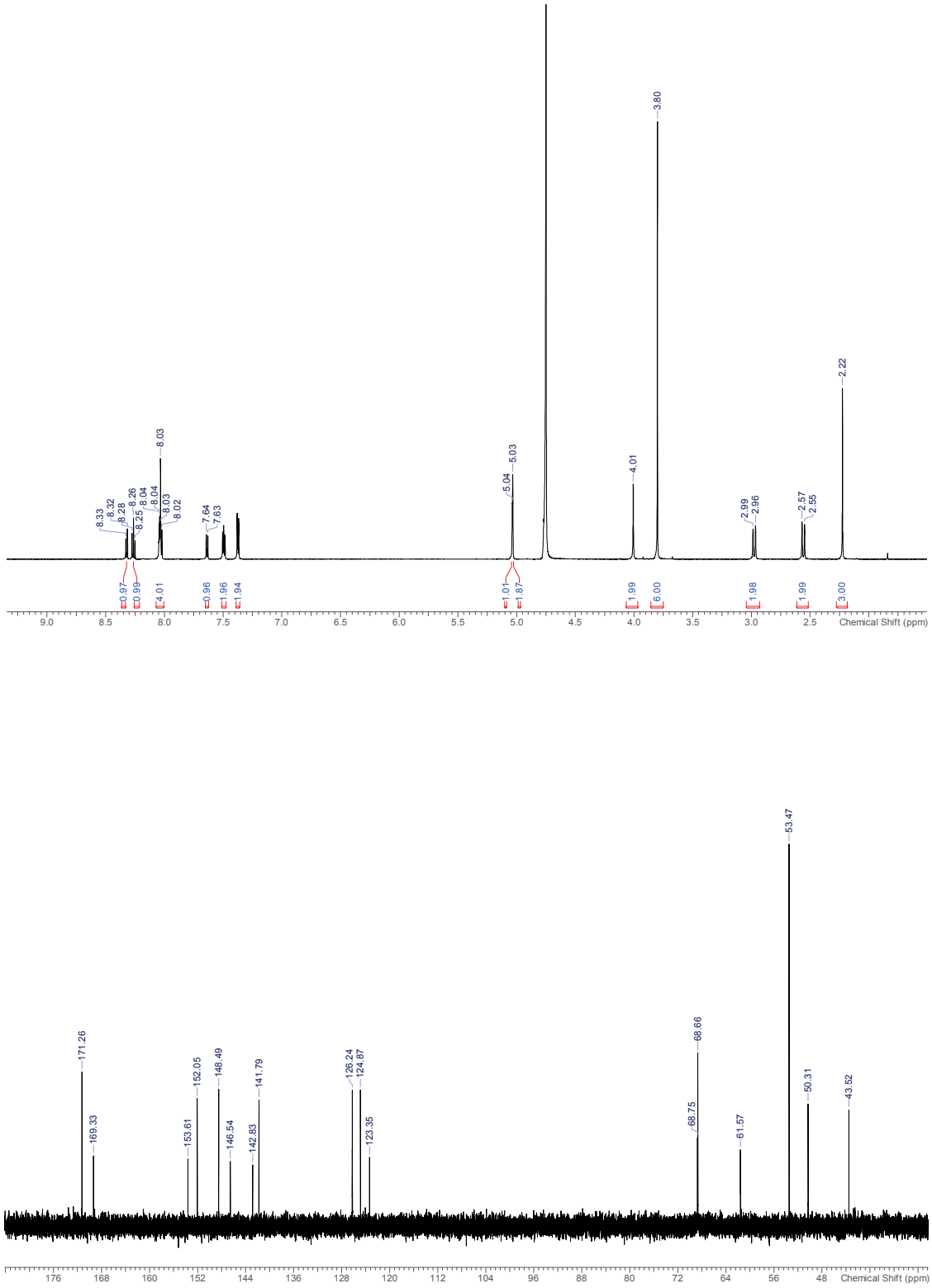

Figure A 12. ^{1}H-NMR (600.13 MHz, 22 °C, D_2O) spectrum (top) and ^{13}C-NMR (150.92 MHz, 22 °C, D_2O) spectrum (bottom) of compound [Zn^{II}(**B1a**)](TFA).

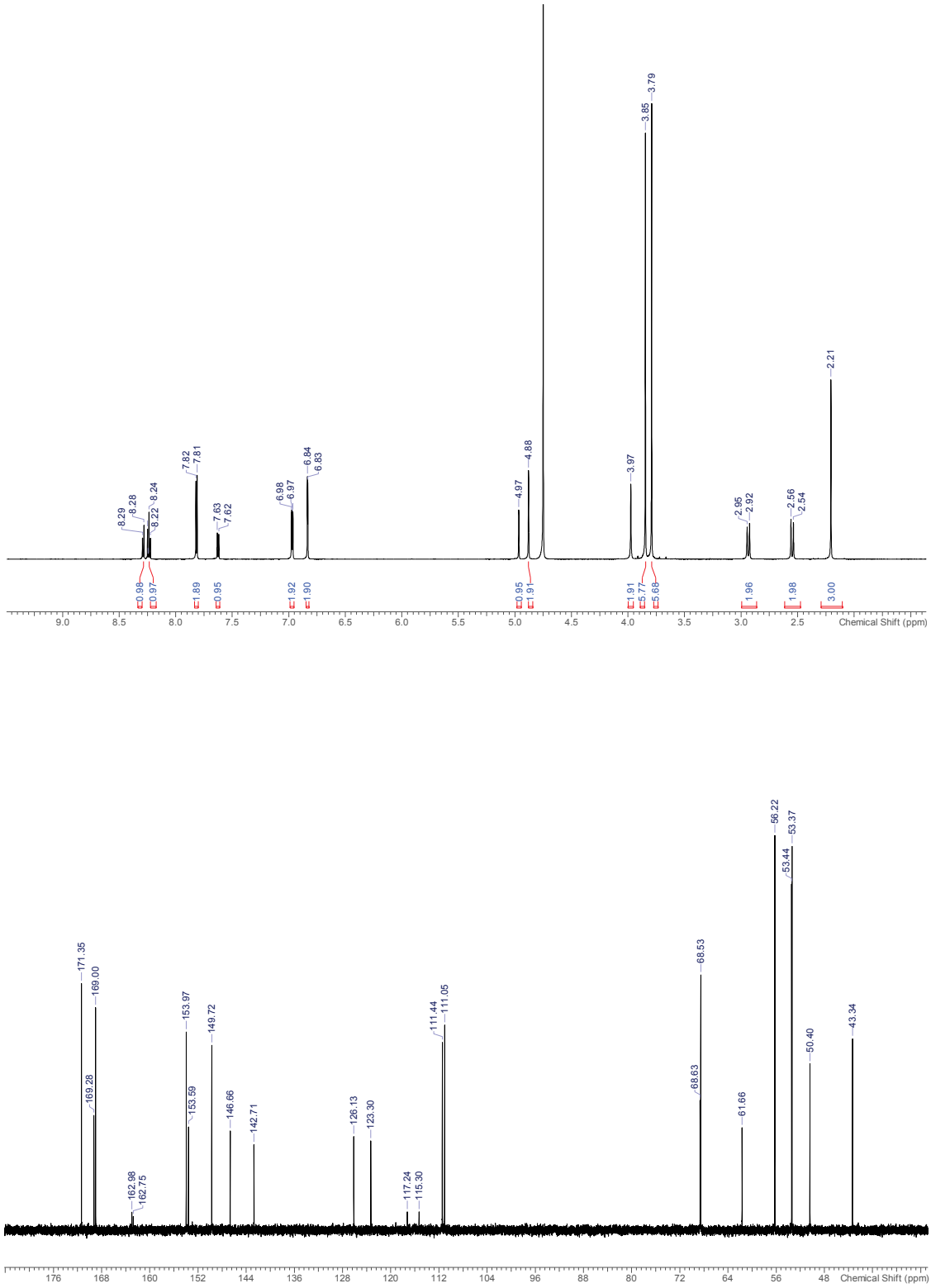

Figure A 13. ^{1}H-NMR (600.13 MHz, 22 °C, D_2O) spectrum (top) and ^{13}C-NMR (150.92 MHz, 22 °C, D_2O) spectrum (bottom) of compound [Zn^{II}(**(*p*-MeO)B1a**)](TFA).

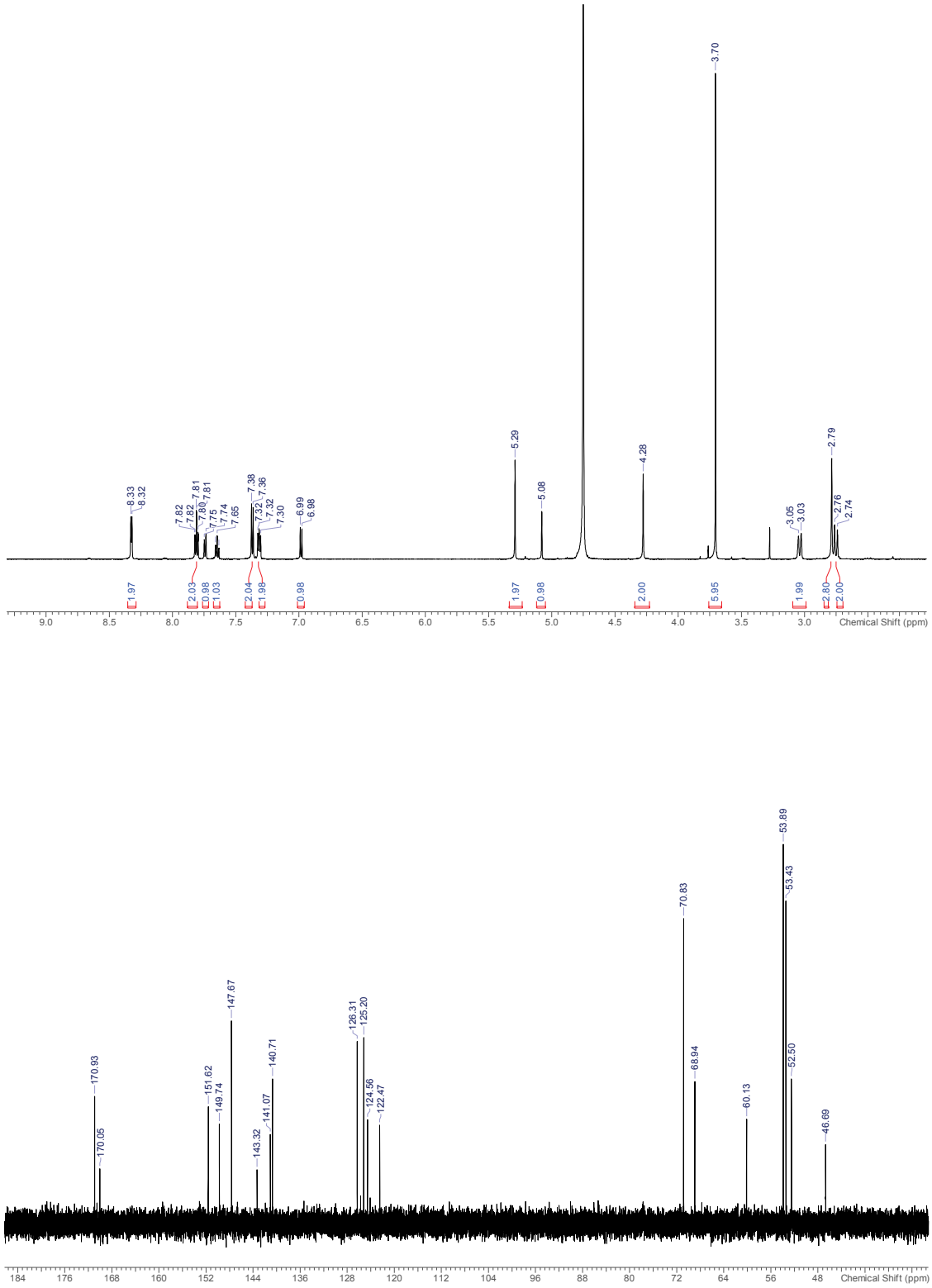

Figure A 14. ^{1}H-NMR (600.13 MHz, 22 °C, D_2O) spectrum (top) and ^{13}C-NMR (150.92 MHz, 22 °C, D_2O) spectrum (bottom) of compound [Zn^{II}(**B1b**)](TFA).

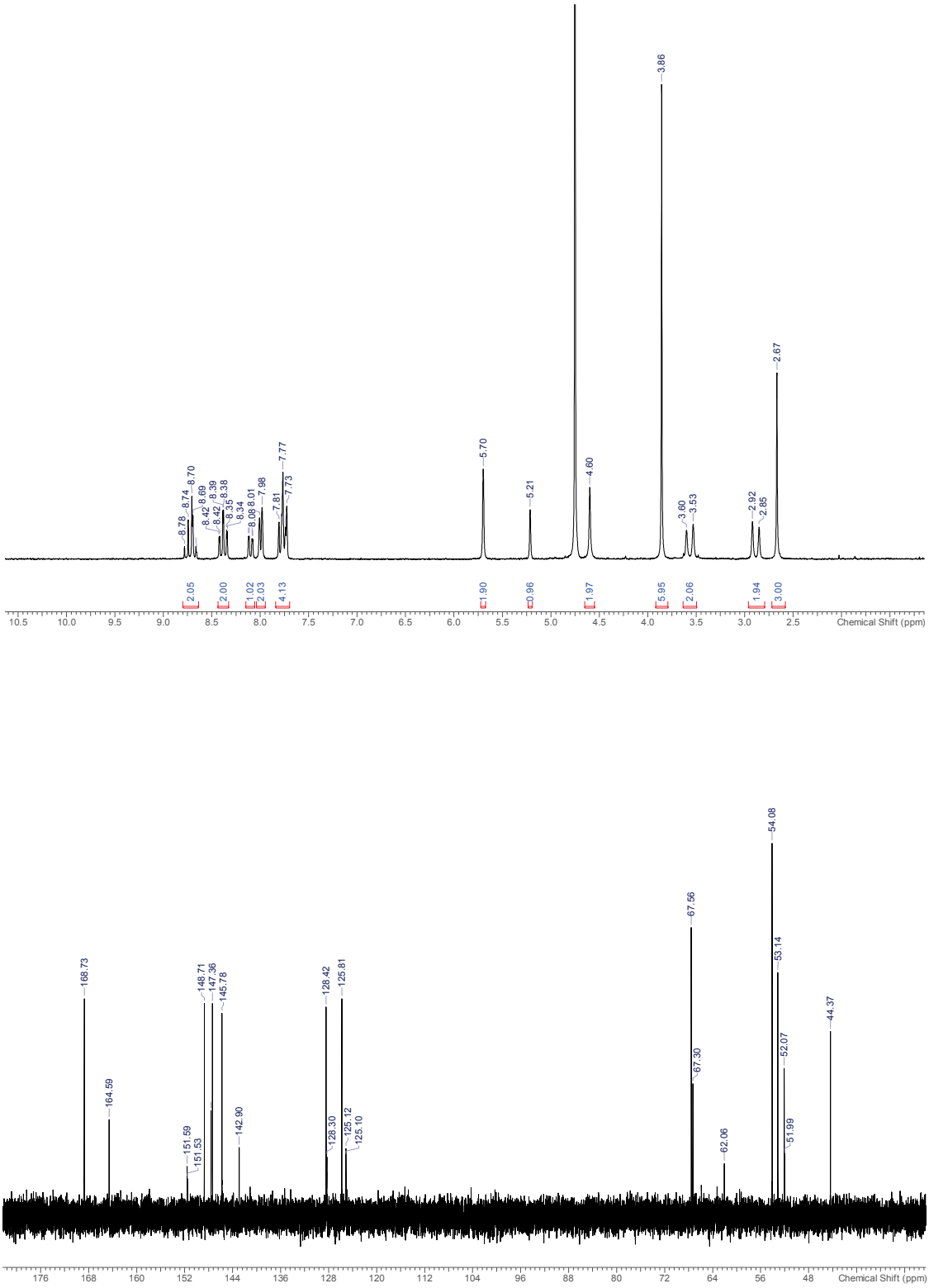

Figure A 15. ^{1}H-NMR (200.13 MHz, 27 °C, D_2O) spectrum (top) and ^{13}C-NMR (150.92 MHz, 22 °C, D_2O) spectrum (bottom) of compound [Ga^{III}(**B1a**)](TFA)(NO_3).

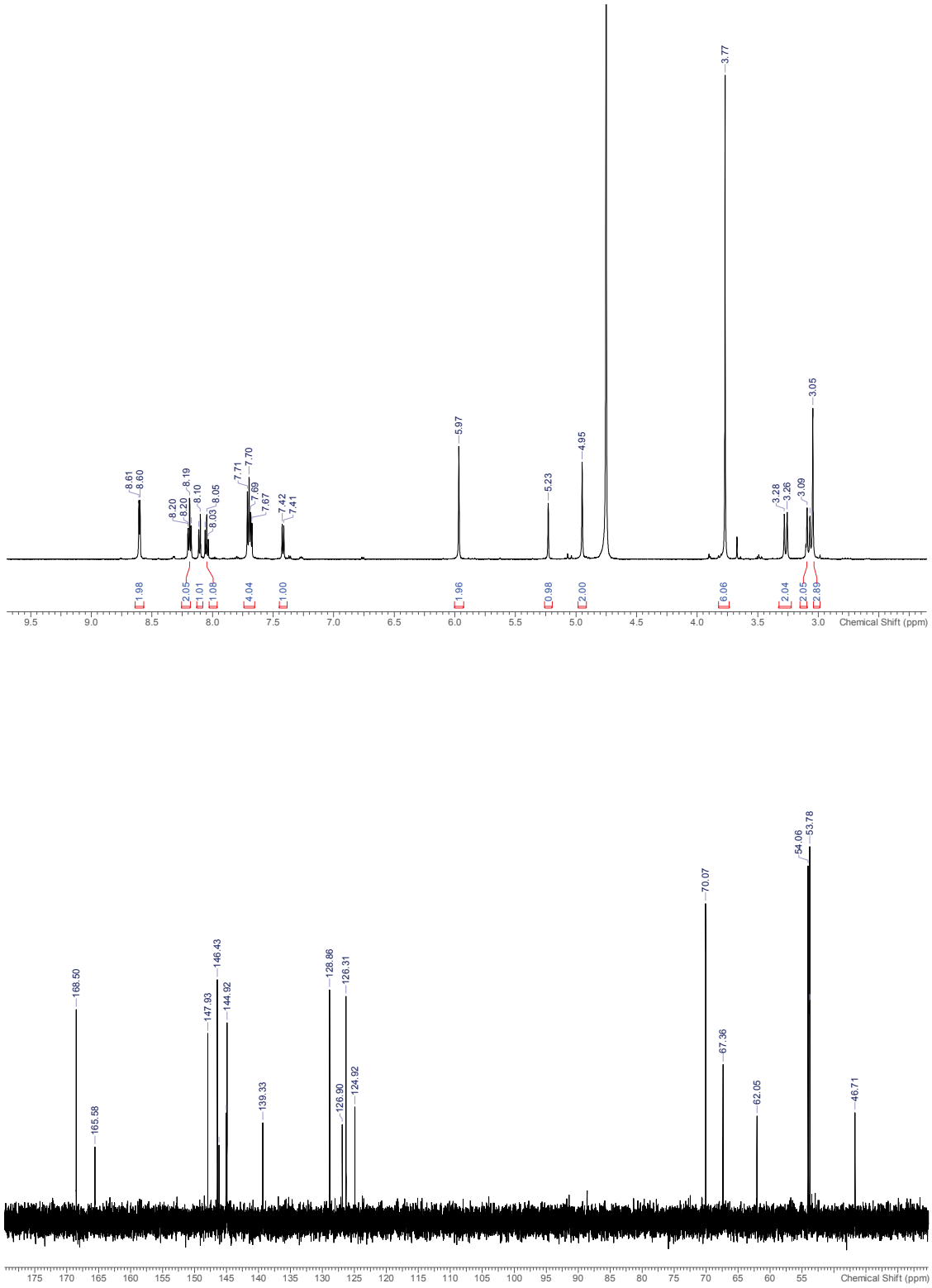

Figure A 16. ^{1}H-NMR (600.13 MHz, 22 °C, D_2O) spectrum (top) and ^{13}C-NMR (150.92 MHz, 22 °C, D_2O) spectrum (bottom) of compound $[Ga^{III}(\mathbf{B1b})](NO_3)_2$.

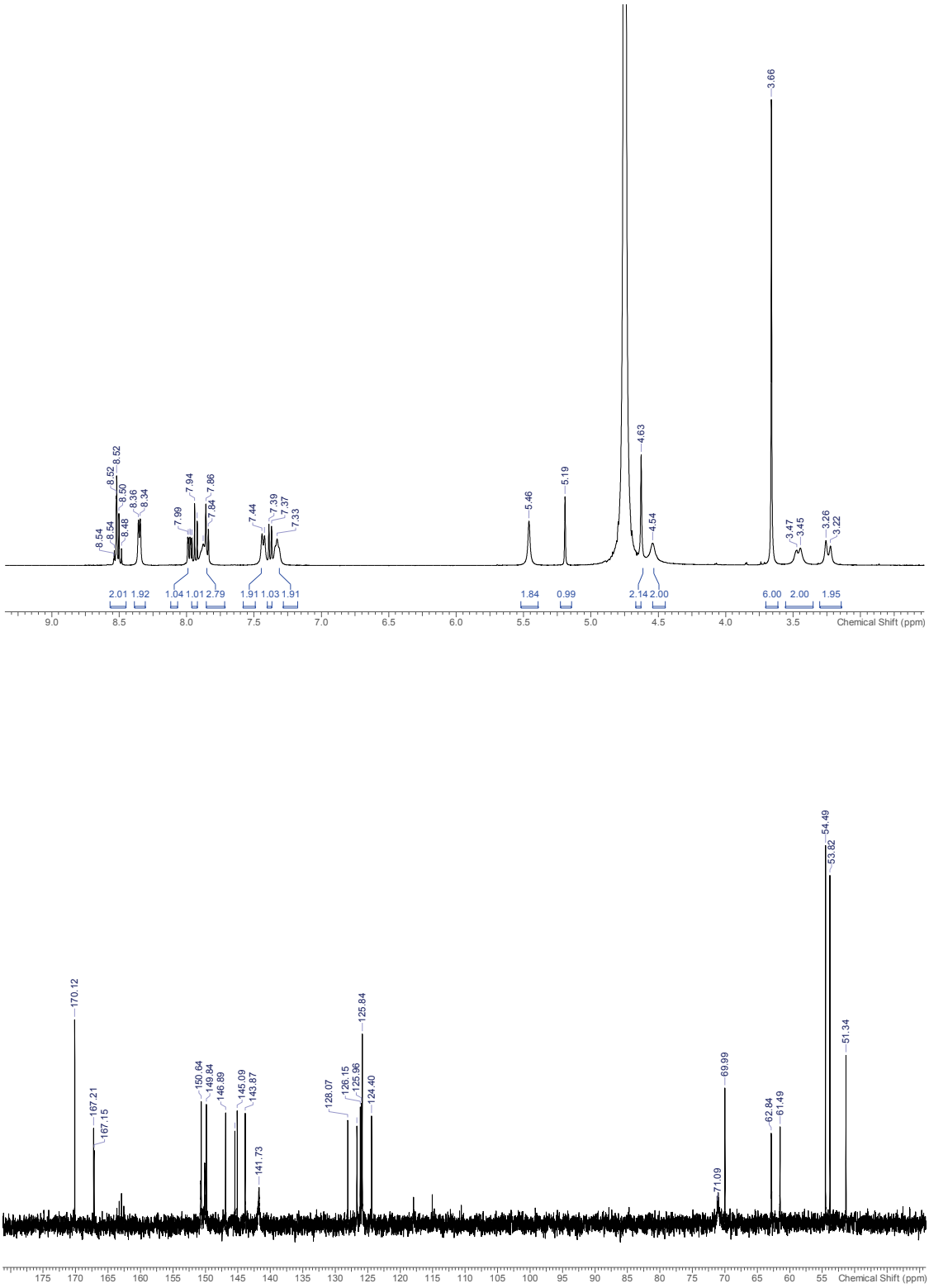

Figure A 17. ^{1}H-NMR (400.19 MHz, 25 °C, D_2O) spectrum (top) and ^{13}C-NMR (100.64 MHz, 25 °C, D_2O) spectrum (bottom) of [In^{III}(**B2**)](TFA).

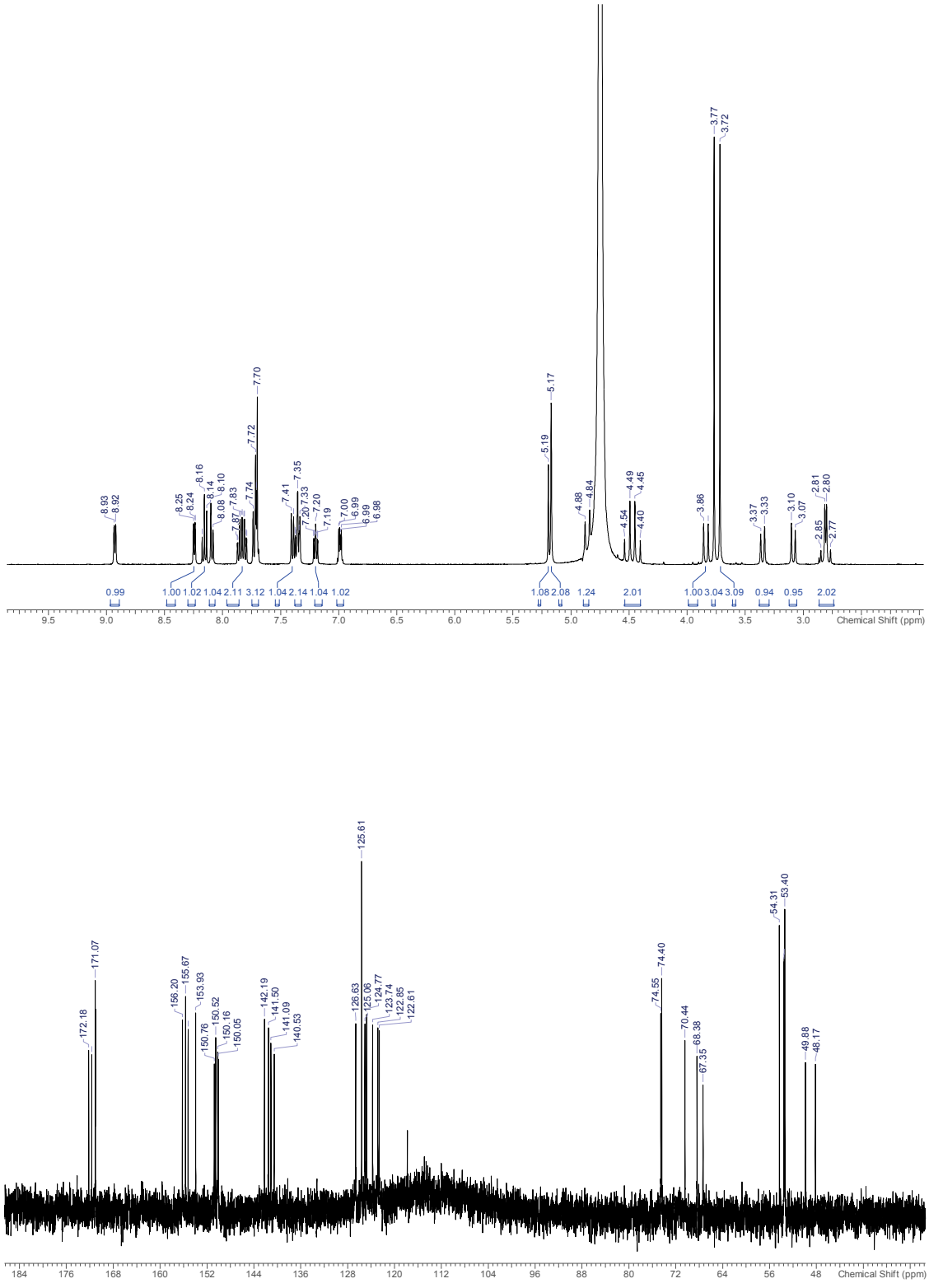

Figure A 18. ^{1}H-NMR (400.13 MHz, 25 °C, D_2O) spectrum (top) and ^{13}C-NMR (100.62 MHz, 25 °C, D_2O) spectrum (bottom) of [Lu^{III}(**B2**)](TFA).

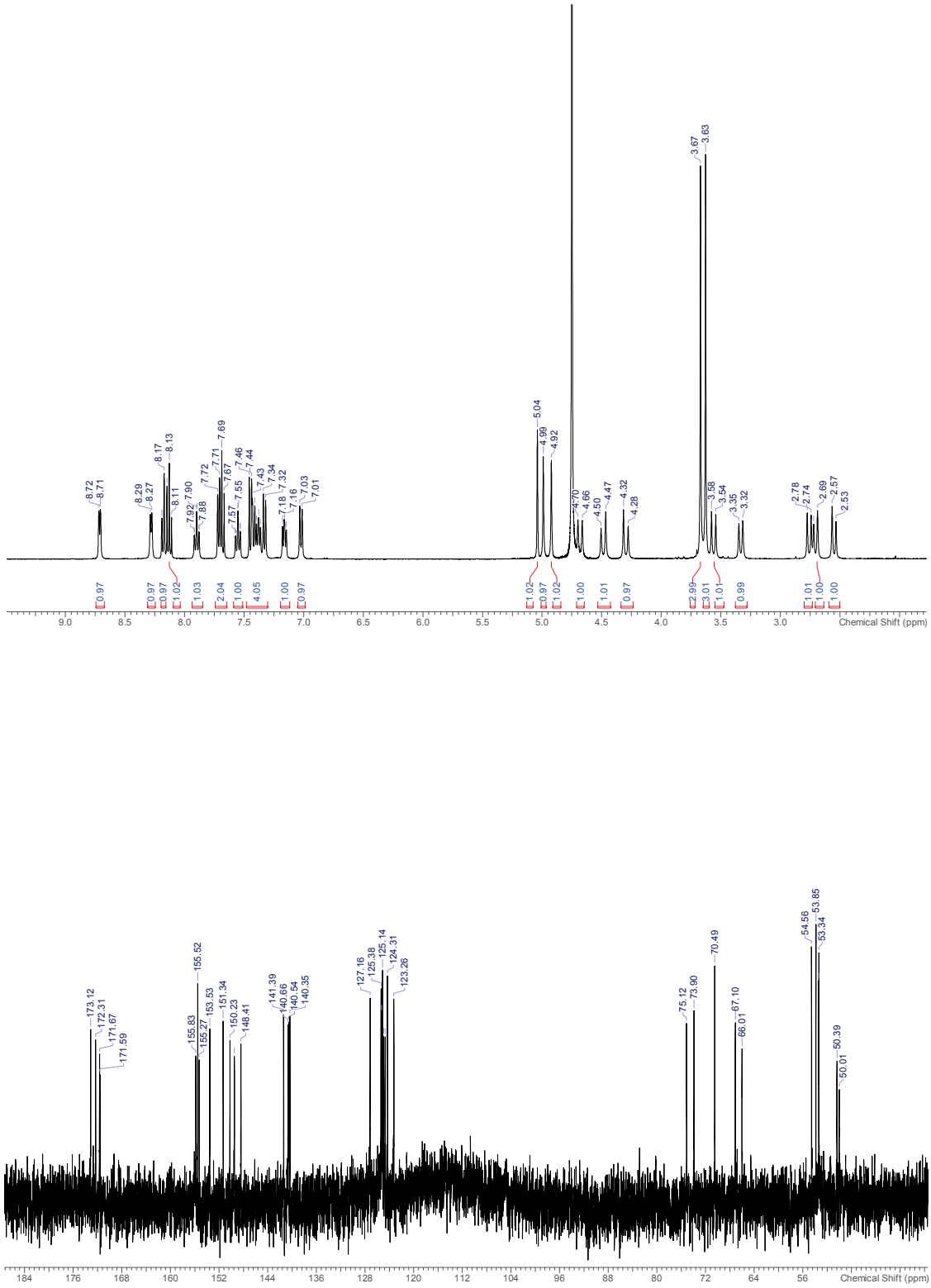

Figure A 19. ^{1}H-NMR (400.13 MHz, 25 °C, D_2O) spectrum (top) and ^{13}C-NMR (100.62 MHz, 25 °C, D_2O) spectrum (bottom) of [La^{III}(**B2**)](TFA).

Appendix B: Details of the solid state structure determinations

The experimental structures reported herein are or will be deposited at the Cambridge Crystallographic Data Centre (CCDC) and can thus be obtained free of charge *via* https://www.ccdc.cam.ac.uk/structures/. The corresponding CCDC-reference codes of the compounds are given in the following tables. Note that the numbering scheme in the present thesis slightly differs from the crystallographic numbering scheme.

	B1a•H(TFA)	**B12**•0.5H_2O	**B13**•0.5(1,4-dioxane)
identification code	co_kr09	co_kr14	co_kr15
CCDC number	1481459	1547413	1547414
formula	$C_{31}H_{32}F_3N_5O_9$	$C_{31}H_{35}N_4O_{7.5}$	$C_{33}H_{40}N_4O_8$
crystal system	triclinic	triclinic	monoclinic
space group	*P* –1	*P* –1	*P* $2_1/c$
a /Å	10.785(6)	13.795(7)	14.759(6)
b /Å	11.054(7)	14.223(7)	11.471(5)
c /Å	15.067(9)	17.438(9)	18.289(8)
α /°	75.338(8)	110.369(9)	90
β /°	71.848(15)	107.207(12)	95.841(12)
γ /°	71.608(9)	99.843(15)	90
V /Å^3	1595.6(16)	2917(2)	3080(2)
Z	2	4	4
M_r	675.61	583.63	620.69
F_{000}	704	1236	1320
d_c /Mg·m^{-3}	1.406	1.329	1.338
μ /mm^{-1}	0.116	0.096	0.096
max., min. transmission factors	0.7464, 0.7004 [(a)]	0.7464, 0.6952 [(a)]	0.7464, 0.7143 [(a)]
X-radiation, λ /Å	Mo-*K*α, 0.71073	Mo-*K*α, 0.71073	Mo-*K*α, 0.71073
data collect. temperat. /K	100(1)	100(1)	100(1)
θ range /°	2.0 to 32.5	1.6 to 29.6	2.1 to 32.6
index ranges *h*,*k*,*l*	–16 ... 16, –16 ... 16, –22 ... 22	–19 ... 19, –19 ... 19, –24 ... 24	–21 ... 21, –17 ... 17, –27 ... 27
reflections measured	40054	68517	78152
unique [R_{int}]	10692 [0.0334]	16340 [0.0649]	10620 [0.0471]
observed [$I \geq 2\sigma(I)$]	7720	10732	8303

	B1a•H(TFA)	**B12**•0.5H_2O	**B13**•0.5(1,4-dioxane)
data / restraints /parameters	10692 / 0 / 442	16340 / 0 / 779	10620 / 83 / 469
GooF on F^2	1.026	1.030	1.025
R indices [$F>4\sigma(F)$] $R(F)$, $wR(F^2)$	0.0526, 0.1278	0.0562, 0.1353	0.0448, 0.1069
R indices (all data) $R(F)$, $wR(F^2)$	0.0792, 0.1443	0.0971, 0.1564	0.0636, 0.1183
largest residual peaks /e·Å^{-3}	0.977, –0.847	0.531, –0.782	0.515, –0.231
instrument	Smart 1000	Smart 1000	Smart 1000

[(a)] empirical absorption correction.

	B14•MeOH	(***p*-MeO**)(***t*Bu)B1a**	**B1b**•H(TFA)
identification code	co_kr17a	co_kr20	co_kr23
CCDC number	1547415	1547416	1481465
formula	$C_{25}H_{34}N_4O_8$	$C_{35}H_{34}N_5O_9$	$C_{31}H_{32}F_3N_5O_9$
crystal system	monoclinic	triclinic	monoclinic
space group	*P* $2_1/c$	*P* –1	*P* $2_1/c$
a /Å	12.493(7)	11.050(4)	15.6763(4)
b /Å	20.536(11)	12.145(5)	15.6292(3)
c /Å	11.051(6)	13.994(6)	13.6985(4)
α /°	90	85.073(11)	90
β /°	112.618(12)	76.819(8)	109.606(3)
γ /°	90	68.427(10)	90
V /Å^3	2617(3)	1700.4(12)	3161.65(15)
Z	4	2	4
M_r	518.56	677.74	675.61
F_{000}	1104	720	1408
d_c /Mg·m^{-3}	1.316	1.324	1.419
μ /mm^{-1}	0.099	0.096	0.117
max., min. transmission factors	0.8620, 0.7681 [(a)]	0.8623, 0.8137 [(a)]	1.0000, 0.9186 [(b)]
X-radiation, λ /Å	Mo-$K\alpha$, 0.71073	Mo-$K\alpha$, 0.71073	Mo-$K\alpha$, 0.71073
data collect. temperat. /K	100(1)	100(1)	120(1)
θ range /°	2.0 to 26.5	2.2 to 32.5	3.3 to 32.6 °
index ranges *h*,*k*,*l*	–15 ... 15, –24 ... 25, –13 ... 13	–16 ... 16, –18 ... 18, –21 ... 21	–22 ... 23, –23 ... 23, –20 ... 20
reflections measured	44523	44381	89608
unique [R_{int}]	5387 [0.0641]	11478 [0.0292]	11017 [0.0651]
observed [$I \geq 2\sigma(I)$]	3850	9747	8190
data / restraints /parameters	5387 / 1 / 361	11478 / 0 / 515	11017 / 91 / 545
GooF on F^2	1.042	1.028	1.068
R indices [$F>4\sigma(F)$] $R(F)$, $wR(F^2)$	0.0521, 0.1405	0.0399, 0.1062	0.0563, 0.1341
R indices (all data) $R(F)$, $wR(F^2)$	0.0798, 0.1575	0.0485, 0.1136	0.0809, 0.1472
largest residual peaks /e·Å^{-3}	0.987, –0.274	0.514, –0.216	0.427, –0.302
instrument	Smart 1000	Smart 1000	Supernova

[(a)] empirical absorption correction. [(b)] numerical absorption correction.

	B19•H(TFA)	[Na^{I}(**(*t*Bu)$_2$B2**)]Br	**B2**•7H_2O
identification code	co_kr32	co_kr33_sq	co498
CCDC number	1547417	1547418	1550809
formula	$C_{23}H_{25}F_3N_4O_7$	$C_{47}H_{58}BrN_6NaO_{11}$	$C_{35}H_{48}N_6O_{16}$
crystal system	monoclinic	orthorhombic	orthorhombic
space group	*P* $2_1/c$	*A e a* 2	*P n a* 2_1
a /Å	10.617(5)	13.19166(6)	16.1688(5)
b /Å	16.091(8)	35.73270(15)	12.4691(4)
c /Å	14.083(6)	22.02932(13)	19.1512(6)
α /°	90	90	90
β /°	102.890(10)	90	90
γ /°	90	90	90
V /Å^3	2345.4(19)	10384.04(9)	3861.1(2)
Z	4	8	4
M_r	526.47	985.89	808.79
F_{000}	1096	4128	1712
d_c /Mg·m^{-3}	1.491	1.261	1.391
μ /mm^{-1}	0.126	1.663	0.941
max., min. transmission factors	0.7464, 0.6908 [(a)]	0.929, 0.704 [(b)]	0.877, 0.800 [(a)]
X-radiation, λ /Å	Mo-$K\alpha$, 0.71073	Cu-$K\alpha$, 1.54184	Cu-$K\alpha$, 1.54184
data collect. temperat. /K	100(1)	120(1)	90
θ range /°	2.0 to 32.5	2.0 to 32.5	133.4 [(c)]
index ranges *h*,*k*,*l*	–15 ... 15, –24 ... 23, –21 ... 20	–16 ... 16, –43 ... 43, –26 ... 26	–19 ... 19, –14 ... 14, –22 ... 22
reflections measured	59693	199437	26819
unique [R_{int}]	8074 [0.0460]	9874 [0.0354]	6470 [0.036]
observed [$I \geq 2\sigma(I)$]	6359	9730	6124
data / restraints /parameters	8074 / 205 / 425	9874 / 273 / 611	6470 / - / 584
GooF on F^2	1.045	1.033	1.06
R indices [$F>4\sigma(F)$] $R(F)$, $wR(F^2)$	0.0473, 0.1133	0.0355, 0.0936	0.029, 0.069
R indices (all data) $R(F)$, $wR(F^2)$	0.0662, 0.1237	0.0359, 0.0941	-
largest residual peaks /e·Å^{-3}	0.723, –0.531	0.856, –0.977	0.27, –0.17
instrument	Smart 1000	Supernova	Bruker APEX DUO

[(a)] empirical absorption correction. [(b)] numerical absorption correction. [(c)] 2θ max.

	[Co^{II}(**B1a**)](TFA) •2MeOH	[Co^{II}(**B1b**)](TFA) •MeOH	[Ni^{II}(**B1a**)](TFA) •7H_2O
identification code	co_kr30	co_kr31	co_kr12
CCDC number	1481460	1481466	1481461
formula	$C_{33}H_{38}CoF_3N_5O_{11}$	$C_{32}H_{34}CoF_3N_5O_{10}$	$C_{31}H_{44}F_3N_5NiO_{16}$
crystal system	triclinic	triclinic	triclinic
space group	*P* –1	*P* –1	*P* –1
a /Å	10.74834(19)	9.7429(7)	11.172(5)
b /Å	11.9384(2)	10.3992(7)	11.783(5)
c /Å	14.7516(2)	18.0310(11)	15.767(7)
α /°	80.4845(14)	83.892(5)	79.170(8)
β /°	74.3407(15)	84.613(5)	78.226(6)
γ /°	71.9137(16)	66.113(7)	66.386(13)
V /Å^3	1725.70(6)	1658.3(2)	1848.7(14)
Z	2	2	2
M_r	796.61	764.57	858.42
F_{000}	826	790	896
d_c /Mg·m^{-3}	1.533	1.531	1.542
μ /mm^{-1}	4.647	4.788	0.620
max., min. transmission factors	0.723, 0.547 [(b)]	0.853, 0.601 [(b)]	0.7464, 0.7104 [(a)]
X-radiation, λ /Å	Cu-*K*α, 1.54184	Cu-*K*α, 1.54184	Mo-*K*α, 0.71073
data collect. temperat. /K	120(1)	120(1)	100(1)
θ range /°	3.9 to 70.2	4.7 to 70.8	1.9 to 32.4
index ranges *h*,*k*,*l*	–13 ... 13, –14 ... 14, –17 ... 17	–11 ... 11, –12 ... 11, –20 ... 21	–16 ... 16, –17 ... 17, –23 ... 23
reflections measured	98093	19546	47875
unique [R_{int}]	6536 [0.0386]	6261 [0.0460]	12406 [0.0256]
observed [$I \geq 2\sigma(I)$]	6412	5306	11261
data / restraints /parameters	6536 / 0 / 486	6261 / 168 / 530	12406 / 66 / 574
GooF on F^2	1.046	1.032	1.042
R indices [$F>4\sigma(F)$] $R(F)$, $wR(F^2)$	0.0415, 0.1192	0.0393, 0.0884	0.0328, 0.0867
R indices (all data) $R(F)$, $wR(F^2)$	0.0422, 0.1198	0.0505, 0.0932	0.0370, 0.0898
largest residual peaks /e·Å^{-3}	0.761, –0.622	0.344, –0.272	1.325, –0.914
instrument	Supernova	Supernova	Smart 1000

[(a)] empirical absorption correction. [(b)] numerical absorption correction.

	[Ni^{II}(**B1b**)](TFA) •MeOH	[Cu^{II}(**B1a**)](TFA) •2.5MeOH	[Cu^{II}((***p*-MeO**)**B1a**)] (TFA)•MeCN•5.2H_2O
identification code	co_kr27	co_kr08	co_kr22
CCDC number	1481467	1481462	-
formula	$C_{32}H_{34}F_3N_5NiO_{10}$	$C_{33.50}H_{40}CuF_3N_5O_{11.50}$	$C_{35}H_{49.4}CuF_3N_6O_{17.2}$
crystal system	triclinic	monoclinic	triclinic
space group	*P* –1	*P* $2_1/n$	*P* –1
a /Å	9.75342(18)	14.0568(2)	9.183(4)
b /Å	10.3822(2)	17.4975(2)	15.117(7)
c /Å	17.9979(3)	15.9217(2)	15.651(6)
α /°	84.1480(16)	90	92.310(11)
β /°	84.4177(15)	113.9347(17)	101.567(6)
γ /°	66.7227(19)	90	96.516(13)
V /Å^3	1662.20(6)	3579.33(9)	2110.4(15)
Z	2	4	2
M_r	764.35	817.24	949.94
F_{000}	792	1696	990
d_c /Mg·m^{-3}	1.527	1.517	1.495
μ /mm^{-1}	0.666	0.695	0.611
max., min. transmission factors	0.950, 0.899 [(a)]	1.0000, 0.8932 [(a)]	0.7464, 0.6979 [(a)]
X-radiation, λ /Å	Mo-*K*α, 0.71073	Mo-*K*α, 0.71073	Mo-*K*α, 0.71073
data collect. temperat. /K	120(1)	120(1)	100(1)
θ range /°	3.2 to 32.9	3.3 to 32.9	1.3 to 32.5
index ranges *h*,*k*,*l*	–14 ... 14, –15 ... 15, –26 ... 27	–20 ... 21, –25 ... 26, –23 ... 23	–13 ... 13, –22 ... 22, –23 ... 23
reflections measured	94547	226734	55228
unique [R_{int}]	11605 [0.0486]	12735 [0.0718]	14264 [0.0299]
observed [$I \geq 2\sigma(I)$]	10112	11542	12529
data / restraints /parameters	11605 / 73 / 507	12735 / 0 / 506	14264 / 11 / 616
GooF on F^2	1.073	1.176	1.034
R indices [$F>4\sigma(F)$] $R(F)$, $wR(F^2)$	0.0399, 0.0968	0.0491, 0.1016	0.0334, 0.0873
R indices (all data) $R(F)$, $wR(F^2)$	0.0480, 0.1008	0.0576, 0.1047	0.0404, 0.0923
largest residual peaks /e·Å^{-3}	0.600, –0.620	0.538, –0.475	0.685, –0.593
instrument	Supernova	Supernova	Smart 1000

[(a)] empirical absorption correction.

	[Cu^{II}(**B1b**)](TFA) •MeOH	[Zn^{II}(**B1a**)](TFA) •2H_2O	[Zn^{II}((***p*-MeO**)**B1a**)] (TFA)•MeOH
identification code	co_kr24	co_kr11	co_kr19
CCDC number	1481468	1481463	-
formula	$C_{32}H_{34}CuF_3N_5O_{10}$	$C_{31}H_{34}F_3N_5O_{11}Zn$	$C_{34}H_{38}F_3N_5O_{12}Zn$
crystal system	triclinic	triclinic	monoclinic
space group	*P* –1	*P* –1	*P* $2_1/c$
a /Å	9.759(4)	8.07052(9)	12.00403(14)
b /Å	10.509(4)	11.30254(11)	20.1822(3)
c /Å	18.061(7)	18.06615(14)	14.46784(15)
α /°	83.634(12)	84.1173(7)	90
β /°	85.035(12)	88.3010(8)	91.0765(11)
γ /°	65.796(12)	80.5013(8)	90
V /Å^3	1677.3(12)	1616.66(3)	3504.47(7)
Z	2	2	4
M_r	769.18	775.00	831.06
F_{000}	794	800	1720
d_c /Mg·m^{-3}	1.523	1.592	1.575
μ /mm^{-1}	0.733	0.847	0.790
max., min. transmission factors	0.7464, 0.6954 [(b)]	0.903, 0.870 [(b)]	1.00000, 0.88470 [(a)]
X-radiation, λ /Å	Mo-*K*α, 0.71073	Mo-*K*α, 0.71073	Mo-*K*α, 0.71073
data collect. temperat. /K	100(1)	120(1)	120(1)
θ range /°	2.1 to 32.5	3.4 to 29.0	3.3 to 32.8
index ranges *h*,*k*,*l*	–14 ... 14, –15 ... 15, –26 ... 27	–10 ... 11, –15 ... 15, –24 ... 24	–18 ... 17, –30 ... 30, –21 ... 21
reflections measured	43907	91634	122913
unique [R_{int}]	11360 [0.0282]	8194 [0.0284]	12338 [0.0498]
observed [$I \geq 2\sigma(I)$]	10145	7968	11198
data / restraints /parameters	11360 / 73 / 507	8194 / 6 / 476	12338 / 91 / 554
GooF on F^2	1.048	1.085	1.214
R indices [$F>4\sigma(F)$] $R(F)$, $wR(F^2)$	0.0337, 0.0847	0.0429, 0.1016	0.0570, 0.1172
R indices (all data) $R(F)$, $wR(F^2)$	0.0395, 0.0879	0.0443, 0.1023	0.0648, 0.1201
largest residual peaks /e·Å^{-3}	0.980, –0.369	1.674, –1.358	0.927, –0.548
instrument	Smart 1000	Supernova	Supernova

[(a)] empirical absorption correction. [(b)] numerical absorption correction.

	[Zn^{II}(**B1b**)](TFA)•xsolv	[Ga^{III}(**B1a**)](TFA)(NO_3)•7H_2O[359]	[Ga^{III}(**B1b**)](NO_3)$_2$•2.5MeOH
identification code	co_kr25	co_kr07	co_kr26
CCDC number	1481469	1481464	1481470
formula	$C_{31}H_{30}F_3N_5O_9Zn$	$C_{31}H_{44}F_3GaN_6O_{19}$	$C_{31.50}H_{40}GaN_7O_{15.50}$
crystal system	monoclinic	triclinic	triclinic
space group	$P\,2_1/c$	$P\,\bar{1}$	$P\,\bar{1}$
a /Å	13.297(5)	10.5773(3)	9.142(5)
b /Å	15.114(7)	14.1652(4)	12.371(6)
c /Å	16.383(7)	15.4132(4)	16.188(10)
α /°		62.650(3)	101.721(11)
β /°	92.816(6)	72.710(2)	100.771(9)
γ /°		77.138(2)	92.801(15)
V /Å^3	3289(2)	1948.41(10)	1753.9(17)
Z	4	2	2
M_r	738.97	931.44	834.42
F_{000}	1520	964	866
d_c /Mg·m^{-3}	1.492	1.588	1.580
μ /mm^{-1}	0.825	0.808	0.870
max., min. transmission factors	0.7464, 0.6986 [(b)]	0.928, 0.880 [(a)]	0.7464, 0.6617 [(a)]
X-radiation, λ /Å	Mo-$K\alpha$, 0.71073	Mo-$K\alpha$, 0.71073	Mo-$K\alpha$, 0.71073
data collect. temperat. /K	100(1)	110(1)	100(1)
θ range /°	1.83 to 32.5	3.3 to 28.8 °	2.3 to 30.5
index ranges h,k,l	–19 ... 19, –22 ... 22, –23 ... 24	–14 ... 14, –19 ... 19, –20 ... 20	–13 ... 13, –17 ... 17, –22 ... 23
reflections measured	84609	87392	39960
unique [R_{int}]	11409 [0.0363]	9592 [0.0561]	10642 [0.0518]
observed [$I \geq 2\sigma(I)$]	9324	8735	8138
data / restraints / parameters	11409 / 129 / 503	9592 / 44 / 600	10642 / 0 / 455
GooF on F^2	1.023	1.128	1.028
R indices [$F>4\sigma(F)$] $R(F)$, $wR(F^2)$	0.0415, 0.1091	0.0508, 0.1224	0.0436, 0.1010
R indices (all data) $R(F)$, $wR(F^2)$	0.0555, 0.1191	0.0575, 0.1255	0.0655, 0.1090
largest residual peaks /e·Å^{-3}	1.210, –0.661	0.697, –0.824	0.753, –0.580
instrument	Smart 1000	Supernova	Smart 1000

[(a)] empirical absorption correction. [(b)] numerical absorption correction.

	$[In^{III}(\mathbf{B2})](TFA)\bullet 4H_2O$
identification code	co500
CCDC number	1550810
formula	$C_{37}H_{40}InF_3N_6O_{15}$
crystal system	monoclinic
space group	*C* 2/*c*
a /Å	18.4408(9)
b /Å	13.2688(7)
c /Å	32.7981(19)
α /°	90
β /°	105.509(2)
γ /°	90
V /Å^3	7733.1(7)
Z	8
M_r	980.57
F_{000}	4000
d_c /Mg·m^{-3}	1.684
μ /mm^{-1}	0.708
max., min. transmission factors	0.919, 0.864 [(a)]
X-radiation, λ /Å	Mo-*K*α, 0.71073
data collect. temperat. /K	100
2θ max	61.4
index ranges *h*,*k*,*l*	–26 ... 26, –18 ... 18, –46 ... 46
reflections measured	105852
unique [R_{int}]	11855 [0.036]
observed [$I \geq 2\sigma(I)$]	10863
data / restraints / parameters	10863 / - / 607
GooF on F^2	1.05
R indices [$F>4\sigma(F)$] $R(F)$, $wR(F^2)$	0.023, 0.055
R indices (all data) $R(F)$, $wR(F^2)$	-
largest residual peaks /e·Å^{-3}	0.66, –0.62
instrument	Bruker X8 APEX II

[(a)] empirical absorption correction.

Appendix C: Potentiometric titrations – simulated titration curves, species distribution diagrams, and stability data of selected metal complexes

Simulated titration curves

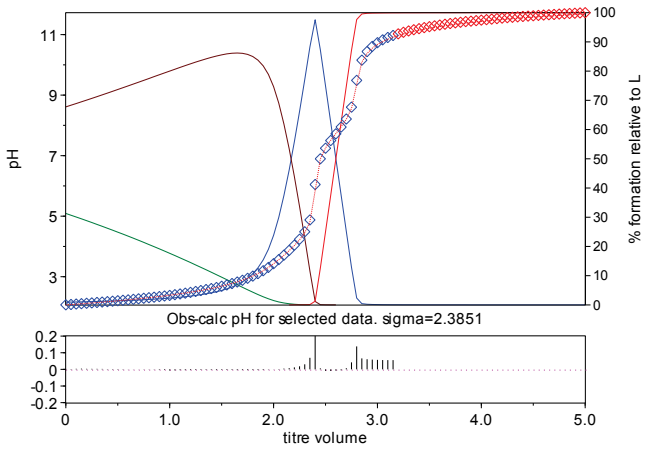

Figure C 1. Titration curve of an aqueous solution of **B1a** with 0.1 M KOH.

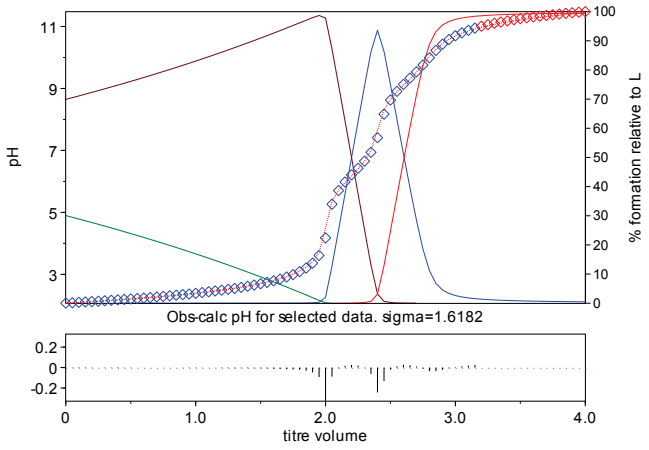

Figure C 2. Titration curve of an aqueous solution of **B1b** with 0.1 M KOH.

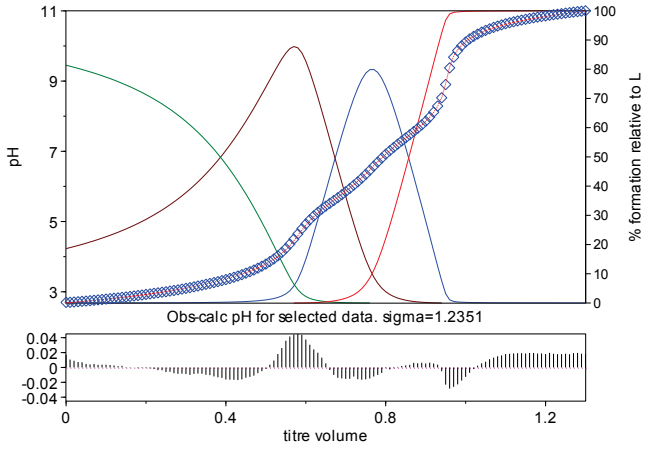

Figure C 3. Titration curve of an aqueous solution of **B2** with 0.1 M KOH.

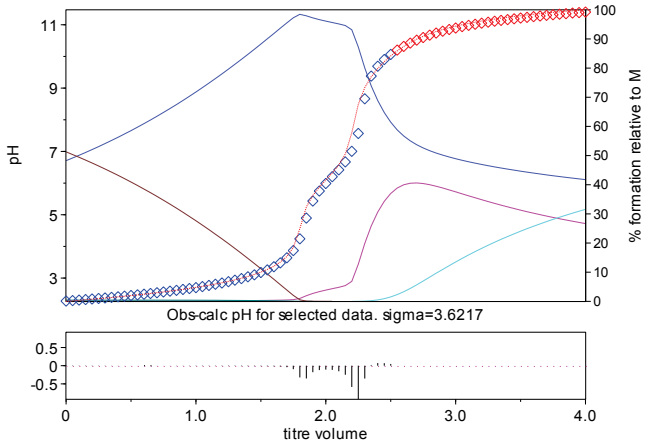

Figure C 4. Titration curve of an aqueous solution of **B1a**, EDTA, and Cu^{II} (1:1:1) with 0.1 M KOH.

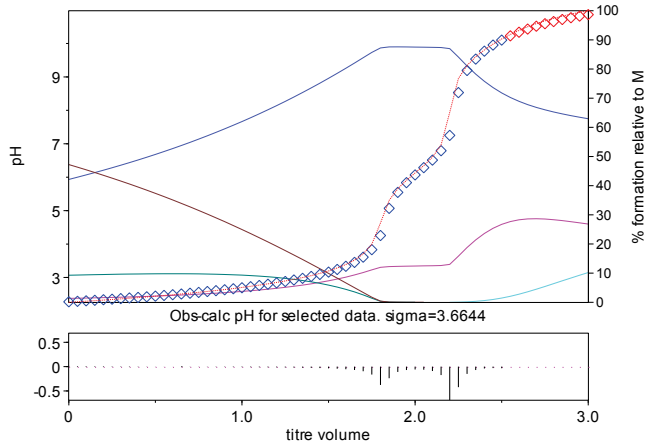

Figure C 5. Titration curve of an aqueous solution of **B1b**, EDTA, and Cu^{II} (1:1:1) with 0.1 M KOH.

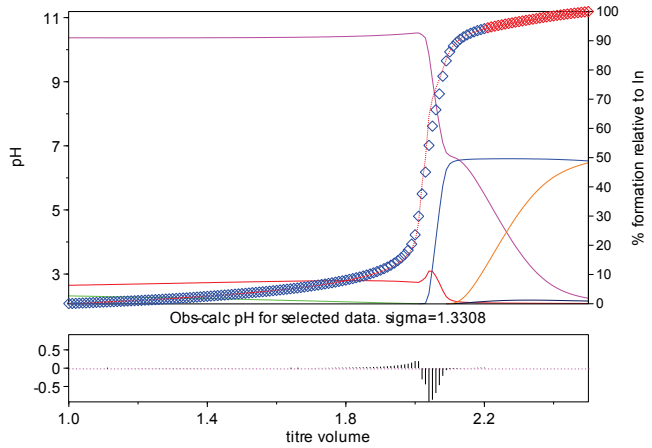

Figure C 6. Titration curve of an aqueous solution of **B2**, EDTA, and In^{III} (1:1:0.5) with 0.1 M KOH.

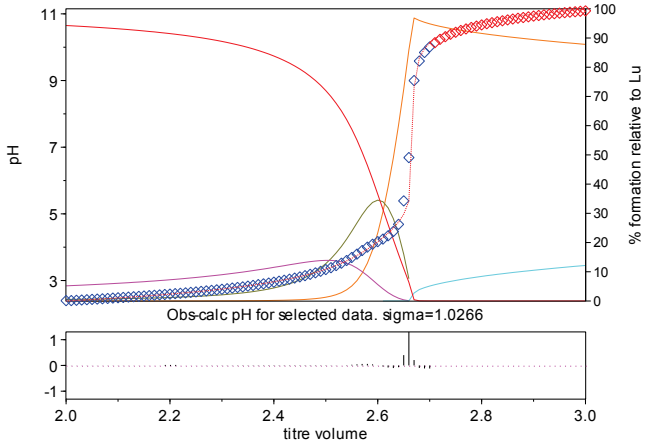

Figure C 7. Titration curve of an aqueous solution of **B2** and Lu^{III} (1:1) with 0.1 M KOH.

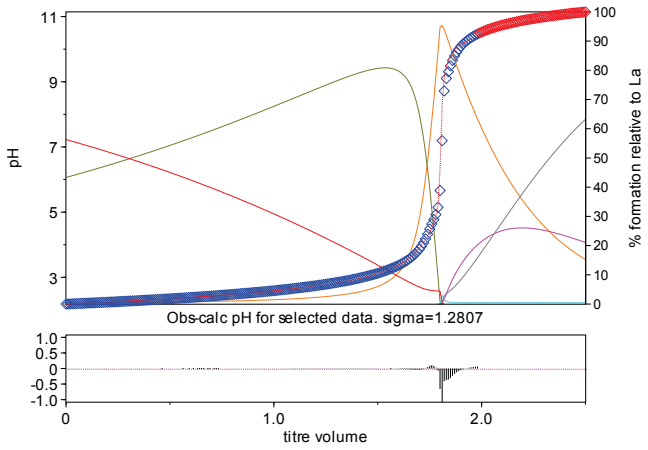

Figure C 8. Titration curve of an aqueous solution of **B2** and La^{III} (1:1) with 0.1 M KOH.

Species distribution diagrams

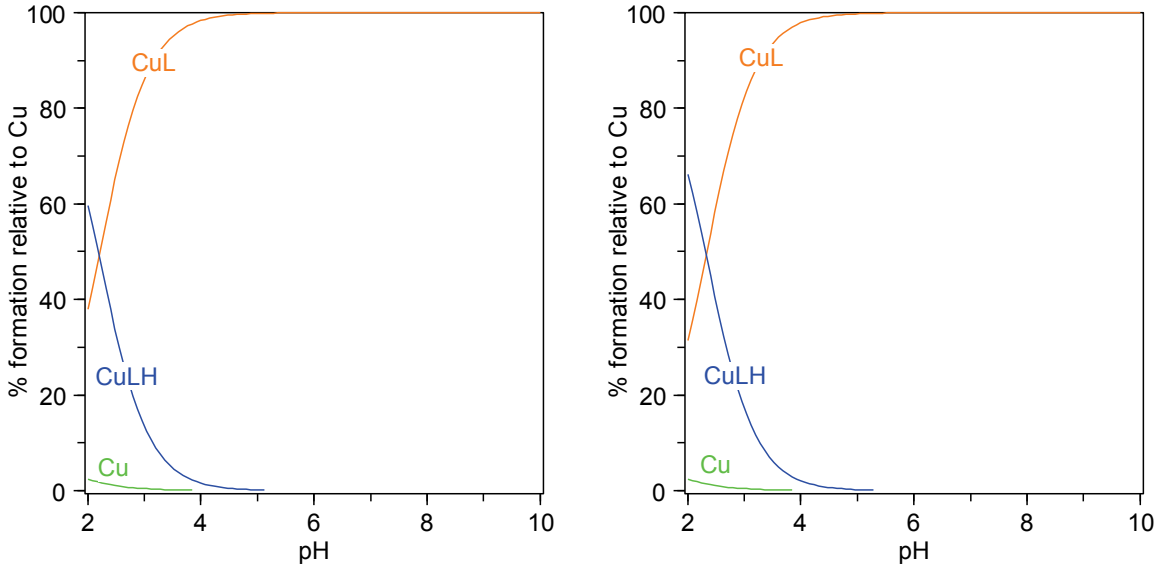

Figure C 9. Species distribution diagram of Cu^{II} in presence of **B1a** (left) and **B1b** (right) in aqueous solution for $c(Cu^{II}) = c(ligand) = 10^{-3}$ M.

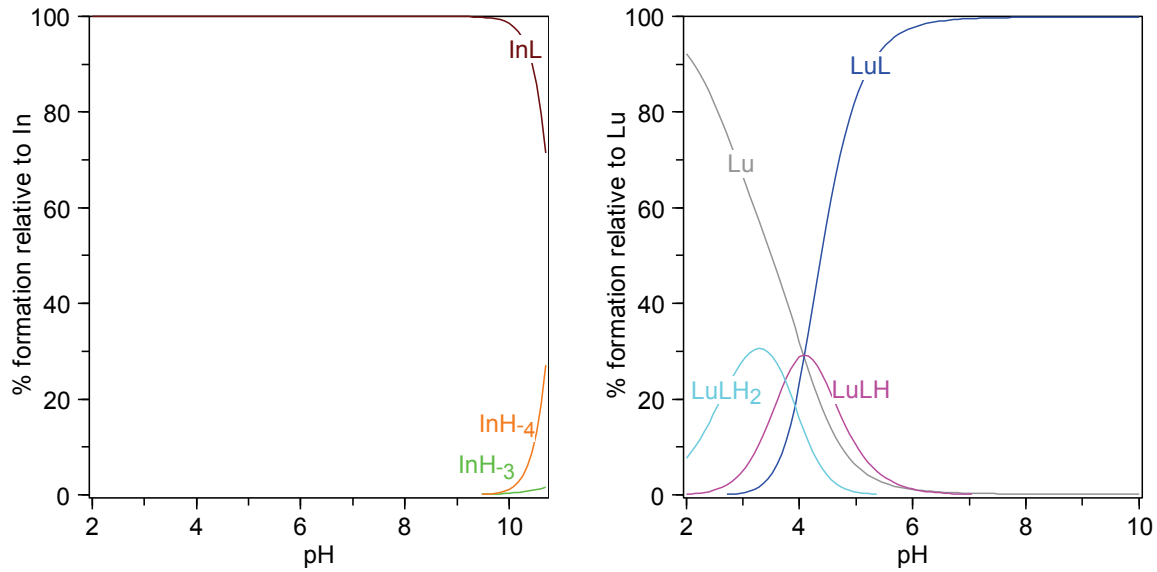

Figure C 10. Species distribution diagram of In^{III} (left) and Lu^{III} (right) in presence of **B2** in aqueous solution for $c(M^{III}) = c(\mathbf{B2}) = 10^{-3}$ M.

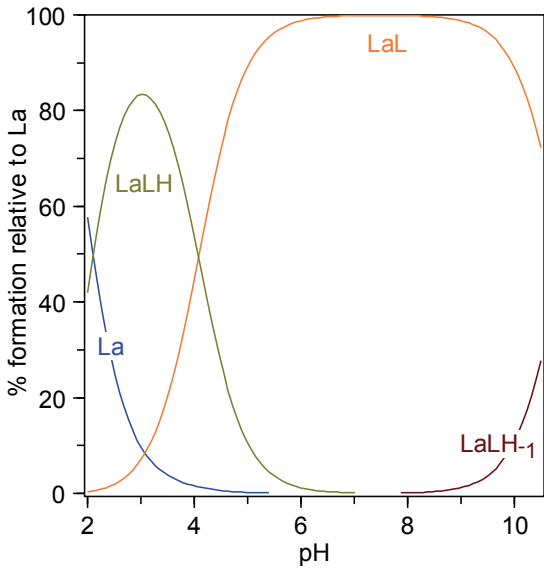

Figure C 11. Species distribution diagram of La^{III} in presence of **B2** in aqueous solution for c(La^{III}) = c(**B2**) = 10^{-3} M.

Stability data for selected metal complexes

Table C 1. Stability constants (log β_{ML}) and $pM_{7.4}$ values for selected Lu^{III} complexes.

ligand	log β_{ML}	$pM_{7.4}$ [(a)]	ref
DOTA (**L5**)	23.9	18.7	[415]
DTPA (**L10**)	22.46(2)	19.1	[58,415]
H_4octapa (**L35**)	20.08(9)	19.8	[58]
H_2bispa^2 (**B2**)	8.51(3)	9.1	

[(a)] Calculated for 10 µM total ligand and 1 µM total metal ion concentration at pH 7.4 and 25 °C.

Table C 2. Stability constants (log β_{ML}) and $pM_{7.4}$ values for selected La^{III} complexes.

ligand	log β_{ML}	$pM_{7.4}$ [(a)]	ref
DOTA (**L5**)	22.0(3)	16.8	[415]
PEPA (**L7**)	13.57(5)	9.7	[117]
HEHA (**L8**)	19.11(5)	20.8	[117]
H_2bispa^2 (**B2**)	11.42(6)	12.0	

[(a)] Calculated for 10 µM total ligand and 1 µM total metal ion concentration at pH 7.4 and 25 °C.

Appendix D: UV-vis-NIR spectra

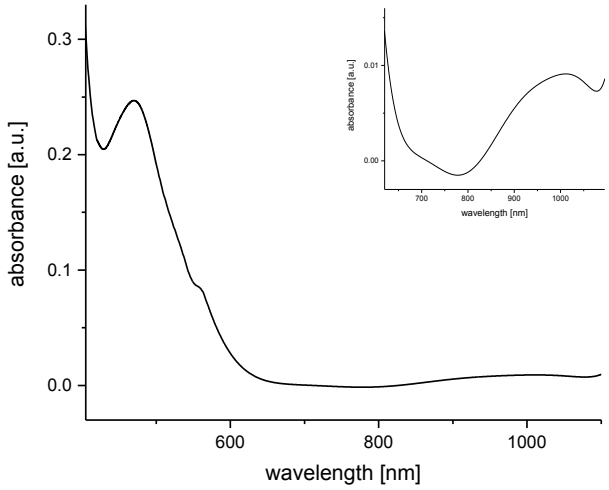

Figure D 1. UV-vis-NIR spectrum of [Co^{II}(**B1a**)](TFA) (DMSO, rt).

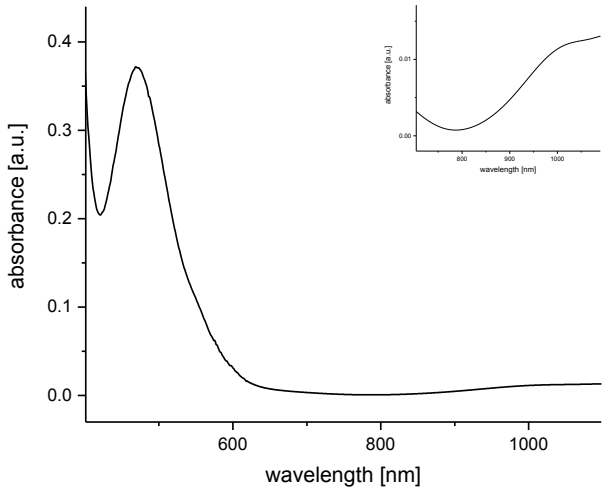

Figure D 2. UV-vis-NIR spectrum of [Co^{II}(**(*p*-MeO)B1a**)](TFA) (DMSO, rt).

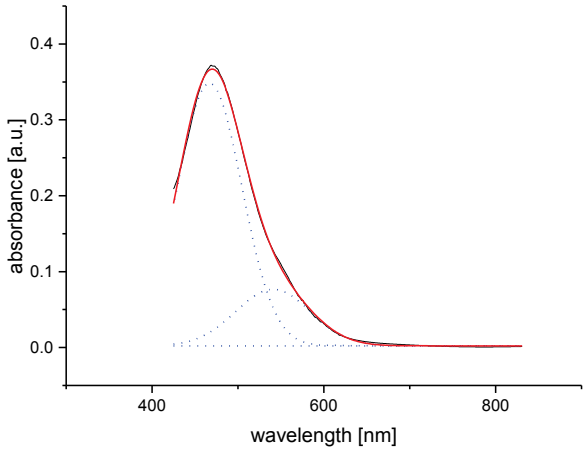

Figure D 3. Part of the UV-vis-NIR spectrum of [Co^{II}(**(*p*-MeO)B1a**)](TFA) (black) and simulation (red) with two Gaussian envelopes (blue, dotted line).

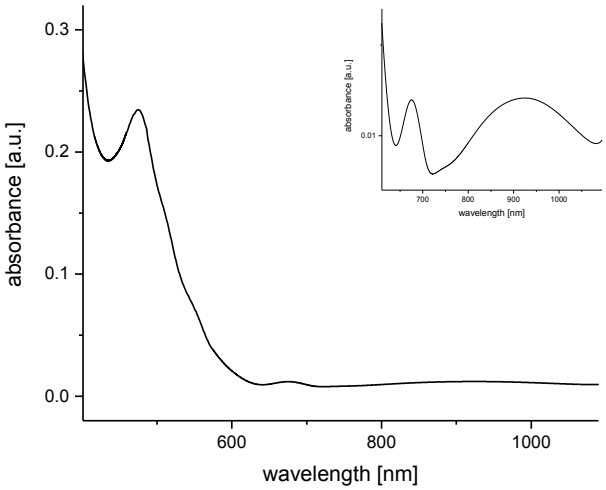

Figure D 4. UV-vis-NIR spectrum of [Co^{II}(**B1b**)](TFA) (DMSO, rt)

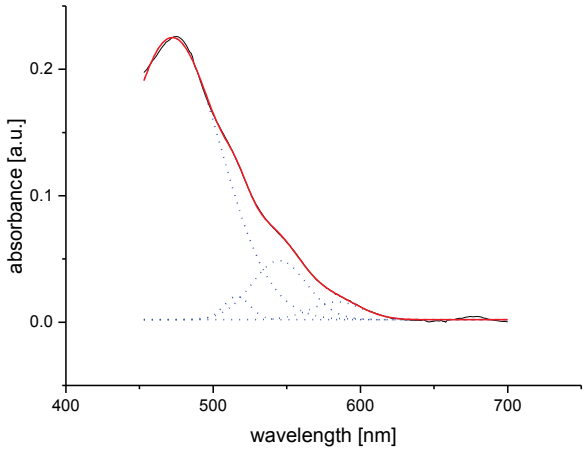

Figure D 5. Part of the UV-vis-NIR spectrum of [Co^{II}(**B1b**)](TFA) (black) and simulation (red) with four Gaussian envelopes (blue, dotted line).

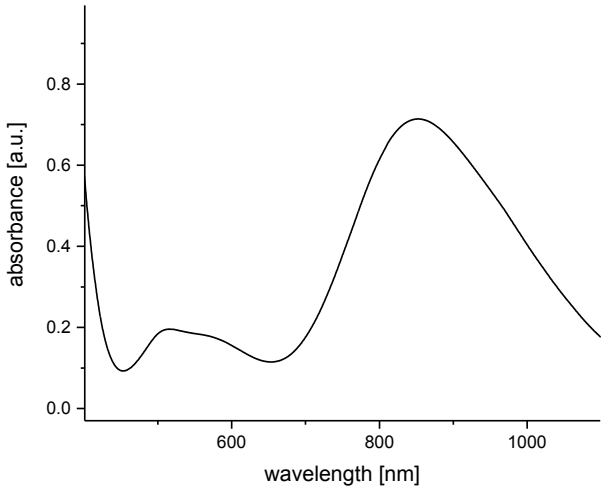

Figure D 6. UV-vis-NIR spectrum of [Ni^{II}(**B1a**)](TFA) (MeOH, rt).

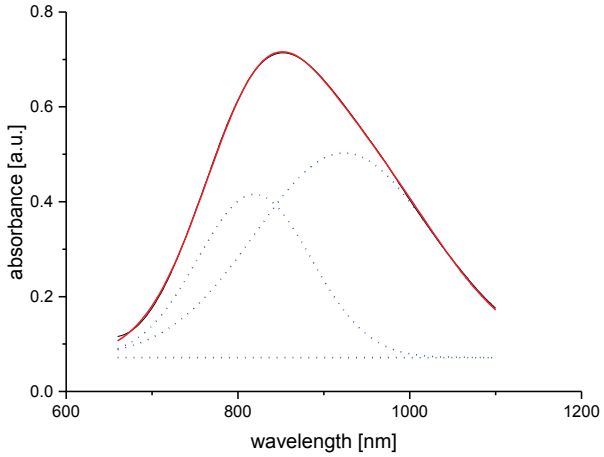

Figure D 7. Part of the UV-vis-NIR spectrum of [Ni^{II}(**B1a**)](TFA) (black) and simulation (red) with two Gaussian envelopes (blue, dotted line).

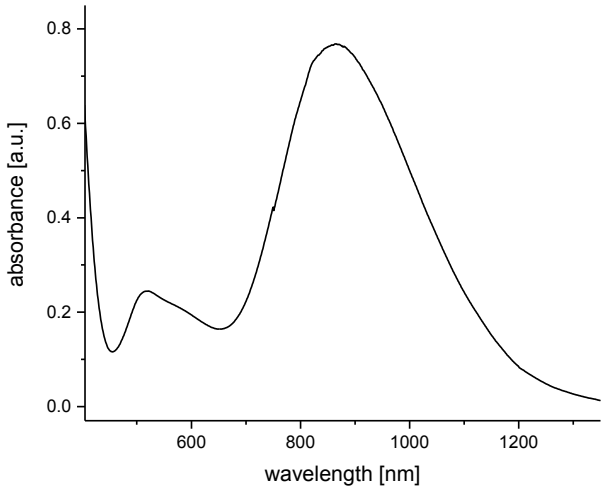

Figure D 8. UV-vis-NIR spectrum of [Ni^{II}((***p*-MeO**)**B1a**)](TFA) (MeOH, rt).

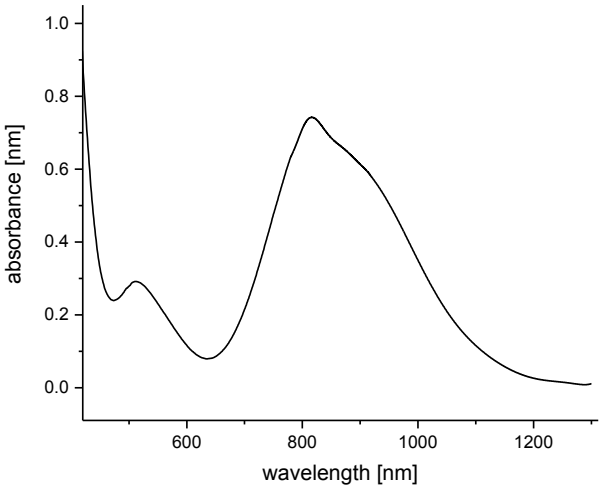

Figure D 9. UV-vis-NIR spectrum of [Ni^{II}(**B1b**)](TFA) (MeOH, rt).

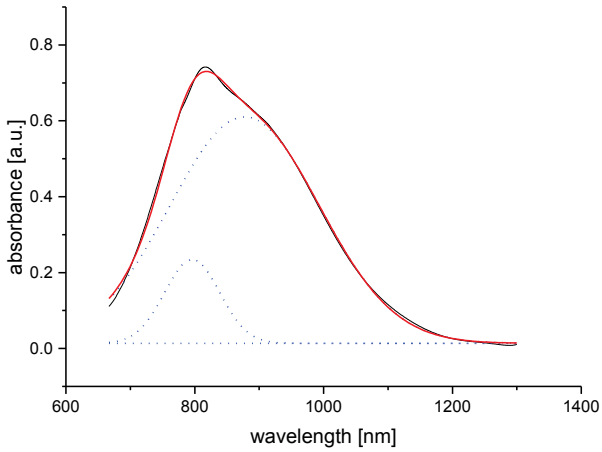

Figure D 10. Part of the UV-vis-NIR spectrum of [Ni^{II}(**B1b**)](TFA) (black) and simulation (red) with two Gaussian envelopes (blue, dotted line).

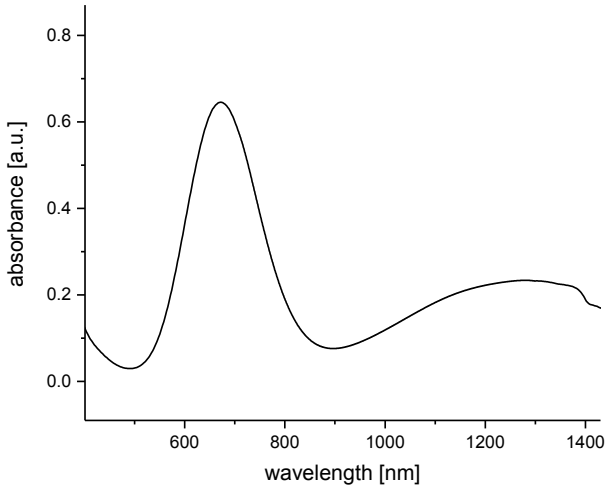

Figure D 11. UV-vis-NIR spectrum of [Cu^{II}(**B1a**)](TFA) (MeOH, rt).

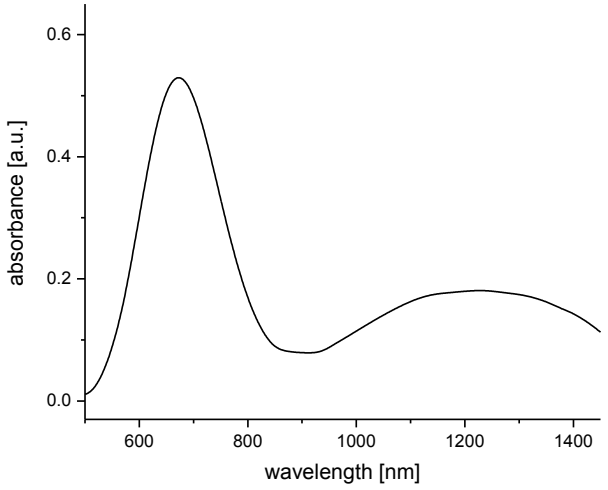

Figure D 12. UV-vis-NIR spectrum of [Cu^{II}(**(*p*-MeO)B1a**)](TFA) (MeOH, rt).

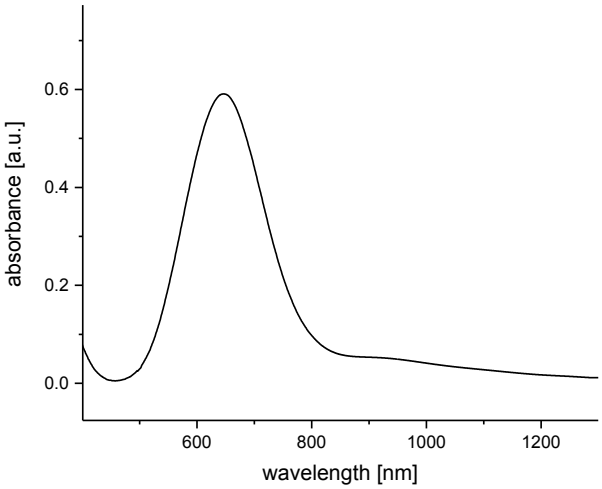

Figure D 13. UV-vis-NIR spectrum of [Cu^{II}(**B1b**)](TFA) (MeOH, rt).

Appendix E: ESR spectra

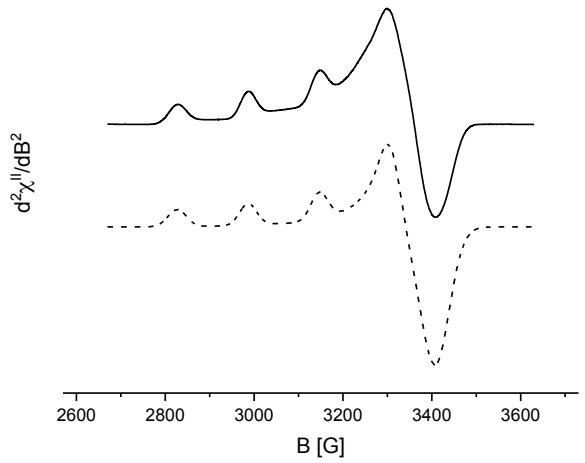

Figure E 1. ESR spectrum (frozen solution, X band) of [Cu^{II}(**B1a**)](TFA) (MeOH, 8 K). Solid line: experimental spectrum, dashed line: simulation with XSophe ($g_{x,y}$ = 2.059, g_z = 2.243, $A_{x,y}$ = 13 [10^{-4} cm], A_z = 164 [10^{-4} cm], f = 9.63491 GHz).

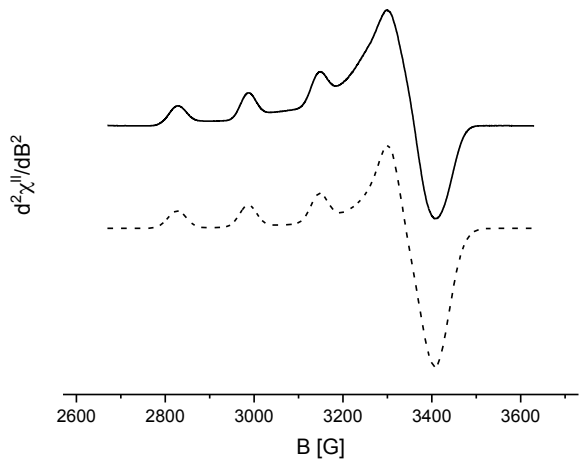

Figure E 2. ESR spectrum (frozen solution, X band) of [Cu^{II}(**(*p*-MeO)B1a**)](TFA) (MeOH, 8 K). Solid line: experimental spectrum, dashed line: simulation with XSophe ($g_{x,y}$ = 2.057, g_z = 2.244, $A_{x,y}$ = 10 [10^{-4} cm], A_z = 170 [10^{-4} cm], f = 9.636852 GHz).

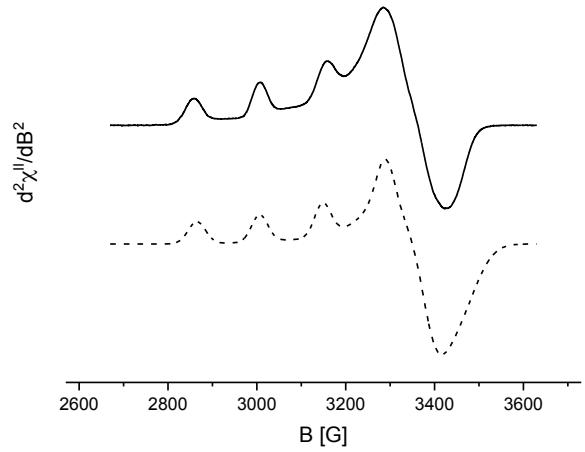

Figure E 3. ESR spectrum (frozen solution, X band) of [Cu^{II}(**B1b**)](TFA) (MeOH, 8 K). Solid line: experimental spectrum, dashed line: simulation with XSophe (g_x = 2.016, g_y = 2.068, g_z = 2.236, A_x = 27 [10^{-4} cm], A_y = 21 [10^{-4} cm], A_z = 164 [10^{-4} cm], f = 9.635967 GHz).

Appendix F: Details of the AOM analysis

AOM parameters

donor group	interaction	published parameter [cm^{-1}] (for M-L = 1 Å)	adjusted parameter [cm^{-1}] (for M-L = 1 Å)
amine[385]	e_σ	492471	492471
pyridine[390]	e_σ	432598	375000
	e_π	64890	85000
carboxylate[393]	e_σ	294458	250000
	e_π	73314	62500

In the calculations ds-mixing was considered by assigning each ligand an additional bonding parameter e_{ds} with e_{ds} = 1/4 e_σ.[330,390]

CAMMAG input

Cu^{II}-**B1a**

Setup-file based on structure CCDC 1481462:

```
TITL 1A
CELL 1 1 1 90.0 90.0 90.0
CONF 2 9
BASE 2D
CU1  -3.050719 6.332817 10.939760
N7   -3.679929 8.547090 10.592288
N3   -1.191356 7.061325 11.165078
NPY1 -2.400448 6.065630  9.042959
NPY2 -3.040171 6.469892 12.969834
NPA  -5.017398 6.098928 10.753094
OPA  -3.361979 4.048186 11.119674
CPY1 -2.904762 5.250649  8.100358
CPY2 -3.875976 5.888135 13.844606
CPA  -5.565974 4.877130 10.921177
MULT 1
XREF 2 1 6
LGND 1 2 1 3
LGND 2 3 1 2
LGND 3 4 1 8
LGND 4 5 1 9
LGND 5 6 1 10
LGND 6 7 1 6
END
```

Run-file with published parameters:

```
TITL 1A
CALC 3
LATT 1
LIST 1 1 1 0 0 0 1 1 0 1
B    0
K    0.7
ZETA 406
ESIG 1 3094
ESIG 2 7475
ESIG 3 6061
EPIX 3 0
EPIY 3 909
ESIG 4 6276
EPIX 4 0
EPIY 4 941
ESIG 5 6939
EPIX 5 0
EPIY 5 1041
ESIG 6 1924
EPIX 6 0
EPIY 6 0
LINK 34 33 0.25
LINK 35 33 0.25
LINK 12  8 0.25
LINK 17 13 0.25
LINK 22 18 0.25
LINK 27 23 0.25
LINK 32 28 0.25
LINK 37 33 0.25
END
```

Cu^{II}-**B1b**

Setup-file based on structure CCDC 1481468:

```
TITL 1B
CELL 1 1 1 90.0 90.0 90.0
CONF 2 9
BASE 2D
CU1  5.439298 5.748974 3.074448
N7   5.556156 7.284103 1.785827
N3   4.146473 6.852681 4.262388
NPY1 6.892935 6.724293 4.744298
NPY2 3.289752 5.008898 2.373942
NPA  5.234356 4.428460 4.443221
OPA  6.692553 4.363589 2.327716
CPY1 8.064439 6.340780 5.272901
CPY2 2.853520 3.859104 1.838293
CPA  5.955613 3.310090 4.317310
MULT 1
XREF 5 1 3
LGND 1 2 1 3
LGND 2 3 1 2
LGND 3 4 1 8
LGND 4 5 1 9
LGND 5 6 1 10
LGND 6 7 1 6
END
```

Run-file with published parameters:

```
TITL 1B
CALC 3
LATT 0
LIST 1 1 1 0 0 0 1 1 0 1
B    0
K    0.7
ZETA 406
ESIG 1 7520
ESIG 2 6191
ESIG 3 2158
EPIX 3 0
EPIY 3 324
ESIG 4 2387
EPIX 4 0
EPIY 4 358
ESIG 5 8829
EPIX 5 0
EPIY 5 1324
ESIG 6 4440
EPIX 6 0
EPIY 6 0
LINK 34 33 0.25
LINK 35 33 0.25
LINK 12  8 0.25
LINK 17 13 0.25
LINK 22 18 0.25
LINK 27 23 0.25
LINK 32 28 0.25
LINK 37 33 0.25
END
```

Appendix G: Cyclovoltammograms and details of the RORABACHER plot

Cyclovoltammograms

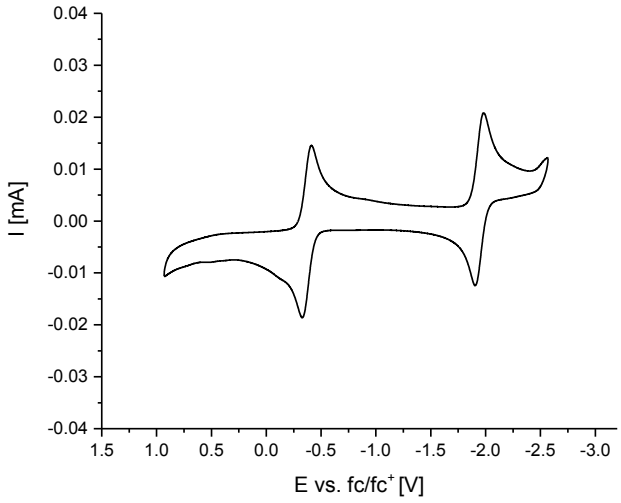

Figure G 1. Cyclovoltammogram of [Co^{II}(**B1a**)](TFA) (DMF, 0.1 M (*n*-Bu_4N)(ClO_4)).

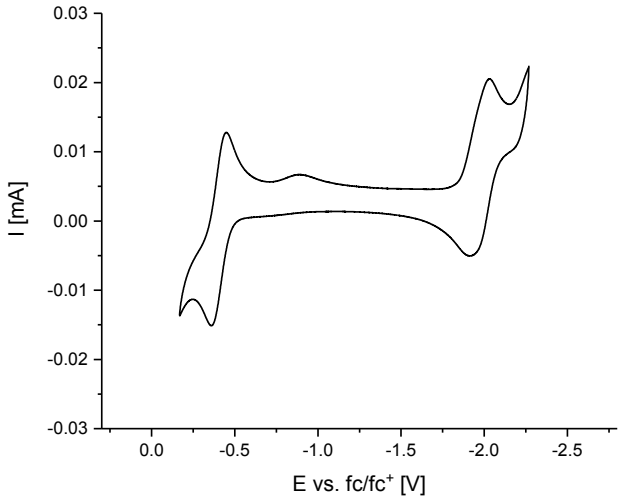

Figure G 2. Cyclovoltammogram of [Co^{II}(**(*p*-MeO)B1a**)](TFA) (DMF, 0.1 M (*n*-Bu_4N)(ClO_4)).

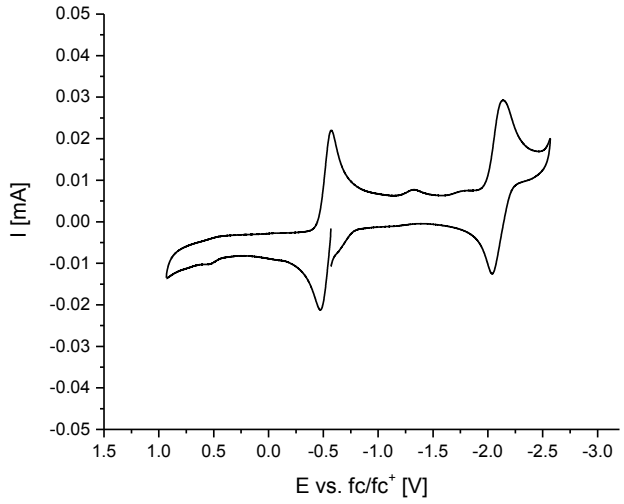

Figure G 3. Cyclovoltammogram of [Co^{II}(**B1b**)](TFA) (DMF, 0.1 M (*n*-Bu_4N)(ClO_4)).

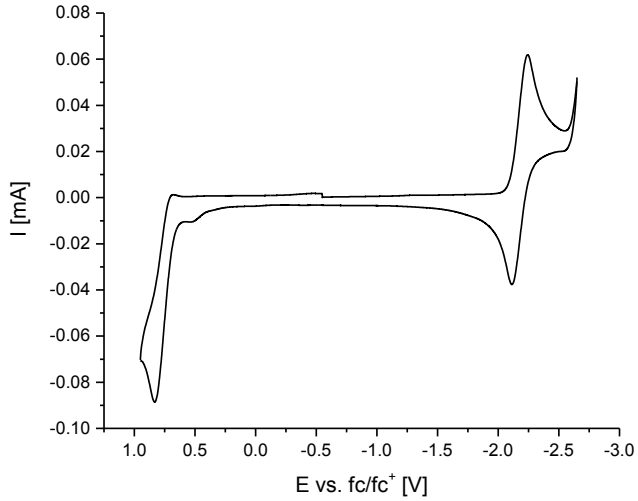

Figure G 4. Cyclovoltammogram of [Ni^{II}(**B1a**)](TFA) (DMF, 0.1 M (*n*-Bu_4N)(ClO_4)).

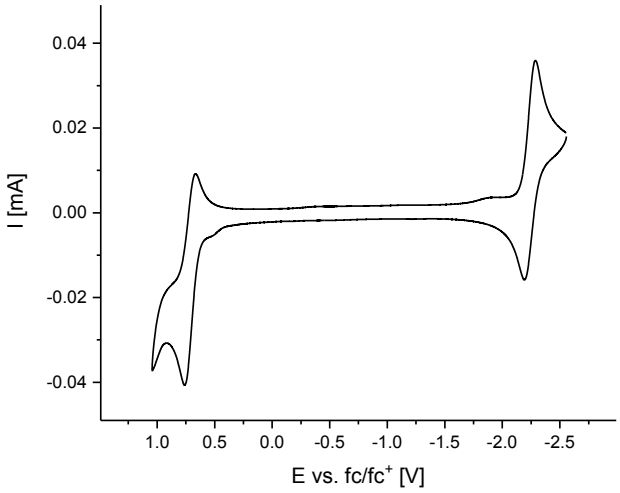

Figure G 5. Cyclovoltammogram of [Ni^{II}(**(*p*-MeO)B1a**)](TFA) (DMF, 0.1 M (*n*-Bu_4N)(ClO_4)).

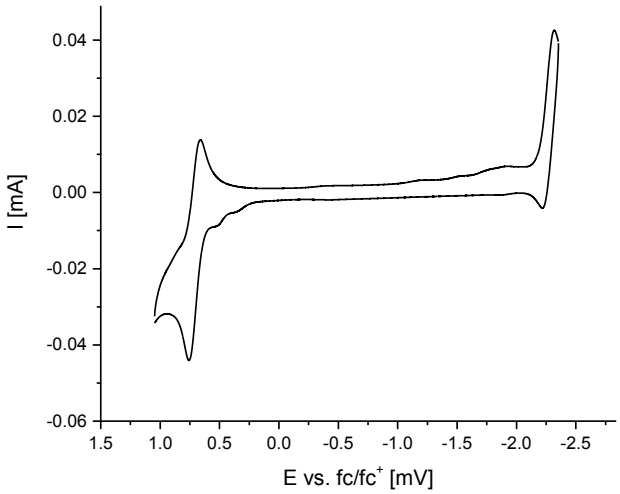

Figure G 6. Cyclovoltammogram of [Ni^{II}(**B1b**)](TFA) (DMF, 0.1 M (*n*-Bu_4N)(ClO_4)).

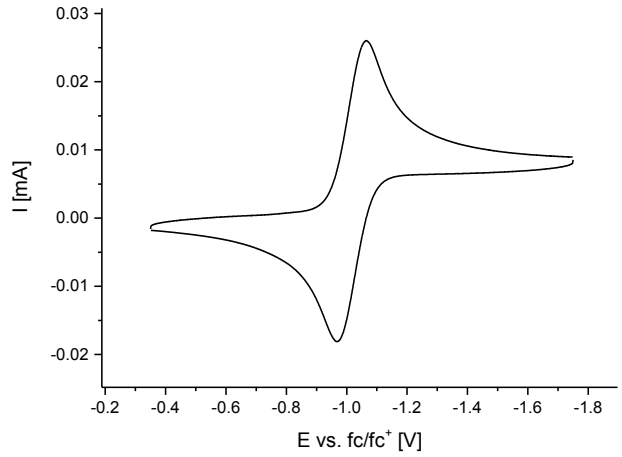

Figure G 7. Cyclovoltammogram of [Cu^{II}(**B1a**)](TFA) (DMF, 0.1 M (*n*-Bu_4N)(ClO_4)).

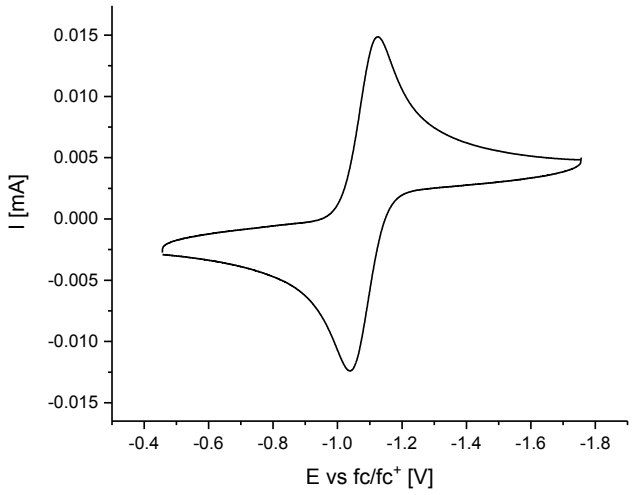

Figure G 8. Cyclovoltammogram of [Cu^{II}((***p*-MeO**)**B1a**)](TFA) (DMF, 0.1 M (*n*-Bu_4N)(ClO_4)).

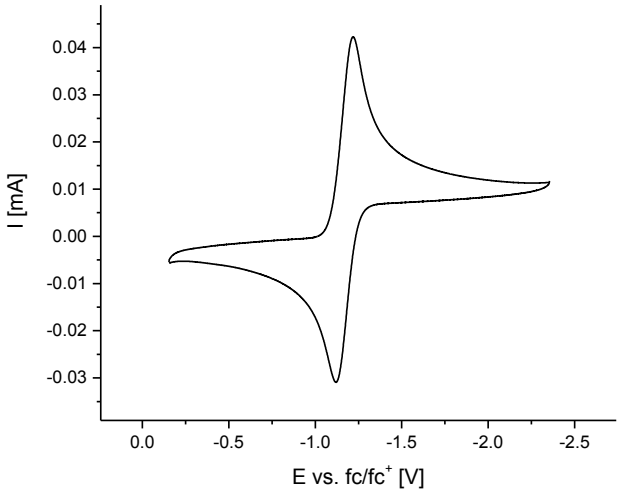

Figure G 9. Cyclovoltammogram of [Cu^{II}(**B1b**)](TFA) (DMF, 0.1 M (*n*-Bu_4N)(ClO_4)).

Potentials of $Cu^{II/I}L$ redox couples and $Cu^{II}L$ formation constants used for the plot in **Figure 50** (Chapter 4.1.6)

ligands	E *vs.* SHE [V] (a)	E *vs.* $Ag/AgNO_3$ [V] (b)	E *vs.* Ag/AgCl [V] (c)	E *vs.* fc/fc^+ [V] (d)	log K_{CuL} (e)	ref.
[21]aneS6	0.89			0.49	1.09	[167,280]
[15]aneS5	0.68			0.28	4.18	[167,280]
[15]aneNS4	0.46			0.06	9.8	[167,280]
[15]aneN2S3	0.1			–0.3	16.02	[167,280]
[14]aneNS3	0.38			–0.02	9.25	[167,280]
[14]aneN2S2	0.04			–0.36	15.26	[167,280]
[14]aneNSSN	–0.01			–0.41	15.72	[167,280]
[14]aneN3S	–0.24			–0.64	20	[167,280]
[14]aneN4	–0.66			–1.06	27.2	[167,280]
[9]aneS3	0.72			0.32	4.42	[167,280]
[13]aneS4	0.52			0.12	3.44	[167,280]
[14]aneS4	0.58			0.18	4.34	[167,280]
[15]aneS4	0.64			0.24	3.17	[167,280]
[16]aneS4	0.71			0.31	2.2	[167,280]
oxathiane-[12]aneS4	0.72			0.32	3.02	[167,280]
[13]aneS4-ol	0,54			0.14	3.1	[167,280]
[14]aneS4-ol	0.49			0.09	5.59	[167,280]
[15]aneS4-ol	0.71			0.31	2.28	[167,280]
[16]aneS4-ol	0.73			0.33	1.51	[167,280]
Me2-2.3.2-S4	0.79			0.39	1.97	[167,280]
Me2-3.2.3-S4	0.83			0.43	1.18	[167,280]
cis-cyhx-Me2-3.2.3-S4	0.75			0.35	2.45	[167,280]
trans-cyhx-Me2-3.2.3-S4	0.77			0.37	2.94	[167,280]
TMMEA	0.68			0.28	6.29	[167,280]
TEMEA	0.67			0.27	6.35	[167,280]
PMMEA	0.38			–0.02	11.06	[167,280]
PMAS	0.4			0	10.48	[167,280]

PEMEA	0.6			0.2	7.89	[167,280]
PEAS	0.61			0.21	7.87	[167,280]
BPMMEA	0.06			–0.34	16.1	[167,280]
BPMEEA	0.08			–0.32	15.82	[167,280]
BPEMEA	0.46			0.06	9.1	[167,280]
BPEEEA	0.47			0.07	9.2	[167,280]
TPMA	–0.15			–0.55	17.6	[167,280]
TPEA	0.51			0.11	9.35	[167,280]
N_2py_2		–0.42	–0.43	–0.51 / –0.6	16.56	[303]
$(Me)N_2py_2$		–0.1	–0.05	–0.19 / –0.22	9.6	[303]
$N_2py_3^o$		–0.6	–0.52	–0.69 / –0.69	18.31	[303]
$N_2py_3^u$		–0.49	–0.41	–0.58 / –0.58	15.66	[303]
N_2py_4		–0.57	–0.5	–0.66 / –0.67	16.28	[303]
$Hbispa^{1a}$			–0.47 (–0.63)	–1.02 (–1.06)	18.88	([359])
$Hbispa^{1b}$			–0.62	–1.17	19.44	

[(a)] H_2O, 0.1 M $NaClO_4$. [(b)] MeCN, 0.1 M (n-Bu_4N)(PF_6). [(c)] H_2O, 0.1 M KNO_3 for the bispidines or DMF (MeCN), 0.1 M (n-Bu_4N)(ClO_4) (0.1 M (n-Bu_4N)(PF_6)) for the bispa ligands. [(d)] Potentials of fc/fc^+ used for the conversion of the measured redox values: –0.4 V (*vs.* SHE, H_2O), –0.09 V (*vs.* $Ag/AgNO_3$, MeCN),[303] –0.17 V (*vs.* Ag/AgCl, H_2O),[303] –0.43 (*vs.* Ag/AgCl, MeCN),[359] and –0.55 (*vs.* Ag/AgCl, DMF). [(e)] H_2O, 25 °C, μ = 0.1.

Appendix H: Details of the radiochemical investigations of the hexadentate bispa ligands

SOD challenge experiment

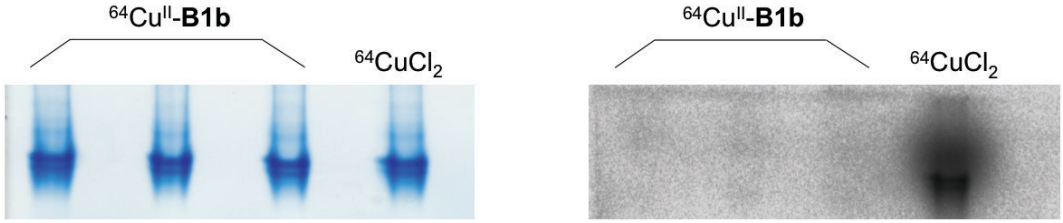

Figure H 1. Analysis of $^{64}Cu^{II}$ transchelation to human erythrocyte superoxide dismutase (SOD) for $^{64}Cu^{II}$-**B1b**. Colloidal Coomassie stained native polyacrylamide gel (left) and autoradiography showing $^{64}Cu^{II}$-labeled bands of SOD (right).

Serum stability assay analyzed by gel electrophoresis

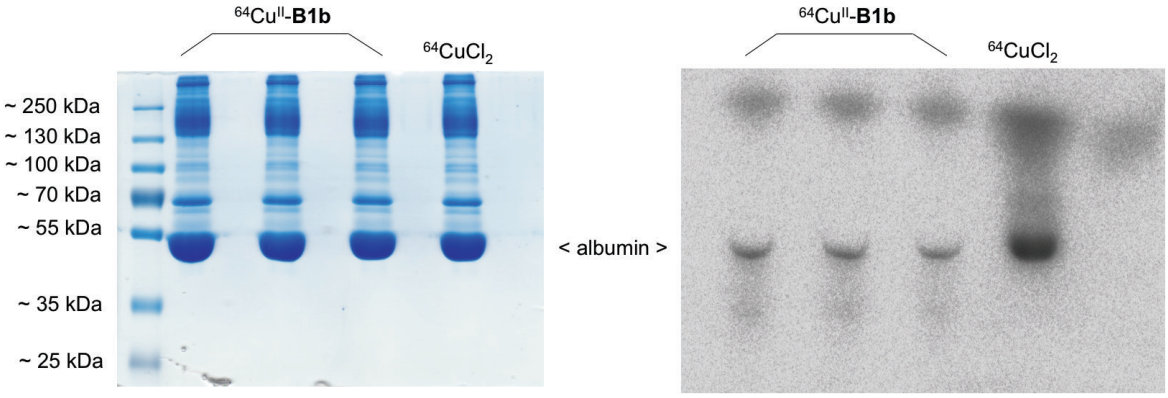

Figure H 2. Analysis of $^{64}Cu^{II}$ transchelation to human serum proteins for $^{64}Cu^{II}$-**B1b**. Colloidal Coomassie stained native polyacrylamide gel (left) and autoradiography showing $^{64}Cu^{II}$-labelled bands of human serum proteins (right).

Biodistribution data

Table H 1. Amount of $^{64}Cu^{II}$-**B1a** in selected organs, tissues and excretion in rats at 5 min, 60 min, and 24 h p.i. (four Wistar Kyoto rats per time point, mean value ± standard deviation SD).

%ID/g	5 min	± SD	60 min	± SD	24 h	± SD
Blood	0.825	0.156	0.040	0.013	0.014	0.013
Heart	0.373	0.089	0.028	0.011	0.015	0.009
Lung	0.625	0.123	0.063	0.020	0.021	0.012
Muscle	0.232	0.047	0.222	0.314	0.006	0.003
WAT	0.614	0.469	0.120	0.112	0.009	0.009
BAT	0.315	0.070	0.043	0.013	0.015	0.011
Bone	0.382	0.098	0.044	0.016	0.014	0.009
Spleen	0.391	0.260	0.241	0.222	0.018	0.010
Adrenals	0.596	0.327	0.129	0.087	0.022	0.008
Kidneys	4.266	1.681	0.760	0.202	0.414	0.210
Liver	0.413	0.162	0.156	0.034	0.059	0.035
Brain	0.033	0.005	0.005	0.001	0.002	0.001
Pancreas	0.556	0.405	0.250	0.155	0.014	0.007
Thymus	0.276	0.049	0.029	0.011	0.017	0.013
Thyroid	0.576	0.080	0.054	0.011	0.030	0.017
Harderian	0.363	0.119	0.062	0.020	0.015	0.007
Testes	0.258	0.063	0.032	0.014	0.016	0.012
Skin	0.624	0.121	0.058	0.008	0.029	0.011
%ID	5 min	± SD	60 min	± SD	24 h	± SD
Stomach	0.789	0.296	0.254	0.234	0.127	0.175
Intestine	3.194	0.487	3.116	2.521	11.388	14.977
Feces	0.000	0.000	0.000	0.000	5.219	4.992
Urine	35.735	6.846	82.458	6.201	87.220	9.906

Table H 2. Amount of $^{64}Cu^{II}$-**B1b** in selected organs, tissues and excretion in rats at 5 min, 60 min, and 24 h p.i. (four Wistar Kyoto rats per time point, mean value ± standard deviation SD).

%ID/g	5 min	± SD	60 min	± SD	24 h	± SD
Blood	1.116	0.062	0.149	0.029	0.013	0.001
Heart	0.493	0.016	0.085	0.013	0.021	0.004
Lung	0.824	0.036	0.194	0.021	0.026	0.002
Muscle	0.309	0.016	0.101	0.087	0.012	0.008
WAT	0.490	0.103	0.230	0.246	0.010	0.009
BAT	0.545	0.051	0.142	0.034	0.025	0.005
Bone	0.549	0.024	0.114	0.015	0.019	0.003
Spleen	0.346	0.037	0.200	0.178	0.033	0.005
Adrenals	0.579	0.058	0.196	0.117	0.036	0.014
Kidneys	3.913	0.482	1.245	0.174	0.219	0.004
Liver	0.517	0.024	0.287	0.049	0.086	0.005
Brain	0.051	0.007	0.013	0.002	0.003	0.000
Pancreas	0.703	0.096	0.758	0.264	0.061	0.009
Thymus	0.427	0.033	0.126	0.018	0.033	0.006
Thyroid	0.960	0.053	0.498	0.235	0.030	0.007
Harderian	0.429	0.042	0.138	0.049	0.017	0.003
Testes	0.264	0.021	0.073	0.018	0.023	0.001
Skin	0.962	0.072	0.390	0.155	0.035	0.003
%ID	5 min	± SD	60 min	± SD	24 h	± SD
Stomach	1.187	0.563	5.244	3.836	0.640	0.840
Intestine	4.470	0.536	15.980	10.693	1.368	0.482
Urine	18.687	1.311	48.454	13.734	94.784	1.934

Table H 3. Amount of $^{68}Ga^{III}$-**B1a** in selected organs, tissues and excretion in rats at 5 min and 60 min p.i. (four Wistar Kyoto rats per time point, mean value ± standard deviation SD).

%ID/g	5 min	± SD	60 min	± SD
Blood	1.870	0.241	1.616	0.051
Heart	0.698	0.076	0.494	0.057
Lung	0.952	0.072	0.953	0.158
Muscle	0.256	0.043	0.186	0.018
WAT	1.244	0.640	1.327	0.948
BAT	0.508	0.152	0.482	0.198
Bone	0.618	0.046	0.980	0.108
Spleen	0.373	0.175	0.849	0.675
Adrenals	0.463	1.350	0.818	0.363
Kidneys	1.576	0.255	0.931	0.120
Liver	0.700	0.140	0.683	0.079
Brain	0.062	0.012	0.065	0.013
Pancreas	0.472	0.126	0.942	0.979
Thymus	0.413	0.041	0.376	0.096
Thyroid	0.874	0.216	0.768	0.236
Harderian	0.638	0.124	0.786	0.234
Testes	0.337	0.115	0.359	0.019
Skin	0.692	0.072	0.458	0.040
%ID	5 min	± SD	60 min	± SD
Stomach	0.741	0.113	0.571	0.256
Intestine	3.722	1.242	3.472	0.374
Feces	0.000	0.000	0.000	0.000
Urine	22.666	11.263	39.480	5.204

10 Acknowledgements – Danksagung

An erster Stelle danke ich Prof. Dr. Peter Comba für die interessante und anwendungsbezogene Themenstellung, die sehr guten Arbeitsbedingungen, und die großen Freiräume. Ebenso bedanke ich mich für die bereichernde Möglichkeit, auch an anderen Orten forschen zu dürfen.

Für die Übernahme der Zweitkorrektur möchte ich Prof. Dr. Roland Krämer danken.

In addition, I would like to express my gratitude to Dr. Holger Stephan (HZDR) and Prof. Dr. Chris Orvig (UBC) for welcoming me in their research groups and for supervising me during my stay.

In this context, I would like to thank our collaborators at HZDR (Dr. Holger Stephan and Prof. Dr. Jens Pietzsch), and at UBC / TRIUMF (Prof. Dr. Chris Orvig and Dr. Caterina Ramogida) for the very constructive cooperation. I am especially thankful to Karin Landrock for performing numerous experiments with the bispa[1] ligands, as well as to Dr. Caterina Ramogida for the very efficient and important work she has done for us. The excellent research facilities at the respective institutions are also gratefully acknowledged.

For collecting the X-ray data and for solving the corresponding structures I would like to thank Prof. Dr. Hubert Wadepohl and Dr. Brian Patrick.

Vielen Dank an die Mitarbeiter der Service-Einrichtungen der chemischen Institute der Universität Heidelberg für die schnelle und sorgfältige Bearbeitung der Proben; insbesondere Prof. Dr. Hubert Wadepohl und Heidrun Haungs für das Aufsetzen der Kristalle, Prof. Dr. Markus Enders und Beate Termin für die NMR-Experimente, Dr. Jürgen Gross und Mitarbeitern für die massenspektrometrischen Messungen, sowie den Mitarbeitern des Mikroanalyse-Labors für die Elementaranalysen. Ebenso danke ich den Schlossern, den Elektrikern, den Feinmechanikern, den Reinigungskräften, und den Mitarbeitern der Chemikalienausgabe.

Für die finanzielle Unterstützung im Rahmen eines Promotions- bzw. Auslandsstipendiums danke ich der Landesgraduiertenförderung Baden-Württemberg sowie dem Deutschen Akademischen Austauschdienst.

Ein großer Dank gilt meinen fleißigen Korrekturlesern Dr. Annika Eisenschmidt, Bianca Pokrandt, Asha Roberts, Peter Rübenacker, Dr. Ursula Rübenacker, Miriam Starke, Dr. Holger Stephan, und Dr. Johannes Straub.

Bei meinen Bachelor- und Forschungsstudenten Miriam Starke, Thomas Josephy, Vanessa Müller, Saskia Krieg, Laura Grimm, Friedrich Bialas, Maren Haas, und Hendrik Hoffmann bedanke ich mich für die stets exzellente Arbeit.

Dem gesamten Arbeitskreis Comba (Kathrin Benzing, Simone Bosch, Peter Comba, Katharina Diehm, Annika Eisenschmidt, Dieter Faltermeier, Tulika Gupta, Michael Großhauser, Maik Jakob, Marko Hermsen, Marion Kerscher, Saskia Krieg, Anna-Maria Löhr, Bodo Martin, Nina Mehrkens, Michael Morgen, Dennis Müller, Bianca Pokrandt, Asha Roberts, Markus Rössler, Henning Rudolf, Miriam Starke, Karin Stelzer, Johannes Straub, Marlies von Schoenebeck-Schilli, Arkadius Waleska, Michael Westphal), sowie unseren Nachbarn, dem Arbeitskreis Linti (Julian Anton, Philipp Butzug, Tanju Eligüzel, Michael Gast, Philipp Siebenbürger, Yasi Riahi) danke ich für die familiäre Atmosphäre, die guten Unterhaltungen, und die große Unterstützung von allen Seiten.

Bei Marion Kerscher möchte ich mich für die Aufnahme der ESR-Spektren bedanken.

Bodo Martin danke ich für die Hilfe und die Geduld bei Computerproblemen, sowie für die interessanten Gespräche.

Dennis Müller danke ich ganz herzlich für die Unterstützung bei den AOM-Rechnungen.

Unseren großartigen Sekretärinnen Karin Stelzer und Marlies von Schoenebeck-Schilli danke ich für die Hilfe bei jeglichen Verwaltungsangelegenheiten und beim Einreichen von Publikationen.

Ganz besonders danke ich Maik Jakob, der mir von meinem ersten Tag in der Gruppe an jederzeit mit Rat und Tat zur Seite stand. Für deine Hilfsbereitschaft danke ich dir von Herzen.

Annika Eisenschmidt danke ich nicht nur für das gründliche Korrekturlesen dieser Arbeit, sondern auch für den frischen Wind und die Denkanstöße. Liebe Annika, ich bin unglaublich froh, dass dich die Wissenschaft in den Südwesten verschlagen hat. Mit deiner schier unendlichen Energie hast du mich inspiriert und motiviert. Da ich weiß, dass du kein Fan großer Worte bist, belasse ich es jetzt dabei und würde mich einfach freuen, wenn das mit uns so bliebe.

Bianca Pokrandt danke ich für die unglaublich große Hilfsbereitschaft, für die immense Fürsorglichkeit, und für die stets offenen Ohren. Liebe Bianca, du gehörst zu den Menschen, die einen den Glauben an das Gute nicht verlieren lassen. Dafür danke ich dir ganz besonders.

Johannes Straub, dem weltbesten Laborpartner, danke ich für die Hilfe bei Computer- und Softwareproblemen, für die ansteckend gute Laune und für die gute Musik. Du hast mir damit mehr als nur einmal den Tag gerettet.

Miriam Starke danke ich für die Fortführung unseres Projektes. Ich hätte mir definitiv keine bessere Nachfolgerin wünschen können.

I also would like to thank Sarah Spreckelmeyer and Lupe Jaraquemada Peláez from the Orvig group for making my stay in Vancouver so nice and enjoyable, and, of course, for taking me on my very first camping trip.

Wolfgang Schad danke ich für die richtigen Worte zur richtigen Zeit.

Meinen Mädels (Sonja Batke, Carolin Braun, Maria Feinstein, Stefanie Mewes, Charlotte Over) und Conrad Wagner danke ich für die schöne gemeinsame Zeit während des Studiums. Ebenso freue ich mich, dass Annika Eisenschmidt und Markus Hiller während der Promotion ihren Weg nach Heidelberg und in unsere kleine Gruppe gefunden haben.

Meiner Familie (Felix Geuder, Julian Geuder, Stefanie Geuder, Torsten Geuder, Lesley Thomson, Benjamin Rübenacker, Brigitta Rübenacker, Christoph Rübenacker, Daniel Rübenacker, Karl Rübenacker (†), Martin Rübenacker, Nicholas Rübenacker, Peter Rübenacker, Ursula Rübenacker, Timothy Rübenacker, Alexander Rück, Augustin Sädtler (†), Eva-Maria Sädtler, Maria Sädtler, Beatrice Weber, Christian Weber, Sophia Weber, und Thomas Weber) danke ich für den Zusammenhalt und die Unterstützung in allen Lebenslagen. Je mehr ich von der Welt sehe, umso deutlicher wird mir bewusst, dass eine Familie wie die unsere in keinster Weise selbstverständlich ist. Es ist schön, dass es euch gibt!

Meiner besten Freundin Aline Walter danke ich für einfach Alles. Du bist für mich wie eine Schwester.

Meinen Bruderherzen Chris und Benni danke ich für das einzigartige Zusammengehörigkeitsgefühl, für moralische sowie tatkräftige Unterstützung, und für Lachanfälle bis der Bauch wehtut.

Für die Dankbarkeit, die ich meinen Eltern gegenüber empfinde, gibt es keine Worte. Dennoch möchte ich es an dieser Stelle versuchen: Mama und Papa, ich danke euch für die bedingungslose Unterstützung in allen Bereichen, für die Geborgenheit und die Liebe, für Wurzeln und für Flügel.

Meinem Mann Alex danke ich dafür, dass er mein Ruhepol ist und ganz besonders dafür, dass er mich nach so vielen Jahren immer noch jeden Tag zum Lachen bringt. Für immer hin und zurück, hin und zurück…

11 Eidesstattliche Versicherung

gemäß § 8 der Promotionsordnung der Naturwissenschaftlich-Mathematischen Gesamtfakultät der Universität Heidelberg

1. Bei der eingereichten Dissertation zum Thema

Synthesis and evaluation of novel picolinic acid-based bispidine ligands and their metal complexes for the application in nuclear medicine

handelt es sich um meine eigenständig erbrachte Leistung.

2. Ich habe nur die angegebenen Quellen und Hilfsmittel benutzt und mich keiner unzulässigen Hilfe Dritter bedient. Insbesondere habe ich wörtlich oder sinngemäß aus anderen Werken übernommene Inhalte als solche kenntlich gemacht.

3. Die Arbeit oder Teile davon habe ich bislang nicht an einer Hochschule des In- oder Auslands als Bestandteil einer Prüfungs- oder Qualifikationsleistung vorgelegt.

4. Die Richtigkeit der vorstehenden Erklärung bestätige ich.

5. Die Bedeutung der eidesstattlichen Versicherung und die strafrechtlichen Folgen einer unrichtigen oder unvollständigen eidesstattlichen Versicherung sind mir bekannt. Ich versichere an Eides statt, dass ich nach bestem Wissen die reine Wahrheit erklärt und nichts verschwiegen habe.

Ort und Datum Unterschrift